THE UNIVERSITY *of* EDINBURGH

Investigating tidewater glacier and iceberg submarine melting in Greenland's fjords

Alexis Noelle Moyer

Thesis submitted in fulfilment of the requirements for the degree of

Doctor of Philosophy

to the

University of Edinburgh

2019

Declaration

The work presented in this thesis is original and my own, unless indicated otherwise as part of jointly-authored publications. The candidate confirms that appropriate credit has been given within the thesis where reference has been made to the work of others. No part of the thesis has been submitted for any other award or professional qualification.

Alexis N Moyer

May 2019

Abstract

Accelerated mass loss from the Greenland Ice Sheet in recent decades has been concentrated around the coastal margins, where glacier ice fronts and the undersides of floating ice are in contact with warm ocean waters. The interaction of the ice sheet with a warming ocean leads to thinning of tidewater glaciers, which has been linked to increased glacier velocity, calving, retreat and subsequent mass loss. Our understanding of these ice-ocean interactions is limited, particularly regarding submarine melting of tidewater glacier ice fronts, which has been proposed as an initial trigger for glacier retreat and acceleration. Understanding the mechanisms promoting changes to tidewater glacier dynamics is critical, as they are currently absent from ice sheet models and present a large source of uncertainty in 21st century sea level rise predictions. This thesis develops two novel remote sensing techniques, to investigate both submarine melt rates under tidewater glacier floating ice tongues and iceberg freshwater fluxes from submarine melting, providing improved datasets and process understanding that can be used to constrain changes to the Greenland Ice Sheet in a warming world.

The first result of this thesis is the development of a methodology to estimate submarine melting under floating ice tongues using satellite imagery. Submarine melt rates were derived by differencing along-flow ice tongue surface elevation, in combination with ice tongue velocity and changes in surface mass balance. Kangiata Nunaata Sermia (KNS), a large tidewater glacier in southwest Greenland, was used as a proof-of-concept study site. Mean submarine melt rates under the seasonal ice tongue at KNS in spring 2013 reach over 0.8 ± 0.3 m d^{-1}, decreasing with distance down-fjord from the glacier grounding line and varying across-fjord. These variations in melt rate likely result from

changes in ice tongue draft and fjord water temperature with depth, but may also reflect the strength of subglacial discharge plumes exiting beneath the glacier grounding line.

Expanding upon these initial melt rate results, the thesis next explores the spatial and temporal variations in submarine melting at KNS from 2012 to 2014. Using the same methodology, derived melt rates vary significantly near the glacier grounding line, both spatially and temporally, with mean melt rates of 1.3 ± 0.6, 0.8 ± 0.3, and 1.0 ± 0.4 m d^{-1} across the ice tongue in 2012, 2013 and 2014, respectively. Areas of higher submarine melting correspond spatially with locations of subglacial discharge plumes and ice front calving activity observed during the melt season using time-lapse camera imagery, as well as to locations of modelled subglacial flow paths with large upstream catchment areas. These results suggest a dynamic subglacial hydrology system capable of rapidly re-routing subglacial discharge to different terminus outlets both within and between melt seasons. Furthermore, they provide an empirically-derived link between the presence of subglacial discharge plumes and areas of high spring submarine melting and calving along glacier termini.

Moving to east Greenland, the final results chapter turns to Sermilik Fjord, where a new methodology for estimating freshwater fluxes from icebergs is developed. The amount, timing and location of meltwater produced via submarine melting of icebergs can significantly impact local fjord water circulation and heat budget, which has implications for glacier calving, retreat and acceleration in addition to nutrient fluxes and primary productivity. Previous methods for estimating iceberg meltwater fluxes have either been complex models, themselves reliant on limited field data and poorly constrained model parameters, or user-intensive, expensive remote sensing techniques. This thesis presents a simplified approach for deriving summer and autumn iceberg freshwater fluxes in 2017, using freely available Sentinel-2 satellite imagery to estimate iceberg velocity and seasonal changes in iceberg volume with distance down-fjord. Integrated 2-month full-fjord freshwater fluxes reach ~1270 ± 650, 1200 ± 610, 3410 ± 1740, and 1150 ± 590 m^3 s^{-1} for June-July, July-August, August-September and September-October, respectively. The estimated iceberg freshwater fluxes are highest across August and September, likely due to a combination of warming fjord water

temperatures at depth as autumn approaches and increased calving into the fjord system in the months prior, and decrease with distance from the head of the fjord. The proportion of solid ice exiting the fjord averages 14% of the total ice volume calved into the fjord from Helheim Glacier, the largest tidewater glacier feeding into Sermilik Fjord, confirming that a significant volume of freshwater is released at depth along the length of the fjord. The volume of freshwater generated from iceberg melt is comparable to or greater than subglacial discharge volume throughout the year, and has important implications for fjord-scale circulation, submarine melt rates and primary productivity.

In terms of future developments, this thesis presents two new methodologies focused on ice-ocean interactions: one to estimate submarine melt rates near tidewater glaciers and one to derive iceberg freshwater fluxes entering glacial fjords. These innovative methods have generated important new datasets in a challenging environment from which it has consistently proven difficult to derive estimates of submarine melt rates. The additional utility of these methods is their potential application to other fjord systems for constraining both fjord-scale and ice-sheet wide ice-ocean models, developments that are critical for understanding the sensitivity of the Greenland Ice Sheet and surrounding ocean basins to future climate change.

Lay Summary

Recent increases in mass loss from the Greenland Ice Sheet are due in part to changes occurring at the margins of the ice sheet, where large glaciers (called tidewater glaciers) drain into the ocean. These changes can include acceleration of the glaciers combined with their thinning and retreat. While it is not clear exactly what causes these changes, the melting of ice beneath the waterline, termed submarine melting, is believed to be a potential initial trigger of tidewater glacier retreat and acceleration. Understanding the causes behind these changes in tidewater glacier behaviour is critical in order to improve predictions of 21st century sea level rise.

There are few observational estimates of submarine melt, as undertaking measurements near active, iceberg-producing glaciers is both difficult and dangerous. Previous estimates of ice front submarine melt are principally derived either from measurements of water properties taken many kilometres from the glacier termini or from ocean circulation models that use the properties and movement of emerging subglacial meltwater along the ice front to predict melt rates. Both of these methods rely on assumed water properties that have only been measured a handful of times at a few locations in the fjord system (which models use to validate unknown parameters), and are therefore unlikely to be representative of the wider fjord conditions. Submarine melt rates and the meltwater fluxes from icebergs floating in glacial fjords have also been estimated using either satellite imagery (a user-intensive, time-consuming and potentially expensive methodology) or complex iceberg models that rely on almost non-existent field data. Given the importance of ice front and iceberg submarine melting for ice sheet stability, fjord circulation and nutrient cycling and productivity, this thesis

aims to develop novel, simple methodologies for estimating submarine melt rates and meltwater fluxes from icebergs and glaciers around the margins of the Greenland Ice Sheet.

A simple methodology is therefore developed for estimating spatial and temporal variations in submarine melt rates beneath floating ice at the front of a large tidewater glacier. This method uses satellite imagery to observe changes in both the elevation and velocity of the floating ice at the terminus of Kangiata Nunaata Sermia in southwest Greenland, from which submarine melt rates of up to 7 metres a day are derived. Melt rates decrease with distance away from the glacier terminus and also vary across the glacier front, with these variations resulting from changes in the thickness of the floating ice, and with changes in fjord water temperature and velocity. The areas beneath the floating ice that show the highest melt rates are found along the ice front where summer meltwaters are predicted to drain from beneath the glacier, and where large quantities of icebergs are calved (as observed from time lapse camera imagery). These results are important to improve our scientific understanding of how tidewater glaciers interact with the ocean, a key control on ice sheet behaviour.

A second methodology is then developed for estimating the freshwater fluxes released into glacial fjords from the melting of icebergs, focussing on icebergs in Sermilik Fjord, southeast Greenland. Freely available satellite imagery is used to estimate both iceberg velocity and seasonal changes in iceberg volume along the fjord, from which meltwater fluxes are derived. Iceberg meltwater fluxes are highest in the late summer and autumn, when fjord water temperatures are warmer than in the spring and early summer, and when more icebergs have been calved into the fjord. Meltwater fluxes also decrease with distance from Helheim Glacier, the main tidewater glacier at the head of the fjord, reflecting the warmer water temperatures at depth where the bottoms of the larger icebergs are located when floating near the head of the fjord. Throughout the year, the volume of freshwater generated from the melting of icebergs is comparable to or greater than the freshwater entering the fjord at the base of the glacier and sourced from melting at the ice sheet surface. As such, the melting of icebergs provides a

significant volume of freshwater to the fjord system, with important implications for fjord-scale circulation and heat budget, nutrient cycling and primary productivity.

This work provides two new methodologies for estimating tidewater glacier submarine melting and iceberg freshwater fluxes released into glacial fjords. These methodologies are effective, simple and inexpensive, can be applied to a variety of glacial fjord systems, and are particularly useful for investigating those that are remote and inaccessible. This work has also confirmed and expanded our knowledge of the key controls impacting the submarine melting of tidewater glaciers and icebergs; notably fjord water temperature and velocity and the presence and location of subglacial meltwater outflows beneath the glacier termini. Furthermore, it has confirmed the importance of meltwater sources from icebergs to the wider fjord system. It is anticipated that the methodologies developed here will be used by the scientific community to improve our understanding of ice-ocean interactions around the margins of the Greenland Ice Sheet, an understanding that is critical for better predictions of the future state of the ice sheet and thus for 21st century sea level rise.

Acknowledgements

Many thanks go to my principal supervisor Pete Nienow for his support throughout the whole PhD process: for spending time discussing research ideas and funding sources, for help (and entertainment) in the field, for taking me on my first Scottish hillwalk and for all the gin & tonics. Thanks are also due to my second supervisor Noel Gourmelen, for helping to develop my research ideas, for his patience in training me in the dark arts of remote sensing and for our shared love of cats. Thank you also to my third supervisor Andrew Sole for his willingness to help wherever possible and for constructing monuments in Greenland that will still be there come the next Ice Age. Additional thanks go to my (unofficial) fourth supervisor Tom Cowton for his time spent discussing research ideas and for his valued career advice.

This research could not have been possible without the generosity of my various funding sources. The University of Edinburgh provided me with a fully-funded PhD studentship through the Principal's Career Development Scholarship. Funding for fieldwork in Greenland was provided by the Mackay Greenland Fund, the Weir Fund for Field Studies, the Institute of Geography and the Scottish Alliance for Geoscience, Environment and Society (SAGES). Support during the final stages of my PhD was provided by the Funds for Women Graduates.

I was lucky enough to take part in a two-month long SAGES-funded research exchange with the University of Oregon, and enormous thanks are due to Dave Sutherland and his research lab for making me feel welcome, for providing an excellent source of research

feedback and ideas, and for taking me to float the Willamette River on one of the hottest days of the summer.

Special thanks to my fellow (and past) PhD students for providing endless entertainment over the past three years. Notable mentions go to Donnie for all his numerical and modelling assistance (and for all the frozen margaritas), to Lizzie for sharing her teas, to Lauren and Monika for two great trips to Iceland, to Charlie for being the better half of Team Tidewater, and to all the rest for making my time at the office so memorable. I am also grateful for the emotional support and lovely times provided by my forever favourite flatmates: Davide, Robyn, Rachel and Jakob.

Final thank you's to Duncan for always being there and for exploring all the castles with me, and to my family for their unwavering support, encouragement and belief in me, no matter how far I wander from home.

Contents

List of Tables

List of Figures

Chapter 1

Introduction

The oceans surrounding the Greenland Ice Sheet are resplendent with life, from the smallest krill and shrimps to the curious ringed seals, the clustered groups of walruses and the magical narwhal, to the lone polar bear hunting on the sea ice and the pods of beluga whales clicking beneath the murky surface. Ocean waters flow across shelves and sills, entering the mouths of glacial fjords once carved by the retreat of ancient glaciers, swirling around giant floating icebergs and eventually reaching the tidewater glaciers found at the head of each fjord. Freshly-calved icebergs topple into the sea while sediment-laden and nutrient-rich subglacial melt waters rise to the fjord surface, attracting flocks of Arctic tern and other birds. The majority of these glaciers are retreating back into the ice sheet, playing a role in the complicated relationship between glacier calving, acceleration and mass loss. The influence of the ocean on the dynamic behaviour of these tidewater glaciers remains unclear, adding to the uncertainty surrounding projections of global sea level rise. The research presented in this thesis seeks to improve our knowledge of the interactions between the ice sheet and the ocean, focusing on floating ice found in glacial fjord systems to better constrain predicted changes to the Greenland Ice Sheet over the coming centuries.

1.1 The cryosphere in a changing climate

The cryosphere encompasses all the cold regions of the Earth, from sea, lake, and ground ice, to snow covered areas, glaciers and ice sheets. These regions are important for natural ecosystems and provide invaluable freshwater sources for human communities worldwide. The two largest bodies of non-seasonal ice cover are the Antarctic and Greenland Ice Sheets. Located around the South Pole, Antarctica contains over 25 million km^3 of ice, of which 22.6 million km^3 lies above sea level and, if melted completely, has the potential rise sea level by 58.3 m (IPCC 2013). In the high latitudes of the Northern Hemisphere, the Greenland Ice Sheet contains 2.6 million km^3 of ice, equivalent to 7.36 m of sea level rise (IPCC 2013). Both ice sheets have lost mass in recent decades, together contributing approximately 11 mm to global sea level rise between 1993 - 2011 (Figure 1.1; Shepherd et al. 2012).

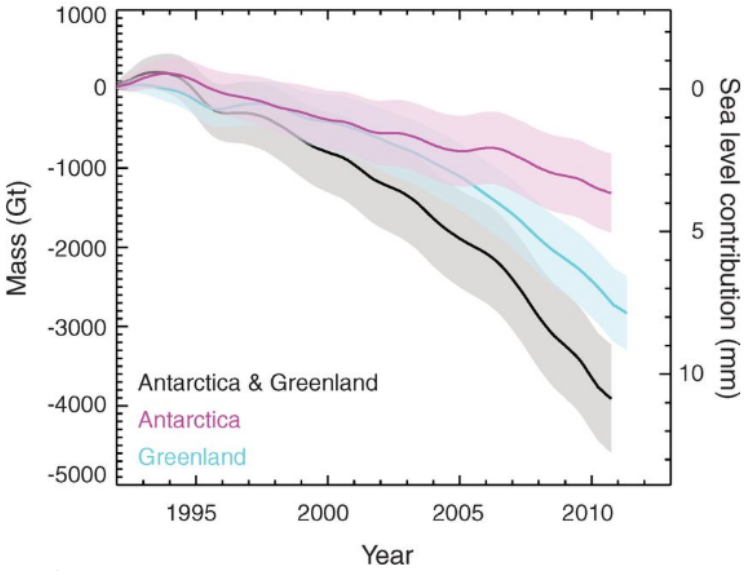

Figure 1.1: The contribution of the Greenland and Antarctic Ice Sheets to global sea level rise from 1993 - 2011; reproduced from Shepherd et al. (2012).

Mass loss from ice sheets can be attributed to changes in surface mass balance (i.e., the accumulation of ice minus surface melting of ice) as well as to the 'dynamic thinning' of tidewater glaciers and ice shelves (Figure 1.2), which lose mass as a result of thinning,

accelerated flow and retreat (Pritchard et al. 2009). Since the mid-1990s, the dynamic thinning of tidewater glaciers has led to increased ice discharge from the Greenland Ice Sheet (Figure 1.3), resulting in 477 ± 51 Gt a^{-1} of ice loss, approximately 0.47 ± 0.23 mm a^{-1} sea level equivalent (Van den Broeke et al. 2016). Despite its importance, the precise mechanisms controlling the dynamic thinning of tidewater glaciers remain unclear, reflecting their complexity (Moon et al. 2012). Recent research has proposed that changes at tidewater glacier fronts are triggered by atmospheric and oceanic warming, resulting in augmented mass loss through glacier acceleration and increased calving (e.g., Nick et al. 2009, Holland et al. 2008, Howat et al. 2007, Cowton et al. 2018) and ice front submarine melting (Truffer & Motyka 2016).

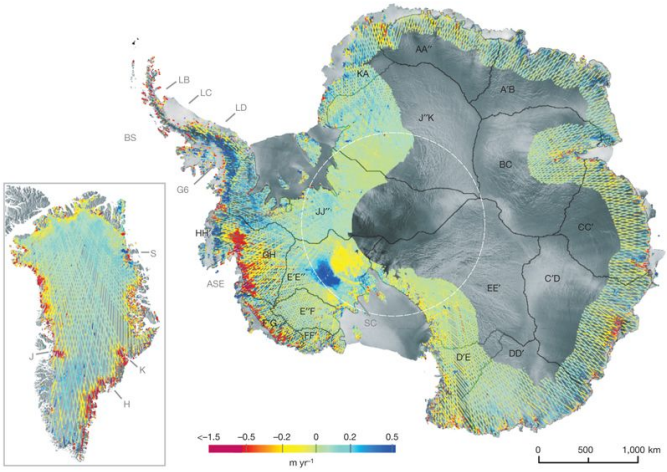

Figure 1.2: Rate of surface elevation change over the Greenland and Antarctic Ice Sheets from 2003-2007, highlighting areas of pronounced thinning in red; reproduced from Pritchard et al. (2009).

The submarine melting of ice fronts is believed to be controlled in part by the temperature and velocity of subglacial discharge plumes (Jenkins 2011, Slater et al. 2015). Subglacial discharge plumes in Greenland are composed primarily of meltwater originating from surface melt on the glaciers upstream, which then flows through the glacier from the surface to the ice-bed interface before exiting beneath the glacier grounding line (i.e., the boundary between grounded and floating glacier ice). Due to their lower density relative to ambient fjord water, subglacial plumes rise buoyantly

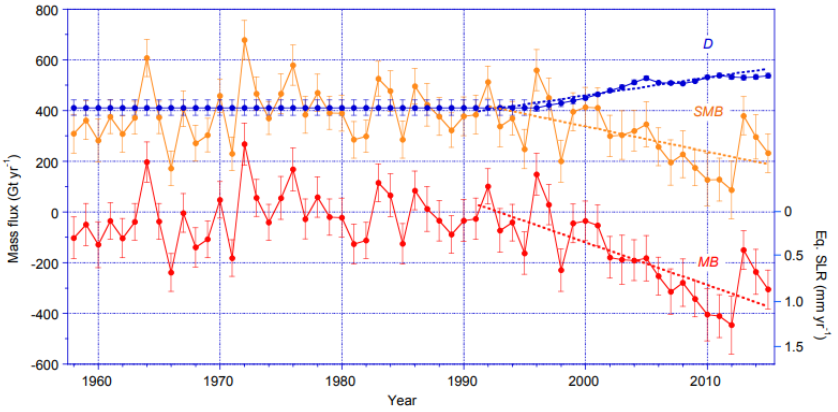

Figure 1.3: Annual discharge (D), surface (SMB) and ice sheet (MB) mass balance and sea level rise equivalent over the Greenland Ice Sheet from 1958-2015, with trends from 1991-2015 shown as dashed lines; reproduced from Van den Broeke et al. (2016).

along the ice front and entrain warm fjord water, melting the ice front as they rise (e.g., Motyka et al. 2003, Jenkins 2011). To date, submarine melt rates are poorly constrained, in part because collecting in-situ measurements near actively-calving glacier termini is both difficult and dangerous. Numerous studies have used hydrographic profiles from glacial fjords (e.g., Motyka et al. 2003, Sutherland & Straneo 2012, Motyka et al. 2013, Inall et al. 2014), general circulation models or plume theory (e.g., Jenkins 2011, Christoffersen et al. 2012, Sciascia et al. 2013, Xu et al. 2013), or remote sensing techniques (e.g., Rignot & Jacobs 2002, Enderlin & Howat 2013, Enderlin et al. 2014) to estimate submarine melt rates. Given the potential importance of tidewater glacier submarine melting to the future response of the ice sheet, as well as to fjord water circulation, nutrient availability and primary productivity, this thesis focusses on developing and refining empirical methods for estimating melt rates, utilising methods that are not dependent on expensive field seasons or uncertain model parameters.

1.2 Outline of thesis

The overall aim of this thesis is to improve our understanding of ice-ocean interactions at tidewater glaciers along the margins of the Greenland Ice Sheet, particularly submarine

melting, believed to be a key control on glacier dynamics, fjord and ocean circulation and primary productivity via the circulation of nutrients. This thesis uses both satellite and terrestrial remote sensing techniques to investigate the role of submarine melting beneath floating ice tongues adjacent to tidewater glaciers and the amount of freshwater released from the melting of icebergs in glacial fjords. Specifically, the thesis seeks to both improve and simplify the methodologies currently used within the scientific research community for estimating variations in submarine melt rates. The thesis is organized into two complementary research themes:

1. **Quantifying the magnitude of and variability in submarine melting beneath floating ice tongues**.

   This part of the thesis develops a methodology for estimating submarine melt rates beneath floating ice tongues adjacent to tidewater glaciers, using a combination of observations of ice surface elevation and ice motion. Spatial and temporal variations in submarine melt rate beneath ice tongues are examined and potential factors controlling these variations are explored, including fjord water temperature stratification and the presence and characteristics of subglacial discharge plumes. A hydropotential analysis is performed to model subglacial flow paths, which are spatially connected with iceberg calving events and subglacial plume surface expressions observed via time-lapse photography.

2. **Quantifying variations in fjord iceberg distribution and freshwater flux**.

   This theme examines the spatial and temporal variations in fjord iceberg volume and the freshwater flux delivered by iceberg melt through the development of a new methodology. Freely available satellite imagery is used to estimate iceberg velocities and changes in iceberg volume, from which freshwater fluxes are derived. These fluxes have previously been estimated using expensive, user-intensive remote sensing techniques and field work, or complex models. The potential controls on variations in freshwater flux along the fjord are explored, including water velocity and temperature stratification and iceberg size and velocity. The percentage of ice exiting the fjord as solid flux is estimated and seasonal variations

in meltwater flux are considered in the context of the wider freshwater budgets delivered to fjord systems.

The thesis then brings together these two themes, exploring the role of tidewater glacier and iceberg submarine melting on glacier dynamics, fjord and wider ocean circulation, nutrient availability and primary productivity. Potential applications and limitations of the developed methodologies are also discussed.

Following on from the Introduction, Chapter 2 provides the motivation and background for this thesis, including information on the Greenland Ice Sheet and a detailed review of tidewater glacier dynamics, with a specific focus on the research and methodology previously developed to estimate submarine melting. Expanded descriptions of the two fjord systems and glaciers studied in this thesis are also provided here. Chapter 3 provides a brief description of the methodologies developed as part of this thesis, with more details found later in the individual results chapters and their supporting information. Chapters 4-6 present the main results of the thesis on the two themes identified above, with Chapters 4 and 5 focussing on submarine melt rates beneath a floating glacier tongue, and Chapter 6 focussing on the estimation of freshwater fluxes from the melting of icebergs in glacial fjords. The thesis closes with a synthesis of the results, reviewing key conclusions and exploring ideas for future research, found in Chapter 7.

1.3 Structure of thesis

Chapters 4, 5, and 6 have been written as stand-alone papers for ease of access to the research community. Chapter 4 has been published (Moyer et al. (2017), *Frontiers in Earth Science*) and both Chapters 5 (submitted to *Journal of Glaciology*, October 2018) and 6 (submitted to *Geophysical Research Letters*, January 2019) are currently in review. Author contribution statements are included at the start of these chapters, as several co-authors have contributed to each paper. The published format of Chapter 4 has been included as an appendix.

Chapter 2

Background

The Greenland Ice Sheet is highly sensitive to small changes in atmospheric and oceanic properties and can thus be used as an indicator of regional and global climate change (e.g., Hanna et al. 2014). Furthermore, the volume of ice stored in the ice sheet and the potential release of this meltwater store have significant implications both for sea level rise and ocean circulation and productivity (Straneo & Heimbach 2013). Recent increases in both atmospheric and oceanic temperatures have influenced mass loss from the ice sheet, including loss driven by tidewater glacier acceleration and retreat (e.g., Straneo & Heimbach 2013). This background chapter provides a broad overview of recent trends in air temperature and general oceanic properties surrounding Greenland before turning its focus on fjord-scale water properties. Ice-sheet wide dynamic changes in tidewater glaciers are then discussed along with controlling factors, followed by a detailed review of the two glacial fjord systems studied in this thesis: Kangersuneq and Sermilik Fjords. The chapter then focusses on ice-ocean interactions, reviewing our current understanding of submarine melting and the associated freshwater flux released into the fjord system.

2.1 The Greenland Ice Sheet

2.1.1 Recent trends in air temperature

Since the 1990s, there has been a general increase in air temperature recorded at weather stations around the margins of the Greenland Ice Sheet (Figure 2.1) (Hanna et al. 2012, Carr et al. 2013). Most of this warming has focused on the western margin of the ice sheet, where air temperatures have increased by 0.35 °C a^{-1} (Carr et al. 2013), with winter temperatures increasing locally by more than 10 °C (Hanna et al. 2012). Since 2001, average winter and summer air temperatures have increased by 2.9 °C and 0.8 °C, respectively, with insignificant changes observed in autumn and spring temperatures (Hanna et al. 2012). Increases in air temperature allow for increased melting of the ice sheet surface (i.e., ablation), which reduces the surface mass balance of the ice sheet. Over the past decade, decreases in surface mass balance have resulted in a substantial increase in mass loss from the Greenland Ice Sheet via surface melting and runoff, of over 250 Gt a^{-1}, which accounts for about 60% of total ice sheet mass loss (Enderlin et al. 2014, Van den Broeke et al. 2016). Notably, air temperatures over the ice sheet in 2012 set new record high mean and extreme temperatures, causing widespread record amounts of surface melt and runoff, and contributing approximately 1.2 mm to global sea level that year alone (Tedesco et al. 2013, Hanna et al. 2014).

2.1.2 General oceanic and fjord-scale properties

The ambient water inside glacier fjords reflects in part the water flowing along the adjacent continental shelves, and connects the ice sheet margin with water from the North Atlantic subpolar gyre, Baffin Bay, the Arctic Ocean, and the Nordic Seas (Figure 2.2). The shallow waters on the continental shelves surrounding Greenland are characterized by cold, fresh Polar Water transported by the East and West Greenland currents and overlay warmer, salty Atlantic Water transported by the North Atlantic and Irminger currents (Holland et al. 2008, Inall et al. 2014, Straneo & Cenedese 2015).

Several circulation processes operate in large glacial fjords that can bring these warm coastal waters to tidewater glacier fronts and thus drive melting and retreat (Figure

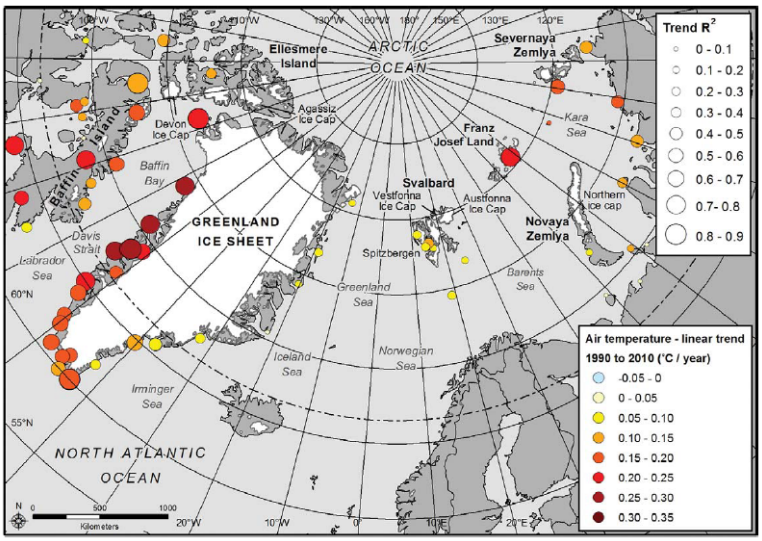

Figure 2.1: Mean annual air temperature trends for weather stations in the Arctic, 1990 - 2010; reproduced from Carr et al. (2013).

2.3). During the melt season (i.e., May to October), buoyancy-driven circulation is typically dominant (Motyka et al. 2003, Jenkins 2011, Cowton et al. 2015). Meltwater created on the surface of the glacier drains to the glacier bed through crevasses and moulins, eventually flowing out from beneath the glacier at the grounding line and entering the fjord. Due to the lower density of the subglacial discharge compared to the ambient fjord water, the discharge plume rises buoyantly along the ice front and either reaches the surface or a density equilibrium with the ambient fjord water at some depth before flowing out of the fjord and onto the shelf (Motyka et al. 2003, Jenkins 2011). The outflow, forced by the subglacial discharge, sets up a counter-current and draws in warm coastal water from the shelf, which flows in a layer below the more buoyant fresher outflow above. This warmer water is thus drawn towards tidewater glacier termini and subsequently entrained into the subglacial plume exiting at the glacial grounding line, melting the ice front as it rises (Motyka et al. 2003, Jenkins 2011). When subglacial discharge volume and velocity are high during the peak of the melt season, debris-laden plumes have been observed at the fjord surface near glacier termini, providing evidence for buoyancy-driven circulation (e.g., Sole et al. 2011, How et al. 2017, Schild et al. 2018).

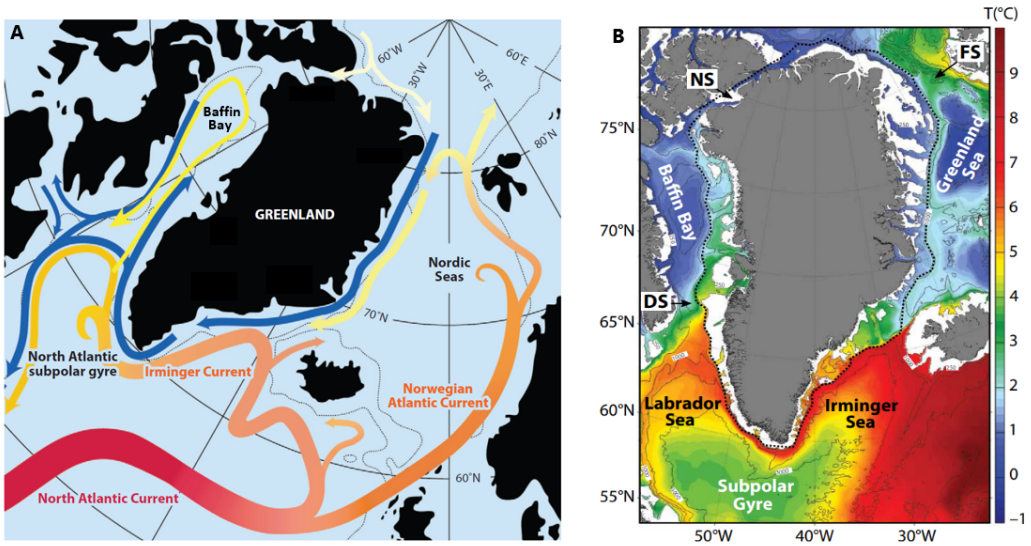

Figure 2.2: (a) Ocean circulation around the Greenland Ice Sheet, where red to yellow colours represent warm, salty Altantic Water and blue represents cold, fresh Polar Water; modified from Straneo & Cenedese (2015); (b) ocean temperatures around Greenland at 250 m depth as simulated by the MITgcm ocean circulation model; reproduced from Fenty et al. (2016).

Intermediary circulation can also be active in large glacial fjords, occurring above the depth of any sills present on the fjord floor (Figure 2.3). The exchange of water driven by intermediary circulation originates from variations in density outside the fjord, driven either by density anomalies or along-shore winds, which create strong upwellings or downwellings (Straneo & Cenedese 2015). These up- and downwellings are strong enough to flush the water above any sills, and can result in the rapid renewal of warm water in the fjord, particularly during the winter months when buoyancy-driven circulation is weaker (Jackson et al. 2014). Using winter hydrographic surveys from September to May in Sermilik and Kangerdlugssuaq Fjords, east Greenland, Jackson et al. (2014) suggest that the large variability seen in the upper water column thickness can be attributed to the rapid exchange of waters driven by frequent, strong sheared flows in the along-fjord direction. These strong flows originate from fluctuations of water density on the shelf and often occur after the presence of strong along-shore winds. In addition, water column properties can fluctuate over timescales as short

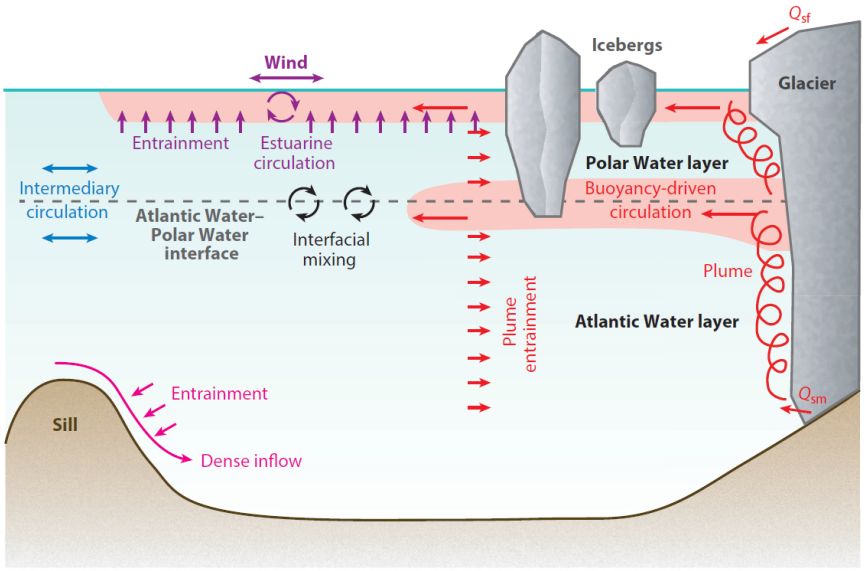

Figure 2.3: Lateral view of different circulations found in a typical large Greenlandic glacial fjord: buoyancy-driven, estuarine, intermediary and dense inflow (or deep water renewal) circulation; note that the colours used do not reflect water temperature; modified from Straneo & Cenedese (2015).

as 3 days (Jackson et al. 2014), suggesting that these wind-driven current pulses can significantly alter fjord heat content on short timescales, and thus submarine melt rates.

Finally, two other types of circulation help transport warm coastal water into the fjord: estuarine circulation and deep-water renewal (Figure 2.3). Estuarine circulation is driven by both meltwater running off the land and by subglacial discharge that reaches the fjord surface, and is concentrated to the very top layer of the water column (Mortensen et al. 2011). This thin layer of surface outflow entrains water to form a shallow current moving in-fjord just below. Deep-water renewal is driven by the inflow of dense warm shelf water at depth, which causes the lifting of isopycnals (i.e., water layers of same densities) and the mixing of the water column (Mortensen et al. 2011, Straneo & Cenedese 2015).

2.2 Tidewater glacier dynamics and controls

2.2.1 Ice sheet-wide trends in glacier behaviour

Tidewater glaciers generally follow an annual cycle of advance and retreat, advancing in the winter and spring due to the combination of the buttressing effect of sea ice and ice mélange (Amundson et al. 2010), and retreating in the summer and autumn once calving begins (e.g., Moon & Joughin 2008, Howat et al. 2010). Aerial photographs from the 1930s reveal that Greenlandic tidewater glaciers retreated throughout the early 20th century in line with increases in air temperature, followed by a brief period of readvance and slowed retreat near the middle of the century (Bjørk et al. 2012). Advances in satellite remote sensing have revealed widespread accelerated glacier front retreat in the early 2000s, outwith the typical seasonal cycle of advance and retreat. Between 2000 and 2010, 188 of the 199 tidewater glaciers studied by Murray et al. (2015) showed sustained and substantial retreat (Figure 2.4), summing to more than 267 km of retreat in total. Along the central western margin of the ice sheet, multi-year retreat is thought to have been triggered by increased air temperature (approximately 2 °C) over the same time period combined with increased sea surface temperatures, resulting in expanded calving seasons following early clearance of the ice mélange (Howat et al. 2010). Along the central eastern margin, tidewater glaciers experienced a threefold increase in retreat rate from 2000 to 2005, when compared to retreat between the 1980s and 2000, potentially triggered by a negative switch in the North Atlantic Oscillation, resulting in increased sea surface temperature and changes in sea ice distribution (Jiskoot et al. 2012).

2.2.2 Regional-scale factors controlling tidewater glacier dynamics

Defining ice sheet-wide controls on tidewater glacier dynamics in order to predict the behaviour of individual glaciers is nearly impossible, as each fjord system is unique and thus has different water and glacier properties and fjord geometry (Carr et al. 2013). However, narrowing down to a regional scale reveals some common glacier behaviours and likely triggers. For example, glaciers on the southeastern margin of the Greenland

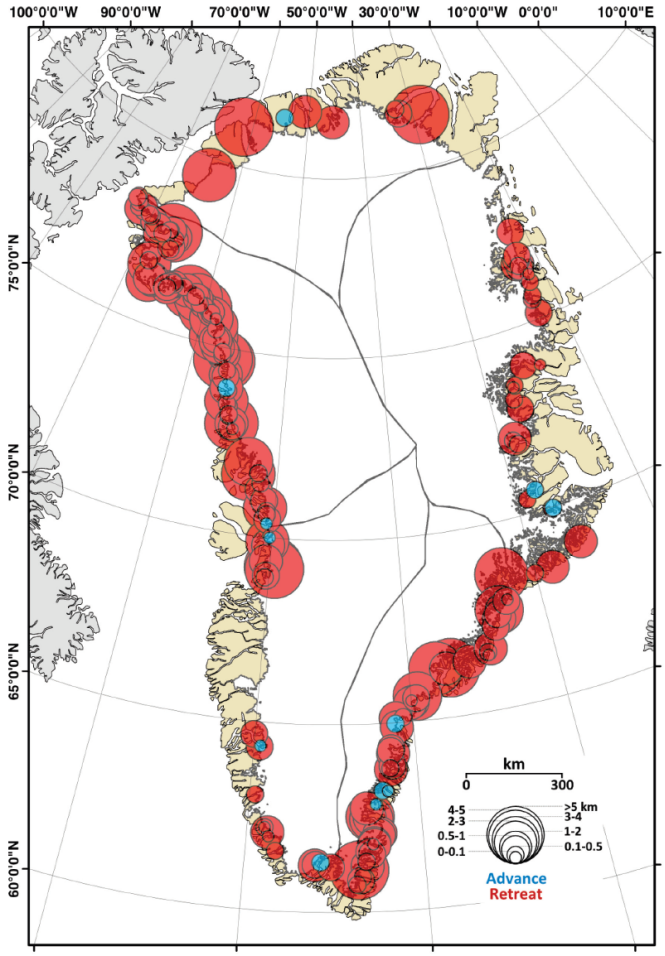

Figure 2.4: Changes in Greenland tidewater glacier ice front positions between 2000 and 2010, where larger symbols indicate greater change and blue and red symbols indicate advance and retreat, respectively; reproduced from Murray et al. (2015).

Ice Sheet displayed significantly different behaviour to those along the northeastern margin before and after 2005 (Seale et al. 2011, Walsh et al. 2012). Above 69 °N, glaciers on the eastern margin of the ice sheet displayed relatively stable terminus positions, whereas those below this latitude retreated significantly prior to 2005, followed by a period of either readvance or decreased retreat from 2005 to 2009. The retreat pattern observed in the south (below 69 °N) has been attributed to an increase in the transport of warm subtropical waters to the Irminger Sea and thus into the nearby glacial fjords until 2004, followed by a subsurface cooling of waters in the same region between 2004 and 2008 (Seale et al. 2011, Walsh et al. 2012).

Cowton et al. (2018) investigated the influence of simple parameters on regional tidewater glacier retreat in East Greenland, including air temperature, meltwater runoff and ocean temperature. While individual glaciers may show a stronger correlation with oceanic influence alone, 76% of the variability in regional retreat from 1993 to 2012 can be attributed to the combined influence of meltwater runoff (itself driven primarily by atmospheric temperature) and ocean temperature (Figure 2.5; Cowton et al. 2018). Importantly, this demonstrates that simple forcing parametrizations may be able to predict future changes in tidewater glacier position anticipated with continued atmospheric and oceanic warming.

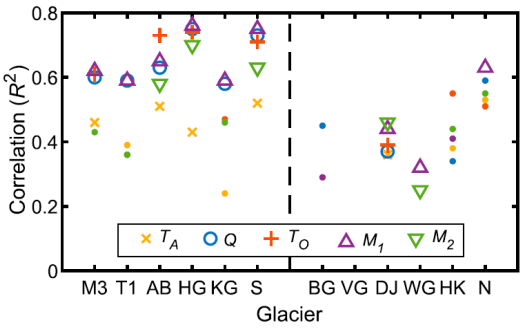

Figure 2.5: Correlation (R^2 values) for relationships of tidewater glacier terminus position with air temperature (T_A), meltwater runoff (Q), ocean temperature (T_O), and the combined effects of ocean and atmospheric forcing (M_1 and M_2). Abbreviations on x-axis represent ten different tidewater glaciers and average regional trends for southern (S) and northern (N) glaciers, split north and south of 69 °N; reproduced from Cowton et al. (2018).

2.3 Kangersuneq and Sermilik Fjords

The main results chapters of this thesis focus on ice-ocean interactions in two large glacial fjord systems in Greenland: Kangersuneq and Sermilik, described in detail below. Chapters 4 and 5 focus on submarine melting beneath a seasonal floating ice tongue adjacent to Kangiata Nunaata Sermia in Kangersuneq Fjord, southwest Greenland (Section 2.3.1). Chapter 6 focuses on iceberg meltwater fluxes in the Sermilik Fjord system in southeast Greenland (Section 2.3.2).

2.3.1 Kangiata Nunaata Sermia and Kangersuneq Fjord

Kangiata Nunaata Sermia (KNS) is the largest tidewater glacier in southwest Greenland, draining approximately 2% of the ice sheet area (Sole et al. 2011). KNS is located about 80 km east of Nuuk at the head of the over 100 km long Godthåbsfjord system and terminates directly into Kangersuneq Fjord. The glacier system has retreated over 20 km from the Little Ice Age (LIA) maximum extent in the 1700s (Figure 2.6), reflecting a strong response to increased air and sea surface temperatures during and since the LIA (Weidick et al. 2012, Lea et al. 2014). Annual ice flux across the KNS grounding line has increased from ~6 km^3 in 1996 (Rignot & Kanagaratnam 2006) to 7.6 $\pm$ 1.5 km^3 per year in more recent years (Mortensen et al. 2013). The increased ice flux reflects increases in ice velocity of 6% from 1996 to 2000 and 27% from 2000 to 2005 (Rignot & Kanagaratnam 2006). Ice velocity along the centreline of the glacier increased by an additional 50% by 2012, reaching 11 km a^{-1} near the ice front (Slater et al. 2017a).

A thick seasonal floating ice tongue forms adjacent to the KNS terminus most winters (Figure 2.7), flowing across the glacier grounding line to advance down-fjord during the winter and early spring (Sole et al. 2011, Motyka et al. 2017). The ice tongue typically merges into a dense ice mélange and rapidly breaks up in the late-spring of each year (Sole et al. 2011), an observation evident from several years of time lapse camera imagery. Generally, the ice tongue extends between 2 and 3 km into the fjord and visibly decreases in freeboard moving away from the ice front (Figure 2.7a). Notably, the ice tongue did not fully form in 2011 or 2015, potentially linked to higher water temperatures observed in the fjord from late-2010 to early-2011 (Motyka et al. 2017). Increased fjord water temperatures could delay the development of and weaken the buttressing effect of the ice mélange (e.g., Amundson et al. 2010) and prevent the formation and advance of the ice tongue.

Several studies have investigated water circulation and properties in Kangersuneq Fjord (Mortensen et al. 2011, 2013, Motyka et al. 2017), finding distinct seasonal differences in circulation patterns and associated water properties. Using hydrographic data collected

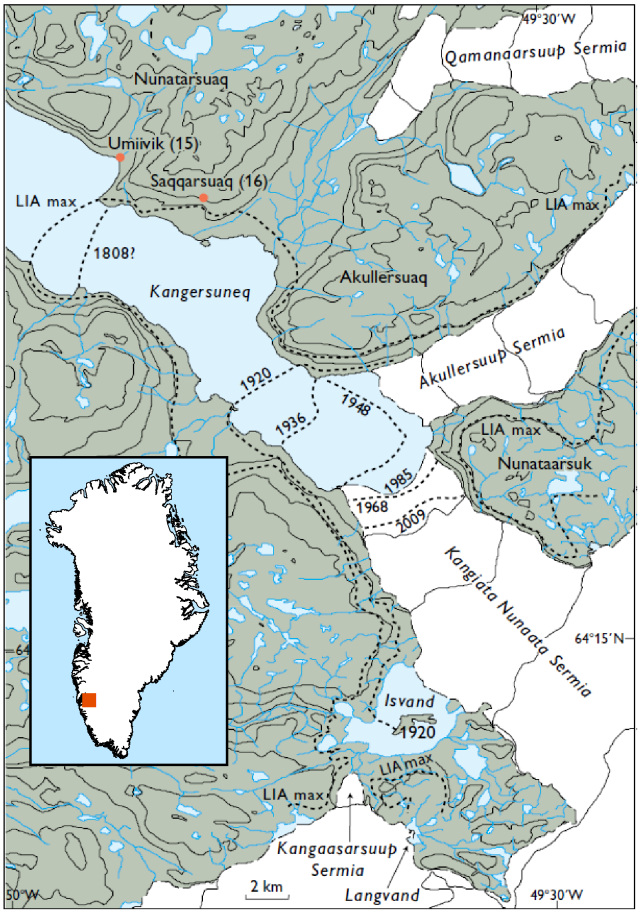

Figure 2.6: Retreat of Kangiata Nunaata Sermia (KNS) since the Little Ice Age (LIA) maximum extent. The contemporary terminus position is close to the 2009 position seen here; modified from Weidick et al. (2012) to include an inset location map.

to within approximately 4 km of the KNS ice front, Mortensen et al. (2011) observed all four previously mentioned circulation patterns (Section 2.1.2 and Figure 2.3) in the fjord. In the summer, both classical estuarine circulation and subglacial (or buoyancy-driven) circulation are strong. Subglacial circulation is the primary mode of circulation during the summer, as subglacial discharge exiting beneath the glacier grounding line is highest during the melt season. Deep-water renewal is active during the winter in the outer part of the fjord, driven by dense waters flowing into the bottom of the fjord from the shelf (~100 km from the ice front), resulting in the rise of fjord-water layers of constant density (Mortensen et al. 2011). Finally, fluctuations in water density drive

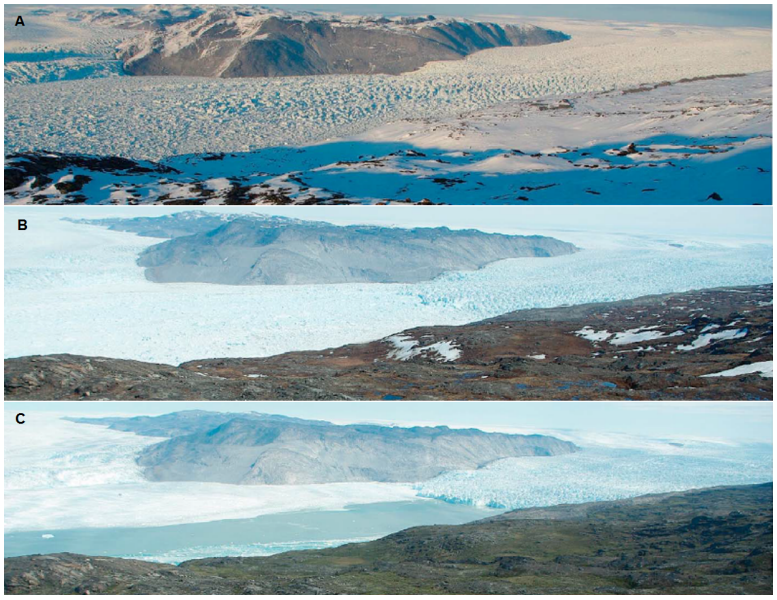

Figure 2.7: Time lapse imagery of (a) the intact seasonal ice tongue at KNS on 12 May 2009, (b) the mélange covered fjord post-ice tongue disintegration on 4 June 2009, and (c) the nearly ice-free fjord on 14 July 2009; modified from Sole et al. (2011).

intermediary circulation in both summer and winter months, resulting in the warming and cooling of intermediate depth waters in the summer and winter, respectively (Mortensen et al. 2011). All of these circulation patterns vary both temporally and spatially and influence the amount of heat reaching the KNS ice front, which controls the rate and distribution of submarine melt.

Temperature and salinity profiles recorded between 4 and 50 km from the summer KNS terminus show distinct seasonal differences (Mortensen et al. 2011, 2013). In winter months, the upper water column shows cool surface waters (typically between -2 and 0 °C) underlain by a warmer (between 1 and 1.8 °C) intermediate layer (Figure 2.8a) (Mortensen et al. 2013). The upper water column is typically warmer in the summer (up to 3 °C) due to surface heating and is underlain by a slightly cooler layer dominated by glacial meltwater (between 0 and 1.5 °C) beneath which is a warm deep layer reaching 3 °C (Figure 2.8b). Salinity profiles are typically fresher near the surface in the summer due to glacial runoff and iceberg melting, and underlain by more saline ambient fjord

water (Mortensen et al. 2013). In the winter, surface waters are more saline than in the summer yet underlain by an even more saline intermediate water layer.

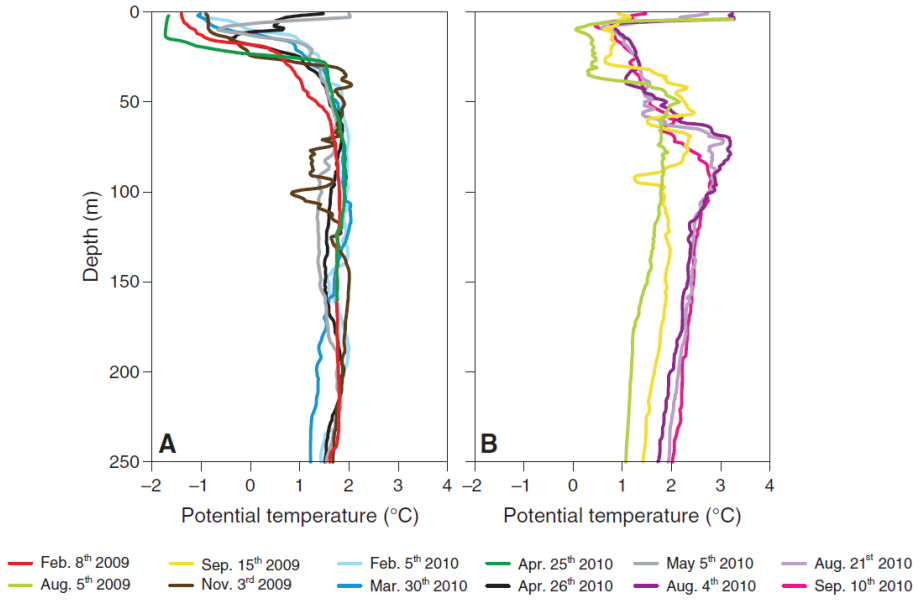

Figure 2.8: Potential temperature profiles during the (a) winter and (b) summer seasons in Kangersuneq Fjord, averaged over 4-50 km from the ice front; reproduced from Mortensen et al. (2013).

2.3.2 Helheim Glacier and Sermilik Fjord

Located on the southeast margin of Greenland, Helheim Glacier drains approximately 7% of the ice sheet area (Rignot & Kanagaratnam 2006) and sits at the head of Sermilik Fjord, along with Midgård and Fenris Glaciers (Figure 2.9a). Helheim Glacier moves at a mean velocity of between 8 to 11 km a^{-1} (Moon et al. 2012), and experienced major acceleration, thinning and retreat in the early 2000s, retreating over 7 km between 2001 and 2005 (Figure 2.9b) (Schild & Hamilton 2013). This was followed by a brief re-advance in 2006 and a reduction in surface thinning due to anomalously low sea surface and air temperatures (Schild & Hamilton 2013). Since 2006, the glacier has retreated roughly another 4 km to its current position (see black line in Figure 2.9b). Contemporary ice flux across the glacier grounding line reaches over 6 km^3 per month

(Sulak et al. 2017), typically peaking in late-summer and with occasional large fluxes in the late-spring post-ice mélange disintegration.

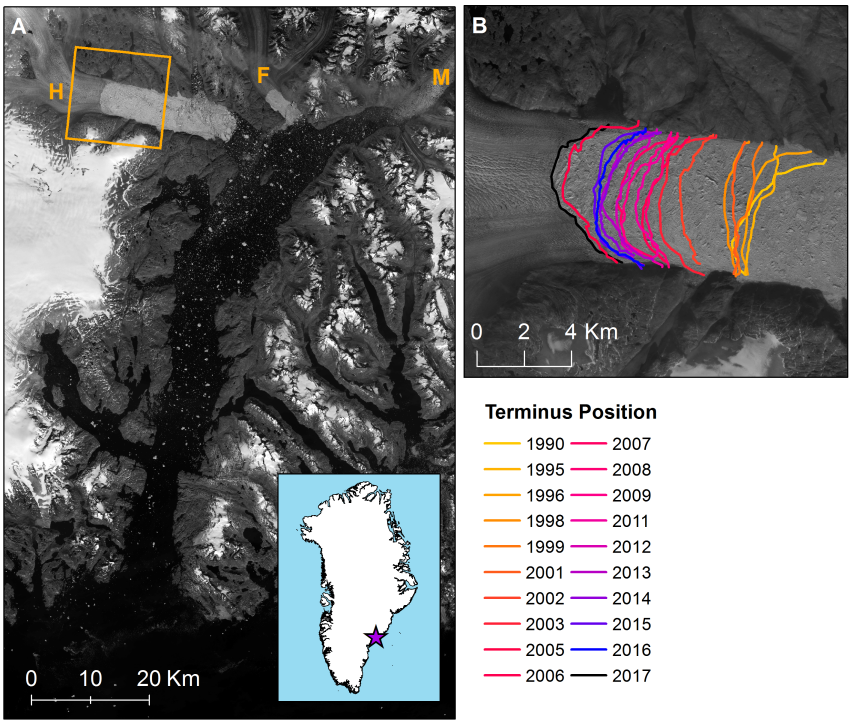

Figure 2.9: (a) Sermilik Fjord from a Sentinel-2 image on 28 July 2017, including Helheim (H), Fenris (F) and Midgård (M) Glaciers. Yellow box indicates the extent of (b), which shows Helheim Glacier terminus positions from 1990 to 2017, overlain on Sentinel-2 image from 30 August 2017. Terminus positions from 1990 to 2016 are from the European Space Agency Greenland Ice Sheet Climate Change Initiative project (http://products.esa-icesheets-cci.org/products/downloadlist/CFL/) and the 2017 terminus position was hand-digitized based on the underlain Sentinel-2 image.

Water circulation in Sermilik Fjord follows the same patterns often found in glacial fjords, including buoyancy-driven estuarine flow and intermediary circulation, the latter of which dominates the exchange of water in the fjord system (e.g., Sutherland & Straneo 2012, Jackson et al. 2014, Jackson & Straneo 2016). Intermediary circulation in Sermilik Fjord is correlated with strong wind events coming off the shelf near the mouth of the fjord, which drive changes in water velocity and total water exchange in the fjord on timescales of as little as three to ten days (Jackson et al. 2014). Similar

to Kangersuneq Fjord, water in Sermilik Fjord is highly stratified (Figure 2.10), with a cool Polar Water layer (0 - 0.5 °C) at depths between approximately 100 - 200 m underlain by a thick layer of warmer, salty Atlantic Water (up to 4 °C) (Sutherland & Straneo 2012, Jackson et al. 2014).

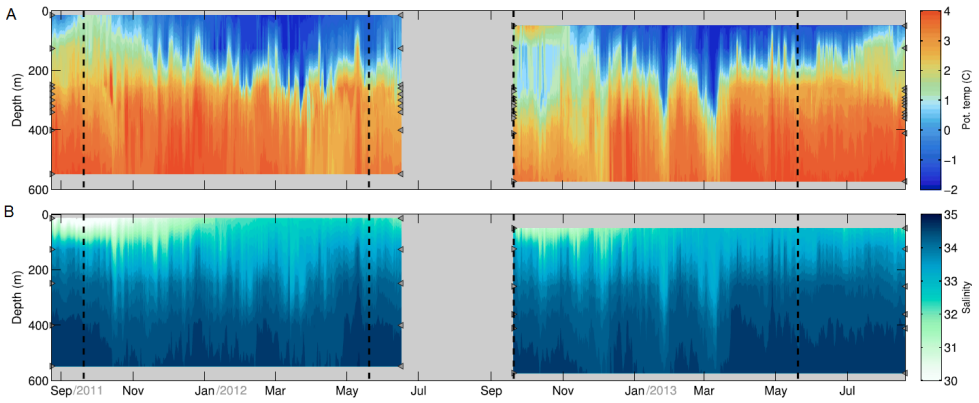

Figure 2.10: Potential (a) water temperature and (b) salinity from two mid-fjord moorings at different depths in Sermilik Fjord; modified from Jackson & Straneo (2016).

Helheim Glacier is the fifth largest producer of icebergs from the Greenland Ice Sheet (Enderlin et al. 2014), calving approximately 25 Gt a^{-1} of both tabular and non-tabular icebergs. Once calved, icebergs travel through a dense ice mélange before turning south for ~80 km to reach the fjord mouth and the Irminger Sea (Figure 2.9a). As there is no shallow sill located near the fjord mouth (Sutherland & Straneo 2012), deep-keeled icebergs can exit the fjord with relative ease. Sutherland et al. (2014a) deployed GPS units on top of large icebergs in Sermilik Fjord to track iceberg movement, speed and residence time in September 2012 and August 2013. Mean speeds of icebergs in the mélange peaked at just 0.0003 m s^{-1}, much slower than those in the open fjord that reached peak mean speeds over 0.07 m s^{-1} (Figure 2.11a). The mean net motion for all icebergs was down-fjord (Figure 2.11c), implying that all icebergs eventually exit the fjord unless completely melted or trapped in one of the side embayments of the fjord.

2.4 Submarine melt rates and their controls

Submarine melting of glacier ice fronts likely plays a crucial role in controlling individual glacier behaviour, and has been proposed as a trigger of glacier calving, retreat and

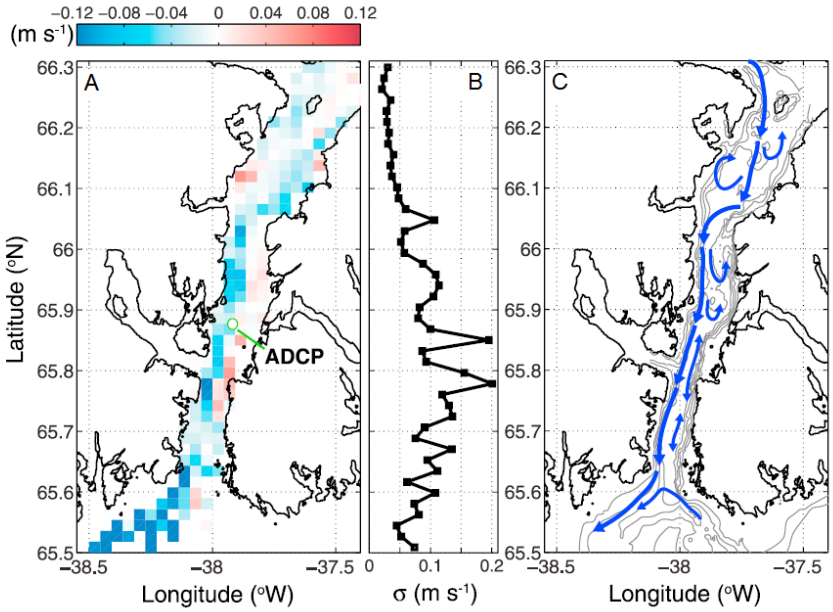

Figure 2.11: (a) Iceberg velocities and (b) standard deviation from GPS-tracking where negative values indicated movement down-fjord; (c) Circulation of icebergs based on GPS-tracked movement; reproduced from Sutherland et al. (2014a).

acceleration (e.g., Nick et al. 2009, O'Leary & Christoffersen 2013, Luckman et al. 2015). Direct measurements of tidewater glacier ice fronts from sonar and modelling studies have demonstrated the ability of submarine melting to undercut glacier termini (O'Leary & Christoffersen 2013, Fried et al. 2015, Slater et al. 2017b), a process believed to enhance calving and the formation of embayments along the ice front. At tidewater glaciers with floating tongues or ice shelves, submarine melting beneath the ice can cause high thinning rates, leading to increased stresses that initiate rifts in the ice tongue, and can cause the floating ice to disintegrate (Truffer & Motyka 2016). Submarine melting of glacier fronts and icebergs is also a significant source of freshwater in glacial fjord systems, and has the potential to alter fjord-scale circulation and local heat budgets (e.g., Truffer & Motyka 2016, Enderlin et al. 2016, Moon et al. 2017).

Numerous studies have estimated glacier and iceberg submarine melt using hydrographic measurements in glacial fjords (e.g., Motyka et al. 2003, Rignot & Steffen

2008, Rignot et al. 2010, Johnson et al. 2011, Sutherland & Straneo 2012, Inall et al. 2014), ocean circulation models (e.g., Jenkins & Holland 2002, Jenkins 2011, Xu et al. 2012, 2013, Sciascia et al. 2013, Slater et al. 2015), or remote sensing observations (e.g., Rignot & Jacobs 2002, Joughin & Padman 2003, Enderlin & Howat 2013, Enderlin et al. 2014, Wilson et al. 2017). Each methodological category is discussed below, prior to a consideration of the key controls on the magnitude of submarine melt rate.

2.4.1 Melt rates from fjord hydrographic profiles

Studies using hydrographic profiles in glacial fjords have estimated submarine melt rates near the grounding lines of ice shelves and tidewater glaciers using a heat flux approach. Equations for the conservation of mass, salinity and heat are used to estimate the net heat flux towards and away from the glacier front, with the net difference assumed to be due to ice melt (Motyka et al. 2003). This flux difference is then converted into a melt rate assuming a given ice front surface area. Using this approach, submarine melt rates were estimated for LeConte Glacier in Alaska (Motyka et al. 2003, 2013), ranging from 6.7 to 16.8 $\pm$ 1.3 m d^{-1}, and for various marine terminating glaciers in western (Rignot et al. 2010, Johnson et al. 2011) and eastern Greenland (Sutherland & Straneo 2012, Inall et al. 2014), ranging from 0.071 to 3.9 m d^{-1} and 0.68 to 10.1 m d^{-1}, respectively.

Most measurements used to derive heat fluxes in glacial fjords (and thus submarine melt rate) are taken far from the glacier grounding line - typically between 15 to 80 km away (e.g., Johnson et al. 2011, Christoffersen et al. 2012, Sutherland & Straneo 2012, Inall et al. 2014). As such, heat flux estimates are integrating many of the various processes occurring between the hydrographic profile and the terminus, most notably the heat lost to the melting of icebergs, sea ice and ice mélange. In addition, heat flux estimates from hydrographic profiles are typically snapshots of fjord conditions for one specific location and time, and therefore do not consider temporal variability in fjord circulation (Jackson & Straneo 2016); it is thus unclear how representative these estimates are of the longer term mean. Given the known spatial complexity in fjord temperature and salinity profiles, the spatial extrapolation of heat flux estimates from

one or several vertical profiles to fjord-wide estimates also introduces error into the derived melt rates (Truffer & Motyka 2016).

2.4.2 Melt rates from ocean circulation models and plume theory

Ocean circulation models have frequently been employed to estimate submarine melting and to investigate controls on its magnitude. The majority of models are based on plume theory, where meltwater from surface ablation is discharged subglacially, flows up the glacier face and captures surrounding warm fjord water, leading to submarine melting of the ice face (Jenkins 2011). Using a simplified one-dimensional plume model fitted with equations conserving mass, momentum, salinity, and heat, Jenkins (2011) derived submarine melt estimates from ice shelves in Antarctica (0.0015 to 0.042 m d^{-1}), Jakobshavn Glacier in Greenland (0.72 to 3.16 m d^{-1}), and LeConte Glacier in Alaska (0.36 to 9.45 m d^{-1}). Advances in ocean modelling have allowed for both two- and three-dimensional plume models, the latter accounting for across-fjord variability in melt rate. Employing a two-dimensional 'flowline' model, Sciascia et al. (2013) and Xu et al. (2012) estimated submarine melting of glaciers in eastern and western Greenland of up to 12.4 m d^{-1}. Using three-dimensional 'conical' plume models to account for variation across the glacier terminus, Xu et al. (2013) and Slater et al. (2015) have estimated submarine melting in Greenland of up to 3.6 m d^{-1}.

In order to avoid complexity, many plume models do not account for the influence of strong katabatic winds or tidal forcings, components that can have significant impacts on fjord circulation, and may alter the estimated melt rates (Jenkins & Holland 2002, Xu et al. 2012, Sciascia et al. 2013). In addition, all models need to be constrained using field observations, which are extremely limited or non-existent for many of the fjord systems around Greenland.

2.4.3 Melt rates from remotely sensed methods

Submarine melt rates have also been derived via remote sensing, using an ice flux balance approach to estimate melt rates beneath floating glacier tongues (e.g., Rignot & Jacobs 2002, Rignot & Steffen 2008, Enderlin & Howat 2013). For this approach, a

steady state is assumed, with no significant temporal changes in ice thickness, negligible ice accumulation, and modest surface ablation (Rignot & Steffen 2008). The difference in ice flux between the grounding line and the ice front of floating glacier tongues is due to a combination of surface melt, submarine melt and iceberg calving, if applicable. Therefore, if the contribution of other attributes is known, submarine melt can be derived. Following this approach, Enderlin & Howat (2013) estimated submarine melt rates beneath 13 floating glacier termini on the western and eastern coasts of Greenland, by subtracting estimated surface melt and runoff from the difference in ice flux through cross-sections of ice at the grounding line and close to the ice front. Submarine melt rates averaged over the area of each floating ice tongue between the grounding line and the terminus ranged from 0.03 ± 0.02 to 2.98 ± 0.65 m d^{-1} (Enderlin & Howat 2013). Similarly, Rignot & Jacobs (2002) estimated melt rates from 23 regions in Antarctica, ranging from 0.011 to 0.11 m d^{-1}. While steady state estimated melt rates are valid for glaciers and ice shelves in equilibrium, they are less accurate for glaciers currently thinning or thickening.

Extensive work has also been undertaken using remotely sensed imagery to estimate iceberg and ice mélange submarine melt rates (e.g., Enderlin & Hamilton 2014, Enderlin et al. 2016, 2018). Enderlin & Hamilton (2014) used very high resolution digital elevation models (DEMs) over Sermilik Fjord to derive changes in iceberg freeboard and thus volume loss (assuming the icebergs were floating in hydrostatic equilibrium). Averaging total volume loss over the full estimated underwater surface area of each iceberg resulted in melt rates ranging between 0.1 and 0.8 m d^{-1}, with an average melt rate of 0.39 ± 0.17 m d^{-1} (Enderlin & Hamilton 2014, Enderlin et al. 2016).

Remotely-sensed methods for estimating submarine melt rate can be quite user-intensive and time-consuming, requiring the user to manually identify icebergs and hand-digitize their outline many times over to avoid user bias. These methods can also involve complex image processing and can be quite expensive if high resolution commercial satellite imagery is required.

2.4.4 Key controls on submarine melt rates

Plume theory combined with fjord circulation models has been used to shed light on some of the major controls on submarine melting, which include the velocity and temperature of the plume, the magnitude of subglacial discharge emerging from the glacier grounding line and the structure of the subglacial drainage system from which meltwater emerges at the grounding line (including for example the spacing of subglacial channels). Several studies (e.g., Jenkins 2011, Xu et al. 2013, Cowton et al. 2015, Slater et al. 2015) have used the knowledge of plume theory - that submarine melt rate increases with plume velocity and temperature - to demonstrate that submarine melt rates often peak at depth directly above subglacial outlet channels and are strongest along the central axis of the plume (Figure 2.12). Slater et al. (2015) used an ocean circulation model to investigate the influence of subglacial hydrology on submarine melting by varying subglacial discharge and channel number along an idealized ice front. If all subglacial discharge is routed through one main channel beneath the ice front, submarine melting is very high locally but nearly non-existent along the rest of the ice front (Figure 2.12i). In contrast, when discharge is routed through more numerous small evenly spaced channels, local submarine melting is reduced (Figure 2.12l); however, when averaged over the entire ice front, melt rates are higher for a distributed channelised system than for a system with a single dominant channel (Slater et al. 2015), as more of the ice front is exposed to a moving plume. These studies demonstrate what is perhaps the greatest strength of ocean circulation models based on plume theory - their ability to derive patterns in and styles and timing of submarine terminus melt.

Remote sensing techniques, laboratory experiments and models based on plume theory have investigated some of the key controls on iceberg melt rate (Mugford & Dowdeswell 2010, Enderlin & Hamilton 2014, Moon et al. 2017, FitzMaurice et al. 2016, 2017). Similar to submarine melt rates of glacier termini, iceberg melt rates increase with fjord water temperature and flow velocity; as such, any processes that increase water velocity will also increase iceberg melt. Iceberg draft has a large influence on melt rate, as icebergs with deeper drafts typically sit in warmer fjord water and thus have increased

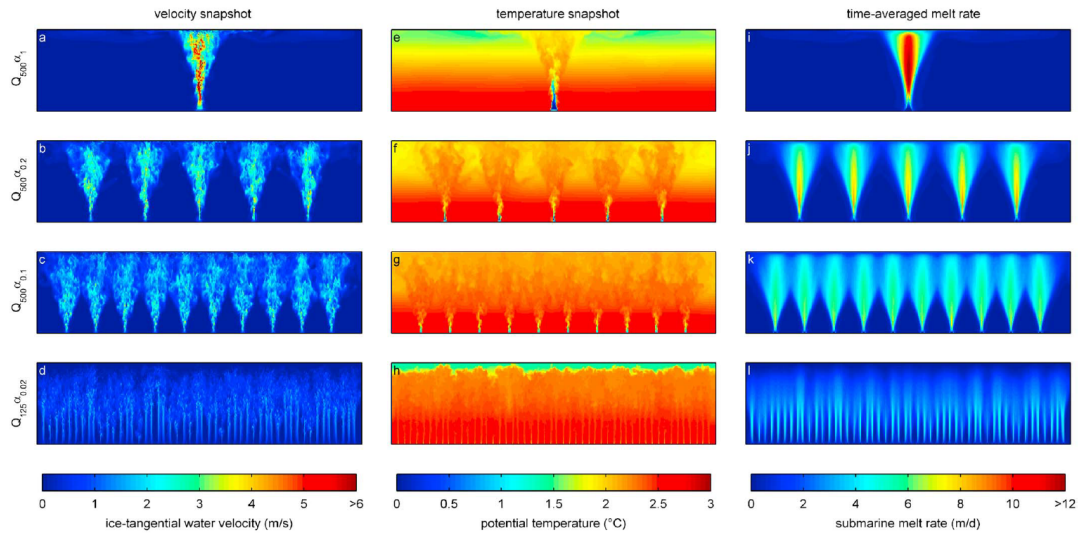

Figure 2.12: Modelled subglacial plume velocity (left column) and temperature (centre column) along with time-averaged ice front submarine melt rate (right column) for various magnitudes of subglacial discharge (125 to 500 m^3 s^{-1}) exiting from between 1 to 50 evenly spaced channels; reproduced from Slater et al. (2015).

local melt rates when compared to more shallow icebergs (Figure 2.13) (e.g., Enderlin et al. 2018). Melt rates also increase with ambient water temperature at any depth in the water column, peaking along the submerged sides of icebergs in the summer months due to warmer water temperatures (Mugford & Dowdeswell 2010). In addition, wind- and subglacial discharge driven changes in fjord circulation can influence iceberg melt rates, changing the location and thickness of velocity shear zones along the underwater length of an iceberg (Mugford & Dowdeswell 2010, FitzMaurice et al. 2016, Moon et al. 2017).

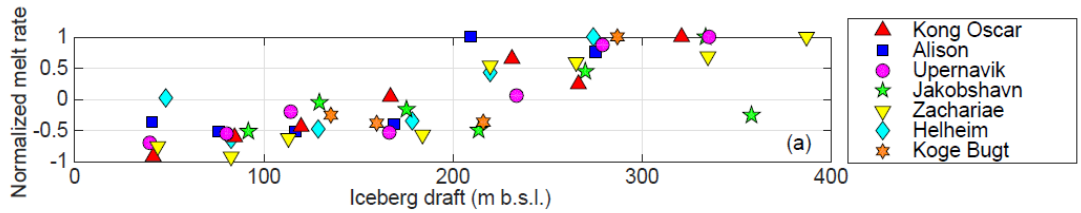

Figure 2.13: Iceberg melt rate variability with draft for seven Greenlandic tidewater glaciers; modified from Enderlin et al. (2018).

2.5 Iceberg freshwater fluxes

Recent studies have demonstrated that freshwater fluxes from the melting of icebergs can dominate the freshwater budget in glacial fjords (Enderlin et al. 2016, Moon et al. 2017), having important implications for glacier dynamics (i.e., through impacting fjord circulation and heat budget), nutrient cycling and fjord productivity. Iceberg freshwater fluxes have been estimated using both full-scale iceberg models (e.g., Mugford & Dowdeswell 2010, Moon et al. 2017) and remote sensing techniques (e.g., Enderlin & Hamilton 2014, Enderlin et al. 2016, 2018). Moon et al. (2017) estimated iceberg melt in Sermilik Fjord (from which freshwater fluxes are derived) using a complex model which incorporated oceanographic and reanalysis data and modelled buoyant plume velocities. The iceberg model accounts for several melt mechanisms, including melt above the fjord waterline from atmospheric influences (e.g., solar radiation and wind), melt at the waterline from wave action, and melt below the waterline from in-situ oceanic conditions and the movement of meltwater plumes along the vertical face of the iceberg (Figure 2.14a).

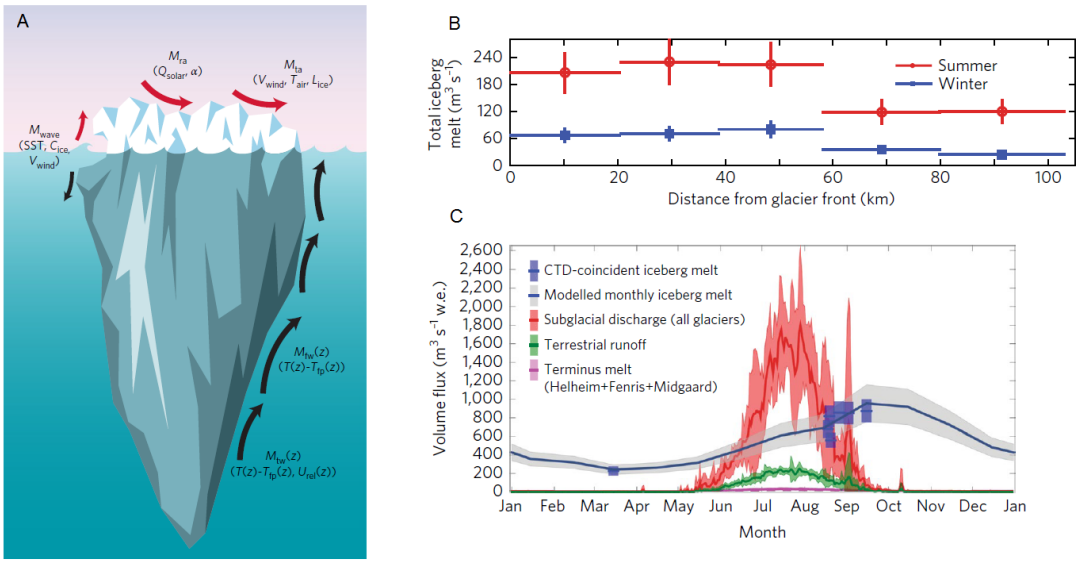

Figure 2.14: (a) Iceberg melt mechanisms included in a full-scale iceberg model, (b) iceberg melt rates with distance from the Helheim Glacier ice front, and (c) intra-annual liquid meltwater flux by source in Sermilik Fjord; modified from Moon et al. (2017).

Modelled iceberg melt (and thus flux) in Sermilik Fjord varies with distance from Helheim Glacier (Figure 2.14b) (Moon et al. 2017). At all distances from the ice front, melt rates are higher in summer than in winter, likely reflecting increased ocean temperatures (Mugford & Dowdeswell 2010, Moon et al. 2017). Modelled fluxes also peak later in the year than other freshwater sources in the fjord (Figure 2.14c), providing increased freshwater at depth in the spring, autumn and winter when other sources have reduced to insignificant levels. Enderlin et al. (2016) also demonstrated that iceberg and ice mélange meltwater fluxes dominate Sermilik Fjord freshwater input for the majority of the year. Using the iceberg freeboard differencing technique developed by Enderlin & Hamilton (2014), mélange freshwater flux was estimated as 126 - 494 m^3 s^{-1} (Enderlin et al. 2016), with the volume depending strongly on the submerged area and depth of the mélange.

Sulak et al. (2017) also estimated freshwater flux from icebergs into Sermilik Fjord. Planform surface areas were hand-delinated for 712 icebergs from WorldView DEMs and iceberg volumes were estimated by assuming that the icebergs were floating in hydrostatic equilibrium (i.e., extrapolating above waterline volume from the DEMs to full iceberg volume). A relationship between the two measures was established and applied to thousands of icebergs that were semi-automatically identified and delineated using a brightness threshold in the open fjord and edge detection in the ice mélange (Sulak et al. 2017). Assuming icebergs have a block underwater configuration (the definition of which is unclear in Sulak et al. (2017)) and applying average melt rates from Enderlin et al. (2016) yielded an iceberg freshwater flux of 620 $\pm$ 140 m^3 s^{-1} (Sulak et al. 2017), the same order of magnitude as the freshwater input from subglacial discharge into the fjord.

There are several limitations to both modelling and remote sensing approaches to deriving iceberg freshwater flux in glacial fjords. Iceberg models are highly complex and rely on limited or non-existent field observations to calibrate model parameters. As with all models, they can also be computationally expensive to run over long periods of time. Previous remote sensing techniques for freshwater flux estimates are user-intensive and time-consuming, particularly if a large number of icebergs and fjord

systems are analysed. In addition, very high resolution satellite data is not often freely available, and coverage for spatially and temporally extensive datasets can be prohibitively expensive.

2.6 Summary of motivation for thesis

As discussed in Sections 2.2 and 2.4, the stability of tidewater glaciers and changes in their dynamics, of which submarine melting is a key control, are critically important for the future state of the Greenland Ice Sheet through their influence on ice thinning, acceleration and retreat. Submarine melting from tidewater glacier termini, ice mélange and icebergs can significantly impact local fjord water circulation and heat budget, with important implications for glacier dynamics, nutrient cycling and fjord productivity. It is, however, very difficult to constrain submarine melt rates, in part due to the dangerous conditions close to tidewater glacier termini, which limit access to the ice front for taking in-situ measurements. Estimates of submarine melt rates from fjord hydrographic profiles and ocean circulation models based on plume theory both rely on fjord measurements taken far from the ice front that do not likely represent conditions directly adjacent to glacier termini, and models also depend on unknown parameters. Remote sensing techniques used to estimate iceberg melt rates and the subsequent meltwater flux into the fjord are often expensive, user-intensive and time-consuming, and models used to estimate the same are very complex and themselves rely on often non-existent field data. As such, this thesis aims to address these methodological limitations by developing novel, simple methodologies for estimating submarine melt rates and meltwater fluxes in glacial fjords, without recourse to expensive field data collection or the complex processing of models.

Chapter 3

Methods

This chapter provides a brief overview of the methodologies used and developed in this thesis. Information is provided on the acquired data sources, the generation of ice elevation and velocity values, the derivation of surface and submarine melt rates, the estimation of catchment-wide basal meltwater flux, the generation of flow routing beneath Kangiata Nunaata Sermia (KNS) using a hydropotential analysis, and finally the derivation of iceberg freshwater fluxes. All of these methods are explained in greater detail in the main results Chapters 4-6 in conjunction with their relevant supporting information.

3.1 Data sources

3.1.1 Satellite data

A variety of radar and optical satellite data were used throughout this thesis, including TerraSAR-X and TanDEM-X radar imagery, and Landsat 7 and 8 and Sentinel-2 optical imagery. TerraSAR-X and TanDEM-X synthetic aperture radar imagery was used in Chapters 4-5 to estimate ice tongue elevation and velocity, respectively. TerraSAR-X has a repeat orbit cycle of 11 days and both sensors have a horizontal spatial resolution of approximately 3 m (Krieger et al. 2007, Eineder et al. 2011). TanDEM-X flies in close orbital configuration with TerraSAR-X, operating at a sampling frequency of

110 MHz and a chirp bandwidth of 100 MHz (Krieger et al. 2007). As these sensors are radars, they enable the acquisition of imagery during non-daylight hours and in cloudy conditions, a benefit of using radar instead of optical sensors. Imagery was made available to Noel Gourmelen by the German Aerospace Centre (DLR) through projects XTI_GLAC0296 and LAN1534, and is available for purchase directly from Airbus Defense and Space (https://www.intelligence-airbusds.com/en/8289-imagery-services).

Landsat imagery was used in Chapter 5 for detecting the fjord surface expression of subglacial discharge plumes near the KNS ice front. The Landsat panchromatic band (band 8, 500 to 680 nm) has a horizontal spatial resolution of 15 m and a 16-day repeat orbit cycle (USGS 2016). Despite this relatively short repeat interval, far fewer images are actually usable due to extensive cloud cover over glacier fjords in the summer and the lack of visibility during the extensive polar 'night' over winter. Surface plumes were hand-digitised from all usable imagery, dates of which can be found in Table S2.2. All imagery is free to download from the United States Geological Society (USGS) Earth Resource Observation and Science (EROS) Center (https://eros.usgs.gov).

Sentinel-2 imagery was used in Chapter 6 for detecting and delineating icebergs in Sermilik Fjord. The Sentinel-2 near-infrared band (band 8, 763 to 908 nm) has a horizontal spatial resolution of 10 m and a full-scene repeat orbit cycle of between 5 and 10 days when both Sentinel-2A and 2B are used (Gatti & Bertolini 2015). The time interval between the images used here ranges from 2 to 50 days (see Table 3.1), with restrictions due to cloud and sea ice cover over and in the fjord, respectively. Sentinel-2 imagery is free to download from the European Space Agency (ESA) Copernicus Open Access Hub (https://scihub.copernicus.eu/).

More details regarding the specific uses of each imagery are found later in this chapter and in the rest of this thesis.

Table 3.1: Acquisition dates, extents, cloud / sea ice cover and usage made of individual Sentinel-2 satellite images over Sermilik Fjord, where SA = iceberg planar surface area.

Acquisition Date	Extent	Cloud / Sea Ice Cover	Usage
11/06/2017	Western half of fjord	None / Low	Velocity
15/06/2017	Full-fjord	Low / High	Velocity
25/06/2017	Full-fjord	Medium / High	Velocity
28/06/2017	Full-fjord	None / High	Velocity
01/07/2017	Western half of fjord	None / High	Velocity
11/07/2017	Western half of fjord	None / Medium	Velocity
21/07/2017	Western half of fjord	None / None	Velocity
23/07/2017	Full-fjord	None / None	SA
28/07/2017	Full-fjord	None / None	SA & Velocity
30/07/2017	Full-fjord	None / None	SA
31/07/2017	Western half of fjord	None / Low	Velocity
04/08/2017	Full-fjord	None / Low	SA & Velocity
10/08/2017	Western half of fjord	None / Low	Velocity
14/08/2017	Full-fjord	None / None	SA & Velocity
17/08/2017	Full-fjord	None / None	SA & Velocity
30/08/2017	Western half of fjord	Low / High	Velocity
03/09/2017	Full-fjord	High / Low	Velocity
13/09/2017	Full-fjord	None / Low	SA & Velocity
02/11/2017	Full-fjord	None / Low	SA

3.1.2 Time-lapse camera imagery

Time-lapse camera imagery was used for detecting the formation, presence and break-up of the seasonal ice tongue at KNS, as well as detecting both the presence and location of subglacial plumes on the fjord surface and calving events along the western side of the ice front in 2012 and 2013. The camera was installed and maintained between 2008 and 2013 by Martin Truffer and Mark Fahnestock from the University

of Alaska Fairbanks and was located on bedrock on the western side of the fjord at 64°17'35.16" N, 49°40'30.18" W (Figure 3.1). The images record the western half of the KNS terminus (Figure 3.2) and were taken every 4 hours. Details regarding the identification of surface plume expressions and calving events from these images are found in Chapter 5.

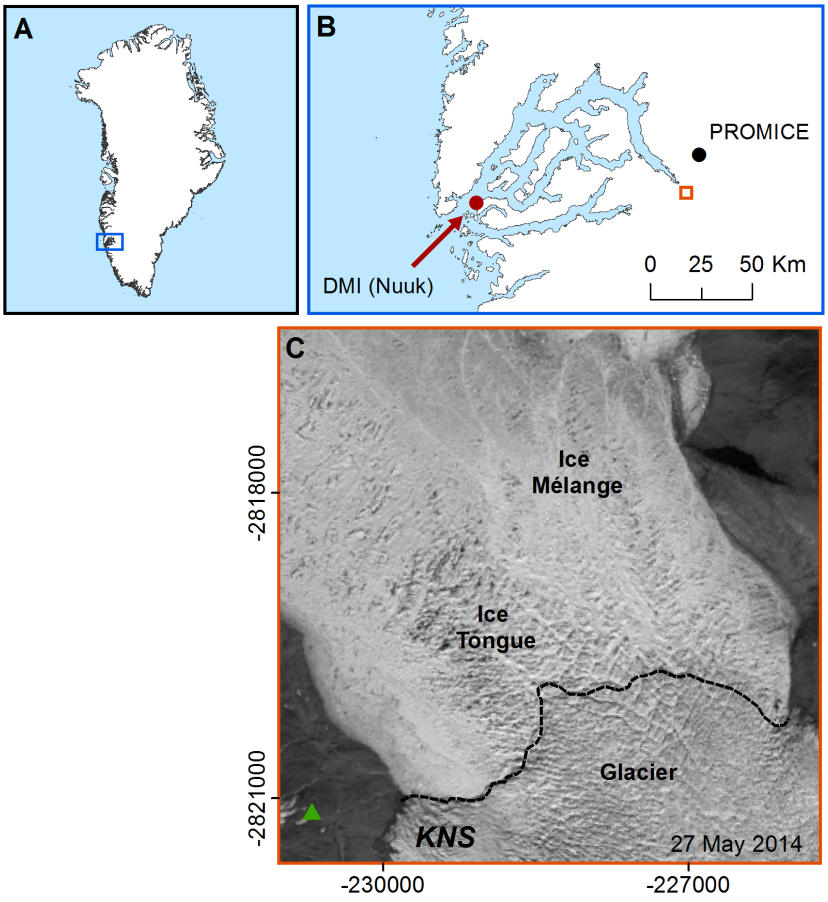

Figure 3.1: Study area for Chapters 4-5, including (a) Greenland location map where blue rectangle indicates the extent of (b); (b) fjord-scale location map within the wider Godthåbsfjord system with location of two weather stations: Danish Meteorological Institute (DMI) Nuuk (red filled circle) and PROMICE NUK_L (black filled circle). The open orange square corresponds to the location of (c); (c) a Landsat 8 band 8 satellite image of the KNS glacier ice tongue (27 May 2014), where the black dashed line indicates the estimated grounding line position and the green triangle indicates the location of the University of Alaska Fairbanks time lapse camera.

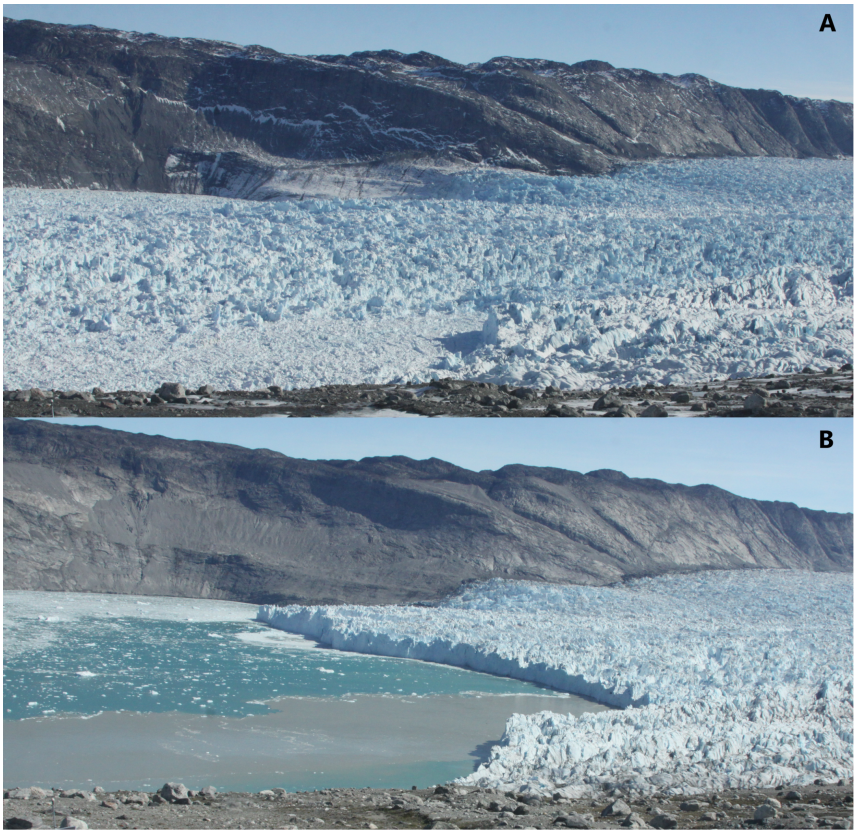

Figure 3.2: Sample time lapse imagery of KNS, including (a) an image showing the intact seasonal ice tongue on 2 April 2012 and (b) an image showing a surfacing subglacial discharge plume and evidence of calving on 16 July 2012. Camera location can be seen in Figure 3.1c.

3.1.3 Meteorological data

Meteorological data from several automatic weather stations were used for estimating ice tongue surface melt and glacier-wide catchment run-off. Near KNS, mean daily air temperature data were acquired for 2012 to 2014 from a Geological Survey of Denmark and Greenland (GEUS) PROMICE weather station located 550 m above sea level on the ice sheet approximately 21 km northeast of the ice front (64°28'55.2" N, 49°31'50.88" W; Figure 3.1b). Daily precipitation data for the same time period were acquired from a Danish Meteorological Institute (DMI) weather station located 80 m above sea level approximately 105 km west of the KNS ice front towards the open coast (64°10'0.12" N, 51°45'0.00" W).

In order to estimate run-off from Helheim Glacier, mean daily air temperature data for 2017 were acquired from a different PROMICE weather station, located 440 m above sea level approximately 78 km southeast of the Helheim Glacier terminus (65.6922°N, 37.8280°W; Figure 3.3a). Daily precipitation data were acquired from a DMI weather station in Tasiliaq, approximately 90 km southeast of the glacier terminus at 54 m above sea level (65°36'0.00" N, 37°38'12.0" W). All PROMICE and DMI data are freely available at http://www.promice.dk and http://www.dmi.dk, respectively.

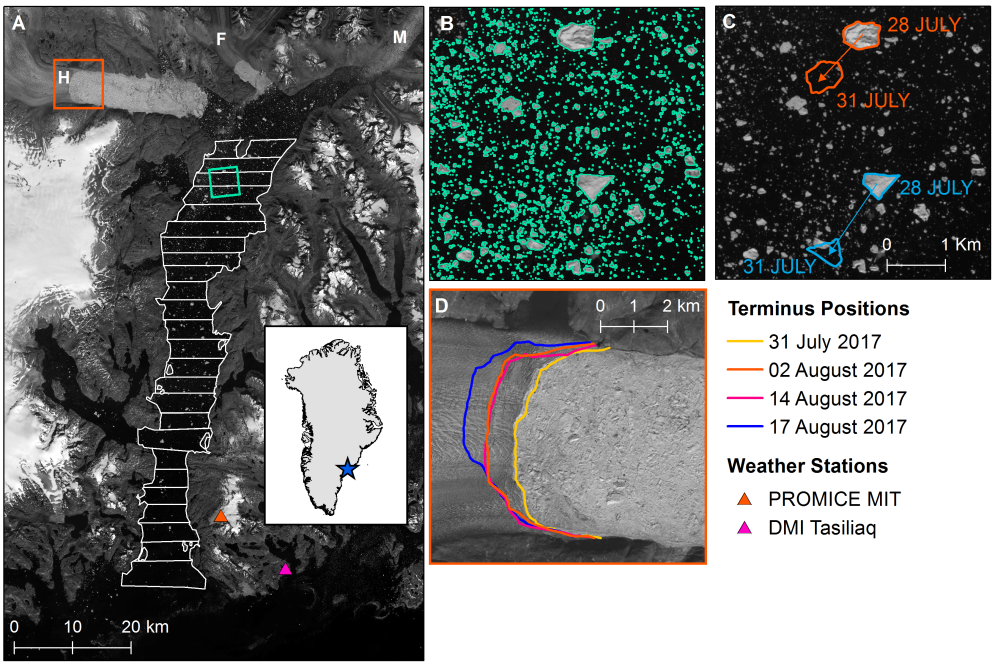

Figure 3.3: (a) Sermilik Fjord from a Sentinel-2 image on 28 July 2017, including three large tidewater glaciers: Helheim (H), Fenris (F), and Midgård (M). White boxes are areas of the fjord included in the analysis, the green box indicates the extent of (b,c) and the orange box indicates the extent of (d); the orange and pink triangles indicate the locations of the PROMICE MIT and DMI weather stations, respectively; (b) automatically classified iceberg polygons, highlighting pixels with TOA reflectance values $\geq$ 0.13; (c) sample polygon tracking for velocity estimation for two distinct icebergs between 28-31 July, overlain on a Sentinel-2 image from 28 July 2017; (d) terminus positions for Helheim Glacier, hand-digitized from Sentinel-2 and Landsat 8 band 8 imagery.

3.2 Generating elevation and velocity values

3.2.1 Ice tongue elevation

Bi-static TanDEM-X radar imagery were used to generate digital elevation models (DEMs) over the KNS ice tongue for five image pairs, resulting in 2.5 m horizontal spatial resolution DEMs for the following dates: 13 May 2012, 17 March 2013, 27 May 2013, 14 May 2014 and 05 June 2014. DEMs were generated from conventional SAR interferometric processing (Dehecq et al. 2016), using the 90 m GIMP DEM (Howat et al. 2014) to minimize unwrapping errors. ICESat elevation data over bedrock areas were used to help correctly align the DEMs, both horizontally and vertically. Operation IceBridge (OIB) Airborne Topographic Mapper (ATM) L1B Elevation and Return Strength data (Krabill 2016) were used to correct for an additional tilt in the generated DEMs; this correction was required because of the limited coverage of ICESat lines over the study area (Figure S1.3). A more detailed description of the DEM generation and associated errors can be found in Chapter 4 and its supporting information.

3.2.2 Ice tongue velocity

Two sources of ice velocity were used for estimating the submarine melt rates beneath the floating ice tongue at KNS, and they were selected to find the best temporal correspondence with the available elevation data. For 2012 and 2014, pre-generated velocity maps were acquired directly from the Technische Universität Dresden in a user-ready format (Rosenau et al. 2015), as derived from combined feature tracking of Landsat 7 and 8 imagery. Velocity maps were acquired from the following image pairs: 6 and 22 May 2012; 27 May and 12 June 2014 (freely available from http://data1.geo.tu-dresden.de/flow_velocity). For 2013, three velocity maps with a horizontal spatial resolution of 20 m were created using conventional feature tracking of TerraSAR-X imagery (Paul et al. 2013, Tedstone et al. 2014) using the following image pairs: 12 and 23 February 2013; 8 and 19 April 2013; 30 April and 11 May 2013.

Uncertainty in ice tongue velocity derived from Landsat imagery was downloaded directly from the Technische Universität Dresden on a pixel-by-pixel basis. Uncertainty

in velocity derived from Terra-SAR-X imagery was calculated as the average velocity estimated over stable bedrock areas, where there should be no movement between two scenes. More details regarding uncertainty and velocity generation are found in Chapters 4 and 5.

3.2.3 Iceberg velocity

In order to derive iceberg freshwater fluxes, mean iceberg velocities were required and these are estimated by visually tracking six distinctly shaped icebergs in Sermilik Fjord through a collection of 16 Sentinel-2 images dated between early June and mid-September 2017 (Table 3.1). The distance moved by each iceberg between successive scenes was hand-measured (Figure 3.3c), and the velocity was estimated by taking this distance divided by the time between successive scenes. These estimates should be considered minimum velocities, as the icebergs are unlikely to move in a linear manner between scenes.

3.3 Deriving melt rates

A decrease in freeboard and thus thinning observed along the flow direction of the KNS ice tongue (as shall be shown in Chapter 4) can be potentially attributed to three main causes: (1) changes in surface mass balance (i.e., melting of the ice tongue surface), (2) lateral or longitudinal spreading of the ice tongue, or (3) submarine melting from below the ice tongue. Each of these components is addressed in brief below and in more detail in Chapter 4. Uncertainties in melt rates are addressed extensively in both Chapters 4 and 5.

3.3.1 Surface melt rates

Surface melt rates over the KNS ice tongue were modelled for 2012 to 2014, using a simple positive degree day (PDD) approach that assumes a relationship between snow and ice melt and air temperature (Hock 2003). This relationship was defined using degree day factors for snow (k_s) and ice (k_i) of 4.5 and 11.9 mm of melt (water equivalent) per positive degree day (mm d^{-1} $^{\circ}C^{-1}$), respectively (Slater et al. 2017a).

Daily air temperature data from the PROMICE station near KNS were adjusted to sea level using a temperature lapse rate of 0.5 °C per 100 m elevation. The accuracy of the precipitation data acquired from the DMI station is discussed in Chapter 4.

Catchment-wide surface run-off was also estimated in order to constrain the amount of surface meltwater potentially exiting beneath the glacier grounding line in the form of subglacial discharge plumes, assuming all of the meltwater produced on the surface eventually reaches the bed of the ice sheet. Similar to estimating ice tongue surface melt rates, run-off from the KNS (2012 to 2014) and Helheim, Fenris and Midgård (all in 2017) glacier catchments was modelled using a PDD approach. However, instead of adjusting the air temperature data to sea level, data were adjusted to the elevations below 2,000 m over each glacier catchment in intervals of 100 m elevation bands derived from the 90 m GIMP DEM (Howat et al. 2014). Elevations were capped at 2,000 m as most meltwater refreezes within the snow pack at higher elevations (e.g., Pfeffer et al. 1991, Langen et al. 2015, 2017). The same degree day factors for snow and ice, used for estimating ice tongue surface melt, were used across the full KNS catchment at elevations below 2,000 m. For Helheim, Fenris and Midgård glacier catchments, surface run-off below 2,000 m elevation was estimated using degree day factors for snow and ice of 3 and 9 mm d^{-1} $°C^{-1}$, respectively (Fausto et al. 2009, Box 2013, Enderlin et al. 2014). A temperature lapse rate of 0.68 °C per 100 m elevation was used to adjust air temperature to catchment elevations in these east Greenland catchments (Hanna et al. 2005, 2011). The degree day model used to estimate both ice tongue and catchment-wide surface melting is detailed below.

In order to accurately estimate surface melt, the snow pack storage at each elevation and time step (i.e., day) was calculated. Following Moore et al. (2012), the first step in calculating snow pack storage was partitioning precipitation as either rain or snow depending on the threshold temperatures, T_{Rain} and T_{Snow}. Here, threshold temperatures were 3 and -5°C for rain and snow, respectively, in line with values developed from studies in glaciated mountainous regions (Kienzle 2008, Moore et al. 2012). If the daily air temperature (T) was greater than T_{Rain}, then all the precipitation from that day was considered to be rainfall. If T was less than T_{Snow}, then all the daily

precipitation was considered to be snowfall. If, however, T fell between T_{Rain} and T_{Snow}, then precipitation (P) was split between rain (R) and snow (S) as follows:

$$S = P\frac{T_{Rain} - T}{T_{Rain} - T_{Snow}} \tag{3.1}$$

and

$$R = P - S \tag{3.2}$$

The degree day model starts by calculating potential melt (M_P), which was considered negligible for days when the mean air temperature is less than 0°C. For days when T was greater than 0°C, M_P was estimated:

$$M_P = k_s T. \tag{3.3}$$

Actual melt (M_A) was then calculated by considering the sum of the previous day's snow storage (SWE_{i-1}) and the current day's new snowfall (S):

$$M_A = min(M_P, SWE_{i-1} + S). \tag{3.4}$$

A new snow storage (SWE_i) was then updated to include any actual melting:

$$SWE_i = SWE_{i-1} + S - M_A. \tag{3.5}$$

If the melt potential exceeded the actual melt, then any excess (M_{EX}) was applied to melting glacier ice (M_I) found beneath the snow layer, where:

$$M_{EX} = \frac{M_P - M_A}{k_s} \tag{3.6}$$

and

$$M_I = k_i M_{EX} \tag{3.7}$$

Daily total melt was then calculated by summing daily actual melt and ice melt, which was multiplied by the area of each elevation band to estimate total melt over the full catchment.

3.3.2 Submarine melt rates

Submarine melt rates were estimated beneath the ice tongue along flowlines, created every 25 m along the KNS ice tongue and approximately 150 m from the glacier grounding line (see Sections 4.3.2 and 5.3.2; Figure 3.4). Ice tongue elevation and velocity were extracted along the flowlines and smoothed separately, using a two-sided moving average with a 625 m window for elevation values and a simple linear regression with distance along-flowline for velocity. Elevation values were then converted to ice thickness assuming hydrostatic equilibrium and using ocean water and ice densities of 1,027 and 900 kg m^{-3}, respectively, as used by Enderlin et al. (2014) for floating ice in Sermilik Fjord.

Submarine melt rates (SMR) were estimated assuming an ice tongue in steady state (i.e., ice thickness at a fixed location does not change in time), justification for which is considered in Sections 4.3.5 and 5.3.3. Melt rates account for thinning due to both longitudinal and lateral stretching:

$$SMR = -v_x \frac{\delta H}{\delta x} - H \frac{\delta v_x}{\delta x} - H \frac{\delta v_y}{\delta y} - SMB \tag{3.8}$$

where H is the ice thickness (m), v_x and v_y are the ice velocity (m d^{-1}) in the along- and across-flowline direction, x and y represent distance in the along- and across-flowline direction, and SMB represents thinning due to changes in surface mass balance (i.e., surface melt). The heavy crevassing along the ice tongue likely produces several instances of unrealistic melt rates due to locally very steep surface topography; thus lines of best fit were applied to flowline melt rates to best capture the general trend.

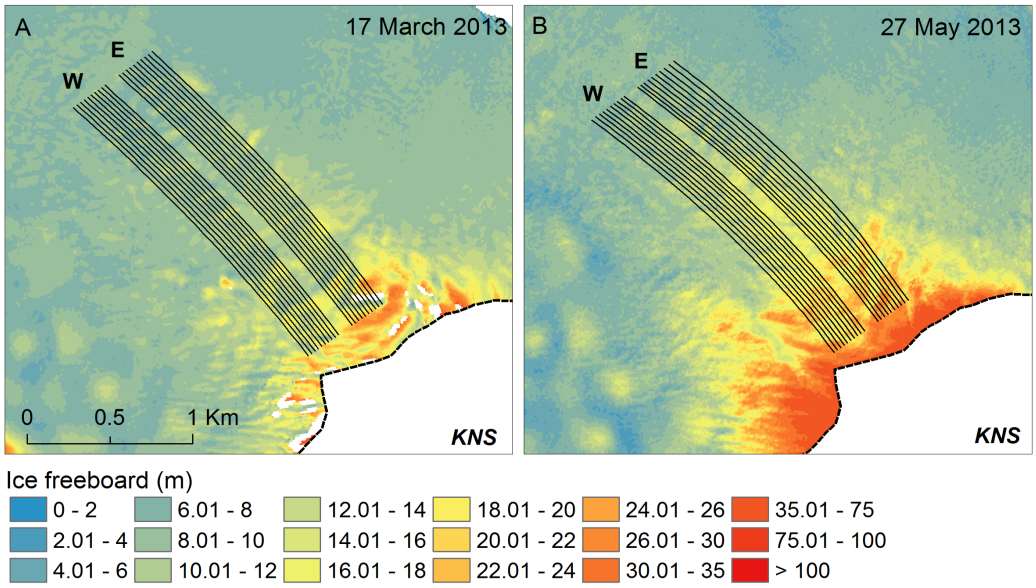

Figure 3.4: Sample flowlines on the eastern (E) and western (W) sides of the KNS ice tongue, underlain by TanDEM-X ice tongue freeboard from (a) 17 March 2013 and (b) 27 May 2013; black dashed line indicates the approximate location of the glacier grounding line.

A more detailed description of how submarine melt rates are estimated, including estimates of non-steady state melt, is found in Chapter 4.

3.3.3 Uncertainties in submarine melt rates

Uncertainties in estimated submarine melt rates are mainly associated with the quality of the elevation and velocity data, the smoothing of flowlines and our assumption of an ice tongue in steady state. All of these uncertainties are discussed in detail in Chapters 4 and 5.

In addition to these main uncertainties, submarine melt rates may experience increased uncertainty associated with the developed methodology, namely: the assumption that the ice tongue is floating in hydrostatic equilibrium near the glacier grounding line; the seasonal migration of the grounding line; the cohesiveness of the glacier, ice tongue and surrounding ice mélange; and the temporal variability of ice tongue velocity (i.e., the

assumption of a linear slowing down of ice tongue motion between February and April 2013). Each assumption and its associated uncertainty is discussed in turn below.

The ice tongue in hydrostatic equilibrium

The assumption that an ice tongue or ice shelf is floating in hydrostatic equilibrium is less valid near the grounding zone of glaciers, as the ice still attached to the grounded ice likely lies higher than the equilibrium level for up to several ice thicknesses downstream of the grounding line (e.g., Khazendar et al. 2016, Wilson et al. 2017, Shean et al. 2018). Ice that lies higher than the equilibrium level will have a higher surface elevation and thus will result in a larger and erroneously estimated ice thickness if hydrostatic equilibrium is incorrectly assumed. To avoid this uncertainty, submarine melt rates beneath long ice tongues and ice shelves are often not estimated within several ice thicknesses of the grounding line (e.g., Khazendar et al. 2016, Wilson et al. 2017, Shean et al. 2018). The ice thickness of KNS at the grounding line is approximated as 250 m; following the general method above, submarine melt rates estimated within ~500 – 1000 m of the grounding line (approximating to 2 - 4 ice thicknesses) should be treated with caution.

However, as the ice tongue at KNS is short (2-3 km) relative to the larger ice tongues of northern Greenland (e.g., Petermann Glacier: 42 km; 79N Glacier: 65 km; and Ryder Glacier: 25 km) and vast ice shelves around the margins of Antarctica, and to maximise the spatial extent of the study, melt rates were estimated starting from approximately 150 m down-fjord of the grounding line. This distance was chosen to address uncertainty in both the grounding line position (see the next section below) and ice velocity over the transition from grounded to floating ice. Ice velocities are extremely noisy in the grounding zone, but become very coherent ~150 m down-fjord.

In order to test the additional uncertainty inherent in the melt rates estimated closer to the glacier grounding line, the ratio of ice volume above versus below the waterline was incrementally decreased from 1:7 near the grounding line to 1:8 at the edge of the ice tongue, with 1:8 representing hydrostatic equilibrium based on the densities of ice and water used in the thesis (1027 and 900 kg m^{-3}, respectively). This was repeated

using starting above and below water line volume ratios of 1:5 and 1:6 as well, to cover a wide range of potential above to below surface ice thicknesses near the grounding line. Using the 17 March 2013 submarine melt rate estimates as a sample, assuming a full ice tongue in hydrostatic equilibrium overestimates melt rates within the first km from the glacier grounding line by on average 15% (compared with the hypothetical above to below waterline ice volume ratio gradient starting with 1:7, see Figure S1.5). Increasing the initial value of the above to below water line ice volume ratio gradient to 1:6 or 1:5 results in an overestimation of melt rates by on average 28 and 41%, respectively, within the first km down-fjord of the grounding line. Melt rates farther down-fjord of the grounding line are not significantly impacted ($< 12\%$) by changes in the starting ice volume ratio, as the ice approaches hydrostatic equilibrium here.

As the underwater configuration of the ice tongue near the grounding line is unknown, it is not clear which initial above to below water line ice volume ratio is appropriate for estimating submarine melt rates. In this study, the ice tongue is assumed to be floating a short distance down-fjord of the grounding line (even if not in perfect hydrostatic equilibrium), as time-lapse imagery of the fjord over numerous years shows that the entire ice tongue disintegrates and floats away within a 1 to 4 hour period each year; as such, the ice was assumed to be in hydrostatic equilibrium, with the caveat that melt rates may be overestimated within the first km of ice by at least 15%.

Seasonal migration of the grounding line

At most marine-terminating glaciers, there is likely some uncertainty associated with the precise position of the glacier grounding line throughout the year. Here, the position of the glacier terminus, after the ice tongue has disintegrated, was assumed to be the grounding line location when the ice tongue was previously present in spring. This position was delineated as the boundary between the glacier terminus and open fjord water from the first available optical satellite image post-ice tongue disintegration, usually in June. As the glacier typically advances in winter, it is possible that the grounding line location over the winter/early spring has actually been farther down-fjord than the selected location following ice tongue disintegration in any given year. If

this is the case, then estimates of submarine melt rate closest to the assumed grounding line are more uncertain, as they could potentially be measuring changes in grounded ice thickness (or changes in the thickness of floating ice not in hydrostatic equilibrium, as discussed above). It could also be possible that the grounding line is located farther up-ice than the selected location, as would be the case if either the local elevation minimum (I_m) or the break-in-slope location (I_b) (see Figure 3.5) were identified as the grounding line. If the grounding line was actually located up-ice of the assumed location, then there would in fact be less uncertainty in the estimated melt rates closer to the grounding line, as this ice would more likely be floating in hydrostatic equilibrium (compared to if the grounding line was farther advanced). As such, estimated submarine melt rates near the assumed grounding line position are more uncertain than melt rates estimated further down-fjord. To partially address this additional uncertainty, submarine melt rates were only estimated starting from a distance approximately 150 m down-fjord of the assumed grounding line, thereby allowing for some fluctuation in its true position.

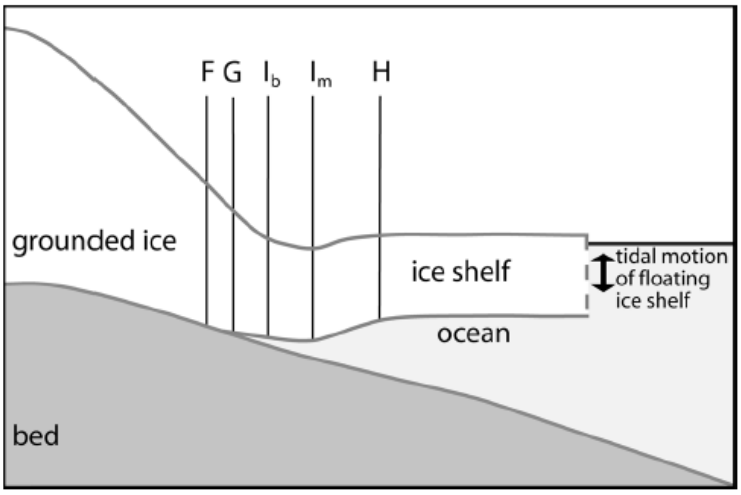

Figure 3.5: A schematic representation of grounding zone features (as typical for large ice shelves and applied here to ice tongues), where F is the landward limit of ice flexure from tidal movement; G is the true grounding line; I_b is the break-in-slope; I_m is the local elevation minimum; and H is the landward limit of the hydrostatic zone of freely-floating ice; reproduced from Fricker et al. (2009).

Cohesiveness of the ice tongue

The cohesiveness (or lack thereof) of the glacier, ice tongue and mélange continuum could also influence estimated melt rates. The methodology developed here would not be suitable for estimating melt rates over non-cohesive areas of ice in the fjord, as changes in ice thickness could be due to the movement of icebergs in a loose mélange, not due to the submarine melting or stretching of the ice. It is difficult to assess the cohesiveness of the fjord ice just by visually inspecting optical satellite or time-lapse imagery. As such, to reduce the uncertainty associated with the potential non-cohesiveness of the fjord ice, ice tongue flowline locations were chosen over areas of very coherent ice velocity, indicating a solid ice tongue moving as one unit (i.e., not randomly moving as would be expected from icebergs within a loose mélange) and thus inferred to represent coherent ice. The inferred coherence of the ice tongue is supported by the detailed inspection of 1000s of seasonal time-lapse images showing the ice tongue as a coherent, connected ice mass with no random or inconsistent movement until the very moment of ice tongue collapse. In addition, ice tongue flowlines were excluded near what appeared (from visual inspection) to be the lateral and terminal edges of the ice tongue, avoiding areas likely to be less cohesive than the main ice tongue (i.e., the transition zones between the ice tongue and looser ice mélange).

As will be seen in Chapter 5, there is not a large variance in melt rate near the edges of the ice tongue (excluding areas near the glacier grounding line). If the ice were less coherent here, melt rates would be expected to vary highly, as blocks of ice shift around in the loose mélange. The low variance in submarine melt rates around the edges of the ice tongue suggests that the defined ice tongue area has high coherence.

Temporal variability in ice tongue velocity

Temporal variability in ice tongue velocity has the potential to significantly change estimated submarine melt rates, given the dependence of melt rate on the absolute and gradient of ice velocity in the flow direction (see Equation 3.8). For most of the DEMs used in the thesis, a temporally-corresponding ice velocity plot was derived or obtained; however, TerraSAR-X imagery used for deriving ice velocity was not available

near the DEM dated 17 March 2013. As such, ice velocity in March was derived by assuming a linear change in ice velocity with time between the two nearest available ice velocity maps from 12 - 23 February and 8 - 19 April 2013, as detailed in Chapter 4. In order to test the potential effect of this assumption on submarine melt rates, both end-member velocities were used separately to estimate melt rate, resulting in an increase and decrease in melt rate by 24 and 35% when using February and April velocities as a proxy for March velocity, respectively (see Figure S1.6).

Detailed observations of seasonal variations in ice motion at 55 tidewater glaciers (Moon et al. 2014) suggests that their 'winter-spring' behaviour typically follows one of three broad patterns, seen in Figure 3.6: (a) a slow down in ice velocity between January and May before speeding up throughout the summer; (b) remains at a relatively constant speed between January and May before speeding up throughout the summer; or (c) a speed up between January and May before slowing throughout the summer (Moon et al. 2014). Given that the ice velocity for KNS in 2013 was slower in April and May than in February, it seems likely that ice speed in March would be characterised by being part of a longer term decrease between February and April.

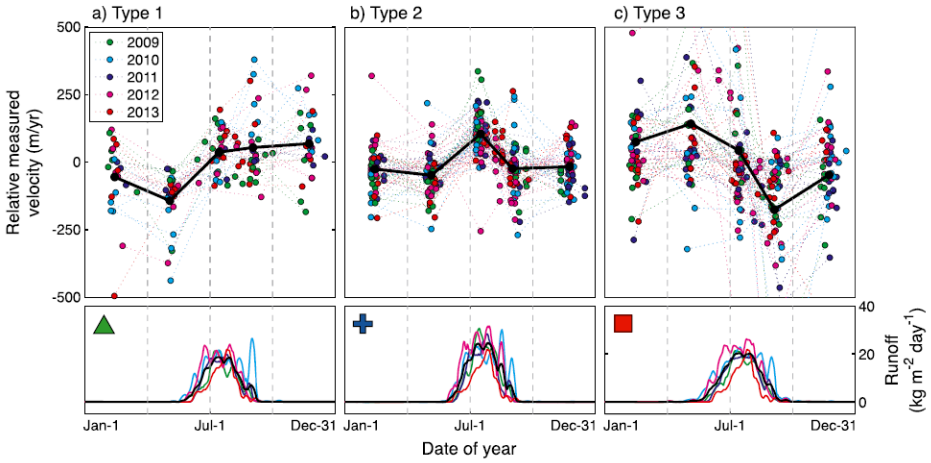

Figure 3.6: Broad patterns in ice motion and associated ice sheet runoff observed from 55 Greenlandic marine-terminating glaciers from 2009 – 2013, including (a) Type 1, (b) Type 2 and (c) Type 3 dominant seasonal velocity modes; reproduced from Moon et al. (2014).

Records for KNS from 2009 to 2018 show varied behaviour in late-winter and early-spring ice velocity (Moon et al. 2014, Davison et al. 2019). Over this 10-year record, five years (2009, 2010, 2013, 2014 and 2018), show either no significant difference or a decrease in ice speed from February to April, followed by an increase in ice speed into the summer months. For the other five years, ice speed increased between February and April, and then continued to increase into the summer. In two of these years (2011 and 2015), the ice tongue did not form (Motyka et al. 2017); this likely reduced the back stress on the glacier, allowing for both increased calving and ice motion throughout the winter months.

Despite these annual differences in late-winter ice velocity behaviour, the record for KNS in 2013 shows a slight decrease in ice velocity between February and April (Moon et al. 2014). Therefore, the assumption of a linear slowing of ice tongue velocity between February and April 2013 is likely valid, reflecting the thickening of sea ice in the fjord and its associated buttressing effect on the ice tongue and glacier (e.g., Amundson et al. 2010). As such, the estimated percent changes in melt rate resulting from velocity variations in March 2013 are not applied here.

3.4 Estimating basal meltwater flux

Basal meltwater flux beneath KNS was estimated for 2012 to 2014 in order to assess the potential influence of basal frictional melting in contributing to the presence of winter and spring discharge plumes prior to the onset of the melt season. Basal drag, the resistance to flow from friction at the glacier bed, is difficult to measure directly. As such, the basal drag (τ) at KNS was assumed to be of the same magnitude as that for Jakobshavn Isbræ, approximately 200 kPa (Iken et al. 1993, Funk et al. 1994), and as used by Christoffersen et al. (2012) for Kangerdlugssuaq Glacier in east Greenland. Basal meltwater flux was estimated using a simplified equation (Christoffersen et al. 2012):

$$\dot{m} = \frac{\tau U}{\rho L} \tag{3.9}$$

where U (m d^{-1}) is grounded ice velocity, ρ (900 kg m^{-3}) is ice density, and L (334 kJ kg^{-1}) is the latent heat of fusion. Geothermal heat flux was not considered here, as due to the high velocity of the glacier ($\geq$ ~20 m d^{-1}) frictional heat is expected to be around two orders of magnitude higher than the geothermal heat flux (Christoffersen et al. 2012). More details regarding estimating basal meltwater flux and the grounded ice velocity data sources are found in the supporting information for Chapter 5.

3.5 Generating prediction of subglacial flow routing

Potential channel locations beneath the grounded portion of KNS were predicted using a standard hydropotential analysis (Shreve 1972). This method assumes that water flows freely through a glacier along the steepest potential gradient and that the englacial drainage system is in a steady state. The subglacial hydraulic potential (Φ) was calculated following Shreve (1972) and using glacier bed and surface topography from BedMachine v3 (Morlighem et al. 2017):

$$\Phi = \rho_w g z + f \rho_i g h \tag{3.10}$$

where ρ_w and ρ_i are the densities of meltwater (1,000 kg m^{-3}) and ice (910 kg m^{-3}), respectively, g is the acceleration due to gravity (9.81 m s^{-2}), z is the bed elevation (m), h is the ice thickness (as provided in the Bed Machine v3 product), and f is the ratio of the subglacial water pressure to the ice overburden pressure (with applied spatial constants ranging from 0.1 to 1.0). The end result is a map of branching conduits fed by a network of upstream englacial channels, depending mainly on the pressure of the conduits (i.e., larger conduits formed under lower pressure and smaller conduits at high pressure). The predicted flow routing of the channels emerging at the glacier terminus was then compared with estimated submarine melt rates and the locations of subglacial discharge plumes along the glacier grounding line inferred from their surface expression observed in time-lapse imagery.

3.6 Deriving iceberg freshwater flux

Freshwater fluxes were derived from the melting of icebergs in Sermilik Fjord, east Greenland. Fluxes were only derived in the open-water areas of the fjord (i.e., excluding the ice mélange) to give confidence in the iceberg detection. In order to explore patterns of iceberg freshwater flux with distance from the Helheim Glacier ice front, fluxes were derived in fjord sections (white boxes in Figure 3.3a) previously defined by Sulak et al. (2017). The freshwater fluxes were derived from iceberg surface area, volume and velocity (Section 3.2.3), as detailed below.

3.6.1 Estimating iceberg surface area and volume

Iceberg surface areas were estimated in Sermilik Fjord by thresholding Sentinel-2 imagery from summer and autumn 2017. All available full-fjord coverage scenes with little to no cloud or sea ice cover (see Table 3.1 for acquired imagery) were converted to Top of Atmosphere Reflectance (TOA) and icebergs were semi-automatically identified using a reflectance threshold of 0.13 for summer images and 0.30 for autumn images (Figure 3.3b). Thresholds were selected to best separate ice and water pixels, while noting that some pixels containing both ice and water are likely misidentified as ice pixels. Adjacent pixels identified as containing ice were then joined into iceberg polygons, which were subsequently visually inspected and manually divided into several icebergs if they had been erroneously joined into one large iceberg. Iceberg polygon areas were then summed into sections with distance along the fjord.

Using high-resolution Worldview DEMs over Sermilik Fjord from 2011 to 2014, Sulak et al. (2017) developed a general power law fit (Figure 3.7) between planar iceberg surface area (A) and iceberg volume (V), which was estimated by assuming icebergs were floating in hydrostatic equilibrium:

$$V = 6.0A^{1.3}. \tag{3.11}$$

This thesis assumes that the above relationship remains true for other years in Sermilik

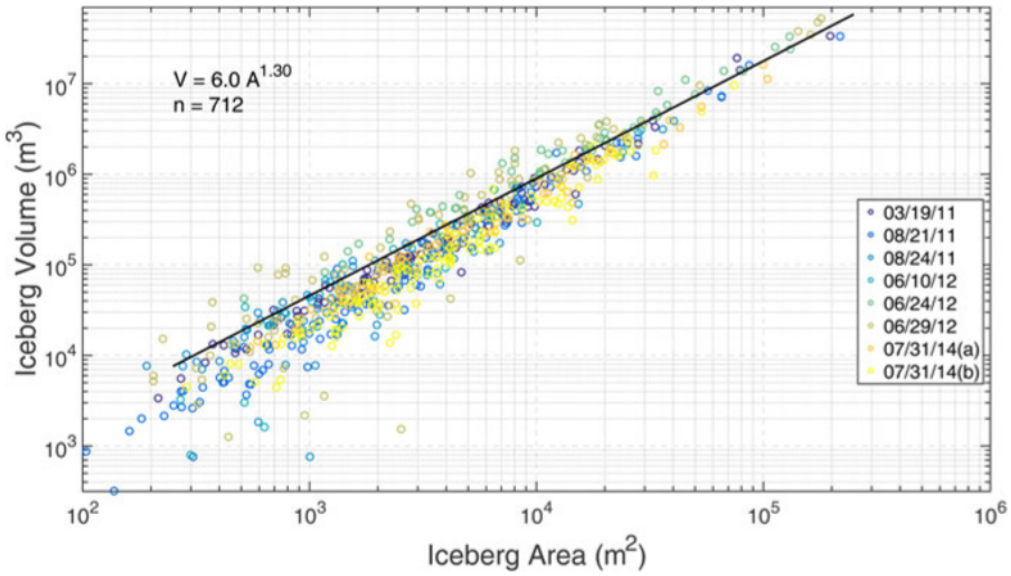

Figure 3.7: Planar surface area versus volume for 712 icebergs in Sermilik Fjord, derived from 8 WorldView DEMs acquired between 2011 and 2014 (each represented by a different colour); the black line is the best fit of all the data. Note the log-log scale; reproduced from Sulak et al. (2017)

Fjord, thus inferring no significant changes to iceberg properties or local water density. Iceberg volume was therefore estimated by applying the power law fit to each individual iceberg surface area estimate, and the volumes were then summed in each fjord section with distance along fjord. However, as the area of the fjord sections are of uneven size, the summed volumes were normalized by dividing by the area of each fjord section.

3.6.2 Estimating iceberg freshwater flux

The methodology for estimating iceberg freshwater flux assumes that icebergs generally move down-fjord through time (e.g., Sutherland et al. 2014a), while experiencing volume loss via melting. As such, freshwater flux (FW) was estimated as follows:

$$FW = \frac{\delta V}{\delta t} + u\frac{\delta V}{\delta x} \tag{3.12}$$

where $\frac{\delta V}{\delta t}$ and $\frac{\delta V}{\delta x}$ are the change in iceberg volume with time ($\mathrm{m}^3\ \mathrm{s}^{-1}$) and distance

(m^3 m^{-1}), respectively, and u is iceberg velocity (m s^{-1}). If it is assumed that the rate of change in iceberg volume with distance down-fjord is constant through time, the first term on the right-hand side of Equation 3.12 can be set to zero. Justification for this assumption is discussed in Chapter 6, as is the uncertainty associated with the freshwater flux estimates.

3.6.3 Estimating solid iceberg flux out-fjord

The percent of icebergs exiting Sermilik Fjord as solid flux was also estimated. The difference in normalized ice volume between the first and last fjord sections, as averaged for all the analysed Sentinel-2 scenes, was taken as an estimate of the percentage of solid ice lost to melting in the fjord. However, a significant amount of iceberg volume is likely lost in the mélange before the icebergs reach the first fjord section approximately 37 km down-fjord of the Helheim Glacier terminus (Figure 3.3a). Previous studies in Greenland indicate that anywhere from 10 to 49% of ice volume is lost to the melting of icebergs in the ice mélange (e.g., Enderlin et al. 2016). Normalized ice volume in the first fjord section was therefore increased by 30% to estimate the initial volume of ice originally calved from Helheim Glacier. It is assumed that the vast majority of icebergs, particularly the large full-thickness icebergs that account for most of the fjord iceberg volume, originate from Helheim Glacier, as a record of calving fluxes spanning nearly a decade shows that the calving fluxes from both Midgård and Fenris Glaciers, located in the far northeast of Sermilik Fjord (Figure 3.3a), are $\leq$ 10% of the flux estimated from Helheim (Moon et al. 2017).

Chapter 4

Estimating Spring Terminus Submarine Melt Rates at a Greenlandic Tidewater Glacier Using Satellite Imagery

Submarine melting of tidewater glacier termini is important for glacier dynamics, and has been proposed as a potential trigger for thinning, calving, retreat and acceleration. However, submarine melt rates are poorly constrained, in part due to the difficulty of collecting in-situ measurements near actively calving termini. In this first results chapter, a novel approach for deriving submarine melt rates near glacier termini is developed, using satellite imagery and changes in floating ice tongue velocity and freeboard (i.e., height of the ice surface above floatation). The results provide near-terminus estimates of submarine melt rate under the floating ice tongue at Kangiata Nunaata Sermia (KNS) in southwest Greenland, which are used to gain insight into potential controls on ice front melt rates. They also motivate the work presented in Chapter 5, which extends the investigation both temporally and spatially.

This chapter was published in *Frontiers in Earth Science* in November 2017:

Moyer AN[1], Nienow PW[1], Gourmelen N[1,2], Sole AJ[3] and Slater DA[1,4] (2017), Estimating Spring Terminus Submarine Melt Rates at a Greenlandic Tidewater Glacier Using Satellite Imagery, *Frontiers in Earth Science*, **5**:107, doi: 10.3389/feart.2017.00107.

[1]School of GeoSciences, University of Edinburgh, Edinburgh, UK.

[2]IPGS UMR 7516, Université de Strasbourg, CNRS, Strasbourg, France.

[3]Department of Geography, University of Sheffield, Sheffield, UK.

[4]Scripps Institution of Oceanography, UCSD, La Jolla, CA, USA.

Author contributions: ANM performed all of the analysis and led the writing of the manuscipt. NG produced the DEMs and ice velocities used for analysis. All authors contributed ideas and methodological developments, and provided editorial input on the manuscript.

Note that this chapter includes minor differences to the published paper to account for changes made following publication to Sections 4.3.5 and 4.4.1.

Abstract

Oceanic forcing of the Greenland Ice Sheet is believed to promote widespread thinning at tidewater glaciers, with submarine melting proposed as a potential trigger of increased glacier calving, retreat and subsequent acceleration. The precise mechanism(s) driving glacier instability, however, remain poorly understood, and while increasing evidence points to the importance of submarine melting, estimates of melt rates are uncertain. Here we estimate submarine melt rate by examining freeboard changes in the seasonal ice tongue of Kangiata Nunaata Sermia (KNS) at the head of Kangersuneq Fjord (KF), southwest Greenland. We calculate melt rates for March and May 2013 by differencing along-fjord surface elevation, derived from high-resolution TanDEM-X digital elevation models, in combination with ice velocities derived from offset feature tracking applied to TerraSAR-X imagery. Estimated steady state melt rates reach up to 1.4 ± 0.5 m d^{-1} near the glacier grounding line, with mean values of up to 0.8 ± 0.3 and 0.7 ± 0.3 m d^{-1} for the eastern and western parts of the ice tongue, respectively. Melt rates decrease with distance from the ice front and vary across the fjord. This methodology reveals spatio-temporal variations in submarine melt rates at tidewater glaciers which develop floating termini, and can be used to improve our understanding of ice-ocean interactions and submarine melting in glacial fjords.

4.1 Introduction

Acceleration of marine-terminating glaciers in Greenland in recent decades has significantly increased the contribution of the ice sheet to sea level (Enderlin et al. 2014). Many of these glaciers are in contact with relatively warm ocean water (Holland et al. 2008, Straneo et al. 2012, Carr et al. 2013, Motyka et al. 2013), and submarine melting at the ice-ocean interface has been proposed as a potential trigger of glacier calving, retreat and acceleration (Nick et al. 2009, O'Leary & Christoffersen 2013, Luckman et al. 2015). The spatial distribution of submarine melting along an ice front can impact grounding line stability and influence ice front shape by undercutting, overcutting and creating embayments (Straneo et al. 2012, Carroll et al. 2015, Fried et al. 2015). These changes in ice front shape likely affect calving processes and can create locations along

the ice front where calving preferentially occurs (Chauché et al. 2014, Luckman et al. 2015). The dynamic coupling between glacier margins and upstream ice enables oceanic forcing of tidewater glaciers to promote widespread thinning, increased glacier retreat, calving and velocity, and consequent mass loss (e.g. Joughin et al. 2004, Van den Broeke et al. 2009, Vieli & Nick 2011, Carr et al. 2013, Goelzer et al. 2013, Sundal et al. 2013, Straneo & Cenedese 2015).

Despite their potential importance for ice dynamics, submarine melt rates (SMRs) are poorly constrained, because collecting in situ measurements near actively-calving glacier termini is both difficult and dangerous (Mortensen et al. 2011, 2013). Numerous studies have instead used hydrographic profiles from glacial fjords to estimate the net heat flux available for melting ice, resulting in SMRs up to 16.8 ± 1.3 m d^{-1} in Alaska (Motyka et al. 2003, 2013) and ranging from 0.7 ± 0.2 to 10.1 m d^{-1} in Greenland (Rignot et al. 2010, Sutherland & Straneo 2012, Inall et al. 2014). Other studies have used general circulation models or plume theory to estimate SMR (Jenkins 2011, Christoffersen et al. 2012, Sciascia et al. 2013, Xu et al. 2013, Slater et al. 2015), resulting in melt rates ranging from 0.12 to 3.6 m d^{-1} in Greenland. However, most measurements used to estimate SMR from heat flux methods or to constrain model parameters are taken far from the grounding line (15-80 km away) (e.g. Johnson et al. 2011, Christoffersen et al. 2012, Sutherland & Straneo 2012, Inall et al. 2014), and are therefore integrating all the processes that will affect the heat flux between the measurement site and the terminus, including heat lost to the melting of icebergs, sea ice and mélange at considerable distances from the grounding line. SMRs estimated from fjord heat flux are also uncertain due to the temporal variability in fjord circulation, so that it is not clear how representative an estimate is of the longer term mean (Jackson & Straneo 2016).

Alternative approaches to estimating glacier submarine melt rate utilize remotely sensed observations. Several studies have quantified SMR by accounting for ice flux divergence and surface mass balance of floating ice shelves and tongues (e.g. Rignot & Jacobs 2002, Depoorter et al. 2013, Enderlin & Howat 2013, Rignot et al. 2013, Gourmelen et al. 2017). This approach has generated SMRs up to 0.11 m d^{-1} beneath

ice shelves in Antarctica (Rignot & Jacobs 2002) and ranging from 0.03 ± 0.02 to 2.9 ± 0.65 m d^{-1} beneath floating glacier tongues in Greenland (Enderlin & Howat 2013). Enderlin & Hamilton (2014) also used remotely sensed observations to estimate submarine melt, using changes in iceberg freeboard derived from high-resolution digital elevation models (DEMs) to estimate iceberg volume loss, which was then used to estimate area-averaged iceberg SMRs. During the summers of 2011 and 2013, estimated iceberg SMR was 0.39 ± 0.17 m d^{-1} in Sermilik Fjord, east Greenland. Here we also employ a remote sensing approach, using satellite radar data to estimate near-terminus SMR from spatial and temporal changes in seasonal ice tongue freeboard adjacent to a large tidewater glacier in southwest Greenland.

4.2 Study area

Located at the head of Kangersuneq Fjord (KF), Kangiata Nunaata Sermia (KNS), the largest tidewater glacier in southwest Greenland, drains ~2% of the ice sheet (Figure 4.1; Sole et al. 2011). The ice front is ~4.5 km wide with a maximum grounding line depth of ~250 m below sea level (Mortensen et al. 2013). KNS has retreated at least 22 km from its Little Ice Age maximum extent, following increased air and sea surface temperatures (Lea et al. 2014). For the past 15 years, with the exception of 2011 and 2015, a thick seasonal ice tongue contiguous with the glacier forms by mid-winter and advances down-fjord prior to rapid break-up in late-spring (Figure 4.2; Motyka et al. 2017). The floating ice tongue flows directly across the glacier grounding line (i.e., with no gap or calving processes occurring between the grounded and floating ice) with near spatially consistent velocity (see Figures S1.1 and S1.2). On average, the ice tongue has a length between 2 and 3 km, and decreases in freeboard with distance from the grounding line (Figure 4.2). The fjord waters adjacent to the front of the ice tongue are typically packed with dense ice mélange (i.e., mixture of sea ice, bergy bits and icebergs) during the winter and spring months before breaking up in late spring.

Mortensen et al. (2011, 2013) performed detailed analyses on the characteristics of the waters and heat sources entering KF and reaching to within ~4 km of the KNS terminus. Classical two-layered buoyancy-driven circulation operates in the fjord primarily during

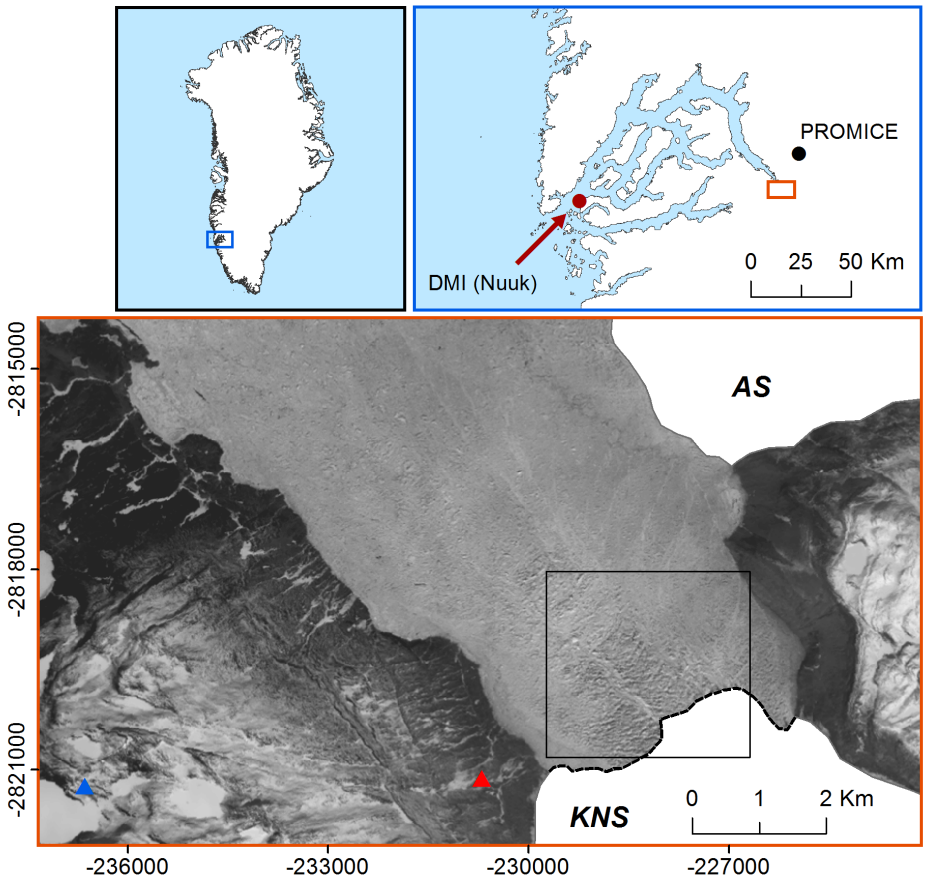

Figure 4.1: Map of study area, including Kangiata Nunaata Sermia (KNS) and Akullersuup Sermia (AS) and ice tongue and mélange, from Landsat 8 satellite image acquired for 01 May 2013 (bottom panel).The red and blue triangles indicate the locations of the University of Alaska Fairbanks (2013) and our (2009) time lapse cameras, respectively, and the black box indicates the extent of Figure 4.4. The red and black dots in the fjord scale locator map (top right panel) indicate the locations of the Danish Meteorological Institute (DMI) and GEUS PROMICE weather stations, respectively.

the spring and summer, where circulation is driven by subglacial meltwater plumes (Figure 4.3). Subglacial discharge exits the glacier at the grounding line, rises buoyantly along the ice front due to its lower density relative to the ambient fjord water, and flows down-fjord once neutral buoyancy is reached (Motyka et al. 2003, Jenkins 2011, Cowton et al. 2015). In fjords with shallow glacier grounding line depths (< 500 m) like KNS, summer discharge meltwater plumes often reach neutral buoyancy and horizontally

Figure 4.2: Example photographs from our 2009 time lapse camera (see Figure 4.1 for location) demonstrating (a) the intact ice tongue on 25 May 2009 and (b) the glacier terminus on 19 July 2009, post-ice tongue disintegration.

enter the fjord within the upper 100 m of the water column (Carroll et al. 2016). The outflow forced by the subglacial discharge establishes an estuarine circulation cell, drawing in coastal waters from the shelf, which flow in a layer beneath the fresher outflow (Motyka et al. 2003, Mortensen et al. 2011). This warm coastal water is then entrained into the subglacial discharge plume, and melts the ice front and underside of the ice tongue as it rises.

4.3 Data and methodology

4.3.1 DEM and ice velocity data generation

We used TanDEM-X and TerraSAR-X imagery from 2013 to estimate ice tongue freeboard and velocity, respectively. TerraSAR-X has a repeat period of 11 days and both satellites have spatial resolution on the order of a metre (Krieger et al. 2007, Eineder et al. 2011), thereby providing excellent temporal and spatial resolution for observing changes in ice tongue velocity and freeboard. The radar platforms enabled

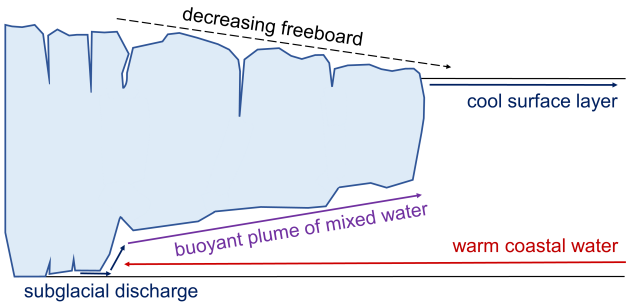

Figure 4.3: Schematic of intact ice tongue showing buoyancy-driven circulation in the fjord, as well as the characteristic decrease in ice tongue freeboard (and thus thickness) away from the ice front.

us to use imagery acquired in non-daylight hours and cloudy conditions, in contrast to optical platforms. Time lapse camera imagery collected near the terminus of KNS (Figure 4.1) every 4 h from January to June 2013 (courtesy of M. Truffer and M. Fahnestock, University of Alaska Fairbanks) was used to visually confirm the formation, presence and break-up of the ice tongue.

We derived two 2.5 m resolution DEMs dated 17 March and 27 May 2013 from conventional SAR interferometric processing of bi-static TanDEM-X imagery (Dehecq et al. 2016). GIMPDEM (Howat et al. 2014) was used as a reference during the unwrapping stage to minimize unwrapping errors. The DEMs produced must be correctly aligned, both horizontally and vertically, using known stable areas (e.g., bedrock outcrops) that are not covered by ice or snow. To perform this calibration, we used ICESat elevation data over non-ice terrain as defined by the GIMP land classification mask (Howat et al. 2014). A horizontal shift (3.9 and 3.3 m in the x and y directions, respectively) between the TanDEM-X derived DEMs and ICESat over non-ice covered terrain was calculated by fitting a sinusoidal relationship between elevation differences and terrain aspect (Nuth & Kääb 2011). A vertical shift with a linear dependence on location (tilt) was estimated for each DEM using a least-squares regression:

$$dh(X, Y) = a_0 + a_1 X + a_2 Y \tag{4.1}$$

where dh are elevation differences in stable areas, X and Y the easting and northing and a_i the parameters to be estimated. This shift was then subtracted at each pixel. For this step, which is more sensitive to outliers, all points with a slope higher than 40° were excluded. The DEMs were then converted from ellipsoid to elevation above the EIGEN-EC4 geoid.

Due to the limited coverage of the ICESat lines over non-ice terrain (see Figure S1.3), an additional tilt in the DEMs was identified and subsequently corrected for using Operation IceBridge (OIB) Airborne Topographic Mapper (ATM) L1B Elevation and Return Strength data (Krabill 2016). OIB ATM elevation points were acquired for three springs when the seasonal ice tongue was present in the fjord (08 April 2011, 25 April 2012 and 15 April 2014). TanDEM-X elevations from 17 March 2013 were extracted for spatially corresponding 2011 OIB ATM points and the difference taken over open water where the OIB data had a slope of near-zero (20 to 25 km from the ice front). The slope of the difference was taken as the trend (or tilt; ~0.45 m height per km distance along-fjord) in the TanDEM-X elevations and was removed, effectively detrending the dataset (see Figure S1.4). The same correction was applied to elevations from the 27 May 2013 DEM, as the tilt was the same as that for the 17 March.

Three 20 m resolution ice tongue velocity maps were created based on conventional feature tracking applied to TerraSAR-X imagery (Tedstone et al. 2014) for the following 2013 image pairs: 12 and 23 February; 8 and 19 April; 30 April and 11 May. Ice velocity on 17 March (Figure S1.1a), the date of our first DEM, was estimated assuming a linear trend in velocity between the velocity maps from 12-23 February and 8-19 April, and ranges from 28.5 to 30.5 m d^{-1} over the ice tongue. The last available velocity map was from 30 April to 11 May (Figure S1.1b), and throughout the paper, we use this velocity epoch to correspond with our second DEM, acquired on 27 May. Ice tongue velocities in May range from 20.5 to 23.5 m d^{-1}.

4.3.2 Ice flowline construction

We constructed flowlines along the ice tongue using our ice velocity results to track flow direction. Ten points near the glacier grounding line were chosen from both the eastern and western side of the ice tongue, with ~25 m between points in the across-flow direction (Figure 4.4). To accommodate temporal changes in ice velocity, two separate sets of flowlines were created, one for March and one for May, using our velocity maps from 17 March and 30 April to 11 May, respectively. Velocity vectors were extracted for each initial point, enabling the extraction of flow direction, which was then taken at points every 50 m moving down-fjord until the end of the ice tongue. The points were then connected, creating flowlines of ice moving down-fjord away from the grounding line (Figure 4.4). Distance from the grounding line was averaged for each set of flowlines (i.e., eastern and western), using the end of spring terminus position (Figure 4.1) digitized from a Landsat 8 image from 10 June 2013.

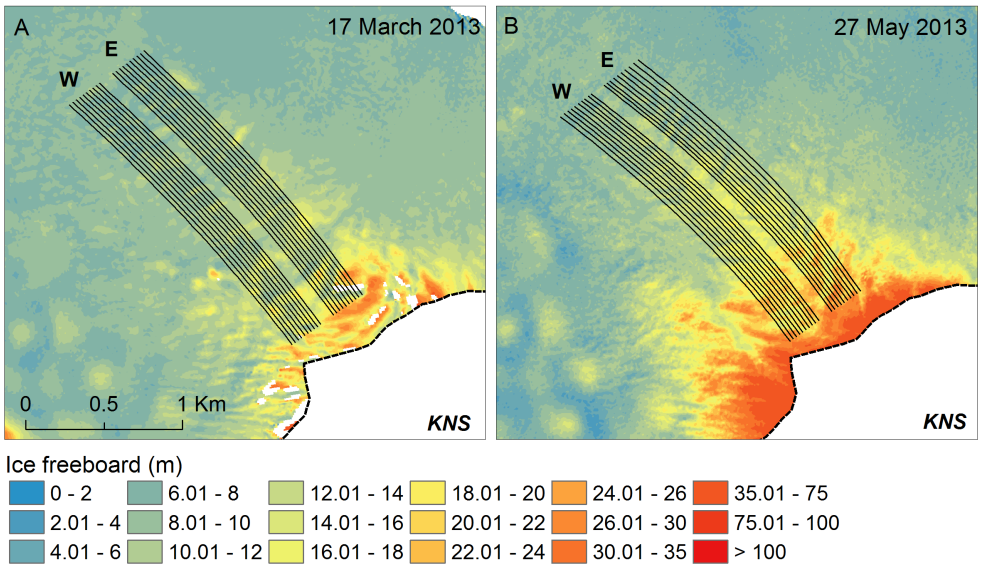

Figure 4.4: Eastern (E) and western (W) ice flowlines, overlain on TanDEM-X ice tongue freeboard from (a) 17 March 2013 and (b) 27 May 2013. Refer to Figure 4.1 for location.

4.3.3 Estimating ice tongue surface melt rates

Observed reduction in ice tongue freeboard as it is advected into the fjord can be attributed to changes in surface mass balance, longitudinal and lateral spreading, and

submarine melting. To assess the potential contribution from surface mass balance, surface melt was estimated using a simple positive degree day (PDD) model (Hock 2003) with a degree day factor for snow (*ddfs*) of 4.5 mm d^{-1} $°C^{-1}$, as used by Slater et al. (2017b) for KNS. Air temperature data were acquired from the nearby Geological Survey of Denmark and Greenland (GEUS) PROMICE weather station (NUK_L, 550 m a.s.l., 64°28'55.2" N, 49°31'50.88" W, ~21 km from KNS) (Figure 4.1; Ahlstrøm et al. 2008), using a lapse rate of 0.5 $°C^{-1}$ per 100 m to adjust the temperatures to sea level (Slater et al. 2017b). Precipitation data were acquired from the Danish Meteorological Institute (DMI) weather station in Nuuk (NUUK 4250, 80 m a.s.l., 64°10'0.12" N, 51°45'0" W, ~105 km from KNS) (Figure 4.1; Cappelen 2016).

4.3.4 Estimating ice tongue submarine melt rates (SMR)

SMR for all ice flowlines were estimated for both steady and non-steady state scenarios. A steady state scenario assumes ice thickness at a fixed location does not change in time, whereas a non-steady state scenario allows for changes in ice thickness at a fixed location (e.g., thinning due to high submarine melting exceeding the delivery of ice across the grounding line or changes in the thickness of ice being advected across the grounding line). As estimating a non-steady state scenario requires at least two elevation estimates, a steady state (i.e., $\frac{\delta H}{\delta t} = 0$) is often assumed due to lack of data (Jenkins & Doake 1991, Smith 1996, Johnson et al. 2011). The two scenarios are presented here for comparison purposes, in part to test the validity of our method for years with only one DEM, when determining SMR by assuming a steady state scenario would be the only option. For a steady state scenario (SS), elevation values along each ice flowline were extracted from both the 17 March and 27 May 2013 DEMs. To reduce the impact of short-length scale elevation changes, including crevasses, in the fractured tongue (see Figure 4.2a) on our melt rate estimates, flowline elevations were smoothed using a two-sided moving average with a 625 m window (see Figures 4.5a and 4.6a). Elevation data were then converted to ice thickness using ocean water (1,027 kg m^{-3}; Ribergaard (2013)) and ice (900 kg m^{-3} following Enderlin & Hamilton (2014)) densities, assuming the ice is floating in hydrostatic equilibrium; an assumption supported by both the best available bathymetry (Mortensen et al. 2013, Motyka et al.

2017) and the observation of the rapid and total disintegration of the ice tongue within just a 4-h time window on 15 June 2013.

SMR_{SS} were calculated for both March and May, accounting for thinning due to stretching in both the flow direction (second term on right-hand side of Equation 4.2) and perpendicular to flow (third term on right-hand side of Equation 4.2):

$$SMR_{SS} = -v_x \frac{\delta H}{\delta x} - H \frac{\delta v_x}{\delta x} - H \frac{\delta v_y}{\delta y} \tag{4.2}$$

where H is the ice thickness (m), v_x and v_y are the ice velocity (m d^{-1}) in the along- and across-flowline direction, and x and y represent distance in the along- and across-flowline direction. Note that a term representing across-flow thinning, -$v_y \frac{\delta H}{\delta y}$ does not contribute because, by definition of a flowline, $v_y = 0$ on the flowline. The final term in Equation 4.2 does however make a small contribution due to the convergence or divergence of different flowlines. Derivatives in Equation 4.2 are evaluated using conventional finite differences with a spacing $\delta x = 50$ m and $\delta y = 25$ m.

For a non-steady state scenario (NSS), a linear trend of thickness change between 17 March and 27 May 2013 was assumed at each point on the flowlines and accounted for by subtracting a daily rate of change (m d^{-1}) from the estimated SMR_{SS} (Rignot et al. 2013):

$$SMR_{NSS} = SMR_{SS} - \frac{\Delta H_{NSS}}{\Delta t} \tag{4.3}$$

where ΔH_{NSS} (m) is the difference in ice thickness between the two dates and Δt (d) is the time between the two dates.

Melt rates were then averaged to produce a mean SMR_{SS} and SMR_{NSS} for the western and eastern flowlines. To capture the general trend in melt rates, lines of best fit were applied to both steady and non-steady state estimates.

4.3.5 Error analysis

Potential errors were traced throughout the analysis and standard error propagation methods were used to calculate the effect of errors in both elevation and ice velocity on estimated SMR. Errors in elevation values are from three primary sources: (1) DEM construction (including correction using ICESat), (2) correcting TanDEM-X elevations using OIB ATM data, and (3) smoothing the elevations for melt rate calculations. Error resulting from DEM construction is ±2 m, a general error for the TanDEM-X derived DEMs over areas with a slope $< 12°$ (Rizzoli et al. 2012), which is likely an overestimate over the relatively low-sloped ice tongue ($< 0.15°$). As our calculations utilize the elevation gradient and not the absolute elevation, we instead account for a gradient error of ±0.35 m over the nearly 2 km ice tongue. This gradient error was estimated over 2 km segments (the same length over which SMRs were estimated) of a section of very thin ice mélange where successive OIB ATM flights show near-constant slope. The gradient error was estimated as the largest difference in slope between the corrected TanDEM-X elevation flowlines and the OIB ATM lines. Fitting the TanDEM-X elevations to the OIB ATM elevations results in a root mean square error of ±0.38 m, and smoothing the flowlines results in maximum mean squared errors of ±0.86 and ± 0.47 m for the eastern and western flowlines, respectively. The maximum total error for any one point in elevation along the eastern and western flowlines is ±1.4 and ±0.64 m, respectively.

Following Paul et al. (2013), error in ice velocity was calculated as ±0.09 m d^{-1}, resulting from the feature tracking process applied to stable areas of the ice tongue, where crevassing is easily trackable and ice deformation is low. Errors in velocity at locations within 150 m of the original position of the previous end of summer vertical ice front (which likely corresponds to the grounding line) and at the edge of the ice tongue are not considered, as we did not use any velocities from these regions in our SMR estimations.

While the error estimates cited alongside our SMRs account for errors in the DEMs and ice velocity maps, there are several additional sources of error that, although difficult

to quantify, must be considered. The assumption of both steady and non-state state scenarios for ice tongue thickness likely introduces error in our SMR estimates. We know the ice tongue is not in steady state between March and May 2013, as the glacier is slower and the ice is thicker in May than in March for any given point. Since we have only two DEMs, we can only assume a linear thickening trend over the time period (see Equation 4.3). Any deviation from this trend would affect our melt rate estimates. For example, if the ice tongue was thickest in April, this would imply the ice tongue was thinning between April and May, increasing NSS melt rates estimated using Equation 4.3. Thus, if the tongue was thickest in April, our May melt rate estimates would be an underestimate; however without additional DEMs we cannot address this possibility.

Another potential source of error derives from smoothing the ice freeboard near the glacier grounding line, where pre-smoothed freeboard values decrease sharply, as compared with smoothed values (see Figures 4.5a, 4.6a). While smoothing out fracturing associated with large crevasses on the ice tongue helps to reduce noise in the SMR estimates, the resultant reduction in freeboard gradient significantly lowers our SMRs near the grounding line, which should therefore be considered minimum estimates of melt rate in this location.

Additional uncertainties in submarine melt rate estimates arise from: the assumption that the ice tongue is floating in hydrostatic equilibrium along its full length, which, if incorrectly assumed, would mean melt rates are overestimated in the first km of ice by at least 15% (see Figure S1.5); the seasonal migration of the glacier grounding line, down-fjord of which melt rates are estimated; the cohesiveness of the ice tongue, which potentially impacts changes in ice thickness and velocity; and temporal variability in ice tongue velocity (see Figure S1.6). All of these additional uncertainties are discussed in detail in Chapter 3.3.3.

4.4 Results

4.4.1 SMR estimates in Kangersuneq Fjord

The reduction in smoothed ice freeboard (and thus thickness) with distance downfjord from the grounded KNS terminus in the March DEM (Figures 4.5a and 4.6a for eastern and western flowlines, respectively), combined with the interpolated ice velocities, results in SMR_{SS} for the eastern and western flowline sets of up to 1.4 ± 0.5 m d^{-1} (mean = 0.7 ± 0.4 m d^{-1}) and 1.0 ± 0.2 m d^{-1} (mean = 0.5 ± 0.2 m d^{-1}), respectively (see lines of fit in Figures 4.5b and 4.6b). Due to thickening of the ice via advection, estimated SMR_{NSS} for each set of flowlines (not shown) are less than those estimated for the steady state scenario, with mean decreases in melt rate of 15 and 28% for the eastern and western flowlines, respectively. For all flowlines, melt rates broadly decrease with distance from the KNS grounding line and moving from east to west across the ice tongue.

SMR_{SS} estimated in May are similar to those in March, with eastern and western flowline SMRs of up to 1.4 ± 0.2 m d^{-1} (mean = 0.8 ± 0.3 m d^{-1}) and 1.0 ± 0.1 m d^{-1} (mean = 0.7 ± 0.3 m d^{-1}), respectively (see lines of fit in Figures 4.5b and 4.6b). Estimated SMR_{NSS} for each set of flowlines are again less than those estimated for the steady state scenario, decreasing by 3 and 10% for eastern and western flowlines, respectively. SMRs in May show the same spatial variability as seen in March.

While the heavily crevassed nature of the ice tongue itself is not unphysical, it leads to unphysical noise in our melt rate estimates. For example, the rapid decrease in thickness between two adjacent points over a crevasse (one on the ice tongue surface and one at the bottom of the crevasse) is interpreted as thinning using our method, and thus the estimated SMR would be erroneously high (e.g., the peak in March SMR ~570 m from the grounding line, Figure 4.5b). In contrast, the rapid increase in thickness between a point at the bottom of the same crevasse and ice tongue surface on the other side is interpreted as thickening of the ice, resulting in a negative melt rate (e.g., negative March SMRs, Figure 4.5b). To exclude these anomalous melt rates, we use

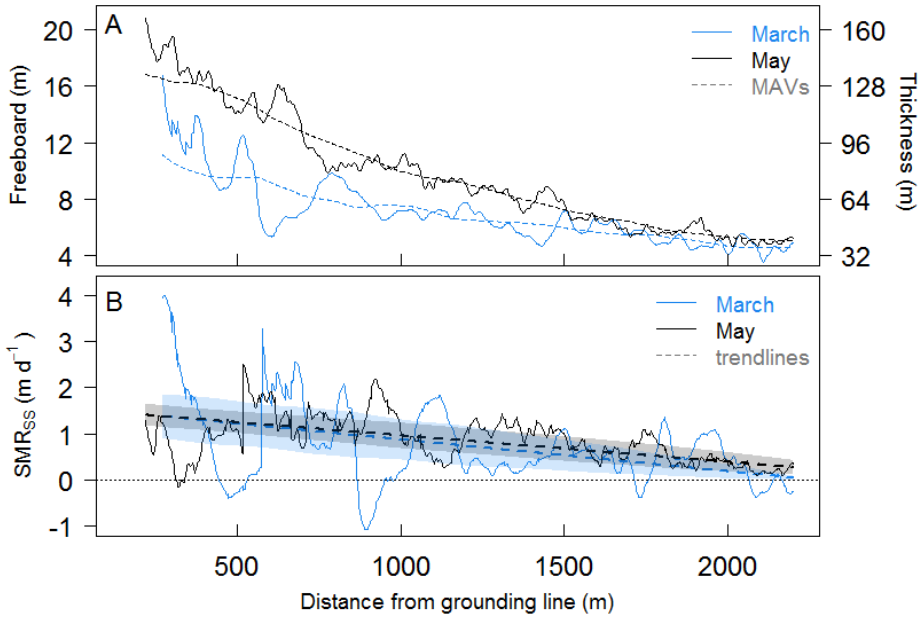

Figure 4.5: (a) Ice tongue freeboard and thickness (m) on 17 March and 27 May 2013 with distance from KNS terminus for the eastern flowlines, where solid lines are means from 10 flowlines (Figure 4.4) and dashed lines are moving averages (MAVs) of the mean; (b) steady state estimated submarine melt rate (SMR_{SS}) for eastern flowlines, with dashed trendlines and shaded error ranges.

the lines of best fit as seen in Figures 4.5b and 4.6b to interpret the broader trends in estimated SMR. As they are the same order of magnitude as the non-steady state scenario, we use our steady state scenario melt rates in our subsequent analyses, which allows for comparison to melt rates estimated in years when only one DEM is available (i.e., assumed steady state). In addition, we note again that our melt rates near the grounding line should be considered minimum estimates as the smoothing of crevasses greatly reduces freeboard gradient here. Melt rates estimated here also have increased uncertainty as the ice tongue might not be floating in perfect hydrostatic equilibrium within the first km down-fjord of the grounding line.

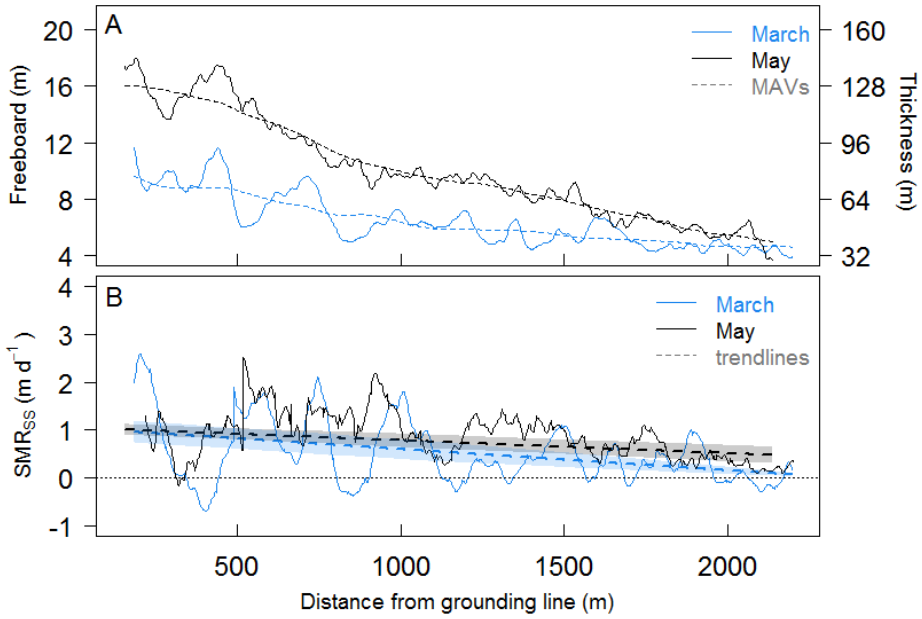

Figure 4.6: (a) Ice tongue freeboard and thickness (m) on 17 March and 27 May 2013 with distance from KNS terminus for the western flowlines, where solid lines are means from 10 flowlines (Figure 4.4) and dashed lines are moving averages (MAVs) of the mean; (b) steady state estimated submarine melt rate (SMR_{SS}) for western flowlines, with dashed trendlines and shaded error ranges.

4.4.2 Surface melt estimates over the ice tongue

For the study period, between 17 March and 27 May 2013, estimated total surface snow melt over the ice tongue was 0.48 m water equivalent and total precipitation as snow was 0.23 m. We expect precipitation to be less over the ice tongue than that recorded in Nuuk, given the low elevation of the ice tongue and the rain shadow effect of the coastal mountains. A previous study estimated spring average precipitation decreases between coastal and inland weather stations in western Greenland between ~0.5 and 0.8 mm per km inland (Abermann et al. 2017). Therefore, if anything, by using the estimates of precipitation from Nuuk we overestimate spring snowfall. Regardless, the estimates of precipitation are still orders of magnitude lower (in terms of water equivalent and impact therefore on freeboard) than our estimated SMRs. The resultant mean surface melt rate, 0.004 m d^{-1}, taken over the 71 days of the study period, is approximately

two orders of magnitude less than the rate of change in ice thickness over the same time period, and thus considered negligible. As the PDD sum for 2013 during our study period (16.3 °C day) is ~75% lower than the mean for the last decade (mean from 17 March to 27 May for 2008 to 2016 of 69.4 °C day), 2013 should be considered a low spring surface melt and runoff year.

4.5 Discussion

4.5.1 Spatial variability in SMR

Submarine melt rates show along-fjord variability, generally decreasing with distance down-fjord from the KNS grounding line. This variability is likely driven by both the velocity and temperature of subglacial meltwater plumes, with SMR scaling with velocity and ambient fjord temperature (e.g. Holland & Jenkins 1999, Jenkins 2011). Mortensen et al. (2013) investigated winter circulation and water properties in 2009 in KF, finding a cool surface layer (ranging from -1.4 to 1.0 °C at 0 and 40 m depth, respectively) overlaying a warmer intermediate-depth layer (increasing from 1.3 to 1.8 °C at 50 to 90 m depth), below which temperature was relatively constant (1.8 °C) with depth. Motyka et al. (2017) investigated summer fjord water properties in 2011, ~22 km from the KNS ice front, again finding a cool surface layer (ranging from 0 to 1.0 °C at 0 and 40 m depth, respectively) overlaying an even warmer intermediate layer (increasing from 2.0 to 2.5 °C at 50 to 150 m depth). Therefore, the ambient fjord water entrained by any subglacial plumes will be cooler with increasing distance from the grounding line, as the thinning ice tongue, and shallower draft, will be submerged in shallower, colder surface water. Plume velocity also decreases with distance from the ice front as the plume loses buoyancy (Jenkins 2011). For these reasons, and as expected, our estimated SMRs approach 0 m d^{-1} down-fjord of the grounding line. The presence of thick sea ice down-fjord of the end of the ice tongue supports this expectation, suggesting the surface waters are very cold, resulting in little or no submarine melting (or else there would be no sea ice). This result is dissimilar to summer melt rates derived from icebergs found tens of kilometres from glacier grounding lines in other Greenlandic fjords (Enderlin & Hamilton 2014), which we would expect to be higher,

due to deeper iceberg keel depths (as compared to the shallow ice tongue depth) and stronger buoyancy-driven circulation from higher subglacial discharge in the summer (Sciascia et al. 2013).

SMRs also show across-fjord variability, with higher melt rates in the eastern section of the main ice tongue, compared to the western part. Across-fjord variability may be driven by water temperature, both in the ambient water column and thus the plume, and by the strength (i.e., velocity) of any buoyant runoff plume present. The eastern part of the ice tongue had the highest March surface elevation, and thus the greatest thickness and deepest keel depth (Figure 4.5a). Reaching over 80 m beneath the fjord surface near the grounding line, ice along the eastern flowlines is exposed to relatively warm, intermediate-depth waters, which promote more rapid submarine melting (Enderlin & Hamilton 2014, Enderlin et al. 2016). In comparison, ice in the western part of the tongue has a keel depth near the ice front of < 70 m, which could explain, in part, the lower SMR in this area of the fjord, as the shallower ice keel is exposed to slightly cooler waters than the eastern part of the tongue.

Across-fjord variability in SMR may also reflect the strength and location of any subglacial meltwater plumes emerging at the glacier grounding line. Uniform across-fjord ice tongue SMR would be expected, if keel depths are constant, where spatially well-distributed meltwaters emerge at the grounding line (Slater et al. 2015). Conversely, spatially-focused, high SMRs near the ice front may indicate a locally dominant subglacial meltwater channel, which in this case could be emerging preferentially under the eastern part of the ice tongue. Slater et al. (2017b) inferred KNS subglacial runoff distribution using plume observations from summer 2009 time lapse imagery, suggesting that runoff likely exits under the grounding line via spatially distributed channels, with sporadic focusing resulting in visible surface plumes. During the mid- to late melt season, plumes typically reach the surface to the west of the grounding line centre, with infrequently visible plumes emerging on the eastern side of fjord (Slater et al. 2017b). However, as the presence of the ice tongue and surrounding thick ice mélange prevents the expression of plumes on the surface, it is difficult to interpret subglacial meltwater distribution during the winter and spring months.

In addition, rotational circulation in the fjord should be considered, which could impact the across-fjord distribution of surface meltwater and water entering the fjord at depth (Cottier et al. 2010, Straneo & Cenedese 2015), and thus the heat available for melting ice. Using data from Mortensen et al. (2013), we assume a 30 m thick fresh surface layer of sea ice/ice tongue/glacier meltwater overlaying transitional layers of ice melt and fjord source water, which gives an internal Rossby radius of ~6 km. As the fjord width varies between 4 and 6 km, rotational effects are unlikely to have a primary role in controlling fjord circulation. However, they may have a secondary effect, focusing the flow of water toward and away from the glacier terminus to the right hand side in the direction of flow (e.g. Cottier et al. 2010, Sutherland et al. 2014b).

4.5.2 Temporal variability in SMR

Estimated mean SMRs do not show significant temporal variability, potentially due to the fact that all melt rates are estimated in the spring, prior to the onset of substantial surface melt. While estimated monthly total surface snow melt from degree day modeling was higher in May (0.26 m) than in March (0.11 m), we do not expect or see significant differences in SMRs given how small these early spring surface melt rates are. However, increased surface melt later in the melt season and the associated enhanced subglacial meltwater plumes, combined with increased intermediate depth water temperatures (Mortensen et al. 2013, Motyka et al. 2017) would be expected to amplify local SMR considerably compared to winter melting (Jackson & Straneo 2016). Such estimates would however not be possible using our method as the ice tongue breaks up in early June each year, and is thus absent during the summer and autumn months.

Seasonal stratification and water temperature at depth are highly dependent on the mode of circulation in KF (Mortensen et al. 2011). In the spring, when we estimate SMR, circulation is mainly driven by dense coastal inflows and tidal mixing, which act to cool and slightly freshen waters at intermediate depths. The presence of subglacial meltwater plumes sourced from frictional basal meltwater emerging at the glacier grounding line (Christoffersen et al. 2012) likely also plays a role in controlling fjord

circulation and submarine melting in the winter and early spring. In the summer, however, tidal mixing and subglacially-driven circulation, via surface-derived meltwater plumes, are dominant and act to freshen and significantly warm the upper intermediate water layer (Mortensen et al. 2013). Temperature differences of nearly 2 °C were seen at intermediate depths (between 120 and 150m) between April and September 2010 (Motyka et al. 2017), an increase which would have a significant impact on the melting of submerged ice.

In order to investigate the potential role that basal frictional meltwater could play in driving plumes in winter, we estimate basal meltwater flux for the area of KNS between the grounding line and ~11 km up-ice from the grounding line. As basal drag is unknown for KNS, we assume drag is of a similar magnitude to that estimated for Jakobshavn Isbræ, ~200 kPa (Iken et al. 1993, Funk et al. 1994), as used for Kangerdlugssuaq Glacier by Christoffersen et al. (2012). Using our TerraSAR-X derived velocities for March and May for the lower 11 km of the glacier, an ice density of 900 kg m^{-3}, and a latent heat of fusion of 334 kJ kg^{-1}, basal meltwater flux was estimated as 3.2 m^3 s^{-1}, for both March and May. Although producing weak plumes, subglacial discharge of this magnitude can generate point source SMRs of between 2 and 4 m d^{-1} (Slater et al. 2015). Due to their lower velocity, weak plumes, such as those expected via basal frictional melting, reach neutral buoyancy before reaching the fjord surface (Christoffersen et al. 2012, Slater et al. 2015, Carroll et al. 2016). However, close to the glacier grounding line, where ice tongue keel depth is greatest, weaker plumes will likely still reach and melt the base of the ice tongue. In comparison, higher subglacial discharge (between 50 and 100 m^3 s^{-1}), as might be expected later in the melt season, can result in point source SMRs up to 7 m d^{-1} (Slater et al. 2015). These stronger plumes may reach the fjord surface before reaching neutral buoyancy, thus allowing for melting of the full ice front depth (Slater et al. 2015).

4.5.3 Comparison with previous SMR estimates from Greenland

Submarine melt rates estimated in this study are greater than, but of the same order of magnitude, as those estimated for icebergs during summer in Sermilik Fjord, southeast

Greenland. Using repeat high-resolution satellite imagery, Enderlin & Hamilton (2014) estimated SMRs of 0.39 ± 0.17 m d^{-1} for icebergs located up to 60 km from the terminus of Helheim Glacier between August 2011 and July 2013. Using our lines of best fit, our estimated SMRs (up to 1.4 m d^{-1}) are more than double those of (Enderlin & Hamilton 2014). Given the close proximity to the grounding line, our estimated SMRs may reflect the influence of melting by plumes enhanced by emerging subglacial meltwater sourced from frictional basal melt (e.g Christoffersen et al. 2012); such plumes will clearly have a diminished influence 60 km from the ice front, where plume velocity has decreased. Estimated SMRs for icebergs stuck in ice mélange in Sermilik and Ilulissat fjords range from 0.1 to 0.8 m d^{-1}, and increase with iceberg draft and submerged ice area (Enderlin et al. 2016). These melt rates are more similar to ours near KNS, due both to the relatively similar distance from the grounding line to the icebergs (from 0 to 20 km away) and our estimates (150 to 2,400 m away), as well as the comparable summer intermediate ambient water temperatures in Ilulissat (up to 2.2 °C) (Mernild et al. 2015), Sermilik (up to 2 °C) (Straneo et al. 2010, 2011), and Kangersuneq (up to 2.5 °C) fjords.

Estimated SMRs for the KNS ice tongue in spring 2013 are one to two orders of magnitude larger than SMRs estimated between 2000 and 2010 for the floating tongue at Petermann Glacier (0.07 ± 0.035 m d^{-1}) (Johnson et al. 2011, Enderlin & Howat 2013). The difference in melt rate magnitude in this case is likely due to both the difference in ambient ocean temperatures at ice keel depth between the two fjords as well as meltwater plume dynamics. The ambient water temperatures in northwest Greenland are much lower at keel depth than those in southwest Greenland, peaking at 0.2 °C at nearly 500 m depth in Peterman Fjord (Johnson et al. 2011), where keel depths in the first few km of the fjord reach ~480 m (Wilson et al. 2017). In contrast, ambient water temperatures at keel depth for KNS (~80 m near the grounding line) fall between 1.3 and 2.0 °C, depending on the season (Mortensen et al. 2013, Motyka et al. 2017). Plume dynamics may also fundamentally differ, with the weak melt-driven convective plumes beneath Petermann (which has a ~70 km long permanent ice tongue) more akin to those at large Antarctic ice shelves, and strong subglacial

discharge-driven plumes beneath the short ice tongue at KNS giving rise to convection-driven melt as observed at tidewater glaciers in midsummer (Jenkins 2011). In addition, the difference in velocity between KNS and Petermann glaciers may play a secondary role in controlling estimated SMRs. The average winter velocity for KNS is ~8 km a^{-1}, eight times that of Petermann Glacier (Johnson et al. 2011). A faster-flowing, warm based glacier will create more basal friction and thus more basal melt (e.g. Holland et al. 2008, Christoffersen et al. 2012), producing more vigorous subglacial meltwater plumes and inducing higher SMRs even in winter (Carroll et al. 2015, Cowton et al. 2015, Slater et al. 2015).

Utilizing summer hydrographic observations between ~35 and 88 km from the Kangerdlugssuaq Glacier terminus, Inall et al. (2014) estimated heat delivery to the calving front equivalent to 10 m d^{-1} of ice melt. Motyka et al. (2017) used parameters derived from models and hydrographic measurements 12 km from the KNS ice front to estimate a near-terminus late-summer SMR of ~3-7 m d^{-1}. Our empirically-derived SMRs are nearly an order of magnitude lower than those estimated by Inall et al. (2014) and the upper range estimates of Motyka et al. (2017), despite similar ambient fjord water temperatures (up to 2.25 °C at depth for Kangerdlugssuaq Fjord; Inall et al. 2014). It is unlikely that hydrographic estimates taken more than 30 km from the terminus realistically represent the heat energy used for melting the ice front, as a large portion of this energy might be lost to melting of any ice mélange and icebergs in the fjord before reaching the glacier (Enderlin et al. 2016). In fjords like Helheim, where icebergs are large enough to cover the full fjord depth (Enderlin & Hamilton 2014), deep water could also be cooled by the melting of icebergs at depth. Heat transport to the ice front can also be reduced through vertical mixing of the water column via wind-driven internal seiches (e.g. Arneborg & Liljebladh 2001, Cottier et al. 2010) or by the convective overturning of water due to the release of brine from sea ice formation (Cottier et al. 2010). In addition, the presence of shallow sills in the fjord alters the fjord circulation and may prevent deeper, warm water from reaching the ice front (e.g. Mortensen et al. 2011, 2013). This suggests that terminus melt rates derived from distal along-fjord heat

flux values may be too high unless heat losses to mid-fjord melting, vertical mixing and fjord bathymetry are considered.

4.5.4 Freshwater flux from submarine melting of the ice tongue

Given the potential importance of meltwater generation to fjord water properties and nutrient productivity (Meire et al. 2017), we here estimate the spring freshwater flux from submarine melting of the ice tongue. Using grounded terminus width (~4,500 m), depth (~250 m), and average velocity from March to May 2013 (~6.9 km a^{-1}), spring ice flux across the KNS grounding line was estimated to be 246 m^3 s^{-1}. Assuming a simplified rectangular submarine configuration of the ice tongue with a width of ~1,800 m and a length of ~2,500 m, total basal submerged area is ~4.5 km^2. Using spatially averaged SMR_{SS} from our western and eastern fjord flowlines, meltwater flux derived from the ice tongue ranges from 26 to 36 m^3 s^{-1} (11 to 15% of spring grounding line ice flux) in March, and from 36 to 42 m^3 s^{-1} in May (15 to 17% of spring grounding line ice flux). This partitioning of freshwater flux entering the fjord is comparable to that estimated by Xu et al. (2013) for Store Glacier in western Greenland, where submarine melting accounted for 20% of August 2010 glacier influx. In contrast, our flux partitioning is much lower than that estimated by Motyka et al. (2003, 2013) for LeConte Glacier in Alaska, where submarine melting accounts for 50-67% of summer frontal ablation. Differences in flux partitioning are likely due to seasonality, fjord temperatures and terminus geometry (Truffer & Motyka 2016).

While ice tongue melt only accounts for 11-17% of the overall spring grounding line flux, it provides a significant amount of freshwater to the fjord in spring months, when surface runoff is largely absent. As such, the associated inputs of freshwater into the fjord at different depths from submarine melting may have a major impact on fjord water stratification, circulation and associated productivity (e.g. Motyka et al. 2013, Sciascia et al. 2013, Sutherland et al. 2014b, Meire et al. 2017).

4.5.5 Potential applications

We have derived SMRs using changes in the freeboard of a seasonally floating ice tongue as it advances down-fjord during the spring, building upon earlier work using freeboard and ice flux divergence to estimate SMRs of floating ice tongues in Greenland (e.g. Motyka et al. 2011, Enderlin & Howat 2013). This technique has considerable potential to further our understanding of ice-ocean interactions and submarine melting in glacial fjords. Using both satellite and time-lapse imagery, seasonal differences in SMR could be evaluated by estimating melting throughout the year, as long as an ice tongue is present in winter and spring, and icebergs are present in summer and autumn sufficiently close to the ice front (following methods of Enderlin & Hamilton (2014)). In addition, analysis of seasonally floating ice tongues presents the opportunity to derive SMR estimates much nearer to glacier calving fronts (when compared with estimates using hydrographic profiles), in the precise location where the key processes controlling calving dynamics and retreat are not well resolved. We anticipate that our estimates of SMR, and others derived using this methodology, will be used to tune fjord circulation and plume models, which in turn will soon be used to force ice sheet models predicting the future of the Greenland Ice Sheet and its contribution to sea level rise.

Our submarine melt rate estimates are derived from an ice tongue that is already floating, thus they do not affect the annual mass balance of the grounded portion of KNS. Nevertheless, the submarine melting of the ice tongue may affect its ability to buttress the winter ice flux and discharge across the grounding line (e.g. Motyka et al. 2011, Krug et al. 2015), with potential negative consequences for annual mass balance. If SMRs increase in the future as is expected under climate projections, the residence time of seasonal ice tongues like that at KNS will decrease, effectively extending the length of the calving season and allowing for greater mass loss from the grounded portion of the ice sheet. In addition, quantifying ice tongue melt rates can tell us a lot about calving front melt processes. For example, the spatial distribution of ice front SMRs (for which our ice tongue SMRs are a proxy) can influence the morphology of the calving front through spatially heterogeneous undercutting, with potential implications for calving frequency and style (Straneo et al. 2012, Chauché et al. 2014, Carroll et al.

2015, Slater et al. 2017b), and ultimately glacier retreat, velocity and ice flux. A better understanding of spatial variations in submarine melting of the ice front may lead to the development of a relationship between melt distribution and calving, which is poorly understood but likely of critical importance for controlling tidewater glacier dynamics.

4.6 Conclusions

Improved estimates of SMR are essential to gain a better understanding of the processes controlling ice dynamics at tidewater glacier termini, and in particular, the potential relationship between submarine melt and tidewater glacier acceleration and retreat. Using high-resolution TerraSAR-X and TanDEM-X satellite imagery, we have estimated SMRs of a seasonal floating ice tongue adjacent to the grounding line of KNS. Changes in freeboard of the ice tongue, both with distance from the grounding line and across the fjord, have been used to estimate spatial variations in melt rate. Our estimates of spring steady state SMR near the grounding line of KNS reach 1.4 $\pm$ 0.5 m d^{-1}, and decrease with distance down-fjord from the glacier grounding line, with mean rates up to 0.8 $\pm$ 0.3 and 0.7 $\pm$ 0.3 m d^{-1} for the eastern and western parts of the ice tongue, respectively. There is also considerable across-fjord variability in SMR which may be driven by variation in the ice tongue draft and the temperature stratification in the fjord, but may also reflect the strength of any subglacial meltwater plumes present. The submarine meltwater flux derived from the ice tongue ranges from 26 to 42 m^3 s^{-1}, which accounts for between 11 and 17% of the grounding line ice flux into the fjord in the spring months, prior to the onset of ice sheet surface melt. Our results demonstrate that using high resolution satellite imagery to analyze changes in freeboard at floating seasonal ice tongues has considerable potential to reveal in detail the temporal and spatial variations in SMR at tidewater glacier termini.

Chapter 5

Spatio-temporal variations in seasonal ice tongue submarine melt rate at a tidewater glacier in southwest Greenland

The previous chapter derived submarine melt rates near the Kangiata Nunaata Sermia (KNS) ice front for spring 2013, showing that mean melt rates reach 1.4 ± 0.5 m d^{-1} and decrease with distance from and vary along the ice front. It is inferred that these spatial variations in submarine melt rate are likely controlled by ocean temperature at depth and by the presence of subglacial discharge plumes at the ice front. This chapter uses the same method developed in Chapter 4, expanding the analysis by deriving submarine melt rates at KNS from 2012 to 2014, and comparing them with the locations of subglacial plumes either observed in time lapse photography or predicted by modelled subglacial flow routing. The results provide spatio-temporal estimates of variations in ice tongue submarine melt rate and make an empirical link between the presence of subglacial discharge plumes and areas of calving and high melt along the glacier terminus.

This chapter was accepted for publication in the *Journal of Glaciology* in March 2019 and is currently in press:

Moyer AN[1], Nienow PW[1], Gourmelen N[1,2], Sole AJ[3], Slater DA[4], Truffer M[5] and Fahnestock M[5], Spatio-temporal variations in seasonal ice tongue submarine melt rate at a tidewater glacier in southwest Greenland, *Journal of Glaciology*, in press.

[1]School of GeoSciences, University of Edinburgh, Edinburgh, UK.

[2]IPGS UMR 7516, Université de Strasbourg, CNRS, Strasbourg, France.

[3]Department of Geography, University of Sheffield, Sheffield, UK.

[4]Scripps Institution of Oceanography, UCSD, La Jolla, CA, USA.

[5]Geophysical Institute, University of Alaska Fairbanks, Fairbanks, AK, USA.

Author contributions: ANM performed all of the analysis and led the writing of the manuscipt. NG produced the DEMs and with AJS produced the ice velocities used for analysis. MT and MF provided the time-lapse camera imagery. ANM, PWN, NG, AJS and DAS contributed ideas and methodological developments, and all authors provided editorial input on the manuscript.

Note that this chapter includes minor differences to the published paper to account for changes made following publication to Section 5.3.3.

Abstract

Submarine melting of tidewater glaciers is proposed as a trigger for their recent thinning, acceleration and retreat. We estimate spring submarine melt rates of Kangiata Nunaata Sermia in southwest Greenland, from 2012 to 2014, by examining changes in along-fjord freeboard and velocity of the seasonal floating ice tongue. Estimated submarine melt rates vary spatially and temporally near the grounding line, with mean rates of 1.3 ± 0.6, 0.8 ± 0.3, and 1.0 ± 0.4 m d^{-1} across the tongue in 2012, 2013 and 2014, respectively. Higher melt rates correspond with locations of subglacial plumes and terminus calving activity observed during the melt season using time-lapse camera imagery. Modelling of subglacial flow paths suggests a dynamic system capable of rapid re-routing of subglacial discharge both within and between melt seasons. Our results provide an empirically-derived link between the presence of subglacial discharge plumes and areas of high spring submarine melting and calving along glacier termini.

5.1 Introduction

In recent decades, decreases in surface mass balance and increases in ice discharge from tidewater glaciers into the ocean have accelerated ice loss from the Greenland Ice Sheet (van den Broeke et al. 2016). Despite the inferred connection between oceanic warming and increased ice discharge (e.g. Holland et al. 2008, Straneo & Heimbach 2013), our understanding of ice-ocean interactions at the margins of the ice sheet remains limited. In particular, submarine melting of glacier termini is poorly understood, with few observational estimates of melt rates due to the difficulty of collecting in-situ data near actively calving glacial termini. Submarine melting has been proposed as a trigger for glacier calving, retreat and acceleration (O'Leary & Christoffersen 2013, Luckman et al. 2015), and is thought to influence ice front morphology by undercutting termini and creating embayments through enhanced calving rates (Carroll et al. 2015, Fried et al. 2015, Slater et al. 2017b).

To date, many studies have used numerical models, observations and laboratory experiments to show that submarine melting is amplified where subglacial discharge

plumes emerge at the glacier grounding line (e.g., Jenkins 2011, Motyka et al. 2013, Slater et al. 2015, Cenedese & Gatto 2016). Due to the lower density of subglacial discharge relative to the ambient fjord water, such plumes rise buoyantly along the ice front, entraining warmer fjord waters and melting the ice front and underside of any ice tongue present (e.g., Motyka et al. 2003, Jenkins 2011). Submarine melt rates are understood to be a function of the water temperature and velocity of the rising subglacial plume (Jenkins 2011), factors which are themselves influenced by the ambient fjord temperature, stratification and the volume and distribution of the emerging subglacial meltwater (e.g. Carroll et al. 2015, Slater et al. 2015).

Here, we connect variations in floating ice tongue spring submarine melt rates with the presence and location of summer subglacial meltwater plumes and of locally enhanced calving from 2012 to 2014 at Kangiata Nunaata Sermia, southwest Greenland.

5.2 Study area

Our study is focused on Kangiata Nunaata Sermia (KNS), the largest tidewater glacier in southwest Greenland, which drains into Kangersuneq Fjord as part of the wider Godthåbsfjord system (Figure 5.1). The glacier front is 4.5 km wide and has a maximum grounding line depth of approximately 250 m below sea level (Mortensen et al. 2013). In common with many Greenlandic tidewater glaciers, KNS forms a floating ice tongue over the winter, which extends 2-3 km from the glacier grounding line and decreases in freeboard with distance down-fjord (Figure 5.1d and 5.2a). Analyses of fjord water properties show that Kangersuneq Fjord is stratified with relatively warm subsurface waters (up to 2.5 °C) overlain by cooler water masses (between 0 and 1 °C) (Mortensen et al. 2013, Motyka et al. 2017).

5.3 Data and methodology

5.3.1 Elevation and ice velocity data

Five 2.5 m resolution digital elevation models (DEMs) of the study area were generated from conventional SAR interferometric processing of bi-static TanDEM-X imagery

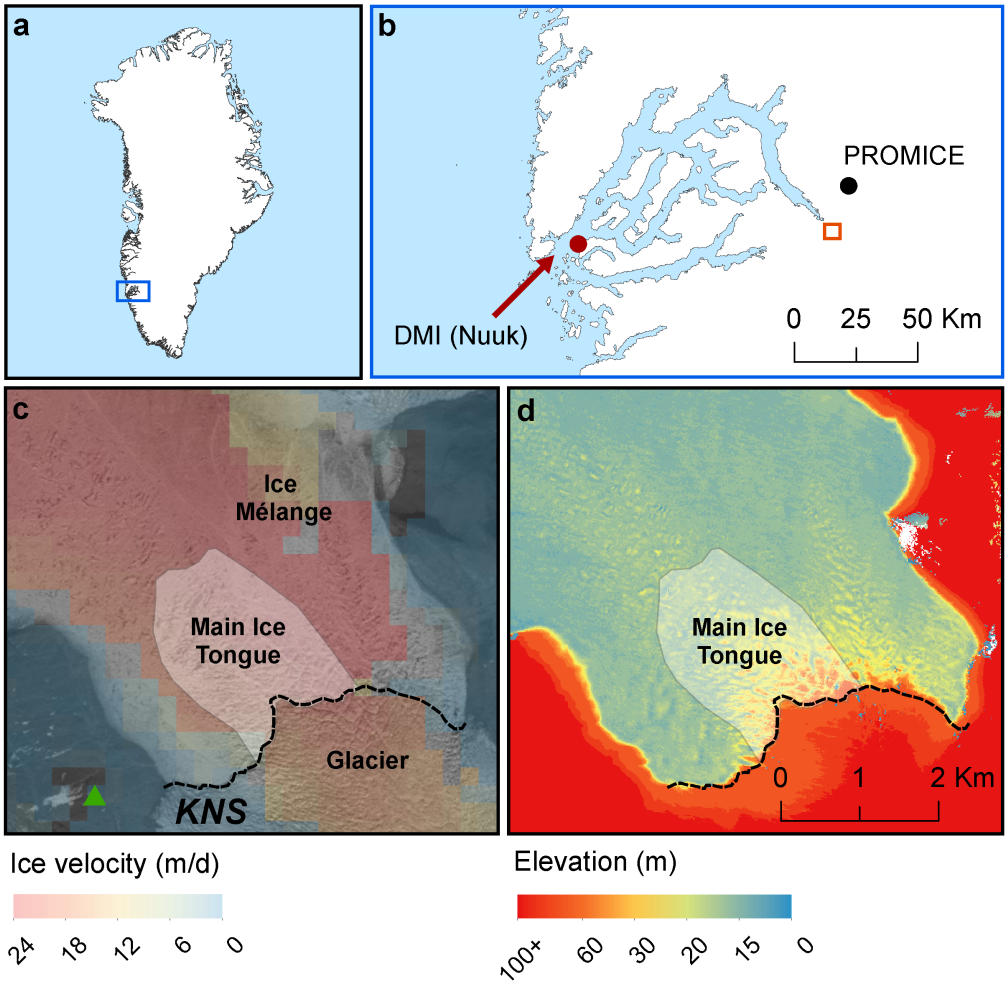

Figure 5.1: Study area, including (a) Greenland location map where blue rectangle indicates the extent of (b); (b) fjord-scale location map within the wider Godthåbsfjord system with location of two weather stations: Danish Meteorological Institute (DMI) Nuuk (red filled circle) and PROMICE NUK_L (black filled circle). The open orange square corresponds to the location of Figure 1(c,d); (c) a Landsat 8 band 8 satellite image of the KNS glacier ice tongue, acquired on 27 May 2014. The black dashed line indicates the estimated grounding line position (hand-digitized using both a Landsat 8 image from 12 June 2014 and the TanDEM-X DEM from 5 June 2014), the green triangle indicates the location of the University of Alaska Fairbanks time-lapse camera and the semi-transparent white polygon indicates the ice tongue extent. Ice velocity from 27 May to 12 June is overlain, derived from the feature tracking of Landsat 8 imagery (Rosenau et al. 2015); and (d) sample TanDEM-X derived elevation for KNS ice tongue, glacier and surrounding bedrock areas from 14 May 2014.

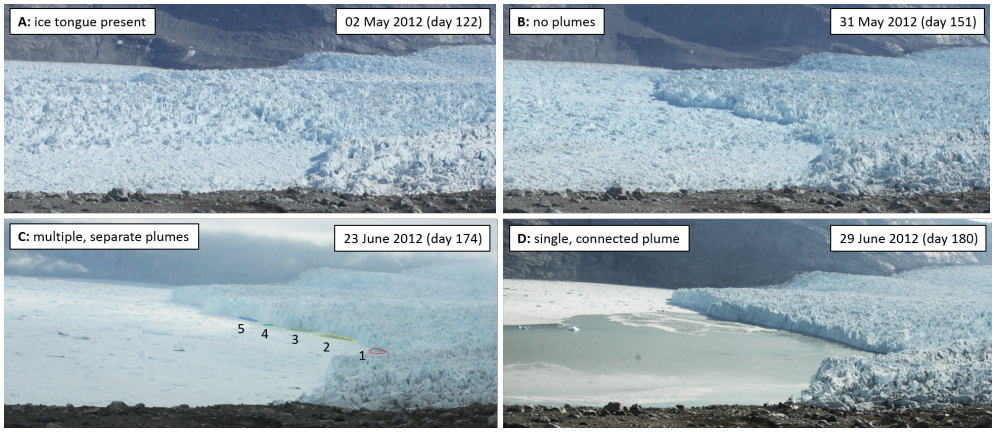

Figure 5.2: Sample time-lapse images used for plume presence detection: (a) ice tongue present; (b) no plumes visible on fjord surface; (c) multiple, separate plumes visible on fjord surface, with colours and numbers used for plume location classification (see Figure 5.4a,b); plumes 6 and 7 (not visible here) are located east (to the left) of plume 5; and (d) a single, connected surface expression of a plume visible on fjord surface.

(Dehecq et al. 2016), as detailed in Chapter 4. DEMs were acquired for the following dates: 13 May 2012, 17 March 2013, 27 May 2013, 14 May 2014 and 5 June 2014. We used both ICESat and Operation IceBridge (OIB) Airborne Topographic Mapper (ATM) elevation data (Krabill 2016) to perform co-registration and corrections to our derived DEMs. ICESat elevations were used for calibration over non-ice covered terrain and OIB ATM elevations were used to correct a tilt in the data over the ice-covered fjord (Figure S2.1) This tilt, ~0.45 m per km down-fjord, was introduced during DEM co-registration due to the limited coverage of the ICESat lines over stable bedrock regions. OIB ATM data from 25 April 2012 and 15 April 2014 were used to correct our 2012 and 2014 DEMs, respectively. As there was no OIB campaign over our study area in 2013, we corrected our 2013 DEMs using OIB ATM data from 8 April 2011, chosen due to similar fjord sea ice cover in both years, likely due to comparable inner-fjord water (Motyka et al. 2017) and air temperatures.

Three 20 m horizontal resolution ice velocity maps were generated using conventional feature tracking of spring 2013 TerraSAR-X imagery (e.g. Paul et al. 2013), and acquired from the following image pairs (to correspond with our 17 March and 27 May

2013 DEMs): 12 and 23 February; 8 and 19 April; 30 April and 11 May (see Chapter 4 for more details). For 2012 and 2014, we use velocity maps generated from combined feature tracking of Landsat 7 and 8 imagery (Rosenau et al. 2015) for the following image pairs: 6 and 22 May 2012 (to correspond with our 13 May 2012 DEM) and 27 May and 12 June 2014 (to correspond with both our 14 May and 5 June 2014 DEMs). These velocities are freely available from the Technische Universität Dresden's Geodetic Data Portal (https://data1.geo.tu-dresden.de/flow_velocity/). All velocity maps can be seen in Figure S2.2.

5.3.2 Ice tongue surface and submarine melt rates

To assess potential elevation changes driven by surface mass balance, ice tongue surface melt rates were estimated using a simple positive degree day approach (Hock 2003), details of which can be found in Section 3.3.1. Degree day modelling was also used to estimate catchment-wide runoff from surface melting during the melt season at elevations below 2000 m, above which most meltwater refreezes within the snow pack (e.g. Pfeffer et al. 1991, Langen et al. 2015, 2017). Daily air temperatures were acquired from a Geological Survey of Denmark and Greenland PROMICE weather station located approximately 21 km NE from the KNS terminus (Figure 5.1b; Ahlstrøm et al. 2008). Daily precipitation data were acquired from the Danish Meteorological Society (DMI) weather station in Nuuk, approximately 105 km west of the KNS terminus (Figure 5.1b; Cappelen, J. (ed.) 2016). The ArcticDEM (Morin et al. 2016), sampled to 90 m horizontal resolution, was used to estimate KNS catchment-wide runoff.

Ice tongue submarine melt rates were estimated by differencing along-fjord flowline surface elevation in combination with ice velocities, following the methodologies in Chapter 4. Flowlines were created every 25 m along the KNS ice tongue, starting 150 m from the grounding line (in order to exclude noise in velocity data as the ice moves across the grounding line) and extending approximately 2 km down-fjord (see Figure 5.3). To accommodate temporal changes in ice velocity, separate flowlines were created for each DEM date, resulting in a different ice tongue shape each year. Elevations along each flowline were smoothed using a two-sided moving average with a 625 m

window, which was the smallest smoothing window that significantly reduced the effect of large crevasses on the ice elevation gradient, and then converted to thickness values assuming ice tongue floatation and hydrostatic equilibrium. Noise in velocity data along each flowline was reduced by using a linear regression between ice tongue velocity and distance down-fjord. As we only have one DEM for 2012 and for comparison purposes, we estimate steady state submarine melt rates, assuming ice thickness at a fixed location does not change in time. Submarine melt rate (SMR) accounts for thinning due to stretching in both the flow direction and perpendicular to flow:

$$SMR = -v_x \frac{\delta H}{\delta x} - H \frac{\delta v_x}{\delta x} - H \frac{\delta v_y}{\delta y} - SMB \tag{5.1}$$

where H is the ice thickness (m), v_x and v_y are the ice velocity (m d^{-1}) in the along- and across-flowline direction, and x and y represent distance in the along- and across-flowline direction. We include a potential contribution from surface mass balance (SMB), although it will later be shown that this is negligible in our case. Note that a term representing across-flow thinning, $-v_y \frac{\delta H}{\delta y}$, does not contribute as, by definition of a flowline, $v_y = 0$ on the flowline. To best capture the general trend in submarine melt rates and in order to smooth out unrealistic melt rate estimates resulting from the heavily-crevassed nature of the ice tongue (and thus short-length scale high amplitude variations in elevation), exponential fits were applied to estimated flowline melt rates (see Chapter 4).

5.3.3 Uncertainties in submarine melt rate estimates

Uncertainties in our submarine melt rate estimates are associated with the quality of the elevation and velocity data, the smoothing of our flowlines, and our assumption of an ice tongue in steady state. There are two types of errors surrounding the elevation data: the absolute error in elevation (and thus thickness, H) and the gradient error in elevation, which impacts $\frac{\delta H}{\delta x}$ in Eq. 5.1. Error in the absolute measured elevation derived from the TanDEM-x data results from the DEM construction process and typically has an uncertainty of ± 2 m over areas of slope less than 12°(Rizzoli et al.

2012). As the ice tongue at KNS has a low gradient (less than 0.15°), ±2 m is likely an overestimate of elevation uncertainty, as we would expect a greatly reduced slope to significantly lower this uncertainty (e.g. Toutin 2002, Erasmi et al. 2014). Error in the elevation gradient results from our DEM tilt correction using OIB ATM data, and is defined as the largest difference in slope between the OIB ATM lines and the corrected TanDEM-X elevations, as estimated over 2 km long segments of very thin sea ice where successive OIB ATM flights show near-constant slope (Figure S2.1). The resulting elevation gradient errors are ±1.78 m (for 2012 and 2014) and ±0.38 m (for 2013) over the nearly 2 km long ice tongue.

Uncertainties in ice tongue velocity are often the result of poor image co-registration, surface changes and transformations (e.g., changes in illumination or reflectance of surface features like snow), and mismatches between similar but not corresponding features (in this case, crevasses in the ice tongue) (Paul et al. 2013, Rosenau et al. 2015). Uncertainties in Landsat-derived ice tongue velocity for 2012 and 2014 were downloaded directly from the Technische Universität Dresden's Geodetic Data Portal, with mean uncertainties in velocity of up to ±1.1 and ±0.23 m d^{-1} for 2012 and 2014, respectively. Uncertainty in our 2013 TerraSAR-X derived ice tongue velocity was calculated following Paul et al. (2013), with mean uncertainties in velocity of ±0.09 m d^{-1}.

Uncertainties in both elevation and velocity data were combined via standard error propagation techniques to calculate the preliminary error in our submarine melt rate estimates (ΔSMR), as follows:

$$\Delta SMR = \sqrt{\left[\Delta\left(v_x \frac{\delta H}{\delta x}\right)\right]^2 + \left[\Delta\left(H \frac{\delta v_x}{\delta x}\right)\right]^2 + \left[\Delta\left(H \frac{\delta v_y}{\delta y}\right)\right]^2} \tag{5.2}$$

where $\Delta\left(v_x \frac{\delta H}{\delta x}\right)$, $\Delta\left(H \frac{\delta v_x}{\delta x}\right)$ and $\Delta\left(H \frac{\delta v_y}{\delta y}\right)$ are the errors associated with the first three terms on the right-hand side of Equation 5.1, respectively. The first error term, $\Delta\left(v_x \frac{\delta H}{\delta x}\right)$, was estimated as follows, with the the second and third error terms estimated in a similar fashion:

$$\Delta\left(v_x \frac{\delta H}{\delta x}\right) = \left|v_x \frac{\delta H}{\delta x}\right| \sqrt{\left(\frac{\Delta v_x}{v_x}\right)^2 + \left(\frac{\Delta \frac{\delta H}{\delta x}}{\frac{\delta H}{\delta x}}\right)^2} \tag{5.3}$$

In addition to uncertainty in elevation and velocity data, there are other potential sources of error that must be considered. Smoothing the flowline elevations also results in uncertainty in our final submarine melt rates, which we assess using a sensitivity analysis. Varying the moving average window size by ±125 m results in an additional submarine melt rate uncertainty of ±25%, which has been added to the preliminary submarine melt rate errors, above. In addition, the assumption of an ice tongue in steady state increases uncertainty in our submarine melt rate estimates. We know that the ice tongue is not in steady state between March and May 2013, as seen in thickness changes between our two 2013 DEMs, which result from a slower moving glacier. To estimate potential errors resulting from this assumption, we estimated non-steady state submarine melt rates for March and May 2013. We assumed a linear trend of thickening between the two DEMs (see Equation 4.3 in Chapter 4), accounted for by subtracting a daily rate of thickness change from our 2013 steady state melt rate estimates. On average, ice tongue non-steady state melt rates are 0.12 m d^{-1} (23%) and 0.23 m d^{-1} (27%) lower than steady state estimates for March and May 2013, respectively (Figure S2.3). These average percent differences fall within the mean percent differences in melt rate resulting from uncertainty in our elevation and velocity datasets (see Table S2.1), which range from 26 to 46%. In addition, assuming an ice tongue in steady state does not change the overall magnitude of the melt rates. As such, while the ice tongue is not in a steady state (at least for 2013), we believe that submarine melt rates can be reasonably approximated under the assumption of an ice tongue in steady state, which is necessary for meaningful comparison to years when we only have one DEM for estimating melt rates.

Additional uncertainties in submarine melt rate estimates arise from: the assumption that the ice tongue is floating in hydrostatic equilibrium along its full length, which, if incorrectly assumed, would mean melt rates are overestimated in the first km of ice by at least 15%; the seasonal migration of the glacier grounding line, down-fjord of which

melt rates are estimated; the cohesiveness of the ice tongue, which potentially impacts changes in ice thickness and velocity; and temporal variability in ice tongue velocity. All of these additional uncertainties are discussed in detail in Chapter 3.3.3

5.3.4 Subglacial discharge plumes, calving activity and hydrology

To investigate the correspondence between the presence and location of subglacial discharge plumes post-ice tongue disintegration and spatial patterns in ice tongue submarine melt rates, we created a time series of the expression of runoff plumes at the fjord surface using time-lapse imagery from a camera located on a bedrock ridge approximately 1 km from the western edge of the KNS calving front (Figure 5.1c). Images of the western half of the calving front were taken every 4 hours from 18 May 2012 (day 139) until 22 July 2013 (day 203). We assigned each plume a number from 1 to 7, based on location moving west to east along the calving front (Figure 5.2c). Plumes 6 and 7 (not pictured in Figure 5.2c) occur infrequently. To avoid including open water resulting from wind or calving activity, we only identified plumes that were visibly turbid, thereby indicating a subglacial origin. In addition, while plume surface expressions are not visible at the same time as the ice tongue is intact, we assume plume positions are the same for the period prior to the disintegration of the ice tongue.

A time series of calving activity was also created from the time-lapse images, by viewing each image for visible signs of calving and recording the time and location of each event along the calving front (either western or eastern side). Visible signs of calving include actively captured calving events, changes in fjord surface between two images (i.e., non-turbid open water adjacent to ice front with small bergy bits), and obvious changes in ice front morphology between two images.

To assess potential spatial variations in the subglacial hydrological network below the grounded part of KNS and the predicted locations of any emerging subglacial channels along the calving front, we performed a standard hydropotential analysis with the MATLAB toolbox TopoToolBox (Shreve 1972, Schwanghart & Scherler 2014), using BedMachine v3 bed and surface topography (Morlighem et al. 2017) to calculate the subglacial hydraulic potential (Φ):

$$\Phi = \rho_w g z + f \rho_i g h \tag{5.4}$$

where ρ_w and ρ_i are the densities of meltwater (1,000 kg m^{-3}) and ice (910 kg m^{-3}), respectively, g is the acceleration due to gravity (9.81 m s^{-2}), z is the bed elevation (m) and h is the ice thickness (as provided in the Bed Machine v3 product). f is the ratio of the subglacial water pressure to the ice overburden pressure (e.g., Banwell et al. 2013), which is in general poorly known and we thus apply a range of values from $f = 0.1$ to $f = 1$ consistent with sparse observations from Greenland (Meierbachtol et al. 2013, Andrews et al. 2014). A value $f = 0.1$ means that the subglacial water pressure is a tenth of the ice overburden pressure, so that the subglacial hydrological system is at low pressure, such as might be associated with efficient subglacial drainage, while a value $f = 1$ means that the subglacial water pressure is equal to the ice overburden pressure, so that the subglacial system is at high pressure, such as might be associated with inefficient subglacial drainage (Fountain & Walder 1998).

5.4 Results and discussion

5.4.1 Variations in submarine melt rates

Using our flowline methodology, we find that near-terminus spring submarine melt rates for the floating ice tongue at KNS vary both temporally and spatially (Figures 5.3 and S2.4a; Table S2.1), with mean melt rates taken over the full extent of the ice tongue ranging from 0.8 ± 0.3 m d^{-1} in March and May 2013 to 1.3 ± 0.6 m d^{-1} in May 2012. Maximum melt rates occur under the western half of the ice tongue in May 2012, reaching over 7 m d^{-1} approximately 150 m down-fjord from the KNS grounding line. Surface melt rates, estimated using a positive degree day model, are at least one order of magnitude lower than our mean submarine melt rates (Table S2.1), and are thus considered negligible (see Section S2.1).

Our estimated melt rates agree well with those previously estimated in the Godthåbsfjord system. Estimated mean melt rates over the full KNS ice tongue (up

to 1.3 ± 0.6 m d^{-1}) are in line with our previous 2013 mean melt rate estimate of 0.8 ± 0.3 m d^{-1} (see Chapter 4). Our maximum estimated submarine melt rate (just over 7 m d^{-1}) compares well with modelled average KNS ice front estimates of 3 to 7 m d^{-1} (Motyka et al. 2017). Our melt rates are also the same order of magnitude as those estimated between 2000 and 2010 under Greenland tidewater glacier floating termini, which reach over 2.0 m d^{-1} in both central west (Jakobshavn and Rink) and east (Daugaard Jensen) Greenland (Enderlin & Howat 2013).

Variations in submarine melt rates depend on multiple factors, scaling with both ambient water temperature and plume velocity (e.g. Holland & Jenkins 1999, Jenkins 2011). Ambient winter and spring water temperatures measured at depths between 120 and 150 m (in which the deepest draft of the ice tongue sits) in Kangersuneq Fjord do not change substantially from 2012 to 2014, averaging ~1.5 ^{o}C for all months during our study period, with the exception of March 2013, which averaged 2.0 ^{o}C (Mortensen et al. 2013, Motyka et al. 2017). As such, it is unlikely that changes in ambient water temperature at depth (~33% increase from 2012 to 2013) are driving the temporal variations seen in our submarine melt rate estimates (~38% decrease in ice tongue averaged melt rate from 2012 to 2013).

5.4.2 Subglacial discharge plumes

The presence of subglacial plumes, resulting from surface and basally generated meltwaters, also influences submarine melt rates. In the winter and early spring, subglacial discharge from surface meltwater is expected to be negligible. Plumes may however still be generated by subglacial discharge resulting from frictional melting beneath the grounded part of the glacier (Christoffersen et al. 2012). To assess the potential influence of basal frictional melting on driving winter and spring plumes, we estimated basal meltwater flux for the entire KNS catchment using a simplified equation for basal melt rate (Christoffersen et al. 2012), dependent upon ice velocity and density, basal drag and the latent heat of fusion (see Section S2.2 for equation and data sources). Estimated basal meltwater fluxes were 29.4, 28.9 and 29.1 m^3 s^{-1} for 2012, 2013 and 2014, respectively. Frictional melting is likely therefore able to sustain

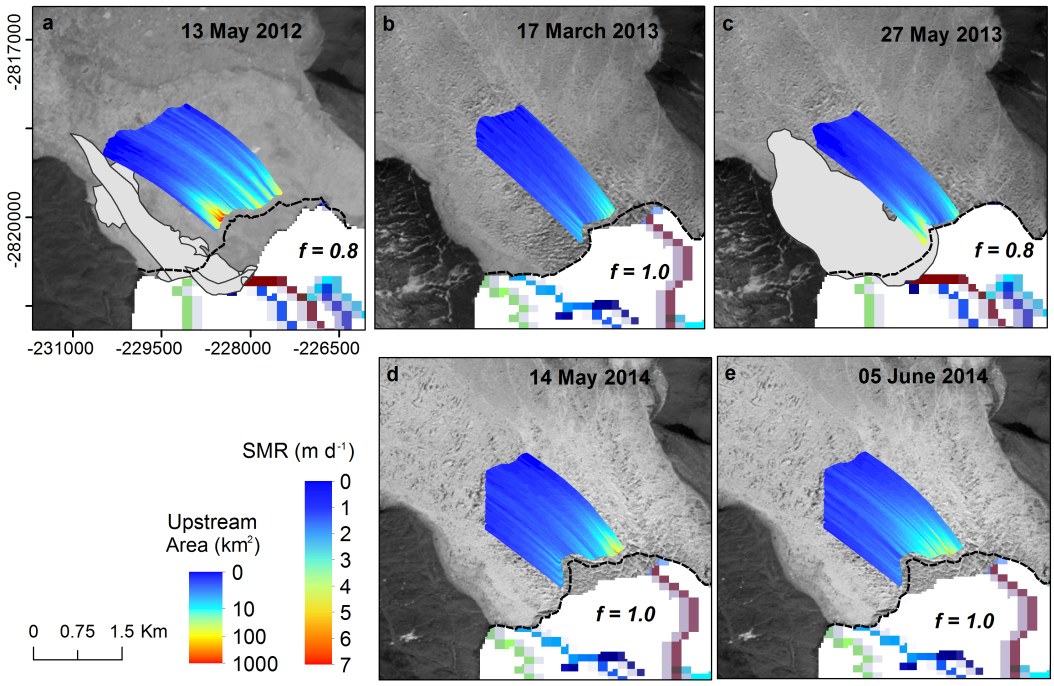

Figure 5.3: Submarine melt rates (SMR) of KNS ice tongue flowlines, locations of plume surface expressions (grey polygons hand-digitized from Landsat images in Table S2.2), and near-terminus flow routing coloured to indicate total upstream drainage area for (a) 13 May 2012, (b) 17 March 2013, (c) 27 May 2013, (d) 14 May 2014 and (e) 05 June 2014. Dashed black lines indicate estimated location of the grounding line in June of each year (hand-digitized from Landsat 8 imagery). Background images are all Landsat 7 and 8, acquired for (a) 25 July 2012, (b,c) 01 May 2013 and (d,e) 12 June 2014. The chosen flow routing f-values show the best spatial association between plume surface expressions and spatial variability in melt rate. Note that some colours seen in the flow routing are not in the colourbar (e.g., purple), as they are the result of overlapping channels (e.g., blue and red channels, but with purple being indicative of a net large upstream area).

active plumes through the winter and into early spring, augmenting submarine melt rates. However, once the melt season begins, runoff from surface melting will dominate, sustaining larger plumes and promoting higher melt rates. This is likely the case in May

2012, when the melt season began early and where we estimate May runoff reaching 500 m^3 s^{-1} (Figure 5.4e) and melt rates exceeding 7 m d^{-1}.

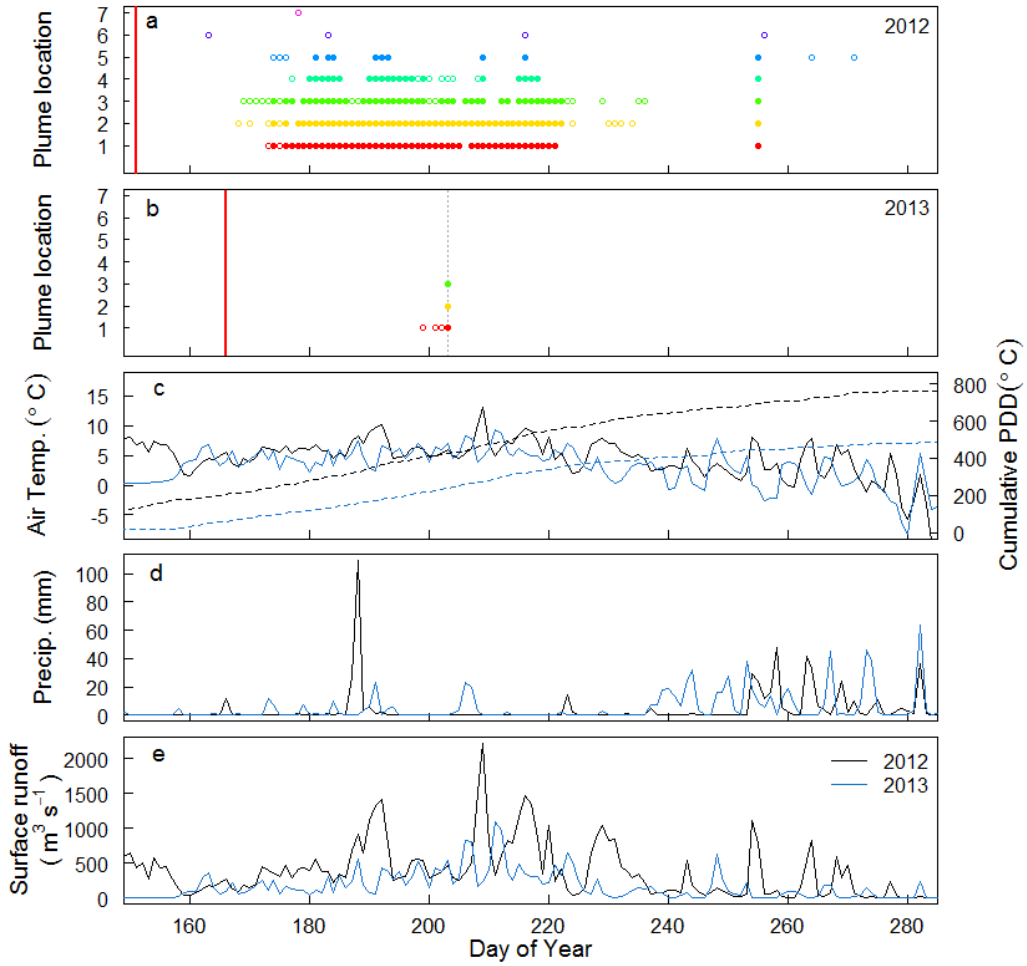

Figure 5.4: (a-b) Time series of subglacial plume surface expression for (a) 2012 and (b) 2013 (see Figure 5.2c for plume locations), where hollow circles indicate separate, individual plumes and filled circles indicate plumes seen as a single large coalesced plume on the fjord surface; the red vertical line indicates the date of ice tongue disintegration and the grey dashed vertical line indicates the date of the last time lapse image; (c-e) time series of (c) daily average air temperature (solid lines, left axis) and cumulative positive degree day (PDD) sum (dashed lines, right axis), (d) daily precipitation, and (e) catchment-wide surface runoff over KNS from degree day modelling for 2012 (black lines) and 2013 (blue lines).

Subglacial plumes, sourced primarily from glacier surface meltwaters exiting at the

grounding line, can be observed at the surface of the fjord near the KNS grounding line in late-spring and summer each year, following ice tongue disintegration. Analysis of time-lapse imagery from 2012 shows that nearly all of the observed plumes on the fjord surface (~97%) occurred along the western half of the calving front (Figures 5.3a and 5.4a, plumes 1-5). We note, however, that due to the restricted view from the time-lapse camera, it is possible we are missing occurrences of surfacing plumes on the eastern side of the calving front. Nevertheless, the surface expression of plumes west of the calving front centre for nearly all of the melt season suggests consistent delivery of meltwater, via a network of several subglacial channels, at corresponding locations along the glacier grounding line (e.g., Slater and others, 2017b). In instances where there is only one large plume visible on the fjord surface, it is impossible to tell which subglacial channels are 'active,' or if the channel network is unstable, particularly if one channel is dominant. Several channels could have persisted from the previous melt season, sustained by the release of frictional meltwater generated from basal sliding or from surface melt runoff due to an early on-set to the melt season, thereby promoting the high melt rates observed in May 2012 under the western side of the ice tongue (e.g., Figure 5.3a). In addition, the presence of plumes at the fjord surface later in the 2012 melt season is likely augmented by the draining of the ice-dammed lake Isvand, present on the bedrock ridge behind the western side of the KNS terminus. Isvand drained sometime between 01 and 17 August, as evident by a decrease in lake surface area by ~7 km^2 between the two dates (as observed from Landsat 7 imagery).

The surface expression of plumes is infrequent in 2013 (Figure 5.4b), likely due to the much lower catchment-wide surface runoff volume across the melt season (2.1 and 4.8 km^3 for May to October 2013 and 2012, respectively, based on degree day estimates), resulting in smaller subglacial discharge at the grounding line and fewer plumes reaching the surface of the fjord (e.g. Slater et al. 2015, Carroll et al. 2016). In addition, the surface expression of plumes occurs much earlier in 2012 (day 156) than 2013 (day 199), likely due to the warmer air temperatures observed in 2012 (Figure 5.4c) causing both an earlier break-up of the ice tongue and an earlier on-set of the melt season.

5.4.3 Subglacial hydrology network

The spatial pattern of our submarine melt rate estimates for 2013 changes between March and May, with higher melt rates under the eastern side of the ice tongue in mid-March, followed by higher melt rates under the western side of the ice tongue by the end of May (Figure 5.3b,c), suggesting a change in the primary location of subglacial plumes exiting the glacier. In 2014, our melt rate estimates are again higher beneath the eastern side of the ice tongue, potentially indicating an oscillating subglacial hydrological network beneath KNS, with the main subglacial channels shifting between the western and eastern side of the ice tongue.

Results from our hydropotential analysis suggest that the location of the emerging subglacial runoff is sensitive to subtle changes in subglacial water pressure. Using a basal water pressure from 90 to 100% of the ice overburden pressure predicts a major subglacial channel on the far eastern side of the calving front, as well as two smaller channels on the western half of the calving front (Figures 5.3b,d-e and S2.5b,c). This channel configuration is consistent with the higher melt rates on the eastern side of the fjord that we observe in March 2013 and May and June 2014. Reducing the basal water pressure to anywhere from 10 to 80% of ice overburden results in a significant change in inferred channel location, with a major subglacial channel now predicted on the western side of the calving front (Figures 5.3a,c and S2.5d-f), closer to where we see most large plumes emerging at the fjord surface in 2012, and where we observe higher submarine melt rates under the spring ice tongue. The predicted locations of subglacial runoff are therefore sensitive to changes in basal water pressure, suggesting that near-terminus subglacial channels are likely mobile and highly dynamic (e.g. Slater et al. 2017a).

5.4.4 Calving and ice front shape changes

Further analysis of the 2012 time-lapse imagery reveals that the majority of the calving events observed during the melt season (~91%) occur where we predominantly see subglacial plume surface expressions and where we estimated higher submarine melt rates under the spring ice tongue. The occurrence of increased calving over areas

of high submarine melting has been observed at tidewater glaciers in central west Greenland (e.g. Fried et al. 2015) and Alaska (e.g. Bartholomaus et al. 2013), where calving is driven by thermal undercutting of the ice front via submarine melting (e.g. O'Leary & Christoffersen 2013). These areas of increased calving can create pronounced embayments along the calving front, often located above subglacial outlet channels (e.g. Chauché et al. 2014, Fried et al. 2015), and as we observe along the western half of the KNS ice front during the 2012 melt season (Figure S2.6). As we have limited time-lapse imagery for 2013 and no imagery for 2014, we cannot determine whether the relationship between subglacial plume presence, submarine melting and calving holds true for other years at KNS. Ice velocities approaching the terminus are not significantly different across the width of the ice tongue in any given year, suggesting a similar ice flux delivery to the terminus across the calving front. We argue therefore that the presence of subglacial meltwater plumes has a large influence on localized calving, which must shift with time along the ice front, or else the terminus planform shape would change gradually to reflect the dominance of calving that we observe on the western side in 2012.

5.5 Conclusions

Dynamic changes in tidewater glaciers have led to increases in ice discharge from the Greenland Ice Sheet over recent decades, yet the processes controlling these dynamic changes remain poorly understood, particularly the role of submarine melting. Here, using high resolution digital elevation models and ice velocity to estimate submarine melt rates under the seasonal ice tongue of KNS in southwest Greenland from 2012 to 2014, we reveal significant near-terminus spatial and temporal variations in spring melt rates. We estimate submarine melt rates of up to 7.3 $\pm$ 2.3 m d^{-1} under the western side of the ice tongue in May 2012, with the spatial pattern of melt rate corresponding to the locations of surface expressions of subglacial discharge plumes during the melt season of the same year. In addition, the greatest abundance of observed calving in 2012 occurs where we predominately see subglacial plumes. The spatial pattern of estimated submarine melt rate varies from 2012 to 2014, with areas of higher melt switching between the western and eastern side of the ice tongue. We attribute these changes to

a switching of subglacial flow paths, a hypothesis supported by modelled subglacial flow routing, which shows that the main channel will emerge on either the eastern or western side of the fjord, dependent on subtle changes in the ratio between basal water pressure and ice overburden pressure. Our results provide a new empirically-derived link (i.e., non-laboratory or modelled result) between the presence of subglacial discharge plumes (and thus subglacial outlet channel locations) and areas of higher submarine melting and calving at tidewater glacier termini, and can be used to improve our understanding of the coupling between tidewater glacier termini and the ocean.

Chapter 6

Seasonal variations in iceberg freshwater flux in glacial fjords from Sentinel-2 imagery

The previous two chapters have investigated submarine melt rates at the terminus of a large tidewater glacier in southwest Greenland, developing a novel approach using remote sensing to observe changes in floating ice tongue velocity and freeboard (Chapter 4) and temporally extending its application (Chapter 5). Both of these chapters have shed light on potential controls on submarine melting, most notably fjord water temperatures with depth, ice tongue draft and the presence and location of subglacial discharge plumes exiting beneath the glacier grounding line.

This chapter moves across to the eastern side of the ice sheet to investigate freshwater fluxes from the submarine melting of icebergs in Sermilik Fjord, southeast Greenland. Icebergs in glacial fjords have received increasing attention over the last few years (e.g., Enderlin et al. 2016, FitzMaurice et al. 2016, Moon et al. 2017, Enderlin et al. 2018), as they can dominate the freshwater budget by contributing meltwater into the fjord system once other sources have been reduced (i.e., subglacial discharge outwith the melt season). This chapter develops a new methodology to derive iceberg freshwater

fluxes using freely available satellite imagery to estimate iceberg velocity and changes in fjord ice volume with distance down-fjord. The results provide seasonal variations in freshwater flux released at depth in Sermilik Fjord, and the method provides an invaluable tool for monitoring icebergs freshwater fluxes across a range of glacial fjord systems.

A shortened version of this chapter was submitted for publication in *Geophysical Research Letters* in January 2019:

Moyer AN[1], Sutherland DA[2], Nienow PW[1] and Sole AJ[3], Seasonal variations in iceberg freshwater flux in glacial fjords from Sentinel-2 imagery, *Geophysical Research Letters*, in review.

[1]School of GeoSciences, University of Edinburgh, Edinburgh, UK.

[2]Department of Earth Sciences, University of Oregon, Eugene, OR, USA.

[3]Department of Geography, University of Sheffield, Sheffield, UK.

Author contributions: ANM performed all of the analysis and led the writing of the manuscipt. DAS provided GPS-tracked iceberg velocity data. All authors contributed ideas and methodological developments, and provided editorial input on the manuscript.

Abstract

Iceberg discharge has been estimated to account for up to 50% of the freshwater flux delivered to fjords surrounding the Greenland Ice Sheet. The amount, timing and location of meltwater produced via submarine melting of icebergs can significantly impact local fjord water circulation and heat budget, with implications for glacier dynamics, nutrient cycling and fjord productivity. Here, we use Sentinel-2 satellite imagery to examine seasonal variations in the size and distribution of open-water icebergs (i.e., excluding the ice mélange) in Sermilik Fjord, southeast Greenland during summer and autumn 2017. Icebergs are identified and delineated using spectral properties, and submerged volumes are estimated using an assumed relationship with iceberg surface area. Distinct icebergs are visually-tracked throughout the year, allowing for the estimation of average iceberg velocities. Using these estimated velocities and changes in total iceberg volume with distance down-fjord from the Helheim Glacier terminus, we estimate integrated 2-month freshwater fluxes along the length of the fjord of ~1270 ± 650, 1200 ± 610, 3410 ± 1740, and 1150 ± 590 m^3 s^{-1} for June-July, July-August, August-September and September-October, respectively. Furthermore, freshwater fluxes decrease with distance from the head of the fjord while on average ~86% of total iceberg volume is lost before reaching the fjord mouth. The method utilized offers a simplified approach for estimating both spatial and temporal variations in iceberg freshwater flux entering glacial fjords, without recourse to expensive field data collection or complex processing of commercial satellite data, thereby providing an invaluable tool for monitoring iceberg freshwater fluxes across a range of Greenlandic fjords.

6.1 Introduction

Recent studies have shown that meltwater fluxes from icebergs can dominate the freshwater budget in glacial fjords surrounding the Greenland Ice Sheet (Enderlin et al. 2016, Moon et al. 2017). The amount, timing and location where meltwater from icebergs enters the fjord has important glaciological and ecological implications. The energy lost through the melting of icebergs and the input of cold freshwater

at various depths in the water column alters the amount of heat reaching tidewater glacier termini (Enderlin et al. 2016), with implications for terminus submarine melt rates. This is of particular importance, as submarine melting of glacier termini has been proposed as a trigger for glacier calving, retreat and acceleration (O'Leary & Christoffersen 2013, Luckman et al. 2015). The input of freshwater at various fjord locations and depths also alters fjord salinity gradients, impacting not only buoyancy-driven circulation important to submarine melting, but also nutrient budgets and associated primary productivity and thus fishery stocks crucial for local economies (e.g., Rose 2005, Smith Jr. et al. 2013).

Previous studies have used either models (e.g., Mugford & Dowdeswell 2010, Moon et al. 2017) or remote sensing methods (e.g., Enderlin & Hamilton 2014, Enderlin et al. 2016) to estimate iceberg melt rates and freshwater fluxes into glacial fjords. Moon et al. (2017) modelled iceberg melt using oceanographic and reanalysis data and modelled buoyant plume velocities to account for iceberg melting above, below and at the waterline. While providing a valuable methodology, modelling iceberg melt and freshwater flux is very complex, relying heavily on both sparse field data (e.g., ocean temperature and salinity, water velocity, air temperature and wind speed) and poorly constrained model parameterizations. Enderlin and Hamilton (2014) and Enderlin et al. (2016) used changes in iceberg freeboard derived from high-resolution digital elevation models (DEMs) to estimate iceberg volume loss, from which area-averaged iceberg melt rates and fluxes were derived. Both of these methodologies are impressive in their scope and conclusions; they are however both very user-intensive (i.e., hand-digitizing hundreds of icebergs), data-heavy, expensive (i.e., commercial satellite data and field data collection costs) and time-consuming. In addition, both methods assume standard iceberg underwater shapes, which significantly affects estimates of the submerged surface area and thus derived iceberg melt and freshwater fluxes.

Here, we use freely available Sentinel-2 satellite imagery from summer and autumn 2017 to estimate iceberg velocity and changes in iceberg volume with distance down-fjord from the Helheim Glacier terminus in Sermilik Fjord, east Greenland, assuming a constant iceberg surface area to volume relationship. These data are utilized to

generate seasonal, spatial estimates of iceberg freshwater flux into Sermilik Fjord, and our methodology can be transferred easily to other glacial fjords, thereby providing a valuable tool for generating widespread iceberg freshwater flux estimates.

6.2 Physical setting

We use Sermilik Fjord in east Greenland as our study site (Figure 6.1a), as there are numerous oceanographic and glaciological measurements taken here (e.g., Straneo et al. 2010, 2011, Sutherland et al. 2014a,b, Kehrl et al. 2017), as well as previous estimates of iceberg freshwater flux (e.g., Enderlin et al. 2016, Moon et al. 2017, Sulak et al. 2017). At the head of the fjord are three large tidewater glaciers: Helheim, Fenris, and Midgård. Of these, Helheim Glacier is the most prolific iceberg producer, ~25 Gt a^{-1} (Enderlin et al., 2014), reaching speeds up to 11 km a^{-1} near the terminus (Kehrl et al. 2017). After exiting the ice mélange, which extends ~20 km from the terminus, icebergs travel south for ~80 km before reaching the fjord mouth and the Irminger Sea. GPS-tracked icebergs from September 2012 and August 2013 show movement of ice within the fjord (see Figure 2.11) and while there is some inner-fjord iceberg recirculation, there is an overall net down-fjord movement of icebergs over time. Mooring data from the fjord in summer show a fresh, cool Polar Water layer (0 - 0.5 °C) at depths between ~100 - 200 m underlain by a layer of salty, warm Atlantic Water (up to 5.2 °C) (Sutherland et al. 2014b, Jackson et al. 2014).

6.3 Methodology

6.3.1 Estimating iceberg surface area and volume

To derive estimates of iceberg surface area in Sermilik Fjord, we use seven Sentinel-2 images covering the full extent of the fjord, acquired between July and November 2017 (Table 6.1). Images were selected based on the presence of little to no cloud and sea ice cover, which excluded all images prior to July and many autumnal images. We only use the near-infrared band (band 8), with a spatial resolution of 10 m. All images were converted to Top of Atmosphere Reflectance (TOA) by dividing the digital number

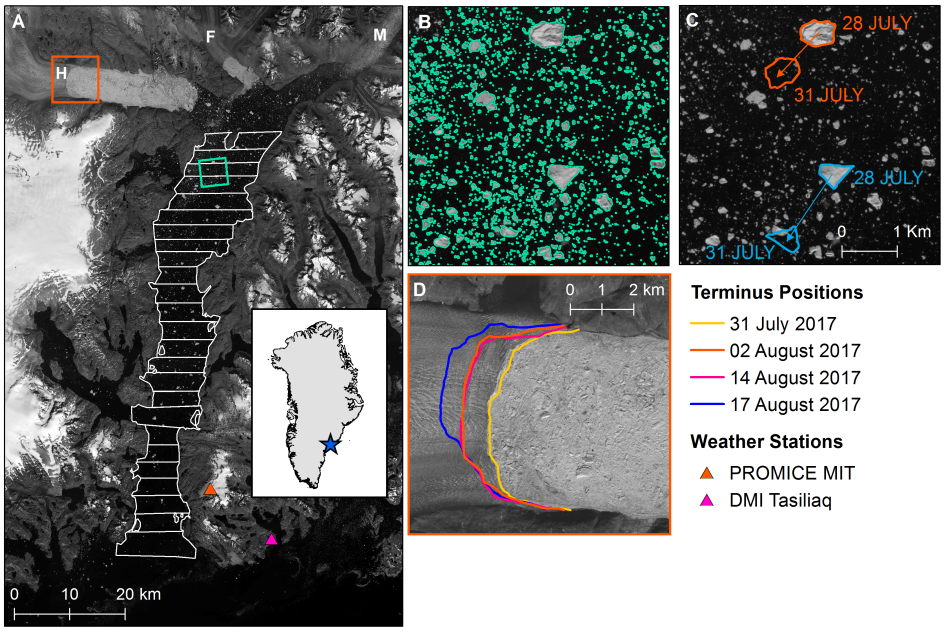

Figure 6.1: (a) Sermilik Fjord from a Sentinel-2 image on 28 July 2017, including three large tidewater glaciers: Helheim (H), Fenris (F), and Midgård (M). White boxes are areas of the fjord included in the analysis, the green box indicates the location of (b,c) and the orange box indicates the location of (d); orange and pink triangles indicate locations of PROMICE MIT and DMI weather stations, respectively; (b) automatically classified iceberg polygons (from 28 July 2017), highlighting pixels with TOA reflectance values $\geq$ 0.13; (c) sample polygon tracking for velocity estimation for two distinct icebergs between 28-31 July; (d) terminus positions for Helheim Glacier, hand-digitized from Sentinel-2 and Landsat 8 band 8 imagery.

of each pixel by the quantification value provided in each image's metadata (Gatti & Bertolini 2015). We then applied a threshold to each image in order to separate ice pixels from those containing water. A threshold value of 0.13 was used for all summer images, chosen from a wide range of threshold values to best separate ice and water pixels. Due to lower lighting conditions in the autumn, we used a threshold value of 0.30 for the November image. Pixels with values greater than or equal to our chosen thresholds were automatically classified as ice (Figure 6.1b). We then connected adjacent ice pixels into polygons, which were identified as icebergs. For each image,

we visually inspected all polygons, manually dividing any erroneously joined pixels into separate icebergs. Surface area was then calculated for each iceberg polygon and summed per section of the fjord (see white boxes in Figure 6.1a).

Table 6.1: Area of fjord analysed, number of icebergs, total iceberg area, percent of fjord covered by ice and volume for each 2017 Sentinel-2 image.

Image Date	Fjord Area (km^2)	No. of Icebergs	Total Iceberg Area (km^2)	Ice-covered % of Fjord	Total Iceberg Volume (km^3) [normalized by area]
23/07	721	39,909	49 ± 7	6.8 ± 1.0	4.7 ± 2.1 [0.0065]
28/07	721	34,813	50 ± 8	6.9 ± 1.1	5.2 ± 2.3 [0.0072]
30/07	658	32,494	57 ± 9	8.7 ± 1.3	5.6 ± 2.5 [0.0085]
04/08	469	19,028	28 ± 4	6.0 ± 0.8	2.9 ± 1.3 [0.0061]
14/08	628	44,186	55 ± 8	8.8 ± 1.2	5.2 ± 2.3 [0.0083]
17/08	613	33,371	48 ± 7	7.8 ± 1.2	4.9 ± 2.2 [0.0080]
13/09	721	37,304	46 ± 7	6.4 ± 1.0	4.0 ± 1.8 [0.0055]
02/11	628	14,467	20 ± 3	3.2 ± 0.5	2.1 ± 0.9 [0.0033]

Iceberg volume was estimated by applying an empirical surface area to volume relationship, as previously developed for Sermilik Fjord by Sulak et al. (2017). In their study, icebergs were hand-delineated from Worldview DEMs of Sermilik Fjord between 2011 and 2014, from which they estimated both above and below waterline iceberg volume. A general power law was then fitted between iceberg surface area (A) and estimated iceberg volume (V) (Sulak et al. 2017):

$$V = 6.0A^{1.3} \tag{6.1}$$

We assume that this relationship between iceberg surface area and volume holds true for other years in Sermilik Fjord, as we do not expect significant changes in calved ice properties or fjord water density. We recognize the uncertainty in the calculated power law constant and exponent, and we account for this in our estimation of iceberg freshwater flux uncertainty (see Section 6.3.4). In addition, as the unequal areas of

each fjord section could lead to false trends in surface area with distance down-fjord, we normalized each section's summed iceberg volume by dividing by the total area of the fjord section.

6.3.2 Estimating iceberg velocity

Iceberg velocity was estimated by visually tracking distinctly shaped icebergs throughout a collection of 16 Sentinel-2 images between early June and mid-September 2017. Six distinctly shaped icebergs were identified and hand-delineated from band 8 imagery. The straight-line distance moved by the centre of each iceberg between successive images was measured, and velocity was estimated by dividing this distance by the time between images (Figure 6.1c). As it is unlikely that icebergs move in a linear fashion, our estimates of both distance and velocity are considered minimums.

6.3.3 Estimating iceberg freshwater flux

Following Sutherland et al. (2014a), we assume that mean iceberg movement is down-fjord, and that icebergs lose volume with movement due to melting. Thus it is possible to estimate iceberg freshwater flux using the change in volume with time ($\frac{\delta V}{\delta t}$, $m^3\ s^{-1}$) and distance ($\frac{\delta V}{\delta x}$, $m^3\ m^{-1}$), and iceberg velocity (u):

$$FW_{flux} = \frac{\delta V}{\delta t} + u\frac{\delta V}{\delta x} \tag{6.2}$$

We also assume that there is a constant rate of change of iceberg volume with distance down-fjord. This allows us to set the first term on the right-hand side of Equation 6.2 to zero. Justification for this assumption is shown in Section 6.4.2. Our freshwater flux estimates are integrated 2-month meltwater fluxes for the two months prior to the date of each Sentinel-2 scene, as it takes icebergs approximately 2 months to travel the length of the fjord (as estimated using mean iceberg velocity). For example, the freshwater fluxes derived from the image acquired on 13 September are integrated fluxes from mid-July to mid-September, as ice near the mouth of the fjord on 13 September

would have been located near the head of the fjord in mid-July. Throughout this paper, freshwater fluxes are temporally identified by the satellite image acquisition month.

Our analysis excludes all areas of the fjord covered by ice mélange, limiting our analysis to areas 37 km or greater in distance down-fjord from the Helheim Glacier terminus. In addition, we exclude both embayments found on the western side of the fjord (Figure 6.1a), as icebergs can become stuck here, not following the down-fjord trend in movement assumed by our methodology.

6.3.4 Iceberg freshwater flux uncertainty

We trace potential uncertainty throughout our analysis using standard error propagation methods to estimate the effect of errors in both iceberg volume and velocity on our freshwater flux estimates. Uncertainty in iceberg volume can be derived from two main sources: the calculation of iceberg surface area from the thresholding of Sentinel-2 imagery and the conversion of these calculated surface areas to volume using the assumed relationship from Sulak et al. (2017). Uncertainty in iceberg surface area is mainly due to mixed pixels from automatically identifying icebergs via thresholding. Pixels along the perimeter of icebergs may be a mix of both water and ice, yet these are all classified as ice in our analysis. To estimate the extent of this potential overestimate, we calculated the surface area of a 1-pixel (i.e., 10 m) band along the inside of the perimeter of each large iceberg. We chose only to use large icebergs ($\geq 10^5$ m^2) for this uncertainty estimate, as they make up the bulk of the fjord-wide iceberg volume. On average, automatically thresholding icebergs can overestimate the surface area by ~12 to 18% of each iceberg, which we then applied to our fjord-wide surface areas. For the conversion of iceberg surface area to volume, we used the uncertainty cited by Sulak et al. (2017) for their power law equation (6.0 $\pm$ 2.59 and 1.3 $\pm$ 0.04 for a and b, respectively, in $V = 6.0A^{1.3}$).

We apply a conservative 50% uncertainty range to our iceberg velocity estimates, as it is unlikely that icebergs move in a linear fashion between two Sentinel-2 scenes. There is also uncertainty associated with using a linear regression to characterize iceberg volume change with distance from the glacier terminus. Using the mean change in

area-normalized iceberg volume with distance for all scenes to estimate freshwater fluxes results in standard error of ~1.2 m^3 m^{-2} per km down-fjord.

6.3.5 Estimating surface melt over Helheim, Fenris and Midgård Glaciers

In order to compare our iceberg freshwater fluxes with other fluxes in the fjord system, we estimate surface melt over the Helheim, Fenris and Midgård glacier catchments (Lewis 2009), which we assume all exits each glacier at its respective grounding line. We use a positive degree day (PDD) approach (Hock 2003), with degree day factors for snow and ice of 3 and 9 mm °C d^{-1}, respectively (Fausto et al. 2009, Box 2013, Enderlin & Hamilton 2014) and a threshold snow melt temperature of 0 °C. Daily air temperature data for 2017 were acquired from a Geological Survey of Denmark and Greenland PROMICE weather station located ~78 km SE of the Helheim Glacier terminus (Figure 6.1a; Ahlstrøm et al. 2008), and adjusted to glacier elevations using a Greenland-wide mean annual lapse rate of 6.8 °C km^{-1} (Fausto et al. 2009). Precipitation data were acquired from the Danish Meteorological Institute (DMI) weather station in Tasiliaq, approximately 90 km SE of the glacier terminus (Figure 6.1a; Cappelen, J. (ed.) 2018).

6.4 Results and discussion

6.4.1 Iceberg velocity

Velocities from our visually-tracked icebergs range from 0.0002 ± 0.0001 to 0.14 ± 0.07 m s^{-1}, with an average velocity of 0.018 ± 0.009 m s^{-1}, and show an overall down-fjord trend in movement (Figure 6.2; Table 6.2). Despite large uncertainty, these velocities are in good agreement with down-fjord velocities measured using GPS-trackers in Sermilik Fjord in summer 2017, which averaged 0.017 m s^{-1} (D. Sutherland, unpublished data). Similarly, we find that along-fjord velocities, particularly down-fjord velocities, are much higher than across-fjord velocities (Figure 6.2), and generally increase with distance down-fjord upon approach to the shelf break (as reported by Sutherland et al. 2014a). Due to the uncertainty surrounding our velocity

measurements, we only use the mean iceberg velocity, 0.018 m s^{-1}, to estimate freshwater fluxes.

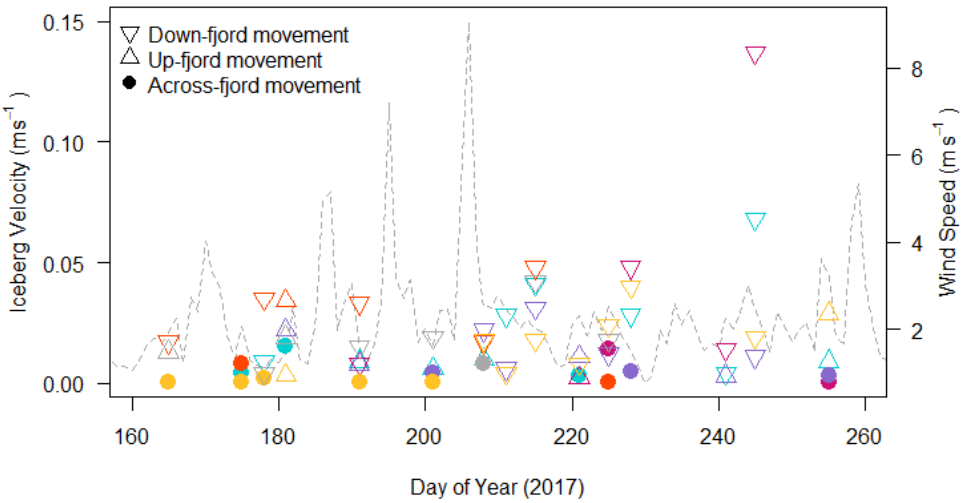

Figure 6.2: Visually-tracked iceberg velocities down-, up- and across-fjord for six icebergs, where each colour represents a different iceberg, and wind speed (dashed line) from PROMICE MIT weather station (see Figure 6.1a for location).

Table 6.2: Initial surface areas and minimum, maximum and mean velocities for visually-tracked icebergs.

Iceberg	Initial Surface Area (km^2)	u_{min} (m s^{-1})	u_{max} (m s^{-1})	$\overline{u}$ (m s^{-1})
1	0.58 ± 0.09	0.003	0.068	0.018 ± 0.009
2	0.43 ± 0.06	0.0004	0.14	0.022 ± 0.011
3	0.39 ± 0.06	0.0002	0.048	0.024 ± 0.012
4	0.39 ± 0.06	0.003	0.031	0.012 ± 0.006
5	0.57 ± 0.09	0.0004	0.040	0.012 ± 0.006
6	0.46 ± 0.07	0.004	0.042	0.017 ± 0.009

6.4.2 Iceberg volume distributions

Total iceberg volume estimated for our study area ranges from 2.1 km^3 in early November to 5.6 km^3 in late July (Table 6.1), covering approximately 3.2 and 8.7%

of the analyzed fjord surface, respectively. Although there is a greater abundance of smaller icebergs ($\leq 10^4$ m^3, 79 to 88% of all icebergs) in all months of our study period, larger icebergs ($\geq 10^5$ m^3) dominate the fjord's iceberg volume, on average making up 84% (Figure 6.3). This iceberg volume class distribution is similar to that seen in other Greenlandic fjord systems (e.g., Rink, Kangerlussuup, and Ilulissat), as well as previously observed in Helheim Fjord (e.g., Enderlin et al. 2016, Sulak et al. 2017). While variable through time, there is a strong and statistically significant (p-values from 1.0 x 10^{-10} to 0.002) observational decrease in area-normalized iceberg volume with distance down-fjord from the Helheim Glacier terminus throughout our study period (Figure 6.4).

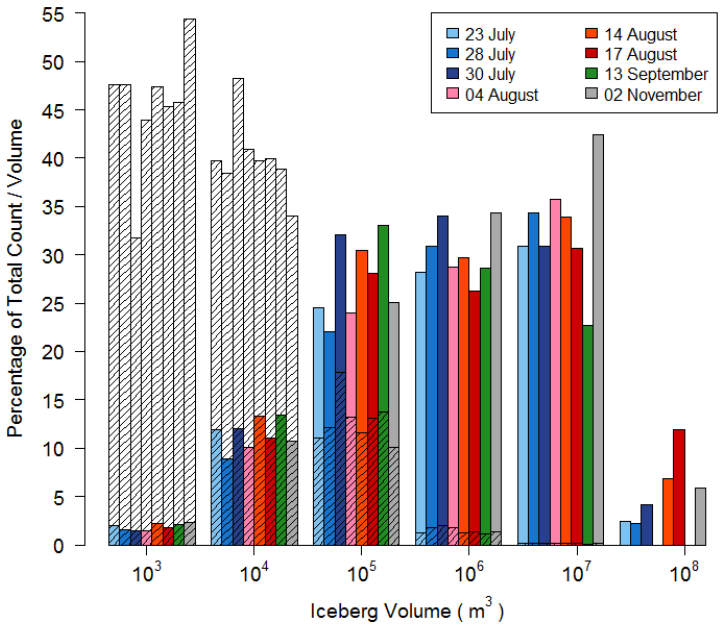

Figure 6.3: Percent of total count (hatched bars) and total volume (coloured bars) of all icebergs classified by volume for each Sentinel-2 image.

September has both the highest volume of icebergs near the head of the fjord as well as the lowest volume of icebergs towards the mouth of the fjord, with iceberg volume dropping rapidly by mid-fjord (kms 61-64; Figure 6.4d). This distribution could result from a combination of increased iceberg calving rates in the months prior (Sulak et al.

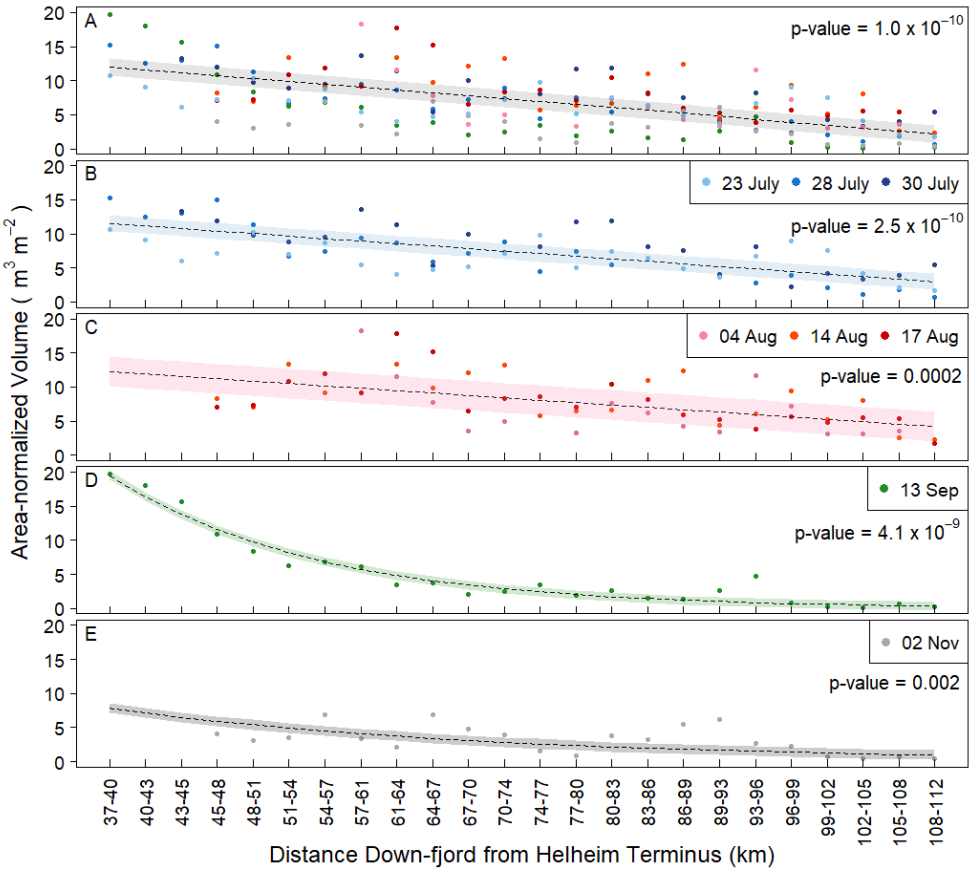

Figure 6.4: Area-normalized iceberg volume with distance down-fjord from the Helheim Glacier terminus for (a) all analysed Sentinel-2 scenes, (b) July scenes, (c) August scenes, (d) September scenes, and (e) November scenes. Dashed black lines are either linear (a-c) or log (d-e) regressions between area-normalized iceberg volume and distance down-fjord. P-values for regression significance are shown. Coloured shading indicates 1σ around regressions.

2017) and warmer fjord-water temperatures in September (Moon et al. 2017). Due to the presence of a thick ice mélange, there is a lag between when icebergs calve from the glacier terminus and when they enter the open-water part of the fjord (i.e., where we begin our measurements 37 km down-fjord from the terminus). This lag time varies from year to year in Sermilik Fjord, and has been previously estimated as between 16 and 39 days in September 2012 and over 120 days in August 2013 (Sutherland et al. 2014a). Based on average ice mélange speed in summer 2017 (estimated here from tracking

distinctive icebergs caught in the mélange), icebergs spend ~2 months travelling through the mélange before they reach the open fjord. As such, generally higher iceberg calving fluxes from late June to early August (Sulak et al. 2017) would not be reflected farther down-fjord until September, when we see higher iceberg volumes near the fjord head (Figure 6.4d). In addition, large, tabular calving events can accelerate the ice mélange and flush a considerable volume of ice into the open fjord (e.g., Amundson et al. 2010, Murray et al. 2013). For example, a large calving event (~5 km^2 in surface area) occurred between 31st July and 02 August 2017 (Figure 6.1d), which accelerated the ice mélange velocity from ~40 m d^{-1} to just over 4 km d^{-1} and pushed a large volume of ice closer to the open fjord. A similar event occurred between the 14th and 17th of August (~4 km^2 in surface area), releasing more ice into the mélange and subsequently, open fjord, where their volume is reflected in our September estimates.

Warmer waters in Sermilik Fjord in September could cause a rapid decrease in iceberg volume consistent with our observations. On average, reported fjord water temperatures at various locations along Sermilik Fjord in the summer are cool just below the surface (between approximately -1.5 and 0.5 °C), warming up to 4 °C at 450 m depth (Sutherland et al. 2014b, Moon et al. 2017). Average measurements taken in the autumn, from September to November, show both a warmer surface layer (between 0.5 and 1.5 °C, $<$ 100 m depth) and an extended warm layer between 100 to 250 m depth (Moon et al. 2017). In addition, water on the East Greenland Shelf (which eventually enters Sermilik Fjord) typically increases in temperature throughout the autumn (Straneo et al. 2010). Warmer waters at middle depths in the water column accelerate iceberg melting, as larger icebergs have their keel depths here (e.g., Barker et al. 2004, Enderlin & Hamilton 2014, Enderlin et al. 2016), while warmer surface waters accelerate the melting of smaller bergy bits and growlers. A combination of both warmer surface and mid-depth waters would thus reduce iceberg volume more rapidly moving down-fjord, as compared to months with cooler water temperatures. Lower calving fluxes in September and October (Sulak et al. 2017), in combination with warmer fjord waters, likely result in the iceberg volume distribution observed in November (i.e., low volumes both near the head and mouth of the fjord; Figure 6.4e).

We assume that iceberg volume has a constant rate of change with distance down-fjord during our study period. To test this assumption, we analysed the slopes of our linear and log regressions for each Sentinel-2 scene used in our analysis. If iceberg volume has a constant rate of change, the slopes of our regression lines should not be significantly different. As seen in Figure 6.5, our six regression slopes for the months of July and August (whether linear or log fits) all fall within approximately two standard deviations of each other, indicating our assumption is valid for these months. However, the slopes for September and November fall outside these standard deviation bounds, indicating a different distribution of iceberg volume in the fjord during those two months. It is likely that increased calving in the two months prior result in the large volume of ice we see at the head of the fjord in September, which promotes a more negative slope in our relationship between iceberg volume and distance down-fjord. Without additional September scenes for comparison, it is difficult to confirm if this spatial relationship is consistent throughout the month. As such, based on the relationship we have for one scene, freshwater fluxes near the head of the fjord for September may be skewed too high, and should be considered maximum fluxes. We also note that our methodology would likely not work in a fjord where icebergs tend to form flotillas and move down-fjord as large units, as previously seen in Rink Fjord (Sulak et al. 2017) and which would affect the relationship between volume and distance.

6.4.3 Freshwater flux from icebergs

Iceberg freshwater fluxes in Sermilik Fjord vary both seasonally and with distance down-fjord from the Helheim Glacier terminus (Figure 6.6). Freshwater flux from icebergs peaks across August and September, reaching approximately 3410 $\pm$ 1740 $m^3\ s^{-1}$ along the length of the fjord (Figure 6.6a). Iceberg freshwater flux is relatively constant throughout June, July, October and November, ranging between 1150 $\pm$ 590 and 1270 $\pm$ 650 $m^3\ s^{-1}$ (Figure 6.6a). As with iceberg volume distributions, temporal variations in freshwater flux likely reflect seasonal ocean temperatures and calving fluxes, with warmer waters from September to November enhancing iceberg melt and generating greater freshwater fluxes. Similar seasonal patterns have been seen in modelled iceberg melt rates and fluxes (e.g., Mugford & Dowdeswell 2010, Moon et al. 2017), which

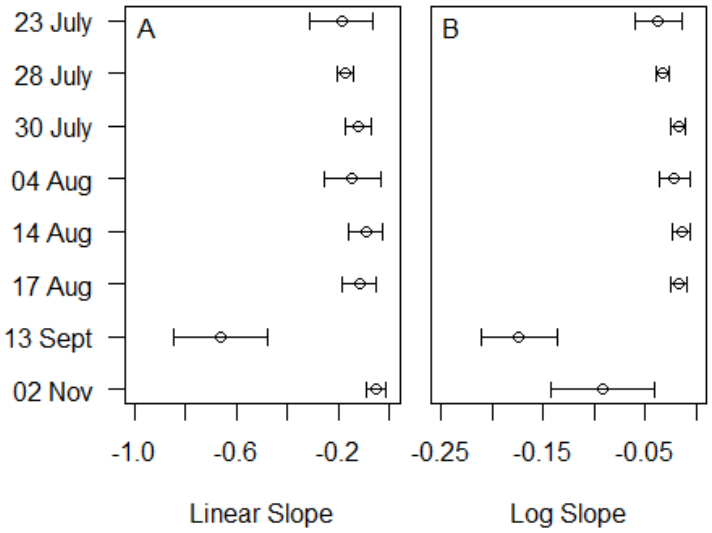

Figure 6.5: Slopes of (a) linear and (b) log regressions between area-normalized iceberg volume and distance down-fjord from the Helheim Glacier terminus. Bars indicate 2 standard deviations from the slopes.

show peak iceberg melt in early September, primarily due to warmer surface waters. In addition, our estimated iceberg freshwater fluxes peak later in the summer than our modelled subglacial discharge from Helheim, Fenris and Midgård Glaciers (Figure 6.6a), which peaks around 1400 m^3 s^{-1} on 26 July 2017.

Iceberg freshwater fluxes are highest near the head of the fjord (Figure 6.6b) where iceberg surface areas are largest, peaking at ~2800 ± 1430 m^3 s^{-1} between 37 and 64 km down-fjord of Helheim Glacier for the two months prior to our mid-September scene (Figure 6.6c). As icebergs with larger surface areas have deeper drafts, a higher percentage of ice near the head of the fjord will be exposed to the warmest (up to 5.2 °C) waters located at depth in the water column, promoting higher levels of submarine melting and increased freshwater flux. Icebergs with smaller drafts located down-fjord will sit in the cooler Polar Water layer, leading to comparatively smaller meltwater fluxes. The spatial pattern in our estimated iceberg freshwater fluxes is similar to that modelled by Moon et al. (2017), who showed a general decrease in freshwater flux with distance from the Helheim Glacier front, with a reduction of ~50% in the summer between 20 - 40 km and 80 - 100 km down-fjord. This is comparable to our July and

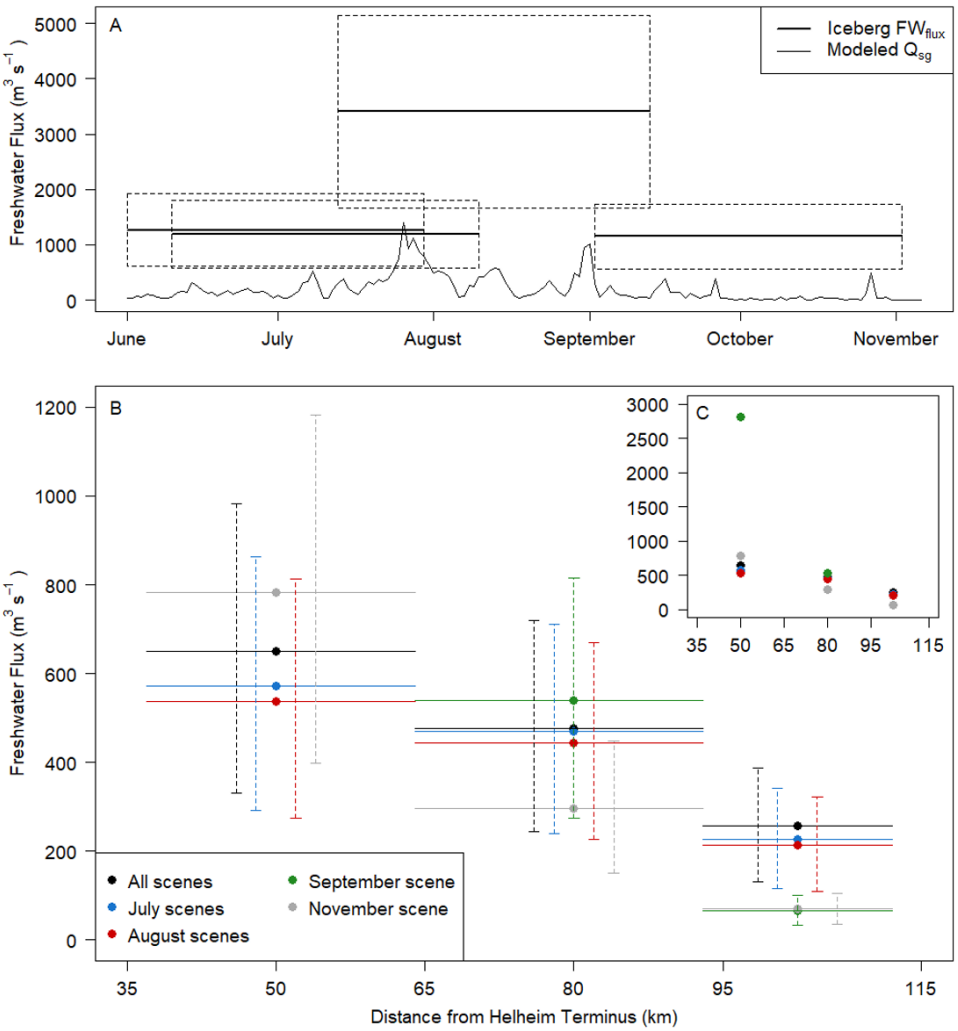

Figure 6.6: (a) Integrated 2-month iceberg freshwater fluxes for full length of Sermilik Fjord (bold lines spanning duration of flux, with dashed uncertainty boxes) and modelled subglacial discharge (Q_{sg}) from Helheim, Fenris and Midgård glaciers (thin line) through time; (b) integrated 2-month iceberg freshwater fluxes with distance from the glacier terminus, where dashed vertical lines represent uncertainty in flux estimates. Note that for clarity, the dashed uncertainty lines for each month are slightly separated from their respective points; (c) the same freshwater fluxes in (b), but now including iceberg freshwater flux from 37-64 km down-fjord for the September scene (~2800 m^3 s^{-1}) which was not shown in (b) to allow for easier visualization of the other scenes.

August freshwater flux estimates, which both decrease by ~60% between 37 - 64 km and 93 - 112 km down-fjord (Figure 6.6b).

Iceberg freshwater fluxes are also greatly influenced by water velocities both at the surface of the fjord and at depth, with fluxes increasing with velocity (Moon et al. 2017, Enderlin et al. 2018) in line with theoretical considerations of submarine melt (Jenkins 2011). For example, a four-fold increase in deep-drafted iceberg melt rate was observed previously in Ilulissat Icefjord between late March and early April 2011, likely driven by an increase in turbulent-driven melt rate at depth due to an increase in water velocity triggered by a large calving event (Enderlin et al. 2018). Water velocities in Sermilik Fjord have been observed to vary significantly over a range of timescales, driven in part by velocity pulses from the shelf outside the fjord mouth (Jackson et al. 2014) and likely in part by subglacially melt driven fjord circulation (Cowton et al. 2015). Past observations in Sermilik Fjord show water velocities ranging from 0 - 0.8 m s^{-1} (Jackson et al. 2014), fluctuating on timescales as short as three to ten days and showing a slight reduction in velocity in June and July (as compared to September through May). Water velocities of down-fjord currents are also expected to increase with increasing subglacial runoff into the fjord system (Cowton et al. 2015), which peaks in late July with a secondary peak in early September 2017 (Figure 6.6a). As such, high water velocities in the late summer and autumn could be contributing to our large freshwater fluxes estimated across August and September.

We also estimate a first order approximation of the percentage of ice leaving the fjord as solid flux. We take the difference in normalized ice volume between our first (12.0 m^3 m^{-2}) and last (2.3 m^3 m^{-2}) fjord sections, as averaged for all the Sentinel-2 scenes used in our study (Figure 6.4a), as an estimate of the percentage of solid ice lost to melting in the fjord. However, a significant amount of iceberg volume is likely lost in the mélange before the icebergs reach our first fjord section ~37 km down-fjord of the Helheim Glacier terminus. Previous studies in Greenland indicate that anywhere from 10 to 49% of ice volume is lost to the melting of icebergs in the ice mélange (e.g., Enderlin et al. 2016). We therefore increase the normalized ice volume in our first fjord section by 30% to estimate the initial volume of ice originally calved from

Helheim Glacier, giving a value of 15.6 m^3 m^{-2}. We assume that the vast majority of icebergs, particularly the large full-thickness icebergs that account for most of the fjord iceberg volume, originate from Helheim Glacier, as a record of calving fluxes spanning nearly a decade shows that the calving fluxes from both Midgård and Fenris glaciers, located in the far northeast (Figure 6.1a) of Sermilik Fjord, are $\leq$ 10% of the flux estimated for Helheim (Moon et al. 2017). For the months of July, August, September and November, we estimate that on average only 14% of the calved input leaves the fjord as solid flux, indicating that the majority of the calved flux melts within the fjord thus delivering a significant amount of freshwater at depth to the fjord during the summer and autumn. Our results therefore support the previous conclusions on the critical importance of iceberg freshwater flux to the fjord budget (e.g., Enderlin et al. 2016, Moon et al. 2017).

The simple and easily transferable method for deriving iceberg freshwater fluxes in glacial fjords presented here confirms that iceberg melt contributes a significant volume of freshwater to the fjord, and that this freshwater enters the water column at depth along the full length of the fjord. The volume of freshwater generated by the melting of icebergs in Sermilik Fjord is comparable to the volume of subglacial discharge entering the fjord throughout the melt season and exceeds the subglacial discharge during spring, autumn and winter. These findings support the previous work of Enderlin et al. (2016, 2018) and Moon et al. (2017) in Sermilik Fjord, and demonstrate the importance of iceberg melt for fjord circulation, submarine melt rate (e.g., Enderlin et al. 2016) and primary productivity (e.g., Rose 2005, Smith Jr. et al. 2013) within fjord systems. In addition, these findings provide an independent estimate of iceberg melt, which could be used in future studies to differentiate between iceberg and terminus subglacial melt, a partitioning that is difficult to model or directly measure in glacial fjords.

6.5 Conclusions

We present a new methodology for estimating iceberg freshwater fluxes along glacial fjords, using freely available Sentinel-2 satellite imagery to estimate iceberg velocity and changes in iceberg volume with both distance and time during the summer and

autumn of 2017. We estimate iceberg velocities up to 0.14 m s^{-1}, and find that in all months of our study iceberg volume decreases with distance from the head of the fjord (i.e., moving down-fjord away from the Helheim Glacier terminus). We estimate an integrated 2-month total freshwater flux of ~1270 ± 650, 1200 ± 610, 3410 ± 1740, and 1150 ± 590 m^3 s^{-1} for June-July, July-August, August-September and September-October, respectively. Iceberg freshwater fluxes peak across August and September, likely reflecting warmer ocean temperatures and higher calving rates, and decrease with distance from the glacier terminus. We find that on average 14% of the ice calved into the fjord exits as solid flux, demonstrating that a significant volume of freshwater is released at depth along the length of the fjord. The volume of freshwater generated from iceberg melt is comparable to or greater than subglacial discharge volume throughout the year, and has important implications for fjord-scale circulation, submarine melt rates, nutrient availability and primary productivity. Our method provides a valuable tool for monitoring iceberg freshwater fluxes, and is a valid alternative to more complex methods for estimating flux from inaccessible fjords with no or limited field observations. We anticipate that our method and resulting fluxes could be used for constraining both fjord-scale and ice sheet wide ice-ocean models, which are critical for understanding future changes to the Greenland Ice Sheet and surrounding ocean basins.

Chapter 7

Conclusions

The overall aim of this thesis has been to improve our understanding of ice-ocean interactions at tidewater glaciers, with a particular focus on submarine melting of ice fronts and freshwater fluxes into glacial fjords. This work has broadly been motivated by the response of the Greenland Ice Sheet to recent climatic change (and notably to increased air and ocean temperatures), as demonstrated by the widespread thinning, acceleration and retreat of tidewater glaciers around the ice sheet margins in the 2000s (Pritchard et al. 2009, Carr et al. 2013, Murray et al. 2015). Despite the connection between increased ocean and air temperatures and glacier change (e.g., Seale et al. 2011, Walsh et al. 2012, Cowton et al. 2018), our understanding of the processes driving change is limited. This reflects in part the complexity of the processes themselves, but also the complexity and expense of the methods currently used to understand ice-ocean processes like submarine melting. Deriving estimates of submarine melt rates and freshwater fluxes, and developing constraints on these processes, is crucial for improving the accuracy of fjord and ice sheet scale models used to predict the behaviour of the Greenland Ice Sheet to future climatic change.

The first section of this chapter summarises the main findings of the thesis as previously reported in Chapters 4-6. The chapter then brings these findings together and discusses their wider implications. The limitations of the thesis are discussed, and the chapter

ends with a consideration of recommendations for the future direction of ice-ocean research and concluding remarks.

7.1 Summary of findings

The first results section of the thesis (Chapter 4) developed a new approach for estimating submarine melt rates beneath floating ice tongues in glacial fjords, using the ice tongue from Kangiata Nunaata Sermia (KNS) in southwest Greenland as a proof-of-concept study site. High-resolution digitial elevation models over the ice tongue were created through the interferometric processing of TanDEM-X satellite radar imagery and maps of ice tongue flow velocity were created by tracking crevasses in the ice surface from TerraSAR-X imagery. Submarine melt rates beneath the ice tongue were estimated for March and May 2013 using observational changes in the derived ice freeboard and flow speed.

Estimated submarine melt rates beneath the ice tongue reach 1.4 ± 0.5 m d^{-1} and are spatially-averaged to 0.8 ± 0.3 and 0.7 ± 0.3 m d^{-1} beneath the eastern and western sides of the ice tongue, respectively. Melt rates were found to decrease significantly with distance down-fjord from the KNS grounding line, approaching 0 m d^{-1} approximately 2.5 km down-fjord near the end of the ice tongue. This result is supported by the presence of thick sea ice down-fjord, which suggests a very cold surface water layer allowing for little or no submarine melting. Submarine melt rates also vary across the glacier terminus, likely driven in part by variations in the ice tongue draft and the temperature stratification in the fjord, whereby deeper drafted ice sits in the warmer fjord water found at depth in the water column; thus melt rates are higher here when compared to parts of the ice tongue with shallow drafts, which sit in relatively cooler water. In addition, the meltwater flux from basal frictional melting beneath the near-terminus (up to 11 km from the ice front) grounded portion of the glacier was found to be of a sufficient magnitude to produce subglacial plumes large enough to generate ice front submarine melt rates of up to 4 m d^{-1} (Slater et al. 2015). As such, the presence of basally-derived meltwater plumes exiting at depth in the winter and spring may also drive some of the across-fjord variability observed in submarine melt rate. These results

demonstrate the significant potential of the new methodology for analysing in detail spatial and temporal variations in submarine melt rate at tidewater glacier termini, and provide insight into some of the key drivers of variability in these melt rates.

In Chapter 5, the same methodology was used to derive submarine melt rates beneath the KNS ice tongue for an additional two other years (2012 and 2014) in order to expand the temporal focus of the study. This work was supplemented by summer time lapse camera imagery close to the glacier terminus (courtesy of Martin Truffer and Mark Fahnestock at the University of Alaska Fairbanks), which was qualitatively analysed for the fjord surface expression of subglacial discharge plumes, and for the frequency of calving events occurring along the length of the terminus. A hydropotential analysis was also performed to derive the potential subglacial flow routing beneath the grounded portion of the glacier catchment, allowing for the prediction of subglacial discharge plume locations along the ice front.

Submarine melt rates beneath the KNS ice tongue were found to vary spatially through time, with a maximum melt rate of 7.3 $\pm$ 2.3 m d^{-1} estimated beneath the western side of the ice tongue in May 2012. In May and June 2014, the higher melt rates were located beneath the eastern side of the ice tongue. This change in the spatial pattern of melt is in part attributed to variations in the location of the dominant subglacial flow channel predicted beneath KNS, which can shift between the eastern and western side of the ice front as driven by small changes in subglacial water pressure. A dominant subglacial channel will produce a subglacial discharge plume with high velocity and volume, attributes that increase submarine melting as the plume rises buoyantly along the ice front (and underside of the ice tongue), as is seen beneath the western side of the ice tongue in 2012. Submarine melt rates also decrease with distance from the KNS grounding line across all years considered, attributed again to variations in fjord water temperature stratification and decreasing ice tongue draft with distance down-fjord. Analysis of the time lapse imagery found that the majority of the calving events observed during the 2012 melt season (i.e., May to October) occurred along the western part of the ice front, where subglacial discharge plumes are predominantly observed reaching the fjord surface, and where estimated spring ice tongue submarine

melt rates are highest. These results suggest a highly dynamic hydrological channel network beneath KNS, and provide a new empirically-derived link between the presence of subglacial discharge plumes and areas of high submarine melting and calving along tidewater glacier termini.

The final results chapter develops another new methodology to derive freshwater fluxes from the melting of icebergs in glacial fjords, using Sermilik Fjord in southeast Greenland as a proof-of-concept study site. The work was motivated by the current dearth of iceberg freshwater flux estimates from Greenlandic fjords, despite their importance to fjord circulation and heat budget (and thus tidewater glacier dynamics), nutrient cycling and fjord productivity. The method developed here is simple in comparison to the methods currently used for deriving freshwater flux, namely user-intensive remote sensing techniques and complex models depending on, at best, sparse field data (e.g., Enderlin & Hamilton 2014, Enderlin et al. 2016, Mugford & Dowdeswell 2010, Moon et al. 2017). In this results chapter, freely available Sentinel-2 satellite imagery was used to derive iceberg velocity and changes in iceberg volume with distance from their source (here, Helheim Glacier), from which seasonal variations in freshwater flux were estimated.

The estimated iceberg freshwater fluxes in Sermilik Fjord vary seasonally in 2017, peaking across August and September to deliver $\sim 3410 \pm 1740$ m^3 d^{-1} of cold freshwater along the length of the fjord over the course of two months. This peak in iceberg freshwater flux occurs later in the year than the peak in freshwater delivered by surface melt-fed subglacial discharge, which occurs in late July. In addition, the total volume of freshwater delivered to the fjord via the melting of icebergs is comparable to or greater than the subglacial discharge volume delivered throughout the rest of the year. The observed seasonal signal in iceberg freshwater flux is primarily driven by increases in fjord water temperature as autumn approaches, but also results from increased calving from Helheim Glacier in the months prior (Sulak et al. 2017). It was also estimated that on average 14% of the ice calved into Sermilik Fjord exits as solid flux; thus a significant volume of the calving flux is released as freshwater from iceberg melting at depth during transit along the length of the fjord. These results support previous work on iceberg

freshwater fluxes in Sermilik Fjord (Enderlin & Hamilton 2014, Enderlin et al. 2016, Moon et al. 2017), confirming the importance of icebergs to processes occurring in and proximal to glacial fjords, including local circulation, wider-ocean circulation, fjord heat budget, nutrient availability and fjord primary productivity. This new, simple and easily transferable methodology for deriving iceberg meltwater fluxes in glacial fjords provides an invaluable tool for monitoring freshwater inputs from icebergs across a range of Greenlandic fjords. It is anticipated that future results derived from this method can be used by the scientific community to constrain the ice sheet and ocean-circulation models that are crucial for understanding future changes to the Greenland Ice Sheet and surrounding ocean basins.

7.2 Implications of findings

The findings presented in this thesis build upon previous research focused on ice-ocean interactions and submarine melting in both Kangersuneq and Sermilik Fjords, as well as at other tidewater glacier systems around Greenland. A number of methodologies already exist for estimating submarine melt rates of both tidewater glacier ice fronts and icebergs, which have been discussed in detail (along with their limitations) in Chapter 2. The methodologies developed here provide simpler alternatives for estimating the outcome of a suite of complex processes, a solution necessary for the widespread estimation and monitoring of ice-ocean processes in glacial fjords.

The submarine melt rates and meltwater fluxes estimated here are of the same order of magnitude as other estimates of melt rate (e.g., Motyka et al. 2003, Jenkins 2011, Christoffersen et al. 2012, Inall et al. 2014, Enderlin & Hamilton 2014, Motyka et al. 2017) and freshwater fluxes (e.g., Enderlin et al. 2016, Sulak et al. 2017, Moon et al. 2017) from tidewater glaciers and icebergs in various fjords in Greenland and Alaska. The magnitude of the estimated winter and spring submarine melt rates (maximum of ~7 m d^{-1}) beneath the seasonal ice tongue adjacent to KNS demonstrates the potential importance of winter melting of tidewater glacier ice fronts, likely driven in part by subglacial meltwater emerging at the grounding line and sourced from basal frictional melting (Christoffersen et al. 2012) when there is no surface melt contributing

to subglacial discharge. Submarine melt rates of the ice front are expected to increase later in the melt season, when the influence of subglacial discharge plumes, sourced primarily from surface meltwater, is heightened. As the methodology presented here relies on the presence of an ice tongue or thick ice mélange in the fjord, a limitation discussed further in Section 7.3, summer melt rates have not been estimated. However, an approximate increase in submarine melt volume can be projected using one of the scalings developed between melt volume and subglacial discharge via ocean circulation models based on plume theory (e.g., Jenkins 2011, Xu et al. 2012, 2013, Sciascia et al. 2013, Cowton et al. 2015, Slater et al. 2016). These studies proposed power law relationships whereby submarine melting scales with subglacial discharge to a power ranging from $\frac{1}{3}$ to $\frac{3}{4}$, dependent on several fjord properties including fjord stratification, the height of the ice front and the distribution of emerging subglacial meltwaters and their associated plumes along the ice front. Slater et al. (2016) suggests that an increase in fjord water temperature by 1 ^{o}C, a temperature difference observed in glacial fjords between winter and summer (Mortensen et al. 2013), combined with a 25% increase in subglacial dicharge, results in an increase in submarine melting by up to ~50%. The increase in submarine melting is expected to be even higher transitioning into the melt season at KNS, as subglacial discharge is on average doubled between late-May and mid-July (see Figure 5.4e). It is, however, important to note that the associated decrease in plume temperature (i.e., thermal forcing) with increased subglacial discharge may outweigh the associated increase in plume velocity (which would normally increase submarine melting), resulting in decreased localised melting surrounding the plume near the glacier grounding line (Slater et al. 2016).

As predicted for tidewater glacier ice fronts, using theory-based ocean models incorporating plumes (e.g., Kimura et al. 2014, Cowton et al. 2015, Slater et al. 2015, Carroll et al. 2016), the spatial pattern of estimated submarine melting beneath the KNS ice tongue is in part controlled by the subglacial hydrological channel network. Locations of high submarine melt rates beneath the spring ice tongue coincide with the locations along the ice front of emerging subglacial channels, as predicted by hydropotential flow routing and visually confirmed using time lapse camera imagery of the fjord surface. It

should be noted that the submarine melt rates provided in this thesis are derived for the sloping winter ice tongue in front of KNS, and not the actual 'summer' glacier ice front itself, whatever that geometry may be; for example, near-vertical, gently sloping or undercut. Nevertheless, it is argued that the ice tongue melt rates act as a proxy to ice front submarine melting, at least regarding the spatial pattern of melt, and they provide valuable information about the hydrological system leading into the mélange and thus affecting the glacier ice front itself. In addition, the fact that the melt rates estimated here are of similar magnitude to those estimated elsewhere in Greenland for tidewater ice fronts (on the order of 1 to 10 m d^{-1}) increases the confidence in the magnitude of the derived melt rates and in the validity of the method.

The spatial patterns revealed in the observed submarine melt rates can help to improve our understanding of tidewater glacier terminus behaviour. Numerous studies have suggested that changes in glacier dynamics are driven by both oceanic and atmospheric warming, resulting in ice acceleration and augmented mass loss through increased calving (e.g., Howat et al. 2007, Holland et al. 2008, Nick et al. 2009). Fried et al. (2015) used direct multibeam sonar measurements of the Kangerlussuup Sermia ice front in central West Greenland to demonstrate that distributed submarine melting severely undercuts the terminus, an observation also predicted recently by models (Carroll et al. 2016, Slater et al. 2017b). When intersected with surface crevasses, undercutting can promote increased calving and the formation of embayments along the ice front, often located above larger subglacial outlet channels (O'Leary & Christoffersen 2013, Chauché et al. 2014, Fried et al. 2015). The pattern of submarine melt rate estimated for the KNS ice tongue supports this previous observation, as areas of high melting, connected with subglacial discharge plume outlet locations along the grounding line, coincide with the location of a calving embayment observed on the western side of the ice front in 2012 (see Figure S2.6). The spatial patterns and magnitudes of estimated submarine melting could also be compared with observed terminus retreat over longer timescales, which would provide additional information about the coupling between oceanic warming and tidewater glacier behaviour.

Tidewater glacier retreat is expected when ice front submarine melting outpaces

glacier ice velocity near the grounding line. However, submarine melt rates less than the glacier ice velocity can still impact the ice front position in a number of ways, including through the aforementioned promotion of calving via terminus undercutting and through increased stress potentially leading to the removal of ice front promontories (e.g., Benn et al. 2007, O'Leary & Christoffersen 2013, Todd & Christoffersen 2014, Carroll et al. 2016). As many fast flowing tidewater glaciers are retreating faster than any estimates of submarine melt rate, it is likely that submarine melting acts as a catalyst to calving and retreat, rather than causing direct changes in terminus position.

The distribution and magnitude of freshwater flux from the melting of icebergs in glacial fjords (as derived in Chapter 6) has several important implications for fjord characteristics, including circulation, heat budget, light and nutrient availability and primary productivity. The input of freshwater in the fjord system at various depths and locations along the length of the fjord alters both the temperature and salinity stratification of the water column (Cape et al. 2019), with increased freshwater input tending to enhance stratification and thus stabilize the upper water column (Smith Jr. et al. 2013). The introduction of cold meltwater to the fjord from the melting of icebergs alters the heat content of the waters reaching the head of the fjord (e.g., Enderlin et al. 2016), cooling the water before it reaches the glacier terminus and reducing submarine melting of the ice front. This in turn influences overall tidewater glacier behaviour, as the submarine melting of ice fronts has been suggested as a driver of glacier acceleration, thinning and retreat (e.g., Nick et al. 2009, O'Leary & Christoffersen 2013, Luckman et al. 2015). Despite this potential reduction in heat reaching their termini, tidewater glaciers are still retreating all around the ice sheet; this suggests that the reduction in heat must not be significantly limiting submarine melting of ice fronts, at least not enough to dominate ice front position change.

The local upwelling driven by iceberg movement and melting in glacial fjords augments the local nutrient supply and can create hotspots of productivity surrounding large free-drifting icebergs (Smith Jr. et al. 2013, Meire et al. 2017). In Sermilik Fjord, the upwelling of warm Atlantic Water found at depth along the fjord, driven primarily by the input of subglacial discharge at depth, transports substantial amounts of nitrate,

phosphate and silicate to the upper water column (Cape et al. 2019). These nutrients are particularly important during the summer, when phytoplankton productivity in the region is nitrate and phosphate limited (Meire et al. 2016). While there is uncertainty surrounding the role of icebergs in driving this upwelling (Moon et al. 2017, Cape et al. 2019), it is likely that deep-keeled icebergs reaching into the lower layers of the water column would be able to drive an upwelling of these nutrients, particularly through the buoyant rising of meltwater plumes along the submerged sides of the iceberg (e.g., FitzMaurice et al. 2017). Productivity can also be limited by the presence of icebergs in glacial fjords, as dense patches of icebergs decrease the light penetration necessary for new productivity (Meire et al. 2017).

The monitoring of iceberg distributions and the influx of freshwater to the fjord from their melting is thus of great significance, and the methodology developed in this thesis for deriving these variables should be applied to other fjord systems around Greenland to improve our understanding of the solid-to-liquid transition of ice, and the impacts that transition has on fjord circulation, heat budget, nutrient cycling and primary productivity. This is particularly important for economic reasons in Greenland, where local fisherman rely on productive fjords for their livelihoods (Christensen 2016).

7.3 Limitations

There are a number of limitations associated with the methods presented in the thesis, including some of the assumptions on which the methodologies are based and the applicability of these methods to other glacial fjords. The method developed for estimating submarine melt rates beneath floating ice tongues in Chapter 4 relies on an assumption of steady state ice tongue geometry, meaning that the thickness at any one point of the ice tongue is relatively constant through time. As most glaciers around the Greenland Ice Sheet have experienced thickness changes, typically thinning, over the past decades (e.g., Pritchard et al. 2009), it is unlikely that many are in a steady state geometry. For the case of the ice tongue at KNS, which was slowly thickening between March and May 2013, steady state and non-steady state estimated submarine melt rates were the same order of magnitude and displayed the same spatial pattern.

As such, it is argued that submarine melt rates can be reasonably approximated under the assumption of an ice tongue in steady state. While this is the case for the ice tongue adjacent to KNS, it is unclear whether the same applies for other tidewater glaciers, particularly those that are thinning or thickening at a more rapid rate.

The method adopted in Chapters 4 and 5 also relies on the presence of a floating glacier ice tongue in the fjord system, which is not always the case depending on glacier-fjord specific properties, including fjord and glacier geometry, sea ice and ice mélange presence, and fjord water temperature, velocity and circulation pattern. In fjord systems where no distinct glacier tongue forms, this method could still be used where there is a thick ice mélange abutting the glacier terminus, from which changes in freeboard and velocity could still be derived. Radar data have already been used to derive high resolution maps of ice mélange velocity in Greenlandic fjords (e.g., Foga et al. 2014, Burton et al. 2018), and ice mélange surface elevation can be derived using optical or radar satellite imagery, or could be collected at very high temporal and spatial resolutions using unmanned aerial vehicles (e.g., Bash et al. 2018, Chudley et al. 2019). Furthermore, the method has potential in fjord systems where the glacier itself reaches hydrostatic equilibrium and begins to float. For example, this method could be used to estimate submarine melt rates beneath Petermann Glacier in northern Greenland, which has a floating tongue that persists throughout the year. In addition, the method could be applied to large floating ice shelves in line with similar research undertaken in Antarctica (e.g., Berger et al. 2016, Gourmelen et al. 2017).

One of the main assumptions behind the methodology presented in Chapter 6 to derive iceberg freshwater fluxes from satellite imagery is a constant rate of change in iceberg volume with distance down-fjord from the glacier terminus. This assumption holds true for the majority of months analysed for Sermilik Fjord, with the exception of September and November. Different iceberg volume distributions during these months are likely due to increased calving from Helheim Glacier in the months prior to September and due to less ice overall in the fjord in November. Data from these months were still used for estimating freshwater fluxes in the fjord, noting that the freshwater fluxes might be overestimated for September, as the regression slope used for deriving freshwater flux

is steeper due to increased iceberg volume near the head of the fjord. However, the method is unlikely to work in fjord systems that display a more irregular distribution of iceberg volume; for example, when large volumes of icebergs move down-fjord as flotillas or get stuck temporarily on submarine sills and cause peaks in volume near the middle or mouth of the fjord. In addition, this methodology excludes freshwater flux from the icebergs in the ice mélange, which contribute a significant amount of freshwater flux into the fjord system (e.g., Enderlin et al. 2016). The omission of the ice mélange is discussed below as a future research direction.

7.4 Future research directions

Despite recent advances in the field, and as discussed throughout the thesis, there are a number of significant challenges to overcome in order to gain a fully comprehensive understanding of ice-ocean interactions at tidewater glaciers. One of the key priorities going forward should be better estimates and constraints on submarine melt rates of tidewater glacier termini, ice mélange and icebergs. This priority was identified as one of the main research gaps by members of the ice-ocean research community in attendance at the GReenland Ice Sheet-Ocean interactions (GRISO) Network Greenland Freshwater Fluxes Workshop in December 2018 (https://griso-network.org/events/2018-pre-agu-workshop/). The methods discussed for estimating submarine melt rates, including heat flux changes from hydrographic profiles, plume-based ocean circulation models, and iceberg freeboard differencing, could all be improved to provide better estimates of melt rate. For example, submarine melt rate estimates from fjord hydrographic profiles could be improved by measuring fjord water properties more densely and closer to the glacier terminus, and ideally for much longer time periods. Autonomous underwater vehicles could be used to sample properties beneath floating ice tongues and ice shelves (e.g., Dowdeswell et al. 2008), and multibeam sonar systems can be used to obtain direct observations of submarine terminus faces (e.g., Kimball et al. 2014, Fried et al. 2015). Unmanned aerial vehicles could be used to obtain very high spatial and temporal resolution floating ice tongue or ice mélange elevation data, a technique currently used over grounded ice (e.g., Ryan et al. 2015, Gindraux et al. 2017, Bash et al. 2018,

Chudley et al. 2019); submarine melt rates beneath the floating ice could then be estimated following the methodologies developed here. These field-based improvements would however be logistically complex and very expensive to install and maintain over time.

Plume-based ocean circulation models have made great advances in our conceptual understanding of submarine melt processes and patterns along tidewater glacier termini. Estimates of melt rate magnitude, however, remain uncertain due to the largely unknown turbulent transfer coefficients used in these models, which were developed based on heat transfers beneath ice shelves and sea ice (Holland & Jenkins 1999). Ideally, these coefficients would be tuned to match observed submarine melt rates; however, as direct observations of melt rates are rare, little progress has been made on constraining these coefficients. Using improved estimates of observed melt rates (from improved fjord hydrographic measurements, direct observations of changes to termini faces, or from the new methodology presented here) to tune turbulent transfer coefficients would substantially increase the confidence given to modelled submarine melt rates. In addition, the melting of ice mélange has largely been overlooked in most of these models, and could be included in the future to better examine the importance of the ice mélange (and its melting) to fjord circulation and hydrography, as well as to tidewater glacier calving mechanisms (e.g., Todd & Christoffersen 2014).

Remote sensing techniques for estimating iceberg submarine melt rates and fluxes could be improved by using machine learning to fully automate iceberg identification, thereby speeding up the process and reducing user bias during iceberg delineation. This would be particularly useful for identifying icebergs in the ice mélange close to glacier termini, which are currently either hand-delineated by the user or identified using edge detection software (e.g., Sulak et al. 2017), the latter being a somewhat arbitrary, trial-and-error process. Full automation of these techniques would allow for more numerous estimates of submarine melt rate and freshwater flux from icebergs over larger spatial areas and longer timescales, therefore enabling more detailed monitoring of icebergs and an improved understanding of the associated implications for fjord processes.

Both of the methodologies developed as part of this thesis should be applied more widely to other fjord systems around Greenland to continue to improve our understanding of the coupling between oceanic changes and ice dynamics. These methods can be applied very easily and therefore could be used to generate estimates of these important and poorly known processes across a range of ice-ocean margins. If applied along a north-south transect using key glaciers, it would be possible to derive a transect of margin wide submarine melt rate estimates that could be used by ice sheet and ocean modellers. For example, estimated submarine melt rates of floating ice tongues and ice mélange could be compared between northern and southern tidewater glaciers on the east coast of Greenland. Current knowledge would support that the more northern glaciers sit in colder water (Figure 2.2b) and experience colder air temperatures (Seale et al. 2011, Walsh et al. 2012, Cowton et al. 2018), which leads to decreased ice surface melting and runoff. This decrease in surface runoff, as delivered to the glacier bed via crevasses, would decrease subglacial discharge plume velocity and volume, leading to reduced submarine melting. The same expectation applies to derived iceberg freshwater fluxes, and the method could easily be applied in a fjord farther north than Sermilik, for example in the Scoresby Sund fjord system in east Greenland, where Daugaard Jensen, Charcot and Graah Glaciers terminate, and where lower freshwater fluxes are anticipated due to colder air and ocean temperatures.

Another key priority for future research is to improve our understanding of the solid-to-liquid transition of icebergs in glacial fjords, which has important implications for fjord and wider ocean circulation (e.g., Sutherland et al. 2014a), fjord heat budget and thus glacial dynamics (e.g., Mortensen et al. 2011, Enderlin et al. 2016, Jackson & Straneo 2016), and primary productivity (Smith Jr. et al. 2013, Meire et al. 2017). To better understand this transition, variations in iceberg size and distribution need to be analysed over longer timescales and in more glacial fjords, resulting in better estimates of iceberg residence times around the ice sheet. An improvement and full automation in the remote sensing techniques used for identifying and analysing icebergs over large spatial areas will certainly help achieve this much needed research. In addition, connections need to be made between these iceberg distributions and residence

times and the potential factors controlling them, including air temperature, fjord water temperature and velocity, fjord bathymetry and glacier calving dynamics. Improving our estimates and the understanding of the connections between these properties is critical for a better understanding of current and future ice sheet wide behaviour (Carr et al. 2013, Straneo & Cenedese 2015, Truffer & Motyka 2016).

7.5 Concluding remarks

The research presented in this thesis has contributed to our understanding of ice-ocean interactions at tidewater glaciers and in fjord systems around Greenland. It has developed two novel methodologies for estimating submarine melt rate beneath floating ice tongues and for deriving freshwater fluxes from the melting of icebergs in glacial fjords. Both of these methodologies have provided simple, easily transferable techniques for estimating glacier and iceberg properties that have to date proven both difficult and expensive to measure directly or model. The application of these methodologies throughout the thesis has shed light on some of the key controls on submarine melting, including fjord water temperature stratification, floating ice draft, and subglacial discharge plume location and velocity. An empirical link between submarine melting and subglacial discharge was demonstrated, a connection that has been modelled previously but only observed in a limited number of locations. Finally, estimations of iceberg freshwater fluxes demonstrate the importance of iceberg meltwater volume, location and timing to the fjord system, a result that supports previous analyses in Sermilik Fjord (Enderlin et al. 2016, Sulak et al. 2017, Moon et al. 2017).

Two of the remaining key challenges for improving our understanding of ice-ocean interactions along the margins of the ice sheet include improved and widespread estimates of submarine melt rates of both tidewater glacier ice fronts and icebergs, and a better understanding of the solid-to-liquid transition of ice in glacial fjords. Answering both of these challenges relies on more detailed in-fjord observations and improved methodologies. The methodologies presented in this thesis provide a simple, inexpensive and reliable way forward for obtaining improved ice sheet wide estimates of submarine melting and the consequent release of freshwater into fjord systems, estimates that are

likely to be critical for more accurate predictions in the behaviour of the Greenland Ice Sheet in response to future climatic change.

Chapter S1

Supporting information for 'Estimating Spring Terminus Submarine Melt Rates at a Greenlandic Tidewater Glacier Using Satellite Imagery'

This chapter contains the supporting figures cited in Chapter 4.

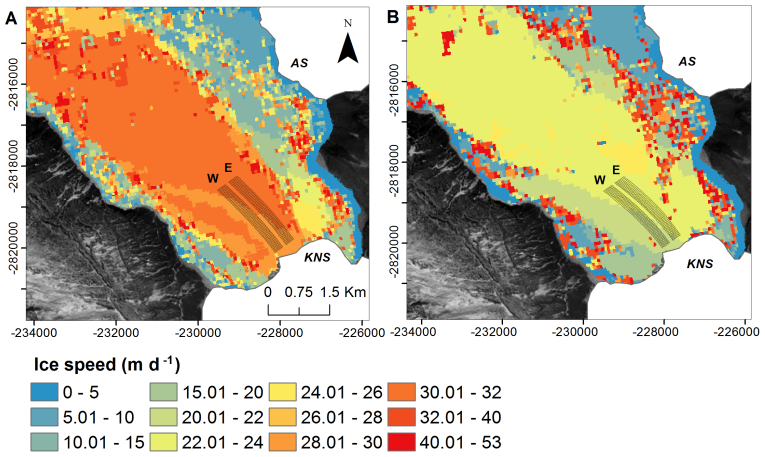

Figure S1.1: Ice speed derived from feature-tracking of TerraSAR-X imagery in Kangersuneq Fjord from (a) average velocities between 12 February and 19 April and (b) 30 April to 11 May 2013. Location of the flowlines (E = eastern, W = western) on the floating ice tongue are also shown.

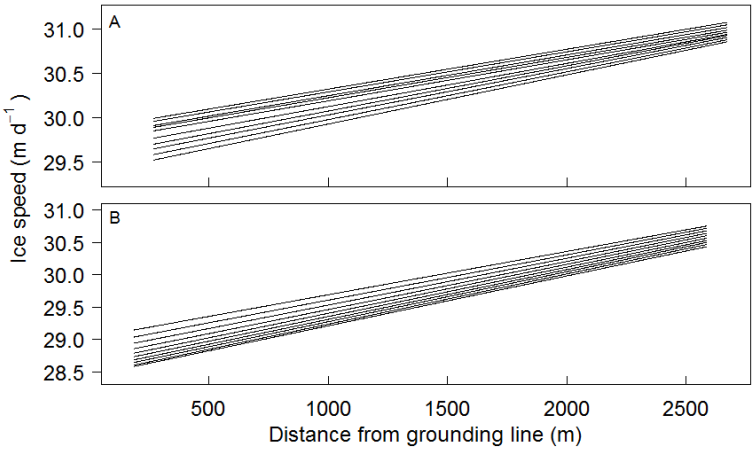

Figure S1.2: Sample plots showing smoothed ice speed (m d^{-1}) with distance from the inferred KNS grounding line, as averaged from velocities between 12 February and 19 April for the (a) eastern and (b) western flowlines. Note limit of y-axes is approximately 2 m d^{-1}.

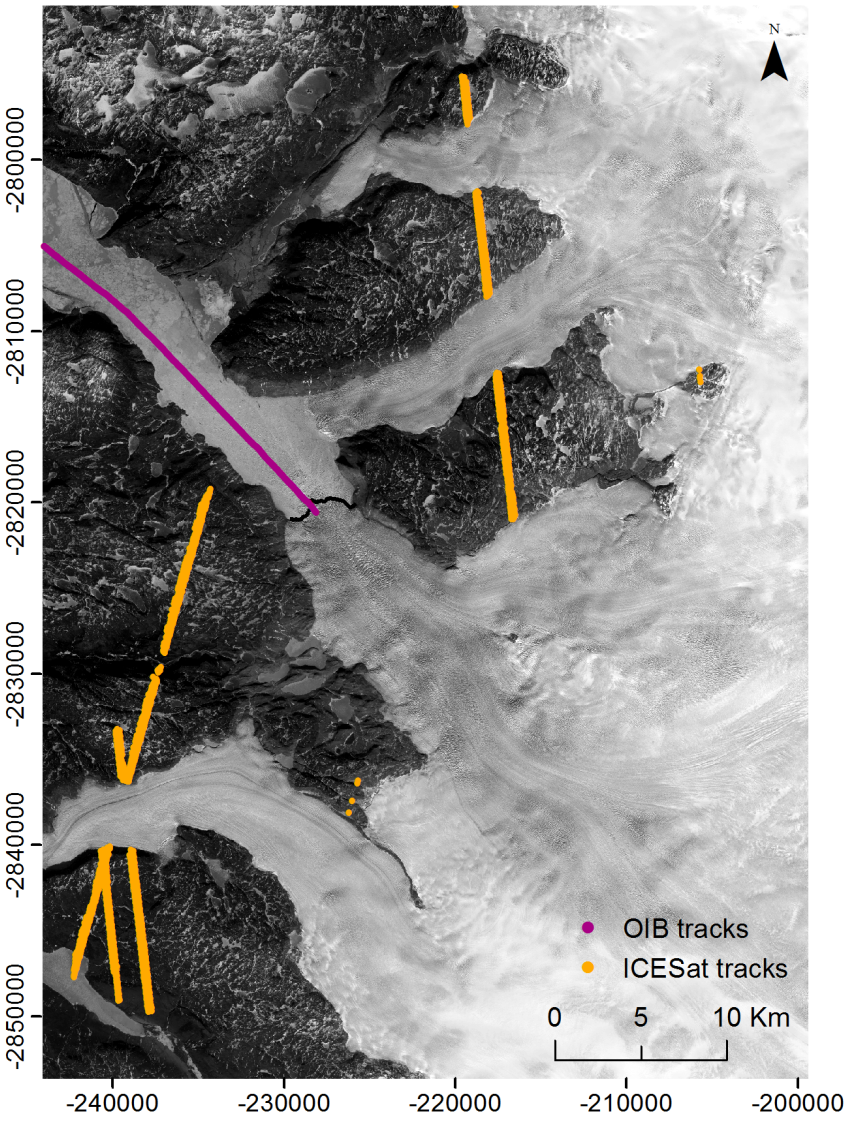

Figure S1.3: ICESat and Operation IceBridge (OIB) Airborne Topographic Mapper (ATM) tracks (08 April 2011) used for calibrating the TanDEM-X DEMs and for correcting a secondary tilt, respectively. The background image is Landsat 8 band 8, acquired on 03 April 2013.

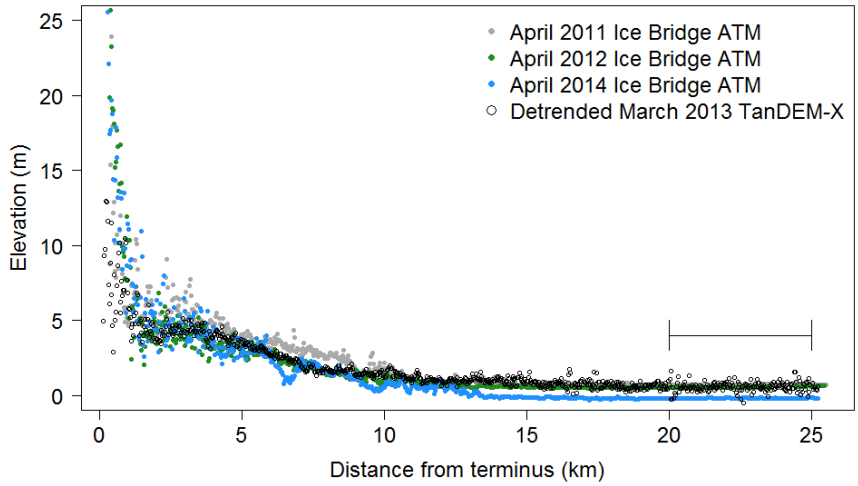

Figure S1.4: Ice Bridge ATM (2011, 2012 and 2014) and detrended TanDEM-X elevation profiles in Kangersuneq Fjord. TanDEM-X elevations are from 17 March 2013, detrended using IceBridge ATM elevations from 08 April 2011 between 20 and 25 km down-fjord of the KNS terminus (segment line).

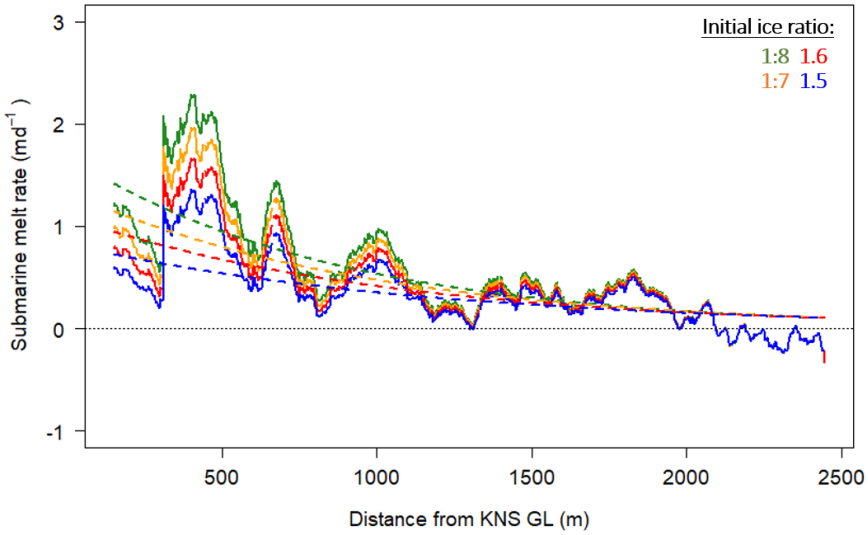

Figure S1.5: Impact of a varying hydrostatic equilibrium on sample submarine melt rates (SMR, m d^{-1}) for 17 March 2013 using the following initial ratios for the above to below waterline ice volume: 1:8 (hydrostatic equilibrium, green), 1:7 (orange), 1:6 (red) and 1:5 (blue). Solid lines are means from all flowlines and dashed lines are trendlines fit to the mean melt rates.

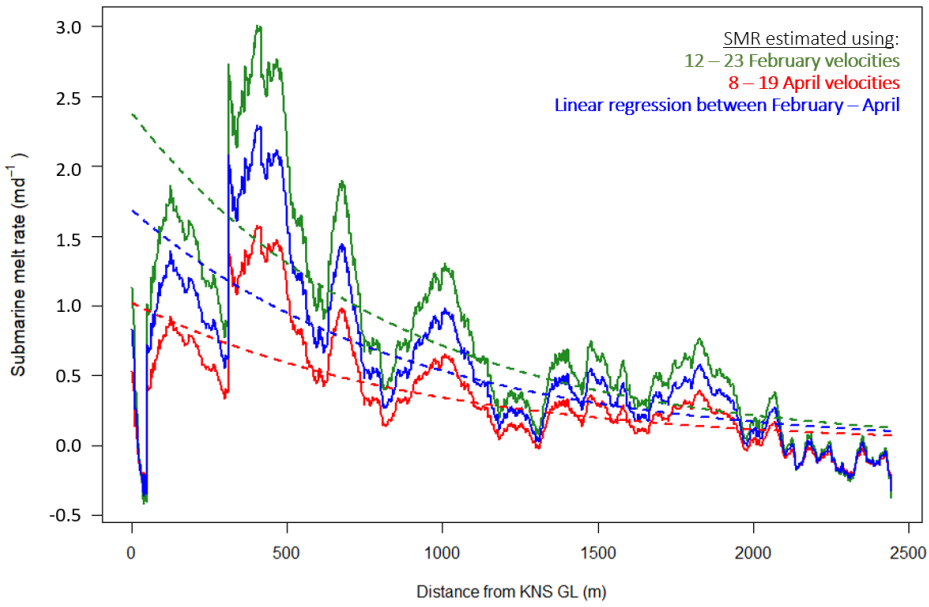

Figure S1.6: Impact of temporal variability in ice tongue velocity on sample submarine melt rates (SMR, m d^{-1}) for 17 March 2013 estimated using 12 - 23 February velocity (green), 8 - 19 April velocity (red) and a linear regression between the two velocities (blue). Solid lines are means from all flowlines and dashed lines are trendlines fit to the mean melt rates.

Chapter S2

Supporting information for 'Spatio-temporal variations in seasonal ice tongue submarine melt rates at a tidewater glacier in southwest Greenland'

This chapter contains additional details regarding the methods presented in Chapter 5, six supporting figures and two tables.

S2.1 Estimating ice tongue surface melt rates

To assess potential changes in surface mass balance (SMB), ice tongue surface melt rates were estimated using a simple positive degree day approach, using degree day factors for snow and ice of 4.5 and 11.9 mm d^{-1} $°C^{-1}$, respectively (Slater et al. 2017a), and a threshold temperature for snow melt of 0 °C. Surface melt rates were averaged over a two week period before the date of each DEM, as surface melt occurring only on the day of the DEM is unlikely to be representative of spring surface melt rates. As

the air temperatures at the PROMICE station are recorded 550 m above sea level, we applied a lapse rate of 0.5 °C per 100 m (Slater et al. 2017a) to adjust temperatures to sea level.

Total surface snow melt and precipitation as snow over the ice tongue were low during the two weeks prior to the date of each of our DEMs (see Table S2.1). We acknowledge that there will be differences between precipitation recorded in Nuuk (approximately 105 km west) and that falling over the KNS ice tongue. Abermann et al. (2017) estimated differences in spring average precipitation between coastal (16 km SE of Nuuk and 7 km from the coast) and inland (75 km from the coast and 34 km NW of the KNS terminus at Kapisillit) weather stations in western Greenland. Using monthly averages from 2008 to 2014, a maximum precipitation gradient of 2 mm per km towards the coast was found for September and a minimum gradient of ~0.3 mm per km was found for February. Gradients between March and June (when we use the Nuuk station data) range from approximately 0.5 to 0.8 mm per km towards the coast. We would therefore expect snowfall to be less over the ice tongue when compared to that recorded in Nuuk, given the low elevation of the ice tongue and the rain shadow effect of the coastal mountains. If anything therefore, we likely overestimate the spring snowfall by using estimates of precipitation from Nuuk. Regardless, the recorded precipitation estimates (in terms of water equivalent) are orders of magnitude smaller than our estimated submarine melt rates, and we do not therefore expect snow to significantly impact estimated changes in ice tongue freeboard. Our estimates of spring surface melt rate, which reach a maximum of 0.050 m d^{-1} in June 2014, are two orders of magnitude less than our estimated submarine melt rates for the same periods, and thus considered negligible.

S2.2 Estimating basal meltwater flux for the grounded portion of KNS

To assess the potential influence of basal frictional melting on driving winter and spring plumes, we estimated basal meltwater flux for the entire KNS catchment (approximately 30,700 km^2, as delineated by hydraulic potential flow routing). We assume that basal

drag (τ) at KNS is of a similar magnitude to that estimated for Jakobshavn Isbræ, approximately 200 kPa, and as used for Kangerdlugssuaq Glacier by Christoffersen et al. (2012). We adopt a simplified equation (Christoffersen et al. 2012) for estimating basal melt rate, $\dot{m}$:

$$\dot{m} = \frac{\tau U}{\rho L} \tag{S1}$$

where U (m d^{-1}) is grounded ice velocity, ρ (900 kg m^{-3}) is ice density and L (334 kJ kg^{-1}) is the latent heat of fusion. We use ice velocities in the lower portion of the catchment derived from feature tracking of Landsat 7 imagery for May 2012 (Rosenau et al. 2015), TerraSAR-X imagery for March and May 2013, and Landsat 8 imagery for May 2014 (see below). Ice velocities in the upper portion of the catchment are from the MEaSUREs Greenland Ice Sheet Velocity Map, as derived from InSAR data for the winters of 2012-2013 and 2014-2015 (Joughin et al. 2010, 2015). We merge the different velocity datasets ~13 km up-glacier from the grounding line for 2012 and 2013, and ~50 km up-glacier for 2014, as dependent on the extent of the satellite data used for velocity generation.

In order to estimate catchment-wide basal meltwater flux in 2014, ice motion between 27 May and 12 June 2014 was derived from cross-correlation between a pair of Landsat 8 Operational Land Imager (WRS2 path 6, row 15) band 8, Level-1 Precision and Terrain (L1TP) corrected images. Prior to image cross-correlation, a high pass Gaussian filter with a standard deviation equivalent to three 15 m pixels was used to isolate the surface features that are advected with ice flow (e.g., crevasses). Cross-correlation was carried out using a modified version of the PIVSuite MATLAB code (https://uk.mathworks.com/matlabcentral/fileexchange/45028-pivsuite written by Jiri Vejrazka, Institute of Chemical Process Fundamentals, Academy of Sciences of the Czech Republic, Prague). We used a multi-pass approach with final image Interrogation areas (IAs) of 32 x 32 pixels (480 x 480 m) and a step between IAs of 8 pixels, resulting in velocity postings of 120 m. Sub-pixel displacements were calculated using nonlinear optimization and matrix-multiply discrete Fourier transforms (Guizar-Sicairos et al.

2008). The resulting velocity field was filtered using a signal-to-noise ratio threshold of 5 between the peak correlation and the mean value for areas outside the 3 by 3 cell region of the highest peak. Remaining spurious correlations were filtered using a two-dimensional histogram of the easting and northing displacements (Adrian & Westerweel 2011) and by removing velocities $> 3\sigma$ greater than the median of a 3 x 3 neighborhood. The geolocation information for Landsat 8 OLI imagery is accurate to approximately half a pixel (Storey et al. 2014); therefore we calculated the mean offset over stationary bedrock regions (Fahnestock et al. 2015) to quantify the residual velocity error for our image pair, deriving a value of ± 27 m yr^{-1}.

S2.3 Supporting figures and tables

This section contains the additional supporting figures and table cited in Chapter 5.

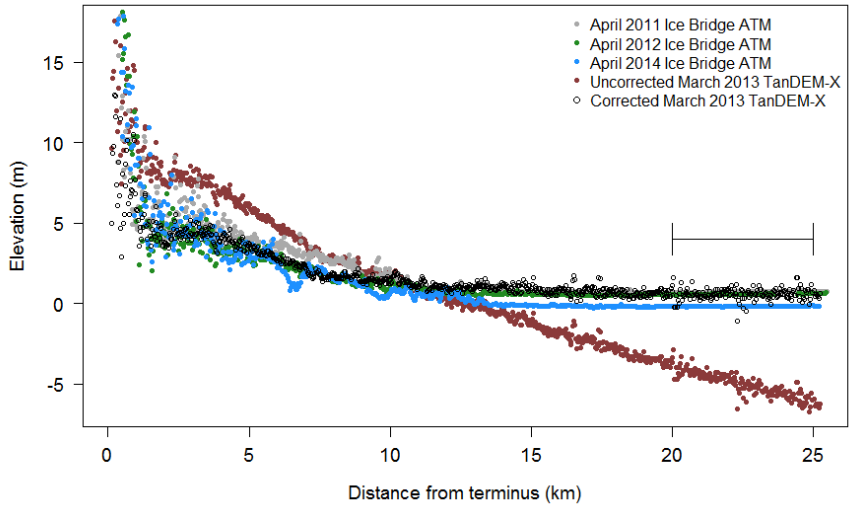

Figure S2.1: IceBridge ATM (2011, 2012 and 2014) and uncorrected and corrected TanDEM-X elevations for profiles in Kangersuneq Fjord from 17 March 2013. TanDEM-X profiles are detrended using IceBridge ATM elevations from 08 April 2011 between 20 and 25 km down-fjord of the KNS terminus (segment line).

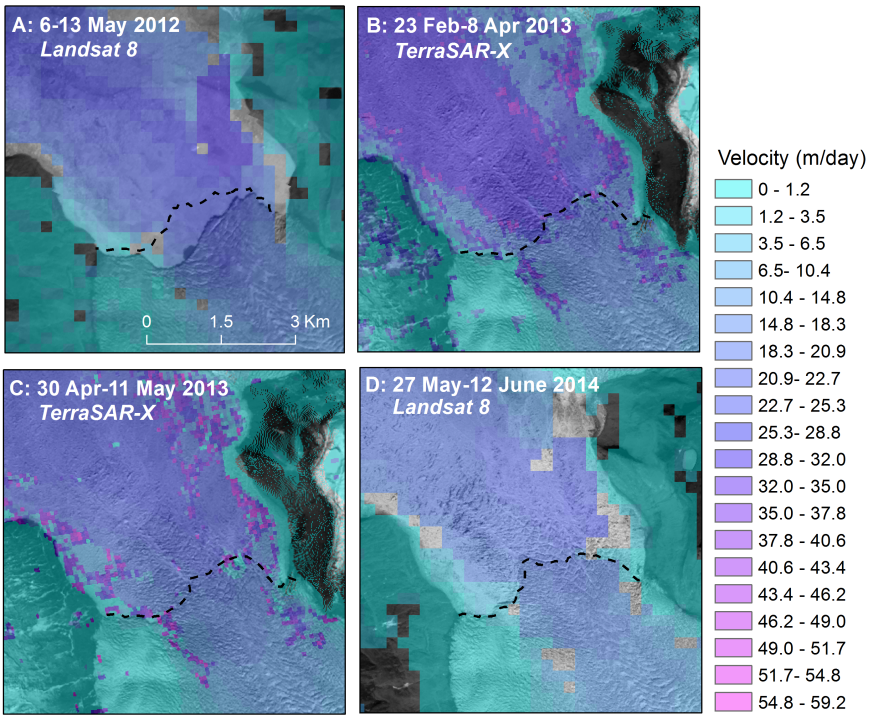

Figure S2.2: Ice velocity maps derived from the feature tracking of (a) Landsat 8 image pair: 6 and 13 May 2012 (underlain by Landsat 7 image from 25 July 2012), (b) TerraSAR-X image pairs: 12 and 23 February and 8 and 19 April 2013 (underlain by Landsat 8 image from 1 May 2013), (c) TerraSAR-X image pair: 30 April and 11 May 2013 (underlain by Landsat 8 image from 1 May 2013), and (d) Landsat 8 image pair: 27 May and 12 June 2014 (underlain by Landsat 8 image from 12 June 2014). Black dashed lines are grounding line positions hand-digitized from Landsat 8 imagery.

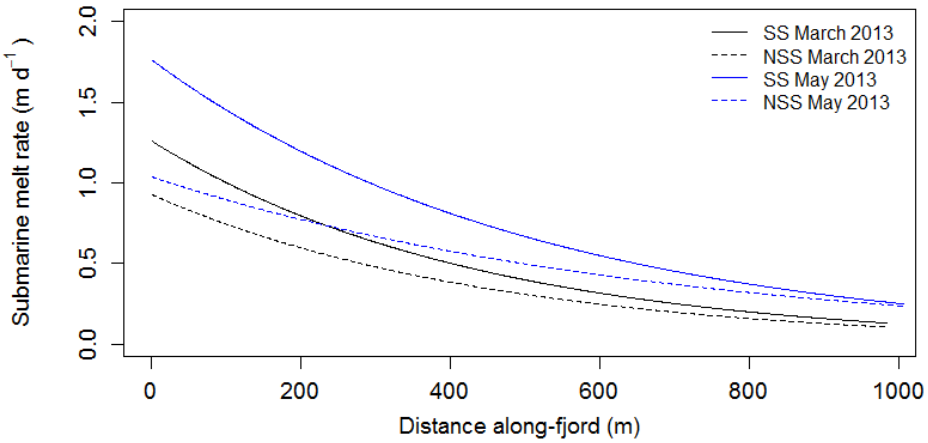

Figure S2.3: Comparison between March (black) and May (blue) 2013 steady state (SS, solid line) and non-steady state (NSS, dashed line) along-fjord submarine melt rate estimates, derived from averaged across-fjord melt rate estimates for the full ice tongue.

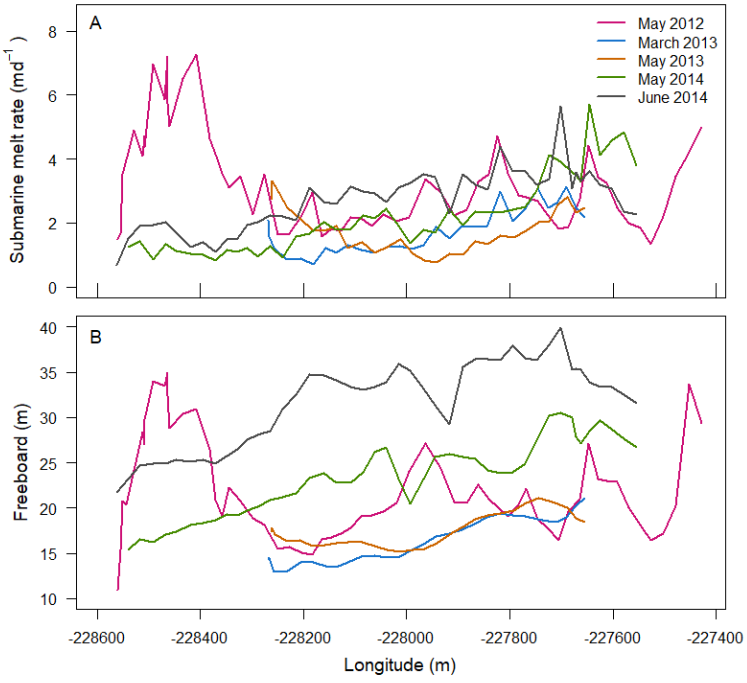

Figure S2.4: Across-fjord profiles of (a) submarine melt rates (m d^{-1}) and (b) freeboard (m) 150 m down-fjord from the KNS grounding line, moving from west to east, for 2012-2014.

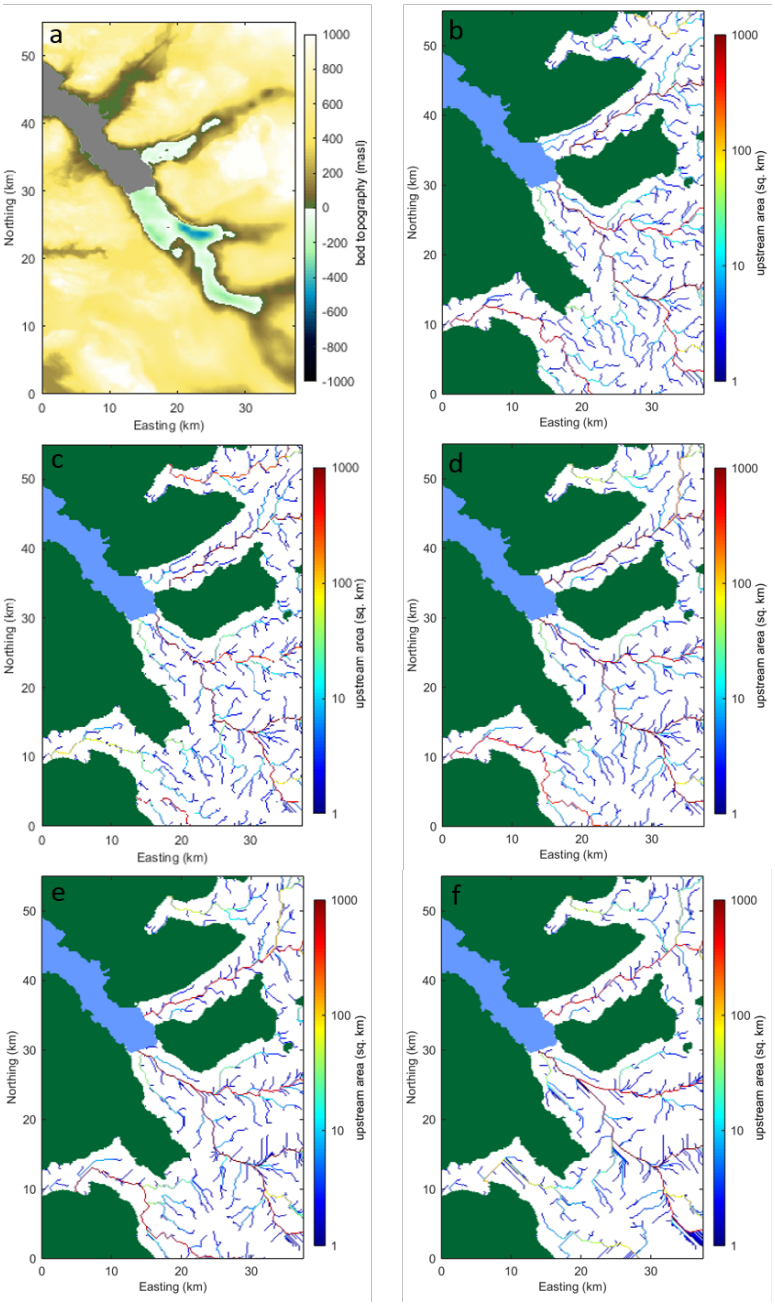

Figure S2.5: (a) BedMachine v3 bed topography for KNS, used in hydropotential analyses for predicting subglacial flow routing with f-values of (b) 1.0, (c) 0.9, (d) 0.8, (e) 0.7, and (f) 0.3.

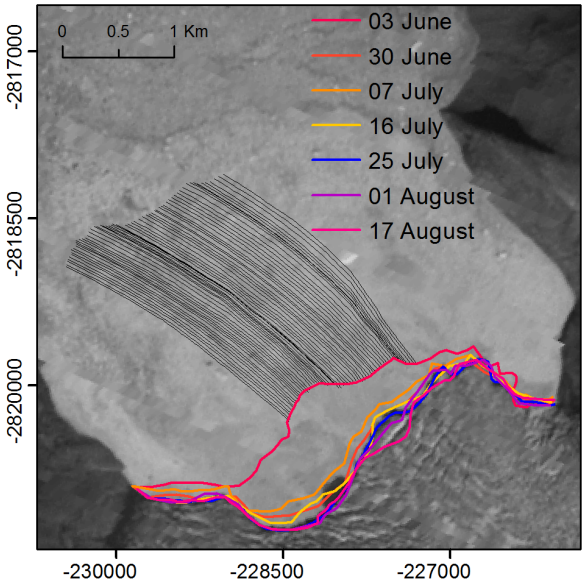

Figure S2.6: Grounding line positions for KNS terminus from June to August 2012, showing the creation of an embayment due to calving on the western side of the ice front. The background image is a Landsat 7 image from 25 July 2012.

Table S2.1: Ice tongue surface melt rates (m d^{-1}) for two weeks prior to the date of each DEM; maximum and mean submarine melt rates (SMR, m d^{-1}) per DEM.

DEM	Surface melt (m d^{-1})	Max. SMR (m d^{-1})	Mean SMR (m d^{-1})
13/05/2012	0.048	7.3 ± 2.3	1.3 ± 0.6
17/03/2013	0.0036	3.1 ± 0.8	0.8 ± 0.3
27/05/2013	0.020	3.8 ± 1.0	0.8 ± 0.3
14/05/2014	0.044	5.8 ± 1.6	0.9 ± 0.4
05/06/2014	0.050	5.7 ± 1.6	1.1 ± 0.4

Table S2.2: Acquisition dates of satellite imagery used for detecting the surface presence of plumes driven by subglacial discharge (as found in Figure 5.3a,c).

Acquisition date	Satellite / Sensor
30/06/2012	Landsat 7
16/07/2012	Landsat 7
25/07/2012	Landsat 7
01/08/2012	Landsat 7
17/08/2012	Landsat 7
28/07/2013	Landsat 7
04/08/2013	Landsat 7

Bibliography

Abermann, J., van As, D., Wacker, S. & Langley, K. (2017), 'Mountain glacier vs ice sheet in Greenland - learning from a new monitoring site in west Greenland', *Geophysical Research Abstracts* **19**, EGU2017–9445.

Adrian, R. J. & Westerweel, J. (2011), *Particle Image Velocimetry*, Cambridge University Press.

Ahlstrøm, J., Gravesen, P., Andersen, S. B., van As, D., Citterio, M., Fausto, R. S., Nielsen, S., Jepsen, H. F., Kristensen, S. S., Christensen, E. L., Stenseng, L., Forsberg, R., Hanson, S. & Petersen, D. (2008), 'A new programme for monitoring the mass loss of the Greenland Ice Sheet', *Geological Survey of Denmark and Greenland Bulletin* **15**, 61–64.

Amundson, J. M., Fahnestock, M., Truffer, M., Brown, J., Lüthi, M. P. & Motyka, R. J. (2010), 'Ice mélange dynamics and implications for terminus stability, Jakobshavn Isbrae, Greenland', *Journal of Geophysical Research: Earth Surface* **115**(1), 1–12.

Andrews, L. C., Catania, G. A., Hoffman, M. J., Gulley, J. D., Lüthi, M. P., Ryser, C., Hawley, R. L. & Neumann, T. A. (2014), 'Direct observations of evolving subglacial drainage beneath the Greenland Ice Sheet', *Nature* **514**, 80–83.

Arneborg, L. & Liljebladh, B. (2001), 'The internal seiches in Gullmar Fjord. Part I: dynamics.', *Journal of Physical Oceanography* **31**, 2549–2566.

Banwell, A. F., Willis, I. C. & Arnold, N. S. (2013), 'Modeling subglacial water routing at Paakitsoq, W Greenland', *Journal of Geophysical Research Earth Surface* **118**, 1282–1295.

Barker, A., Sayed, M. & Carrieres, T. (2004), 'Determination of iceberg draft, mass and cross-sectional areas', *Proc. from the International Conference of Offshore and Polar Engineering* **2**, 899–904.

Bartholomaus, T. C., Larsen, C. F. & O'Neel, S. (2013), 'Does calving matter? Evidence for significant submarine melt.', *Earth and Planetary Science Letters* **380**, 21–30.

Bash, E. A., Moorman, B. J. & Gunther, A. (2018), 'Detecting short-term surface melt on an Arctic glacier using UAV surveys', *Remote Sensing* **10**, 1–17.

Benn, D. I., Warren, C. R. & Mottram, R. H. (2007), 'Calving processes and the dynamics of calving glaciers', *Earth Science Reviews* **82**, 143–179.

Berger, S., Drews, R., Helm, V., Sun, S. & Pattyn, F. (2016), 'Detecting high spatial variability of ice shelf basal mass balance, Roi Baudouin Ice Shelf, Antarctica', *Cryosphere* **11**, 2675–2690.

Bjørk, A. A., Kjær, K. H., Korsgaard, N. J., Khan, S. A., Kjeldsen, K. K., Andresen, C. S., Box, J. E., Larsen, N. K. & Funder, S. (2012), 'An aerial view of 80 years of climate-related glacier fluctuations in southeast Greenland', *Nature Geoscience* **5**, 427–432.

Box, J. E. (2013), 'Greenland Ice Sheet mass balance reconstruction. Part II: Surface mass balance (1840-2010)', *Journal of Climate* **26**(18), 6974–6989.

Burton, J. C., Amundson, J. M., Cassotto, R., Kuo, C. & Dennin, M. (2018), 'Quantifying flow and stress in ice mélange, the world's largest granular material', *Proceedings of the National Academy of Sciences* **115**, 5105–5110.

Cape, M. R., Straneo, F., Beaird, N., Bundy, R. B. & Charette, M. A. (2019), 'Nutrient release to oceans from buoyancy-driven upwelling at Greenland tidewater glaciers', *Nature Geoscience* **12**, 34–39.

Cappelen, J. (ed.) (2016), 'Greenland - DMI Historical Climate Data Collection 1784-2016', *DMI Report* **17-04**.

Cappelen, J. (ed.) (2018), 'Greenland - DMI Historical Climate Data Collection 1784-2017', *DMI Report* **18-04**.

Carr, J. R., Stokes, C. R. & Vieli, A. (2013), 'Recent progress in understanding marine-terminating Arctic outlet glacier response to climatic and oceanic forcing: Twenty years of rapid change', *Progress in Physical Geography* **37**(4), 436–467.

Carroll, D., Sutherland, D. A., Hudson, B., Moon, T., Catania, G. A., Shroyer, E. L., Nash, J. D., Bartholomaus, T. C., Felikson, D., Stearns, L. A., Noël, B. P. & van den Broeke, M. R. (2016), 'The impact of glacier geometry on meltwater plume structure and submarine melt in Greenland fjords', *Geophysical Research Letters* **43**(18), 9739–9748.

Carroll, D., Sutherland, D. A., Shroyer, E. L., Nash, J. D., Catania, G. A. & Stearns, L. A. (2015), 'Modeling turbulent subglacial meltwater plumes: Implications for fjord-Scale buoyancy-driven circulation', *Journal of Physical Oceanography* **45**(8), 2169–2185.

Cenedese, C. & Gatto, V. M. (2016), 'Impact of a localized source of subglacial discharge on the heat flux and submarine melting of a tidewater glacier: A laboratory study', *Journal of Physical Oceanography* **46**(10), 3155–3163.

Chauché, N., Hubbard, A., Gascard, J. C., Box, J. E., Bates, R., Koppes, M., Sole, A., Christoffersen, P. & Patton, H. (2014), 'Ice-ocean interaction and calving front

morphology at two west Greenland tidewater outlet glaciers', *Cryosphere* **8**(4), 1457–1468.

Christensen, A. M. (2016), 'Current Trends in the Greenlandic Economy', *Danmarks National Bank Monetary Review* **2nd Quarter**, 97–104.

Christoffersen, P., O'Leary, M., Van Angelen, J. H. & Van Den Broeke, M. (2012), 'Partitioning effects from ocean and atmosphere on the calving stability of Kangerdlugssuaq Glacier, East Greenland', *Annals of Glaciology* **53**(60), 249–256.

Chudley, T. R., Christoffersen, P., Doyle, S. H., Abellan, A. & Snooke, N. (2019), 'High accuracy UAV photogrammetry of ice sheet dynamics with no ground control', *Cryosphere* **13**, 955–968.

Cottier, F. R., Nilsen, F., Skogseth, R., Tverberg, V., Skardhamar, J. & Svendsen, H. (2010), 'Arctic fjords: a review of the oceanographic environment and dominant physical processes', *Geological Society of London Special Publications* **344**(1), 35–50.

Cowton, T., Slater, D., Sole, A., Goldberg, D. & Nienow, P. (2015), 'Modeling the impact of glacial runoff on fjord circulation and submarine melt rate using a new subgrid-scale parameterization for glacial plumes', *Journal of Geophysical Research: Oceans* **120**(2), 796–812.

Cowton, T., Sole, A. J., Nienow, P. N., Slater, D. A. & Christoffersen, P. (2018), 'Linear response of east Greenland's tidewater glaciers to ocean/atmosphere warming', *Proceedings of the National Academy of Science* **115**(31), 7907–7912.

Davison, B., Sole, A. J., Cowton, T., Lea, J. & Fahrner, D. (2019), 'Subglacial drainage evolution modulates tidewater glacier ice flow variability', *Geophysical Research Abstracts* **21**, EGU2019–522.

Dehecq, A., Millan, R., Berthier, E., Gourmelen, N., Trouvé, E. & Vionnet, V. (2016), 'Elevation changes inferred from TanDEM-X data over the Mont-Blanc area: Impact of the X-band interferometric bias', *IEEE Journal of Selected Topics in Applied Earth Observations and Remote Sensing* **9**(8), 3870–3882.

Depoorter, M. A., Bamber, J. L., Griggs, J. A., Lenaerts, J. T., Ligtenberg, S. R., van den Broeke, M. R. et al. (2013), 'Calving fluxes and basal melt rates of Antarctic ice shelves', *Nature* **502**, 89–92.

Dowdeswell, J. A., Evans, J., Mugford, R., Griffiths, G., McPhail, S., Millard, N., Stevenson, P., Brandon, M. A., Banks, C., Heywood, K. J., Price, M. R., Dodd, P. A., Jenkins, A., Nicholls, K. W., Hayes, D., Abrahamsen, E. P., Tyler, P., Bett, B., Jones, D., Wadhams, P., Wilkinson, J. P., Stansfield, K. & Ackley, S. (2008), 'Autonomous underwater vehicles (AUVs) and investigations of the ice-ocean interface: deploying the Autosub AUV in Antarctic and Arctic waters', *Journal of Glaciology* **54**, 661–672.

Eineder, M., Minet, C., Steigenberger, P., Cong, X. & Fritz, T. (2011), 'Imaging geodesy: Toward centimeter-level ranging accuracy with TerraSAR-X.', *IEEE Transactions on Geoscience and Remote Sensing* **49**, 661–671.

Enderlin, E. M., Carrigan, C. J., Kochtitzky, W. H., Cuadros, A. & Hamilton, G. S. (2018), 'Greenland iceberg melt variability from high-resolution satellite observations', *Cryosphere* **12**, 565–575.

Enderlin, E. M. & Hamilton, G. S. (2014), 'Estimates of iceberg submarine melting from high-resolution digital elevation models: Application to Sermilik Fjord, East Greenland', *Journal of Glaciology* **60**(224), 1111–1116.

Enderlin, E. M., Hamilton, G. S., Straneo, F. & Sutherland, D. A. (2016), 'Iceberg meltwater fluxes dominate the freshwater budget in Greenland's iceberg-congested glacial fjords', *Geophysical Research Letters* **43**(21), 11287–11294.

Enderlin, E. M. & Howat, I. M. (2013), 'Submarine melt rate estimates for floating termini of Greenland outlet glaciers (2000-2010)', *Journal of Glaciology* **59**(213), 67–75.

Enderlin, E. M., Howat, I. M., Jeong, S., Noh, M.-J., Van Angelen, J. H. & Van Den Broeke, M. R. (2014), 'An improved mass budget for the Greenland Ice Sheet', *Geophysical Research Letters* **41**, 866–872.

Erasmi, S., Rosenbauer, R., Buchbach, R., Busche, T. & Rutishauser, S. (2014), 'Evaluating the quality and accuracy of TanDEM-X digital elevation models at archaeological sites in the Cilician Plain, Turkey', *Remote Sensing* **6**(10), 9475–9493.

Fahnestock, M., Scambos, T., Moon, T., Gardner, A., Haran, T. & Klinger, M. (2015), 'Rapid large-area mapping of ice flow using Landsat 8', *Remote Sensing of Environment* **185**, 84–94.

Fausto, R. S., Ahlstrøm, A. P., Van As, D., Bøggild, C. E. & Johnsen, S. J. (2009), 'A new present-day temperature parameterization for Greenland', *Journal of Glaciology* **55**(189), 95–105.

Fenty, I., Willis, J. K., Khazendar, A., Dinardo, S., Forsberg, R., Fukumori, I., Holland, D., Jakobsson, M., Moller, D., Morison, J., Münchow, A., Rignot, E., Schodlok, M., Thompson, A. F., Tinto, K., Rutherford, M. & Trenholm, N. (2016), 'Oceans Melting Greenland: Early results from NASA's ocean-ice mission in Greenland', *Oceanography* **48**(4), 72–83.

FitzMaurice, A., Cenedese, C. & Straneo, F. (2017), 'Nonlinear response of iceberg side melting to ocean currents', *Geophysical Research Letters* **44**, 5637–5644.

FitzMaurice, A., Straneo, F., Cenedese, C. & Andres, M. (2016), 'Effect of a sheared flow on iceberg motion and melting', *Geophysical Research Letters* **43**, 12520–12527.

Foga, S., Stearns, L. A. & van der Veen, C. (2014), 'Application of satellite remote sensing techniques to quantify terminus and ice mélange behavior at Helheim Glacier, East Greenland', *Marine Technology Society Journal* **48**(5), 81–91.

Fountain, A. G. & Walder, J. S. (1998), 'Water flow through temperate glaciers', *Reviews of Geophysics* **36**, 299–328.

Fricker, H. A., Coleman, R., Padman, L., Scambos, T. A., Bohlander, J. & Brunt, K. (2009), 'Mapping the grounding zone of the Amery Ice Shelf, East Antarctica using InSAR, MODIS adn ICESat', *Antarctic Science* **21**, 5637–5644.

Fried, M. J., Catania, G. A., Bartholomaus, T. C., Duncan, D., Davis, M., Stearns, L. A., Nash, J., Shroyer, E. & Sutherland, D. (2015), 'Distributed subglacial discharge drives significant submarine melt at a Greenland tidewater glacier', *Geophysical Research Letters* **42**(21), 9328–9336.

Funk, M., Echelmeyer, K. & Iken, A. (1994), 'Mechanisms of fast flow in Jakobshavns Isbræ, West Greenland: part, II. Modeling of englacial temperatures', *Journal of Glaciology* **40**, 569–585.

Gatti, A. & Bertolini, A. (2015), *Sentinel-2 Products Specification Document*, Thales Alenia Space, Mérignac, France.

Gindraux, S., Boesch, R. & Farinotti, D. (2017), 'Accuracy assessment of digital surface models from unmanned aerial vehicles' imagery on glaciers', *Remote Sensing* **9**, 1–15.

Goelzer, H., Huybrechts, P., Furst, J. J., Nick, F. M., Andersen, M. L., Edwards, T. L., Fettweis, X., Payne, A. J. & Shannon, S. (2013), 'Sensitivity of Greenland Ice Sheet projections to model formulations', *Journal of Glaciology* **59**(216), 733–749.

Gourmelen, N., Goldberg, D. N., Snow, K., Henley, S. F., Bingham, R. G., Kimura, S., Hogg, A. E., Shepherd, A., Mouginot, J., Lenaerts, J. T. M., Ligtenberg, S. R. M. & van de Berg, W. J. (2017), 'Channelized melting drives thinning under a rapidly melting Antarctic ice shelf', *Geophysical Research Letters* **44**, 9796–9804.

Guizar-Sicairos, M., Thurman, S. T. & Fienup, J. R. (2008), 'Efficient subpixel image registration algorithms', *Optics Letters* **33**, 156–158.

Hanna, E., Fettweis, X., Mernild, S. H., Cappelen, J., Ribergaard, M. H., Shuman, C. A., Steffen, K., Wood, L. & Mote, T. L. (2014), 'Atmospheric and oceanic climate forcing of the exceptional Greenland Ice Sheet surface melt in summer 2012', *International Journal of Climatology* **34**(4), 1022–1037.

Hanna, E., Huybrechts, P., Cappelen, J., Steffen, K., Bales, R. C., Burgess, E., McConnell, J. R., Steffensen, J. P., Van den Broeke, M., Wake, L., Bigg, G., Griffiths, M. & Savas, D. (2011), 'Greenland Ice Sheet surface mass balance 1870 to 2010 based on Twentieth Century Reanalysis, and links with global climate forcing', *Journal of Geophysical Research: Atmospheres* **116**, D24121.

Hanna, E., Huybrechts, P., Janssens, I., Cappelen, J., Steffen, K. & Stephens, A. (2005), 'Runoff and mass balance of the Greenland Ice Sheet: 1958 - 2003', *Journal of Geophysical Research: Atmospheres* **110**, D13108.

Hanna, E., Mernild, S. H., Cappelen, J. & Steffen, K. (2012), 'Recent warming in Greenland in a long-term instrumental (1881-2012) climatic context: I. Evaluation of surface air temperature records', *Environmental Research Letters* **7**(4).

Hock, R. (2003), 'Temperature index melt modelling in mountain areas', *Journal of Hydrology* **282**(1-4), 104–115.

Holland, D. M. & Jenkins, A. (1999), 'Modeling thermodynamic ice-ocean interactions at the base of an ice shelf', *Journal of Physical Oceanography* **29**, 1787–1800.

Holland, D. M., Thomas, R. H., De Young, B., Ribergaard, M. H. & Lyberth, B. (2008), 'Acceleration of Jakobshavn Isbrae triggered by warm subsurface ocean waters', *Nature Geoscience* **1**(10), 659–664.

How, P., Benn, D. I., Hulton, N. R., Hubbard, B., Luckman, A., Sevestre, H., Pelt, W. J., Lindbäck, K., Kohler, J. & Boot, W. (2017), 'Rapidly changing subglacial hydrological pathways at a tidewater glacier revealed through simultaneous observations of water pressure, supraglacial lakes, meltwater plumes and surface velocities', *Cryosphere* **11**(6), 2691–2710.

Howat, I. M., Box, J. E., Ahn, Y., Herrington, A. & McFadden, E. M. (2010), 'Seasonal variability in the dynamics of marine-terminating outlet glaciers in Greenland', *Journal of Glaciology* **56**(198), 601–613.

Howat, I. M., Joughin, I. R. & Scambos, T. A. (2007), 'Rapid changes in ice discharge from Greenland outlet glaciers', *Science* **315**, 1559–1561.

Howat, I. M., Negrete, A. & Smith, B. E. (2014), 'The Greenland Ice Mapping Project (GIMP) land classification and surface elevation datasets', *Cryosphere* **8**, 1509–1518.

Iken, A., Echelmeyer, K., Harrison, W. & Funk, M. (1993), 'Mechanisms of fast flow in Jakobshavns Isbræ, West Greenland: part, I. measurements of temperature and water level in deep boreholes', *Journal of Glaciology* **119**, 15–25.

Inall, M. E., Murray, T., Cottier, F. R., Scharrer, K. & Boyd, T. J. (2014), 'Oceanic heat delivery via Kangerdlugssuaq Fjord to the south-east Greenland Ice Sheet', *Journal of Geophysical Research : Oceans* **119**, 631–645.

IPCC (2013), *Climate Change 2013: The Physical Science Basis. Contributions of Working Group I to the Fifth Assessment Report of the Intergovernmental Panel on Climate Change*, [Stocker, T. F. and Qin, D. and Plattner, G. K. and Tignor, M. and Allen, S. K. and Boschung, J. and Nauels, A. and Xia, Y. and Bex, V. and Midgley, P. M. (eds.)]. Cambridge University Press, Cambridge, UK and New York, NY, USA.

Jackson, R. H. & Straneo, F. (2016), 'Heat, Salt, and Freshwater Budgets for a Glacial Fjord in Greenland', *Journal of Physical Oceanography* **46**(9), 2735–2768.

Jackson, R. H., Straneo, F. & Sutherland, D. A. (2014), 'Externally forced fluctuations in ocean temperature at Greenland glaciers in non-summer months', *Nature Geoscience* **7**(7), 503–508.

Jenkins, A. (2011), 'Convection-driven melting near the grounding lines of ice shelves and tidewater glaciers', *Journal of Physical Oceanography* **41**(12), 2279–2294.

Jenkins, A. & Doake, C. S. M. (1991), 'Ice-ocean interactions on Ronne Ice Shelf, Antarctica', *Journal of Geophysical Research* **96**, 791–813.

Jenkins, A. & Holland, D. M. (2002), 'A model study of ocean circulation beneath Filchner-Ronne Ice Shelf, Antarctica: Implications for bottom water formation', *Geophysical Research Letters* **29**(8), 1–4.

Jiskoot, H., Juhlin, D., Pierre, H. S. & Citterio, M. (2012), 'Tidewater glacier fluctuations in central east greenland coastal and fjord regions (1980s-2005)', *Annals of Glaciology* **53**(60), 35–44.

Johnson, H. L., Münchow, A., Falkner, K. K. & Melling, H. (2011), 'Ocean circulation and properties in Petermann Fjord, Greenland', *Journal of Geophysical Research: Oceans* **116**(1), 1–18.

Joughin, I., Abdalati, W. & Fahnestock, M. (2004), 'Large fluctuations in speed on Greenland's Jakobshavn Isbræ Glacier', *Nature* **432**, 608–610.

Joughin, I. & Padman, L. (2003), 'Melting and freezing beneath Filchner-Ronne Ice Shelf, Antarctica', *Geophysical Research Letters* **30**(9).

Joughin, I., Smith, B., Howat, I. & Scambos, T. (2015), 'MEaSUREs Greenland Ice Sheet Velocity Map from InSAR Data, Version 2', *NASA National Snow and Ice Data Center Distributed Active Archive Center* .

Joughin, I., Smith, B., Howat, I., Scambos, T. & Moon, T. (2010), 'Greenland flow variability from ice-sheet-wide velocity mapping', *Journal of Glaciology* **56**, 415–430.

Kehrl, L. M., Joughin, I., Shean, D. E., Floricioiu, D. & Krieger, L. (2017), 'Seasonal and interannual variabilities in terminus position, glacier velocity, and surface elevation at Helheim and Kangerlussuaq Glaciers from 2008 to 2016', *Journal of Geophysical Research: Earth Surface* **122**, 1635–1652.

Khazendar, A., Rignot, E., Schroeder, D. M., Seroussi, H., Schodlok, M. P., Scheuchl, B., Mouginot, J., Sutterley, T. C. & Velicogna, I. (2016), 'Rapid submarine ice melting in the grounding zones of ice shelves in West Antarctica', *Nature Communications* **7**, 13243.

Kienzle, S. W. (2008), 'A new temperature based method to separate rain and snow', *Hydrological Processes* **22**, 5067–5085.

Kimball, P., Bailey, J., Das, S., Geyer, R., Harrison, T., Kunz, C., Manganini, K., Mankoff, K., Samuelson, K., Sayre-McCord, T., Straneo, F., Traykovski, P. & Singh, H. (2014), 'The WHOI Jetyak: An autonomous surface vehicle for oceanographic research in shallow or dangerous waters', *IEEE/OES Autonomous Underwater Vehicles (AUV)* pp. 1–7.

Kimura, S., Holland, P. R., Jenkins, A. & Piggott, M. (2014), 'The effect of meltwater plumes on the melting of a vertical glacier face', *Journal of Physical Oceanography* **44**(12), 3099–3117.

Krabill, W. B. (2016), 'IceBridge ATM L1B Elevation and Return Strength, NASA DAAC at the National Snow and Ice Data Center'.

Krieger, G., Moreira, A., Fiedler, H., Hajnsek, I., Werner, M., Younis, M. et al. (2007), 'TanDEM-X: a satellite formation for high-resolution SAR interferometry', *IEEE Transactions on Geoscience and Remote Sensing* **45**, 3317–3341.

Krug, J., Durand, G., Gagliardini, O. & Weiss, J. (2015), 'Modelling the impact of submarine frontal melting and ice mélange on glacier dynamics', *Cryosphere* **9**(3), 989–1003.

Langen, P. L., Fausto, R. S., Vandecrux, B., Mottram, R. H. & Box, J. E. (2017), 'Liquid water flow and retention on the Greenland Ice Sheet in the regional climate model HIRHAM5: Local and large-scale impacts', *Frontiers in Earth Science* **4**, 110.

Langen, P. L., Mottram, R. H., Christensen, J. H., Boberg, F., Rodehacke, C. B., Stendel, M., van As, D., Ahlstrø m, A. P., Mortensen, J., Rysgaard, S., Petersen, D., Svendsen, K. H., Adalgeirsdóttir, G. & Cappelen, J. (2015), 'Quantifying energy and mass fluxes controlling Godthåbsfjord freshwater input in a 5-km simulation (1991-2012)', *Journal of Climate* **28**, 3694–3713.

Lea, J. M., Mair, D. W. F., Nick, F. M., Rea, B. R., Van As, D., Morlighem, M., Nienow, P. W. & Weidick, A. (2014), 'Fluctuations of a Greenlandic tidewater glacier driven by changes in atmospheric forcing: Observations and modelling of Kangiata Nunaata Sermia, 1859-present', *Cryosphere* **8**(6), 2031–2045.

Lewis, S. (2009), *Hydrological Sub-basins of Greenland. Version 1.*, National Snow and Ice Data Center, Boulder, Colorado, USA.

Luckman, A., Benn, D. I., Cottier, F., Bevan, S., Nilsen, F. & Inall, M. (2015), 'Calving rates at tidewater glaciers vary strongly with ocean temperature', *Nature Communications* **6**, 1–7.

Meierbachtol, T., Harper, J. & Humphrey, N. (2013), 'Basal drainage system response to increasing surface melt on the Greenland Ice Sheet', *Science* **341**, 777–779.

Meire, L., Meire, P., Krawczyk, D. W., Arendt, K. E., Yde, J. C., Pedersen, T. J., Hopwood, M. J., Rysgaard, S. & Meysman, F. J. R. (2016), 'High export of dissolved silica from the Greenland Ice Sheet', *Geophysical Research Letters* **43**, 9173–9182.

Meire, L., Moretensen, J., Meire, P., Jull-Pedersen, T., Sejr, M. K., Rysgaard, S. et al. (2017), 'Marine-terminating glaciers sustain high productivity in Greenland fjords', *Global Change Biology* **23**, 5344–5357.

Mernild, S. H., Holland, D. M., Holland, D., Rosing-Asvid, A., Yde, J. C., Liston, G. E. & Steffen, K. (2015), 'Freshwater flux and spatiotemporal simulated runoff variability into Ilulissat Icefjord, West Greenland, linked to salinity and temperature observations near tidewater glacier margins obtained using instrumented ringed seals', *Journal of Physical Oceanography* **45**(5), 1426–1445.

Moon, T. & Joughin, I. (2008), 'Changes in ice front position on Greenland's outlet glaciers from 1992 to 2007', *Journal of Geophysical Research: Earth Surface* **113**(2), 1–10.

Moon, T., Joughin, I., Smith, B. & Howat, I. (2012), '21st-century evolution of Greenland outlet glacier velocities', *Science* **336**(6081), 576–578.

Moon, T., Joughin, I., Smith, B., Van Den Broeke, M. R., Van De Berg, W. J., Noël, B. & Usher, M. (2014), 'Distinct patterns of seasonal Greenland glacier velocity', *Geophysical Research Letters* **41**(20), 7209–7216.

Moon, T., Sutherland, D. A., Carroll, D., Felikson, D., Kehrl, L. & Straneo, F. (2017), 'Subsurface iceberg melt key to Greenland fjord freshwater budget', *Nature Geoscience* **11**(1), 49–54.

Moore, R. D., Trubilowicz, J. & Buttle, J. (2012), 'Prediction of streamflow regime and annual runoff for ungauged basins using a distributed monthly water balance model', *Journal of the American Water Resources Association* **48**(1), 32–42.

Morin, P., Porter, C., Cloutier, M., Howat, I., Noh, M. J., Willis, M., Bates, B. & Williamson, C. (2016), 'ArcticDEM; a publicly available, high resolution elevation model of the Arctic', *EGU General Assembly Conference Abstracts* **18**, 8396.

Morlighem, M., Williams, C. N., Rignot, E., An, L., Arndt, J. E., Bamber, J. L., Catania, G. A. et al. (2017), 'BedMachine v3: Complete bed topography and ocean bathymetry mapping of Greenland from multi-beam echo sounding combined with mass conservation', *Geophysical Research Letters* **44**, 11051–11061.

Mortensen, J., Bendtsen, J., Motyka, R. J., Lennert, K., Truffer, M., Fahnestock, M. & Rysgaard, S. (2013), 'On the seasonal freshwater stratification in the proximity of fast-flowing tidewater outlet glaciers in a sub-Arctic sill fjord', *Journal of Geophysical Research: Oceans* **118**(3), 1382–1395.

Mortensen, J., Lennert, K., Bendtsen, J. & Rysgaard, S. (2011), 'Heat sources for glacial melt in a sub-Arctic fjord (Godthåbsfjord) in contact with the Greenland Ice Sheet', *Journal of Geophysical Research: Oceans* **116**(1), 1–13.

Motyka, R. J., Cassotto, R., Truffer, M., Kjeldsen, K. K., van As, D., Korsgaard, N. J., Fahnestock, M., Howat, I., Langen, P. L., Mortensen, J., Lennert, K. & Rysgaard, S. (2017), 'Asynchronous behavior of outlet glaciers feeding Godthåbsfjord (Nuup Kangerlua) and the triggering of Narsap Sermia's retreat in SW Greenland', *Journal of Glaciology* **63**(238), 288–308.

Motyka, R. J., Dryer, W. P., Amundson, J., Truffer, M. & Fahnestock, M. (2013), 'Rapid submarine melting driven by subglacial discharge, LeConte Glacier, Alaska', *Geophysical Research Letters* **40**(19), 5153–5158.

Motyka, R. J., Hunter, L., Echelmeyer, K. A. & Connor, C. (2003), 'Submarine melting at the terminus of a temperate tidewater glacier, LeConte Glacier, Alaska, U.S.A', *Annals of Glaciology* **36**, 57–65.

Motyka, R. J., Truffer, M., Fahnestock, M., Mortensen, J., Rysgaard, S. & Howat, I. (2011), 'Submarine melting of the 1985 Jakobshavn Isbræ floating tongue and the triggering of the current retreat', *Journal of Geophysical Research: Earth Surface* **116**(1), 1–17.

Moyer, A. N., Nienow, P. W., Gourmelen, N., Sole, A. J. & Slater, D. A. (2017), 'Estimating spring terminus submarine melt rates at a Greenlandic tidewater glacier using satellite imagery', *Frontiers in Earth Science* **5**, 107.

Mugford, R. I. & Dowdeswell, J. A. (2010), 'Modeling iceberg-rafted sedimentation in high-latitude fjord environments', *Journal of Geophysical Research* **115**, F03024.

Murray, T., Scharrer, K., Selmes, N., Booth, A. D., James, T. D., Bevan, S. L., Bradley, J., Cook, S., Llana, L. C., Drocourt, Y., Dyke, L., Goldsack, A., Hughes, A. L., Luckman, A. J. & McGovern, J. (2015), 'Extensive retreat of Greenland tidewater glaciers, 2000-2010', *Arctic, Antarctic, and Alpine Research* **47**(3), 427–447.

Murray, T., Selmes, N., James, T. D., Edwards, S., Martin, I., O'Farrell, T., Aspey, R., Rutt, I., Nettles, M. & Baugé, T. (2013), 'Dynamics of glacier calving at the ungrounded margin of Helheim Glacier, southeast Greenland', *Journal of Geophysical Research Earth Surface* **120**, 964–982.

Nick, F. M., Vieli, A., Howat, L. M. & Joughin, I. (2009), 'Large-scale changes in Greenland outlet glacier dynamics triggered at the terminus', *Nature Geoscience* **2**, 110–114.

Nuth, C. & Kääb, A. (2011), 'Co-registration and bias corrections of satellite elevation data sets for quantifying glacier thickness change', *Cryosphere* **5**, 271–290.

O'Leary, M. & Christoffersen, P. (2013), 'Calving on tidewater glaciers amplified by submarine frontal melting', *Cryosphere* **7**(1), 119–128.

Paul, F., Bolch, T., Kääb, A., Nagler, T., Nuth, C., Scharrer, K., Shepherd, A., Strozzi, T., Ticconi, F., Bhambri, R., Berthier, E., Bevan, S., Gourmelen, N., Heid, T., Jeong, S., Kunz, M., Lauknes, T. R., Luckman, A., Merryman Boncori, J. P., Moholdt, G., Muir, A., Neelmeijer, J., Rankl, M., VanLooy, J. & Van Niel, T. (2013), 'The glaciers climate change initiative: Methods for creating glacier area, elevation change and velocity products', *Remote Sensing of Environment* **162**, 408–426.

Pfeffer, W. T., Meier, M. F. & Illangasekare, T. H. (1991), 'Retention of Greenland runoff by refreezing: Implications for projected future sea level change', *Journal of Geophysical Research* **96**, 22117–22124.

Pritchard, H. D., Arthern, R. J., Vaughan, D. G. & Edwards, L. A. (2009), 'Extensive dynamic thinning on the margins of the Greenland and Antarctic ice sheets', *Nature* **461**, 971–975.

Ribergaard, M. H. (2013), 'Oceanographic investigations off West Greenland 2012', *NAFO Scientific Council Documents* **13/003**.

Rignot, E., Jacobs, S., Mouginot, J. & Scheuchl, B. (2013), 'Ice-shelf melting around Antarctica', *Science* **341**(6143), 266–270.

Rignot, E. & Jacobs, S. S. (2002), 'Rapid bottom melting widespread near Antarctic ice sheet grounding lines', *Science* **296**(5575), 2020–2023.

Rignot, E. & Kanagaratnam, P. (2006), 'Changes in the velocity structure of the Greenland Ice Sheet', *Science* **311**(5763), 986–990.

Rignot, E., Koppes, M. & Velicogna, I. (2010), 'Rapid submarine melting of the calving faces of West Greenland glaciers', *Nature Geoscience* **3**(3), 187–191.

Rignot, E. & Steffen, K. (2008), 'Channelized bottom melting and stability of floating ice shelves', *Geophysical Research Letters* **35**(2), L02503.

Rizzoli, P., Brä utigam, B., Kraus, T., Martone, M. & Krieger, G. (2012), 'Relative height error analysis of TanDEM-X elevation data', *ISPRS Journal of Photogrammetry and Remote Sensing* **73**, 30–38.

Rose, G. A. (2005), 'On distributional responses of North Atlantic fish to climate change', *ICES Journal of Marine Science* **62**(7), 1360–1374.

Rosenau, R., Scheinert, M. & Dietrich, R. (2015), 'A processing system to monitor Greenland outlet glacier velocity variations at decadal and seasonal time scales utilizing the Landsat imagery', *Remote Sensing of Environment* **169**, 1–19.

Ryan, J. C., Hubbard, A. L., Box, J. E., Todd, J., Christoffersen, P., Carr, J. R., Holt, T. O. & Snooke, N. (2015), 'UAV photogrammetry and structure from motion to assess calving dynamics at Store Glacier, a large outlet draining the Greenland ice sheet', *Cryosphere* **9**(1), 1–11.

Schild, K. M. & Hamilton, G. S. (2013), 'Seasonal variations of outlet glacier terminus position in Greenland', *Journal of Glaciology* **59**(216), 759–770.

Schild, K. M., Renshaw, C. E., Benn, D. I., Luckman, A., L, H. R., How, P., Trusel, L., Cottier, F. R., Pramanik, A. & Hulton, N. R. J. (2018), 'Glacier calving rates due to subglacial discharge, fjord circulation, and free convection', *Journal of Geophysical Research: Earth Surface* **123**, 2189–2204.

Schwanghart, W. & Scherler, D. (2014), 'TopoToolBox 2 - MATLAB-based software for topographic analysis and modelling in Earth surface sciences', *Earth Surface Dynamics* **2**, 1–7.

Sciascia, R., Straneo, F., Cenedese, C. & Heimbach, P. (2013), 'Seasonal variability of submarine melt rate and circulation in an East Greenland fjord', *Journal of Geophysical Research: Oceans* **118**(5), 2492–2506.

Seale, A., Christoffersen, P., Mugford, R. I. & O'Leary, M. (2011), 'Ocean forcing of the Greenland Ice Sheet: Calving fronts and patterns of retreat identified by automatic satellite monitoring of eastern outlet glaciers', *Journal of Geophysical Research: Earth Surface* **116**(3), 1–16.

Shean, D. E., Joughin, I. R., Dutrieux, P., Smith, B. E. & Berthier, E. (2018), 'Ice shelf basal melt rates from a high-resolution DEM record for Pine Island Glacier, Antarctica', *Cryosphere Discuss* (doi: 10.5194/tc-2018-209, in review).

Shepherd, A., Ivins, E. R., A, G., Barletta, V. R., Bentley, M. J., Bettadpur, S. et al. (2012), 'A reconciled estimate of ice-sheet mass balance', *Science* **338**, 1183–1189.

Shreve, R. L. (1972), 'Movement of water in glaciers', *Journal of Glaciology* **11**(62), 2015–214.

Slater, D. A., Goldberg, D. N., Nienow, P. W. & Cowton, T. R. (2016), 'Scalings for submarine melting at tidewater glaciers from buoyant plume theory', *Journal of Physical Oceanography* **46**(6), 1839–1855.

Slater, D. A., Nienow, P. W., Cowton, T. R., Goldberg, D. N. & Sole, A. J. (2015), 'Effect of near-terminus subglacial hydrology on tidewater glacier submarine melt rates', *Geophysical Research Letters* **42**(8), 2861–2868.

Slater, D. A., Nienow, P. W., Goldberg, D. N., Cowton, T. R. & Sole, A. J. (2017b), 'A model for tidewater glacier undercutting by submarine melting', *Geophysical Research Letters* **44**(5), 2360–2368.

Slater, D., Nienow, P., Sole, A., Cowton, T., Mottram, R., Langen, P. & Mair, D. (2017a), 'Spatially distributed runoff at the grounding line of a large Greenlandic tidewater glacier inferred from plume modelling', *Journal of Glaciology* **63**(238), 309–323.

Smith, A. M. (1996), 'Ice shelf basal melting at the grounding line, measured from seismic observations', *Journal of Geophysical Research* **101**, 22749–22755.

Smith Jr., K. L., Sherman, A. D., Shaw, T. J. & Sprintall, J. (2013), 'Icebergs as unique Lagrangian ecosystems in polar seas', *Annual Review of Marine Science* **5**, 14.1–14.9.

Sole, A. J., Mair, D. W., Nienow, P. W., Bartholomew, I. D., King, M. A., Burke, M. J. & Joughin, I. (2011), 'Seasonal speedup of a Greenland marine-terminating outlet glacier forced by surface melt-induced changes in subglacial hydrology', *Journal of Geophysical Research: Earth Surface* **116**(3), 1–11.

Storey, J., Choate, M. & Lee, K. (2014), 'Landsat 8 operational land imager on-orbit geometric calibration and performance', *Remote Sensing* **6**, 11127–11152.

Straneo, F. & Cenedese, C. (2015), 'The dynamics of Greenland's glacial fjords and their role in climate', *Annual Review of Marine Science* **7**, 89–112.

Straneo, F., Curry, R. G., Sutherland, D. A., Hamilton, G. S., Cenedese, C., Våge, K. & Stearns, L. A. (2011), 'Impact of fjord dynamics and glacial runoff on the circulation near Helheim Glacier', *Nature Geoscience* **4**(5), 322–327.

Straneo, F., Hamilton, G. S., Sutherland, D. A., Stearns, L. A., Davidson, F., Hammill, M. O., Stenson, G. B. & Rosing-Asvid, A. (2010), 'Rapid circulation of warm subtropical waters in a major glacial fjord in East Greenland', *Nature Geoscience* **3**(3), 182–186.

Straneo, F. & Heimbach, P. (2013), 'North Atlantic warming and the retreat of Greenland's outlet glaciers', *Nature* **504**(7478), 36–43.

Straneo, F., Sutherland, D. A., Holland, D., Gladish, C., Hamilton, G. S., Johnson, H. L., Rignot, E., Xu, Y. & Koppes, M. (2012), 'Characteristics of ocean waters reaching Greenland's glaciers', *Annals of Glaciology* **53**(60), 202–210.

Sulak, D. J., Sutherland, D. A., Enderlin, E. M., Stearns, L. A. & Hamilton, G. S. (2017), 'Iceberg properties and distributions in three Greenlandic fjords using satellite imagery', *Annals of Glaciology* **58**(74), 92–106.

Sundal, A. V., Shepherd, A., van den Broeke, M., van Angelen, J., Gourmelen, N. & Park, J. (2013), 'Controls on short-term variations in Greenland glacier dynamics', *Journal of Glaciology* **59**(217), 883–892.

Sutherland, D. A., Roth, G. E., Hamilton, G. S., Mernild, S. H., Stearns, L. A. & Straneo, F. (2014a), 'Quantifying flow regimes in a Greenland glacial fjord using iceberg drifters', *Geophysical Research Letters* **41**(23), 8411–8420.

Sutherland, D. A. & Straneo, F. (2012), 'Estimating ocean heat transports and submarine melt rates in Sermilik Fjord, Greenland, using lowered acoustic doppler current profiler (LADCP) velocity profiles', *Annals of Glaciology* **53**(60), 50–58.

Sutherland, D. A., Straneo, F. & Pickart, R. S. (2014b), 'Characteristics and dynamics of two major Greenland glacial fjords', *Journal of Geophysical Research: Oceans* **119**(6), 3767–3791.

Tedesco, M., Fettweis, X., Mote, T., Wahr, J., Alexander, P., Box, J. E. & Wouters, B. (2013), 'Evidence and analysis of 2012 Greenland records from spaceborne observations, a regional climate model and reanalysis data', *Cryosphere* **7**, 615–630.

Tedstone, A. J., Nienow, P. W., Gourmelen, N. & Sole, A. J. (2014), 'Greenland ice sheet annual motion insensitive to spatial variations in subglacial hydraulic structure', *Geophysical Research Letters* **41**, 8910–8917.

Todd, J. & Christoffersen, P. (2014), 'Are seasonal calving dynamics forced by buttressing from ice mélange or undercutting by melting? Outcomes from full-Stokes simulations of Store Glacier, West Greenland', *Cryosphere* **8**, 2353–2365.

Toutin, T. (2002), 'Impact of terrain slope and aspect on radargrammetric DEM accuracy', *ISPRS Journal of Photogrammetry and Remote Sensing* **57**(3), 228–240.

Truffer, M. & Motyka, R. J. (2016), 'Where glaciers meet water: Subaqueous melt and its relevance to glaciers in various settings', *Reviews of Geophysics* **54**(1), 220–239.

USGS (2016), Landsat 8 data users handbook, Technical report, United States Geological Society.

Van den Broeke, M. R., Bamber, J. L., Ettema, J., Rignot, E. J., Schrama, E., van de Berg, W. J., van Meijgaard, E., Velicogna, I., Wouters, B., Broeke, M. V. D., Bamber, J. L., Ettema, J., Rignot, E. J., Schrama, E., Berg, W. J. V. D., Meijgaard, E. V.,

Velicogna, I. & Wouters, B. (2009), 'Partitioning recent Greenland mass loss', *Science* **326**(2009), 984–986.

Van den Broeke, M. R., Enderlin, E. M., Howat, I. M., Munneke, P. K., Noë l, B. P. Y., van de Berg, W. J., van Meijgaard, E. & Wouters, B. (2016), 'On the recent contribution of the Greenland Ice Sheet to sea level change', *Cryosphere* **10**(5), 1933–1946.

Vieli, A. & Nick, F. M. (2011), 'Understanding and modeling rapid dynamical changes of tidewater outlet glaciers: issues and implications', *Surveys in Geophysics* **32**, 437–458.

Walsh, K. M., Howat, I. M., Ahn, Y. & Enderlin, E. M. (2012), 'Changes in the marine-terminating glaciers of central east Greenland, 2000-2010', *Cryosphere* **6**(1), 211–220.

Weidick, A., Bennike, O., Citterio, M. & Nørgaard-Pedersen, N. (2012), 'Neoglacial and historical glacier changes around Kangersuneq Fjord in southern West Greenland', *Geological Survey of Denmark and Greenland Bulletin* **27**.

Wilson, N., Straneo, F. & Heimbach, P. (2017), 'Satellite-derived submarine melt rates and mass balance (2011-2015) for Greenland's largest remaining ice tongues', *Cryosphere* **11**(6), 2773–2782.

Xu, Y., Rignot, E., Fenty, I., Menemenlis, D. & Flexas, M. M. (2013), 'Subaqueous melting of Store Glacier, west Greenland from three-dimensional, high-resolution numerical modeling and ocean observations', *Geophysical Research Letters* **40**(17), 4648–4653.

Xu, Y., Rignot, E., Menemenlis, D. & Koppes, M. (2012), 'Numerical experiments on subaqueous melting of Greenland tidewater glaciers in response to ocean warming and enhanced subglacial discharge', *Annals of Glaciology* **53**(60), 229–234.

Appendix A

Moyer et al., 2017, *Frontiers in Earth Science*

frontiers in Earth Science

ORIGINAL RESEARCH
published: 15 December 2017
doi: 10.3389/feart.2017.00107

Estimating Spring Terminus Submarine Melt Rates at a Greenlandic Tidewater Glacier Using Satellite Imagery

Alexis N. Moyer[1], Peter W. Nienow[1], Noel Gourmelen[1,2], Andrew J. Sole[3] and Donald A. Slater[1,4]*

[1] School of Geosciences, University of Edinburgh, Edinburgh, United Kingdom, [2] IPGS UMR 7516, Université de Strasbourg, CNRS, Strasbourg, France, [3] Department of Geography, University of Sheffield, Sheffield, United Kingdom, [4] Scripps Institution of Oceanography, University of California, San Diego, La Jolla, CA, United States

Oceanic forcing of the Greenland Ice Sheet is believed to promote widespread thinning at tidewater glaciers, with submarine melting proposed as a potential trigger of increased glacier calving, retreat, and subsequent acceleration. The precise mechanism(s) driving glacier instability, however, remain poorly understood, and while increasing evidence points to the importance of submarine melting, estimates of melt rates are uncertain. Here we estimate submarine melt rate by examining freeboard changes in the seasonal ice tongue of Kangiata Nunaata Sermia (KNS) at the head of Kangersuneq Fjord (KF), southwest Greenland. We calculate melt rates for March and May 2013 by differencing along-fjord surface elevation, derived from high-resolution TanDEM-X digital elevation models (DEMs), in combination with ice velocities derived from offset tracking applied to TerraSAR-X imagery. Estimated steady state melt rates reach up to $1.4 \pm 0.5\,\mathrm{m\,d^{-1}}$ near the glacier grounding line, with mean values of up to 0.8 ± 0.3 and $0.7 \pm 0.3\,\mathrm{m\,d^{-1}}$ for the eastern and western parts of the ice tongue, respectively. Melt rates decrease with distance from the ice front and vary across the fjord. This methodology reveals spatio-temporal variations in submarine melt rates (SMRs) at tidewater glaciers which develop floating termini, and can be used to improve our understanding of ice-ocean interactions and submarine melting in glacial fjords.

Keywords: submarine melt, ice/ocean interactions, tidewater glaciers, remote sensing, TanDEM-X

OPEN ACCESS

Edited by:
Timothy C. Bartholomaus, University of Idaho, United States

Reviewed by:
Leigh A. Stearns, University of Kansas, United States
Twila Moon, University of Oregon, United States
David F. Porter, Columbia University, United States

****Correspondence:***
Alexis N. Moyer
a.moyer@ed.ac.uk

Specialty section:
This article was submitted to Cryospheric Sciences, a section of the journal Frontiers in Earth Science

Received: *01 September 2017*
Accepted: *04 December 2017*
Published: *15 December 2017*

Citation:
Moyer AN, Nienow PW, Gourmelen N, Sole AJ and Slater DA (2017) Estimating Spring Terminus Submarine Melt Rates at a Greenlandic Tidewater Glacier Using Satellite Imagery. Front. Earth Sci. 5:107. doi: 10.3389/feart.2017.00107

INTRODUCTION

Acceleration of marine-terminating glaciers in Greenland in recent decades has significantly increased the contribution of the ice sheet to sea level (Enderlin et al., 2014). Many of these glaciers are in contact with relatively warm ocean water (Holland et al., 2008; Straneo et al., 2012; Carr et al., 2013; Motyka et al., 2013), and submarine melting at the ice-ocean interface has been proposed as a potential trigger of glacier calving, retreat and acceleration (Nick et al., 2009; O'Leary and Christoffersen, 2013; Luckman et al., 2015). The spatial distribution of submarine melting along an ice front can impact grounding line stability and influence ice front shape by undercutting, overcutting, and creating embayments (Straneo et al., 2012; Carroll et al., 2015; Fried et al., 2015). These changes in ice front shape likely affect calving processes and can create locations along the

ice front where calving preferentially occurs (Chauché et al., 2014; Luckman et al., 2015). The dynamic coupling between glacier margins and upstream ice enables oceanic forcing of tidewater glaciers to promote widespread thinning, increased glacier retreat, calving and velocity, and consequent mass loss (e.g., Joughin et al., 2004; van den Broeke et al., 2009; Vieli and Nick, 2011; Carr et al., 2013; Goelzer et al., 2013; Sundal et al., 2013; Straneo and Cenedese, 2015).

Despite their potential importance for ice dynamics, submarine melt rates (SMRs) are poorly constrained, because collecting in situ measurements near actively-calving glacier termini is both difficult and dangerous (e.g., Mortensen et al., 2011, 2013; Lea et al., 2014). Numerous studies have instead used hydrographic profiles from glacial fjords to estimate the net heat flux available for melting ice, resulting in SMRs up to 16.8 ± 1.3 m d^{-1} in Alaska (Motyka et al., 2003, 2013) and ranging from 0.7 ± 0.2 to 10.1 m d^{-1} in Greenland (Rignot et al., 2010; Sutherland and Straneo, 2012; Inall et al., 2014). Other studies have used general circulation models or plume theory to estimate SMR (e.g., Jenkins, 2011; Christoffersen et al., 2012; Sciascia et al., 2013; Xu et al., 2013; Slater et al., 2015), resulting in melt rates ranging from 0.12 to 3.6 m d^{-1} in Greenland. However, most measurements used to estimate SMR from heat flux methods or to constrain model parameters are taken far from the grounding line (15–80 km away) (e.g., Johnson et al., 2011; Christoffersen et al., 2012; Sutherland and Straneo, 2012; Inall et al., 2014), and are therefore integrating all the processes that will affect the heat flux between the measurement site and the terminus, including heat lost to the melting of icebergs, sea ice, and mélange at considerable distances from the grounding line. SMRs estimated from fjord heat flux are also uncertain due to the temporal variability in fjord circulation, so that it is not clear how representative an estimate is of the longer term mean (Jackson and Straneo, 2016).

Alternative approaches to estimating glacier submarine melt rate utilize remotely sensed observations. Several studies have quantified SMR by accounting for ice flux divergence and surface mass balance of floating ice shelves and tongues (e.g., Rignot and Jacobs, 2002; Depoorter et al., 2013; Enderlin and Howat, 2013; Rignot et al., 2013; Gourmelen et al., 2017). This approach has generated SMRs up to 0.11 m d^{-1} beneath ice shelves in Antarctica (Rignot and Jacobs, 2002) and ranging from 0.03 ± 0.02 to 2.9 ± 0.65 m d^{-1} beneath floating glacier tongues in Greenland (Enderlin and Howat, 2013). Enderlin and Hamilton (2014) also used remotely sensed observations to estimate submarine melt, using changes in iceberg freeboard derived from high-resolution digital elevation models (DEMs) to estimate iceberg volume loss, which was then used to estimate area-averaged iceberg SMRs. During the summers of 2011 and 2013, estimated iceberg SMR was 0.39 ± 0.17 m d^{-1} in Sermilik Fjord, east Greenland. Here we also employ a remote sensing approach, using satellite radar data to estimate near-terminus SMR from spatial and temporal changes in seasonal ice tongue freeboard adjacent to a large tidewater glacier in southwest Greenland.

STUDY AREA

Located at the head of Kangersuneq Fjord (KF), Kangiata Nunaata Sermia (KNS), the largest tidewater glacier in southwest Greenland, drains ∼2% of the ice sheet (Sole et al., 2011; **Figure 1**). The ice front is ∼4.5 km wide with a maximum grounding line depth of ∼250 m below sea level (Mortensen et al., 2013). KNS has retreated at least 22 km from its Little Ice Age maximum extent, following increased air and sea surface temperatures (Lea et al., 2014). For the past 15 years, with the exception of 2011 and 2015, a thick seasonal ice tongue contiguous with the glacier forms by mid-winter and advances down-fjord prior to rapid break-up in late-spring (Motyka et al., 2017; **Figure 2**). The floating ice tongue flows directly across the glacier grounding line (e.g., with no gap or calving processes occurring between the grounded and floating ice) with near spatially consistent velocity (see Supplementary Figures 1, 2). On average, the ice tongue has a length between 2 and 3 km, and decreases in freeboard with distance from the grounding line (**Figure 2**). The fjord waters adjacent to the front of the ice tongue are typically packed with dense ice mélange (i.e., mixture of sea ice, bergy bits, and icebergs) during the winter and spring months before breaking up in late spring.

Mortensen et al. (2011, 2013) performed detailed analyses on the characteristics of the waters and heat sources entering KF and reaching to within ∼4 km of the KNS terminus. Classical two-layered buoyancy-driven circulation operates in the fjord primarily during the spring and summer, where circulation is driven by subglacial meltwater plumes (**Figure 3**). Subglacial discharge exits the glacier at the grounding line, rises buoyantly along the ice front due to its lower density relative to the ambient fjord water, and flows down-fjord once neutral buoyancy is reached (Motyka et al., 2003; Jenkins, 2011; Cowton et al., 2015). In fjords with shallow glacier grounding line depths (<500 m) like KNS, summer discharge meltwater plumes often reach neutral buoyancy and horizontally enter the fjord within the upper 100 m of the water column (Carroll et al., 2016). The outflow forced by the subglacial discharge establishes an estuarine circulation cell, drawing in coastal waters from the shelf, which flow in a layer beneath the fresher outflow (Motyka et al., 2003; Mortensen et al., 2011). This warm coastal water is then entrained into the subglacial discharge plume, and melts the ice front and underside of the ice tongue as it rises.

DATA AND METHODOLOGY

DEM and Ice Velocity Data Generation

We used TanDEM-X and TerraSAR-X imagery from 2013 to estimate ice tongue freeboard and velocity, respectively. TerraSAR-X has a repeat period of 11 days and both satellites have spatial resolution on the order of a meter (Krieger et al., 2007; Eineder et al., 2011), thereby providing excellent temporal and spatial resolution for observing changes in ice tongue velocity and freeboard. The radar platforms enabled us to use imagery acquired in non-daylight hours and cloudy conditions, in contrast to optical platforms. Time lapse camera

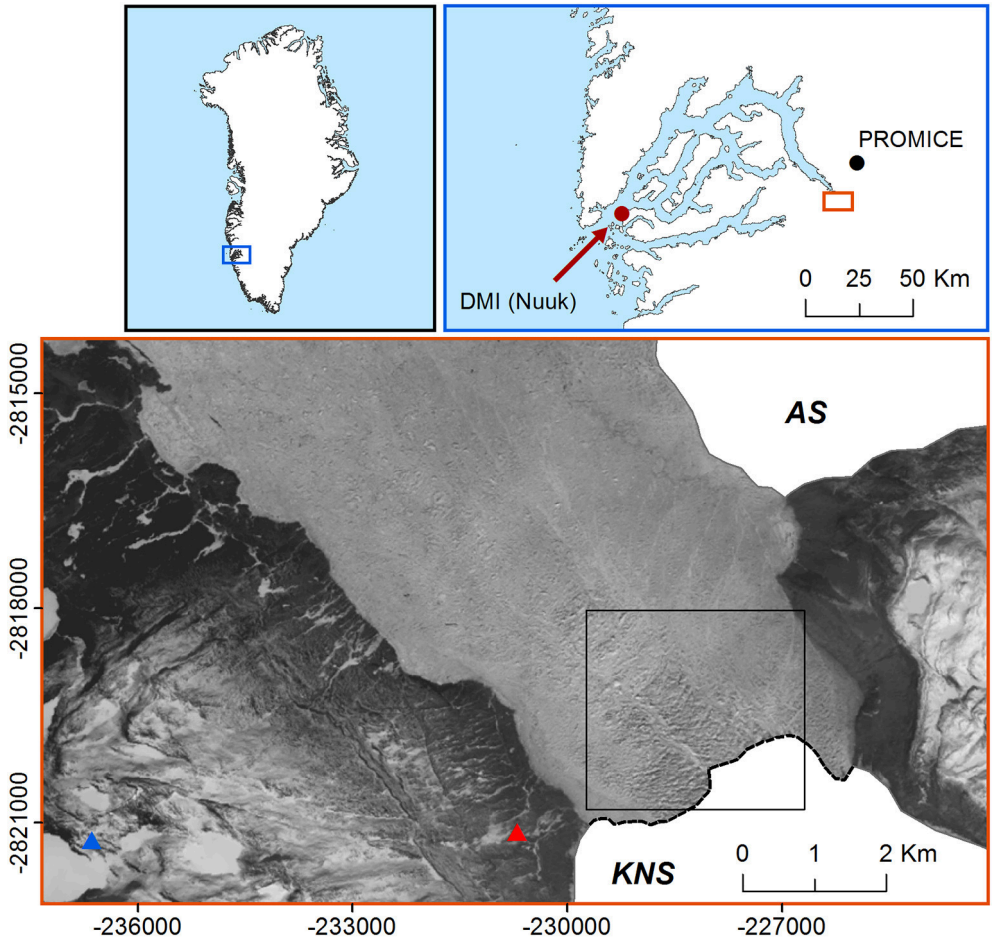

FIGURE 1 | Map of study area, including Kangiata Nunaata Sermia (KNS) and Akullersuup Sermia (AS) glaciers and ice tongue and mélange, from Landsat 8 satellite image acquired for May 1, 2013 (bottom panel).The red and blue triangles indicate the locations of the University of Alaska Fairbanks (2013) and our (2009) time lapse cameras, respectively, and the black box indicates the extent of **Figures 4A,B**. The red and black dots in the fjord scale locator map (top right panel) indicate the locations of the Danish Meteorological Institute (DMI) and GEUS PROMICE weather stations, respectively.

imagery near the terminus of KNS (**Figure 1**) every 4 h from January to June 2013 (courtesy of M. Truffer and M. Fahnestock, University of Alaska Fairbanks) was used to visually confirm the formation, presence, and break-up of the ice tongue.

We derived two 2.5 m resolution DEMs dated 17 March and 27 May 2013 from conventional SAR interferometric processing of bi-static TanDEM-X imagery (Dehecq et al., 2016). GIMPDEM (Howat et al., 2014) was used as a reference during the unwrapping stage to minimize unwrapping errors. The DEMs produced must be correctly aligned, both horizontally and vertically, using known stable areas (e.g., bedrock outcrops) that are not covered by ice or snow. To perform this calibration, we used ICESat elevation data over non-ice terrain as defined by the GIMP land classification mask (Howat et al., 2014). A horizontal shift (3.9 and 3.3 m in the x and y directions, respectively) between the TanDEM-X derived DEMs and ICESat over non-ice covered terrain was calculated by fitting a sinusoidal relationship between elevation differences and terrain aspect (Nuth and Kääb, 2011). A vertical shift with a linear dependence on location (tilt) was estimated for each DEM using a least-squares regression:

$$dh\,(X, Y) = a_0 + a_1 X + a_2 Y \quad (1)$$

where dh are elevation differences in stable areas, X and Y the easting and northing and a_i the parameters to be estimated. This shift was then subtracted at each pixel. For this step, which is more sensitive to outliers, all points with a slope higher than 40° were excluded. The DEMs were then converted from ellipsoid to elevation above the EIGEN-EC4 geoid.

Due to the limited coverage of the ICESat lines over non-ice terrain (see Supplementary Figure 3), an additional tilt in the DEMs was identified and subsequently corrected for using Operation IceBridge (OIB) Airborne Topographic Mapper (ATM) L1B Elevation and Return Strength data (Krabill, 2016). OIB ATM elevation points were acquired for three springs when the seasonal ice tongue was present in the fjord (08 April 2011, 25 April 2012, and 15 April 2014). TanDEM-X elevations from

FIGURE 2 | Example photographs from our 2009 time lapse camera (see **Figure 1** for location) demonstrating **(A)** the intact ice tongue on 25 May 2009 and **(B)** the glacier terminus on 19 July 2009, post-ice tongue disintegration.

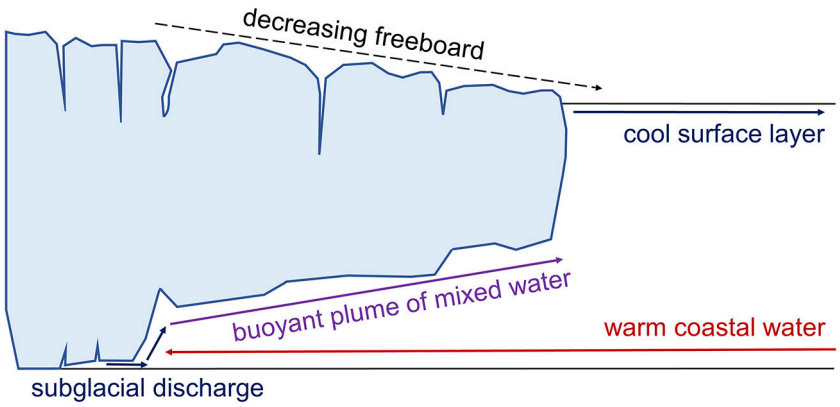

FIGURE 3 | Schematic of intact ice tongue showing buoyancy-driven circulation in the fjord, as well as the characteristic decrease in ice tongue freeboard (and thus thickness) away from the ice front.

17 March 2013 were extracted for spatially corresponding 2011 OIB ATM points and the difference taken over open water where the OIB data had a slope of near-zero (20 to 25 km from the ice front). The slope of the difference was taken as the trend (or tilt; ∼0.45 m height per km distance along-fjord) in the TanDEM-X elevations and was removed, effectively de-trending the dataset (see Supplemental Figure 4). The same correction was applied to elevations from the 27 March 2013 DEM, as the tilt was the same as that for the 17 March.

Three 20 m resolution ice tongue velocity maps were created based on conventional feature tracking applied to TerraSAR-X imagery (Tedstone et al., 2014) for the following 2013 image pairs: 12–23 February, 8–19 April, and 30 April to 11 May. Ice velocity on 17 March (Supplemental Figure 1A), the date of our first DEM, was estimated assuming a linear trend in velocity between the velocity maps from 12–23 February to 8–19 April, and ranges from 28.5 to 30.5 m d^{-1} over the ice tongue. The last available velocity map was from 30 April to 11 May

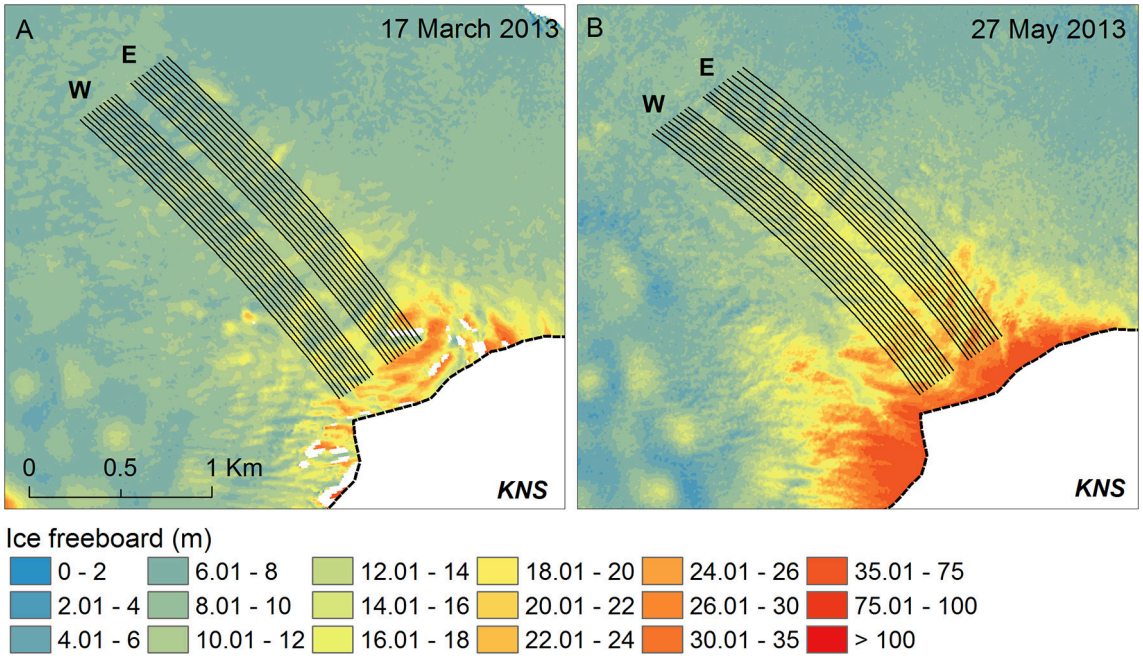

FIGURE 4 | Eastern (E) and western (W) ice flowlines, overlain on TanDEM-X ice tongue freeboard from **(A)** 17 March 2013 and **(B)** 27 May 2013. Refer to **Figure 1** for location.

(Supplemental Figure 1B), and throughout the paper, we use this velocity epoch to correspond with our second DEM, acquired on 27 May. Ice tongue velocities in May range from 20.5 to 23.5 m d^{-1}.

Ice Flowline Construction

We constructed flowlines along the ice tongue using our ice velocity results to track flow direction. Ten points near the glacier grounding line were chosen from both the eastern and western side of the ice tongue, with ∼25 m between points in the across-flow direction (**Figure 4**). To accommodate temporal changes in ice velocity, two separate sets of flowlines were created, one for March and one for May, using our velocity maps from 17 March and 30 April to 11 May, respectively. Velocity vectors were extracted for each initial point, enabling the extraction of flow direction, which was then taken at points every 50 m moving down-fjord until the end of the ice tongue. The points were then connected, creating flowlines of ice moving down-fjord away from the grounding line (**Figure 4**). Distance from the grounding line was averaged for each set of flowlines (i.e., eastern and western), using the end of spring terminus position (**Figure 1**) digitized from a Landsat 8 image from 10 June 2013.

Estimating Ice Tongue Surface Melt Rates

Observed reduction in ice tongue freeboard as it is advected into the fjord can be attributed to changes in surface mass balance, longitudinal and lateral spreading, and submarine melting. To assess the potential contribution from surface mass balance, surface melt was estimated using a simple positive degree day (PDD) model (Hock, 2003) with a degree day factor for snow (*ddfs*) of 4.5 mm d^{-1} $°C^{-1}$, as used by Slater et al. (2017) for KNS. Air temperature (°C) data were acquired from the nearby Geological Survey of Denmark and Greenland (GEUS) PROMICE weather station (NUK_L, 550 m a.s.l., 64°28′55.2″ N, 49°31′50.88″ W, ∼21 km from KNS) (Ahlstrom et al., 2008; **Figure 1**), using a lapse rate of 0.5°C per 100 m to adjust the temperatures to sea level (Slater et al., 2017). Precipitation data were acquired from the Danish Meteorological Institute (DMI) weather station in Nuuk (NUUK 4250, 80 m a.s.l., 64°10′0.12″ N, 51°45′0″ W, ∼105 km from KNS) (Cappelen, 2016; **Figure 1**).

Estimating Submarine Melt Rate (SMR)

SMR for all ice flowlines were estimated for both steady and non-steady state scenarios. A steady state scenario assumes ice thickness at a fixed location does not change in time, whereas a non-steady state scenario allows for changes in ice thickness at a fixed location (e.g., thinning due to high submarine melting exceeding the delivery of ice across the grounding line or changes in the thickness of ice being advected across the grounding line). As estimating a non-steady state scenario requires at least two elevation estimates, a steady state (i.e., $\partial H/\partial t = 0$) is often assumed due to lack of data (e.g., Jenkins and Doake, 1991; Smith, 1996; Johnson et al., 2011). The two scenarios are presented here for comparison purposes, in part to test the validity of our method for years with only one DEM, when determining SMR by assuming a steady state scenario would be the only option. For a steady state scenario (SS), elevation values along each ice flowline were extracted from both the 17 March and 27 May 2013 DEMs. To reduce the impact of short-length scale elevation changes, including crevasses, in the fractured tongue (see **Figure 2**) on our

melt rate estimates, flowline elevations were smoothed using a two-sided moving average with a 625 m window (see **Figures 5A**, **6A**). Elevation data were then converted to ice thickness using ocean water (1,027 kg m^{-3}; Ribergaard, 2013) and ice (900 kg m^{-3} following Enderlin and Hamilton, 2014) densities, assuming the ice is floating in hydrostatic equilibrium; an assumption supported by both the best available bathymetry (Mortensen et al., 2013; Motyka et al., 2017) and the observation of the rapid and total disintegration of the ice tongue within just a 4-h time window on 15 June 2013.

SMR_{SS} were calculated for both March and May, accounting for thinning due to stretching in both the flow direction (second term on right-hand side of Equation 2) and perpendicular to flow (third term on right-hand side of Equation 2):

$$SMR_{SS} = -v_x \frac{\partial H}{\partial x} - H\frac{\partial v_x}{\partial x} - H\frac{\partial v_y}{\partial y} \quad (2)$$

where H is the ice thickness (m), v_x and v_y are the ice velocity (m d^{-1}) in the along- and across-flowline direction, and x and y represent distance in the along- and across-flowline direction.

Note that a term representing across-flow thinning, $-v_y \frac{\partial H}{\partial y}$, does not contribute because, by definition of a flowline, $v_y = 0$ on the flowline. The final term in Equation (2) does however make a small contribution due to the convergence or divergence of different flowlines. Derivatives in Equation (2) are evaluated using conventional finite differences with a spacing $\Delta x = 50$ m and $\Delta y = 25$ m.

For a non-steady state scenario (NSS), a linear trend of thickness change between 17 March and 27 May 2013 was assumed at each point on the flowlines and accounted for by subtracting a daily rate of change (m d^{-1}) from the estimated SMR_{SS} (Rignot et al., 2013):

$$SMR_{NSS} = SMR_{SS} - \frac{\Delta H_{NSS}}{\Delta t} \quad (3)$$

where ΔH_{NSS} (m) is the difference in ice thickness between the two dates and Δt (d) is the time between the two dates.

Melt rates were then averaged to produce a mean SMR_{SS} and SMR_{NSS} for the western and eastern flowlines. To capture the general trend in melt rates, lines of best fit were applied to both steady and non-steady state estimates.

Error Analysis

Potential errors were traced throughout the analysis and standard error propagation methods were used to calculate the effect of errors in both elevation and ice velocity on estimated SMR. Errors in elevation values are from three primary sources: (1) DEM construction (including correction using ICESat), (2) correcting TanDEM-X elevations using OIB ATM data, and (3) smoothing the elevations for melt rate calculations. Error resulting from DEM construction is ±2 m, a general error for the TanDEM-X derived DEMs over areas with a slope <12° (Rizzoli et al., 2012), which is likely an overestimate over the relatively low-sloped ice tongue (<0.15°). As our calculations utilize the elevation gradient and not the absolute elevation, we instead account for a gradient error of ±0.35 m over the nearly 2 km ice tongue. This gradient error was estimated over 2 km segments (the same length over which SMRs were estimated) of a section of very thin ice mélange where successive OIB ATM flights show near-constant slope. The gradient error was estimated as the largest difference in slope between the corrected TanDEM-X elevation flowlines and the OIB ATM lines. Fitting the TanDEM-X elevations to the OIB ATM elevations results in a root mean square error of

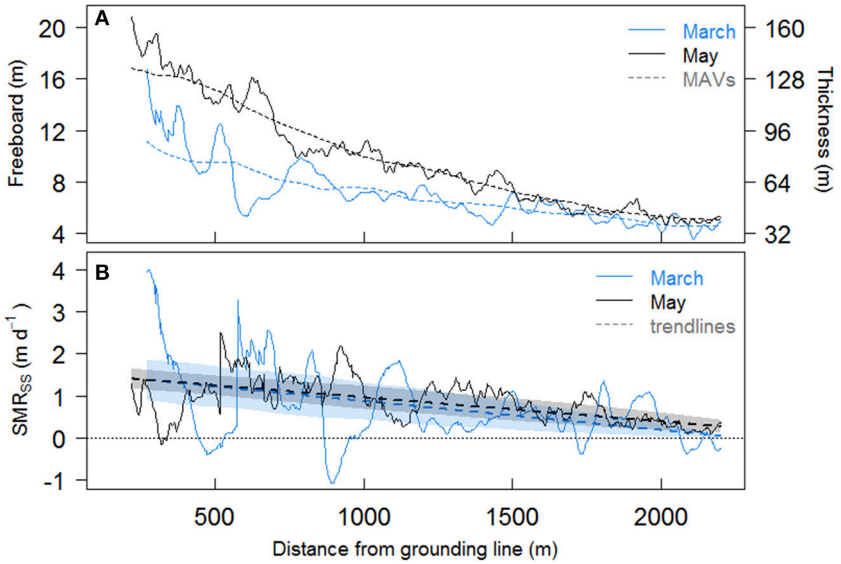

FIGURE 5 | (A) Ice freeboard and thickness (m) on 17 March and 27 May 2013 with distance from KNS terminus for the eastern flowlines, where solid lines are means from 10 flowlines (**Figure 4**) and dashed lines are moving averages (MAVs) of the mean; **(B)** Steady state estimated submarine melt rate (SMR_{SS}) for eastern flowlines, with dashed trendlines and shaded error ranges.

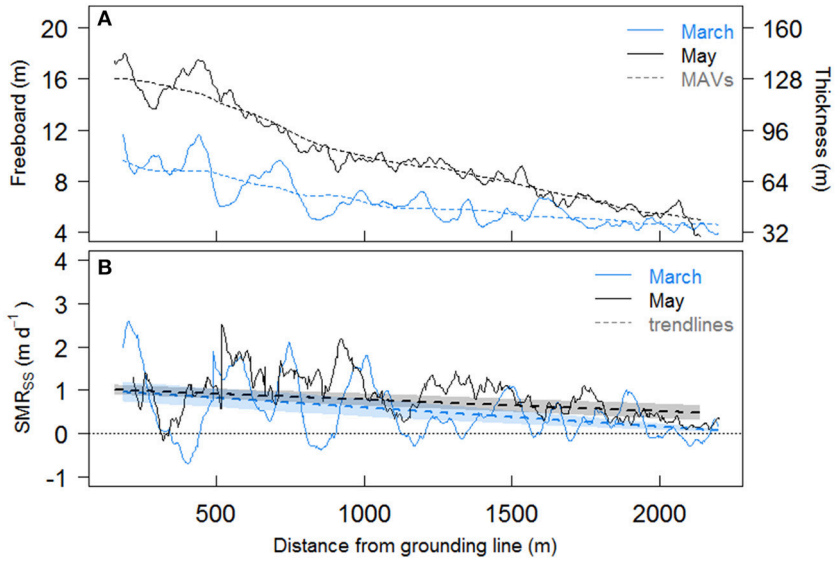

FIGURE 6 | (A) Ice freeboard and thickness (m) on 17 March and 27 May 2013 with distance from KNS terminus for the western flowlines, where solid lines are means from 10 flowlines (**Figure 4**) and dashed lines are moving averages (MAVs) of the mean; **(B)** Steady state estimated submarine melt rate (SMR_{SS}) for western flowlines, with dashed trendlines and shaded error ranges.

±0.38 m, and smoothing the flowlines results in maximum mean squared errors of ±0.86 and ±0.47 m for the eastern and western flowlines, respectively. The maximum total error for any one point in elevation along the eastern and western flowlines is ±1.4 and ±0.64 m, respectively.

Following Paul et al. (2015), error in ice velocity was estimated as ±0.09 m d^{-1}, resulting from the feature tracking process applied to stable areas of the ice tongue, where crevassing is easily trackable and ice deformation is low. Errors in velocity at locations within 150 m of the original position of the previous end of summer vertical ice-front (which likely corresponds to the grounding line) and at the edge of the ice tongue are not considered, as we did not use any velocities from these regions in our SMR estimations.

While the error estimates cited alongside our SMRs account for errors in the DEMs and ice velocity maps, there are several additional sources of error that, although difficult to quantify, must be considered. The assumption of both steady and non-state state scenarios for ice tongue thickness likely introduces error in our SMR estimates. We know the ice tongue is not in steady state between March and May 2013, as the glacier is slower and the ice is thicker in May than in March for any given point. Since we have only two DEMs, we can only assume a linear thickening trend over the time period (see Equation 3). Any deviation from this trend would affect our melt rate estimates. For example, if the ice tongue was thickest in April, this would imply the ice tongue was thinning between April and May, increasing NSS melt rates estimated using Equation 3. Thus, if the tongue was thickest in April, our May melt rate estimates would be an underestimate; however without additional DEMs we cannot address this possibility.

Another potential source of error derives from smoothing the ice freeboard near the glacier grounding line, where pre-smoothed freeboard values decrease sharply, as compared with smoothed values (see **Figures 5A**, **6A**). While smoothing out fracturing associated with large crevasses on the ice tongue helps to reduce noise in the SMR estimates, the resultant reduction in freeboard gradient significantly lowers our SMRs near the grounding line, which should therefore be considered minimum estimates of melt rate in this location.

RESULTS

SMR Estimates in Kangersuneq Fjord

The reduction in smoothed ice freeboard (and thus thickness) with distance down-fjord from the grounded KNS terminus in the March DEM (**Figures 5A**, **6A** for eastern and western flowlines, respectively), combined with the interpolated ice velocities, results in SMR_{SS} for the eastern and western flowline sets of up to 1.4 ± 0.5 m d^{-1} (mean = 0.7 ± 0.4 m d^{-1}) and 1.0 ± 0.2 m d^{-1} (mean = 0.5 ± 0.2 m d^{-1}), respectively (see lines of fit in **Figures 5B**, **6B**). Due to thickening of the ice via advection, estimated SMR_{NSS} for each set of flowlines (not shown) are less than those estimated for the steady state scenario, with mean decreases in melt rate of 15 and 28% for the eastern and western flowlines, respectively. For all flowlines, melt rates broadly decrease with distance from the KNS grounding line and moving from east to west across the ice tongue.

SMR_{SS} estimated in May are similar to those in March, with eastern and western flowline SMRs of up to 1.4 ± 0.2 m d^{-1} (mean = 0.8 ± 0.3 m d^{-1}) and 1.0 ± 0.1 m d^{-1} (mean = 0.7 ± 0.3 m d^{-1}), respectively (see lines of fit in **Figures 5B**, **6B**). Estimated SMR_{NSS} for each set of flowlines are again less than

those estimated for the steady state scenario, decreasing by 3 and 10% for eastern and western flowlines, respectively. SMRs in May show the same spatial variability as seen in March.

While the heavily crevassed nature of the ice tongue itself is not unphysical, it leads to unphysical noise in our melt rate estimates. For example, the rapid decrease in thickness between two adjacent points over a crevasse (one on the ice tongue surface and one at the bottom of the crevasse) is interpreted as thinning using our method, and thus the estimated SMR would be erroneously high (e.g., the peak in March SMR ∼570 m from the grounding line, **Figure 5B**). In contrast, the rapid increase in thickness between a point at the bottom of the same crevasse and ice tongue surface on the other side is interpreted as thickening of the ice, resulting in a negative melt rate (e.g., negative March SMRs, **Figure 5B**). To exclude these anomalous melt rates, we use the lines of best fit as seen in **Figures 5B**, **6B** to interpret the broader trends in estimated SMR. As they are the same order of magnitude as the non-steady state scenario, we use our steady state scenario melt rates in our subsequent analyses, which allows for comparison to melt rates estimated in years when only one DEM is available (i.e., assumed steady state). In addition, we note again that our melt rates near the grounding line should be considered minimum estimates, as the smoothing of crevasses greatly reduces freeboard gradient here.

Surface Melt Estimates over the Ice Tongue

For the study period, between 17 March and 27 May 2013, total surface snow melt over the ice tongue was 0.48 m water equivalent and total precipitation as snow was 0.23 m. We expect precipitation to be less over the ice tongue than that recorded in Nuuk, given the low elevation of the ice tongue and the rain shadow effect of the coastal mountains. A previous study estimated spring average precipitation decreases between coastal and inland weather stations in western Greenland between ∼0.5 and 0.8 mm per km inland (Abermann et al., 2017). Therefore, if anything, by using the estimates of precipitation from Nuuk we overestimate spring snowfall. Regardless, the estimates of precipitation are still orders of magnitude lower (in terms of water equivalent and impact therefore on freeboard) than our estimated SMRs. The resultant mean surface melt rate, 0.004 m d^{-1}, taken over the 71 days of the study period, is approximately two orders of magnitude less than the rate of change in ice thickness over the same time period, and thus considered negligible. As the PDD sum for 2013 during our study period (16.3°C day) is ∼75% lower than the mean for the last decade (mean from 17 March to 27 May for 2008 to 2016 of 69.4°C day), 2013 should be considered a low spring surface melt and runoff year.

DISCUSSION

Spatial Variability in SMR

Submarine melt rates show along-fjord variability, generally decreasing with distance down-fjord from the KNS grounding line. This variability is likely driven by both the velocity and temperature of subglacial meltwater plumes, with SMR scaling with velocity and ambient fjord temperature (e.g., Holland and Jenkins, 1999; Jenkins, 2011). Mortensen et al. (2013) investigated winter circulation and water properties in 2009 in KF, finding a cool surface layer (ranging from −1.4 to 1.0°C at 0 and 40 m depth, respectively) overlaying a warmer intermediate-depth layer (increasing from 1.3 to 1.8°C at 50 to 90 m depth), below which temperature was relatively constant (1.8°C) with depth. Motyka et al. (2017) investigated summer fjord water properties in 2011, ∼22 km from the KNS ice front, again finding a cool surface layer (ranging from 0 to 1.0°C at 0 and 40 m depth, respectively) overlaying an even warmer intermediate layer (increasing from 2.0 to 2.5°C at 50 to 150 m depth). Therefore, the ambient fjord water entrained by any subglacial plumes will be cooler with increasing distance from the grounding line, as the thinning ice tongue, and shallower draft, will be submerged in shallower, colder surface water. Plume velocity also decreases with distance from the ice front as the plume loses buoyancy (Jenkins, 2011). For these reasons, and as expected, our estimated SMRs approach 0 m d^{-1} down-fjord of the grounding line. The presence of thick sea ice down-fjord of the end of the ice tongue supports this expectation, suggesting the surface waters are very cold, resulting in little or no submarine melting (or else there would be no sea ice). This result is dissimilar to summer melt rates derived from icebergs found tens of kilometers from glacier grounding lines in other Greenlandic fjords (Enderlin and Hamilton, 2014), which we would expect to be higher, due to deeper iceberg keel depths (as compared to the shallow ice tongue depth) and stronger buoyancy-driven circulation from higher subglacial discharge in the summer (Sciascia et al., 2013).

SMRs also show across-fjord variability, with higher melt rates in the eastern section of the main ice tongue, compared to the western part. Across-fjord variability may be driven by water temperature, both in the ambient water column and thus the plume, and by the strength (i.e., velocity) of any buoyant runoff plume present. The eastern part of the ice tongue had the highest March surface elevation, and thus the greatest thickness and deepest keel depth (**Figure 5A**). Reaching over 80 m beneath the fjord surface near the grounding line, ice along the eastern flowlines is exposed to relatively warm, intermediate-depth waters, which promote more rapid submarine melting (Enderlin and Hamilton, 2014; Enderlin et al., 2016). In comparison, ice in the western part of the tongue has a keel depth near the ice front of <70 m, which could explain, in part, the lower SMR in this area of the fjord, as the shallower ice keel is exposed to slightly cooler waters than the eastern part of the tongue.

Across-fjord variability in SMR may also reflect the strength and location of any subglacial meltwater plumes emerging at the glacier grounding line. Uniform across-fjord ice tongue SMR would be expected, if keel depths are constant, where spatially well-distributed meltwaters emerge at the grounding line (Slater et al., 2015). Conversely, spatially-focused, high SMRs near the ice front may indicate a locally dominant subglacial meltwater channel, which in this case could be emerging preferentially under the eastern part of the ice tongue. Slater et al. (2017) inferred KNS subglacial runoff distribution using plume observations from summer 2009 time lapse imagery, suggesting that runoff likely exits under the grounding line via spatially

distributed channels, with sporadic focusing resulting in visible surface plumes. During the mid- to late melt season, plumes typically reach the surface to the west of the grounding line center, with infrequently visible plumes emerging on the eastern side of fjord (Slater et al., 2017). However, as the presence of the ice tongue and surrounding thick ice mélange prevents the expression of plumes on the surface, it is difficult to interpret subglacial meltwater distribution during the winter and spring months.

In addition, rotational circulation in the fjord should be considered, which could impact the across-fjord distribution of surface meltwater and water entering the fjord at depth (Cottier et al., 2010; Straneo and Cenedese, 2015), and thus the heat available for melting ice. Using data from Mortensen et al. (2013), we assume a 30 m thick fresh surface layer of sea ice/ice tongue/glacier meltwater overlaying transitional layers of ice melt and fjord source water, which gives an internal Rossby radius of ∼6 km. As the fjord width varies between 4 and 6 km, rotational effects are unlikely to have a primary role in controlling fjord circulation. However, they may have a secondary effect, focusing the flow of water toward and away from the glacier terminus to the right hand side in the direction of flow (e.g., Cottier et al., 2010; Sutherland et al., 2014).

Temporal Variability in SMR

Estimated mean SMRs do not show significant temporal variability, potentially due to the fact that all melt rates are estimated in the spring, prior to the on-set of substantial surface melt. While estimated monthly total surface snow melt from degree day modeling was higher in May (0.26 m) than in March (0.11 m), we do not expect or see significant differences in SMRs given how small these early spring surface melt rates are. However, increased surface melt later in the melt season and the associated enhanced subglacial meltwater plumes, combined with increased intermediate depth water temperatures (Mortensen et al., 2013; Motyka et al., 2017) would be expected to amplify local SMR considerably compared to winter melting (Jackson and Straneo, 2016). Such estimates would however not be possible using our method as the ice tongue breaks up in early June each year, and is thus absent during the summer and autumn months.

Seasonal stratification and water temperature at depth are highly dependent on the mode of circulation in KF (Mortensen et al., 2011). In the spring, when we estimate SMR, circulation is mainly driven by dense coastal inflows and tidal mixing, which act to cool and slightly freshen waters at intermediate depths. The presence of subglacial meltwater plumes sourced from frictional basal meltwater emerging at the glacier grounding line (Christoffersen et al., 2012) likely also play a role in controlling fjord circulation and submarine melting in the winter and early spring. In the summer, however, tidal mixing and subglacially-driven circulation, via surface-derived meltwater plumes, are dominant and act to freshen and significantly warm the upper intermediate water layer (Mortensen et al., 2013). Temperature differences of nearly 2°C were seen at intermediate depths (between 120 and 150 m) between April and September 2010 (Motyka et al., 2017), an increase which would have a significant impact on the melting of submerged ice.

In order to investigate the potential role that basal frictional meltwater could play in driving plumes in winter, we estimate basal meltwater flux for the area of KNS between the grounding line and ∼11 km up-ice from the grounding line. As basal drag is unknown for KNS, we assume drag is of a similar magnitude to that estimated for Jakobshavn Isbræ, ∼200 kPa (Iken et al., 1993; Funk et al., 1994), as used for Kangerdlugssuaq Glacier by Christoffersen et al. (2012). Using our TerraSAR-X derived velocities for March and May for the lower 11 km of the glacier, an ice density of 900 kg m^{-3}, and a latent heat of fusion of 334 kJ kg^{-1}, basal meltwater flux was estimated as 3.2 m^3 s^{-1}, for both March and May. Although producing weak plumes, subglacial discharge of this magnitude can generate point source SMRs of between 2 and 4 m d^{-1} (Slater et al., 2015). Due to their lower velocity, weak plumes, such as those expected via basal frictional melting, reach neutral buoyancy before reaching the fjord surface (Christoffersen et al., 2012; Slater et al., 2015; Carroll et al., 2016). However, close to the glacier grounding line, where ice tongue keel depth is greatest, weaker plumes will likely still reach and melt the base of the ice tongue. In comparison, higher subglacial discharge (between 50 and 100 m^3 s^{-1}), as might be expected later in the melt season, can result in point source SMRs up to 7 m d^{-1} (Slater et al., 2015). These stronger plumes may reach the fjord surface before reaching neutral buoyancy, thus allowing for melting of the full ice front depth (Slater et al., 2015).

Comparison with Previous SMR Estimates from Greenland

Submarine melt rates estimated in this study are greater than, but of the same order of magnitude, as those estimated for icebergs during summer in Sermilik Fjord, southeast Greenland. Using repeat high-resolution satellite imagery, Enderlin and Hamilton (2014) estimated SMRs of 0.39 ± 0.17 m d^{-1} for icebergs located up to 60 km from the terminus of Helheim Glacier between August 2011 and July 2013. Using our lines of best fit, our estimated SMRs (up to 1.4 m d^{-1}) are more than double those of Enderlin and Hamilton (2014). Given the close proximity to the grounding line, our estimated SMRs may reflect the influence of melting by plumes enhanced by emerging subglacial meltwater sourced from frictional basal melt (e.g., Christoffersen et al., 2012); such plumes will clearly have a diminished influence 60 km from the ice front, where plume velocity has decreased. Estimated SMRs for icebergs stuck in ice mélange in Sermilik and Ilulissat fjords range from 0.1 to 0.8 m d^{-1}, and increase with iceberg draft and submerged ice area (Enderlin et al., 2016). These melt rates are more similar to ours near KNS, due both to the relatively similar distance from the grounding line to the icebergs (from 0 to 20 km away) and our estimates (150 to 2,400 m away), as well as the comparable summer intermediate ambient water temperatures in Ilulissat (up to 2.2°C) (Mernild et al., 2015), Sermilik (up to 2°C) (Straneo et al., 2010, 2011), and Kangersuneq (up to 2.5°C) fjords.

Estimated SMRs for the KNS ice tongue in spring 2013 are one to two orders of magnitude larger than SMRs estimated between 2000 and 2010 for the floating tongue at Petermann Glacier (0.07 ± 0.035 m d^{-1}) (Johnson et al., 2011; Enderlin

and Howat, 2013). The difference in melt rate magnitude in this case is likely due to both the difference in ambient ocean temperatures at ice keel depth between the two fjords as well as meltwater plume dynamics. The ambient water temperatures in northwest Greenland are much lower at keel depth than those in southwest Greenland, peaking at 0.2°C at nearly 500 m depth in Peterman Fjord (Johnson et al., 2011), where keel depths in the first few km of the fjord reach ∼480 m (Wilson et al., 2017). In contrast, ambient water temperatures at keel depth for KNS (∼80 m near the grounding line) fall between 1.3 and 2.0°C, depending on the season (Mortensen et al., 2013; Motyka et al., 2017). Plume dynamics may also fundamentally differ, with the weak melt-driven convective plumes beneath Petermann (which has a ∼70 km long permanent ice tongue) more akin to those at large Antarctic ice shelves, and strong subglacial discharge-driven plumes beneath the short ice tongue at KNS giving rise to convection-driven melt as observed at tidewater glaciers in mid-summer (Jenkins, 2011). In addition, the difference in velocity between KNS and Petermann glaciers may play a secondary role in controlling estimated SMRs. The average winter velocity for KNS is ∼8 km a^{-1}, eight times that of Petermann Glacier (Johnson et al., 2011). A faster-flowing, warm based glacier will create more basal friction and thus more basal melt (e.g., Holland et al., 2008; Christoffersen et al., 2012), producing more vigorous subglacial meltwater plumes and inducing higher SMRs even in winter (Carroll et al., 2015; Cowton et al., 2015; Slater et al., 2015).

Utilizing summer hydrographic observations between ∼35 and 88 km from the Kangerdlugssuaq Glacier terminus, Inall et al. (2014) estimated heat delivery to the calving front equivalent to 10 m d^{-1} of ice melt. Motyka et al. (2017) used parameters derived from models and hydrographic measurements 12 km from the KNS ice front to estimate a near-terminus late-summer SMR of ∼3–7 m d^{-1}. Our empirically-derived SMRs are nearly an order of magnitude lower than those estimated by Inall et al. (2014) and the upper range estimates of Motyka et al. (2017), despite similar ambient fjord water temperatures (up to 2.25°C at depth for Kangerdlugssuaq Fjord; Inall et al., 2014). It is unlikely that hydrographic estimates taken more than 30 km from the terminus realistically represent the heat energy used for melting the ice front, as a large portion of this energy might be lost to melting of any ice mélange and icebergs in the fjord before reaching the glacier (Enderlin et al., 2016). In fjords like Helheim, where icebergs are large enough to cover the full fjord depth (Enderlin and Hamilton, 2014), deep water could also be cooled by the melting of icebergs at depth. Heat transport to the ice front can also be reduced through vertical mixing of the water column via wind-driven internal seiches (e.g., Arneborg and Liljebladh, 2001; Cottier et al., 2010) or by the convective overturning of water due to the release of brine from sea ice formation (Cottier et al., 2010). In addition, the presence of shallow sills in the fjord alter the fjord circulation and may prevent deeper, warm water from reaching the ice front (e.g., Mortensen et al., 2011, 2013). This suggests that terminus melt rates derived from distal along-fjord heat flux values may be too high unless the heat lost to mid-fjord melting, vertical mixing, and fjord bathymetry are considered.

Freshwater Flux from Submarine Melting of the Ice Tongue

Given the potential importance of meltwater generation to fjord water properties and nutrient productivity (Meire et al., 2017), we here estimate the spring freshwater flux from submarine melting of the ice tongue. Using grounded terminus width (∼4,500 m), depth (∼250 m), and average velocity from March to May 2013 (∼6.9 km a^{-1}), spring ice flux across the KNS grounding line was estimated to be 246 m^3 s^{-1}. Assuming a simplified rectangular submarine configuration of the ice tongue with a width of ∼1,800 m and a length of ∼2,500 m, total basal submerged area is ∼4.5 km^2. Using spatially averaged SMR_{SS} from our western and eastern fjord flowlines, meltwater flux derived from the ice tongue ranges from 26 to 36 m^3 s^{-1} (11 to 15% of spring grounding line ice flux) in March, and from 36 to 42 m^3 s^{-1} in May (15 to 17% of spring grounding line ice flux). This partitioning of freshwater flux entering the fjord is comparable to that estimated by Xu et al. (2013) for Store Glacier in western Greenland, where submarine melting accounted for 20% of August 2010 glacier influx. In contrast, our flux partitioning is much lower than that estimated by Motyka et al. (2003, 2013) for LeConte Glacier in Alaska, where submarine melting accounts for 50–67% of summer frontal ablation. Differences in flux partitioning are likely due to seasonality and fjord temperatures, and to terminus geometry (Truffer and Motyka, 2016).

While ice tongue melt only accounts for ∼11–17% of the overall spring grounding line flux, it provides a significant amount of freshwater to the fjord in spring months, when surface runoff is largely absent. As such, the associated inputs of freshwater into the fjord at different depths from submarine melting may have a major impact on fjord water stratification, circulation and associated productivity (e.g., Motyka et al., 2013; Sciascia et al., 2013; Sutherland et al., 2014; Meire et al., 2017).

Potential Applications

We have derived SMRs using changes in the freeboard of a *seasonally* floating ice tongue as it advances down-fjord during the spring, building upon earlier work using freeboard and ice flux divergence to estimate SMRs of floating ice tongues in Greenland (e.g., Motyka et al., 2011; Enderlin and Howat, 2013). This technique has considerable potential to further our understanding of ice-ocean interactions and submarine melting in glacial fjords. Using both satellite and time-lapse imagery, seasonal differences in SMR could be evaluated by estimating melting throughout the year, as long as an ice tongue is present in winter and spring, and icebergs are present in summer and autumn sufficiently close to the ice front (following methods of Enderlin and Hamilton, 2014). In addition, analysis of seasonally floating ice tongues presents the opportunity to derive SMR estimates much nearer to glacier calving fronts (when compared with estimates using hydrographic profiles), in the precise location where the key processes controlling calving dynamics and retreat are not well resolved. We anticipate that our estimates of SMR, and others derived using this methodology, will be used to tune fjord circulation and plume models, which in turn will soon be used to force ice sheet models predicting

the future of the Greenland Ice Sheet and its contribution to sea level rise.

Our submarine melt rate estimates are derived from an ice tongue that is already floating, thus they do not affect the annual mass balance of the grounded portion of KNS. Nevertheless, the submarine melting of the ice tongue may affect its ability to buttress the winter ice flux and discharge across the grounding line (e.g., Motyka et al., 2011; Krug et al., 2015), with potential negative consequences for annual mass balance. If SMRs increase in the future as is expected under climate projections, the residence time of seasonal ice tongues like that at KNS will decrease, effectively extending the length of the calving season and allowing for greater mass loss from the grounded portion of the ice sheet. In addition, quantifying ice tongue melt rates can tell us a lot about calving front melt processes. For example, the spatial distribution of ice front SMRs (for which our ice tongue SMRs are a proxy) can influence the morphology of the calving front through spatially heterogeneous undercutting, with potential implications for calving frequency and style (Straneo et al., 2012; Chauché et al., 2014; Carroll et al., 2015; Slater et al., 2017), and ultimately glacier retreat, velocity and ice flux. A better understanding of spatial variations in submarine melting of the ice front may lead to the development of a relationship between melt distribution and calving, which is poorly understood but likely of critical importance for controlling tidewater glacier dynamics.

CONCLUSIONS

Improved estimates of SMR are essential to gain a better understanding of the processes controlling ice dynamics at tidewater glacier termini, and in particular, the potential relationship between submarine melt and tidewater glacier acceleration and retreat. Using high-resolution TerraSAR-X and TanDEM-X satellite imagery, we have estimated SMRs of a seasonal floating ice tongue adjacent to the grounding line of KNS. Changes in freeboard of the ice tongue, both with distance from the grounding line and across the fjord, have been used to estimate spatial variations in melt rate.

Our estimates of spring steady state SMR near the grounding line of KNS reach $1.4 \pm 0.5\,\mathrm{m\ d^{-1}}$, and decrease with distance down-fjord from the glacier grounding line, with mean rates up to 0.8 ± 0.3 and $0.7 \pm 0.3\,\mathrm{m\ d^{-1}}$ for the eastern and western parts of the ice tongue, respectively. There is also considerable across-fjord variability in SMR which may be driven by variation in the ice tongue draft and the temperature stratification in the fjord, but may also reflect the strength of any subglacial meltwater plumes present. The submarine meltwater flux derived from the ice tongue ranges from 26 to 42 $\mathrm{m^3\ s^{-1}}$, which accounts for between 11 and 17% of the grounding line ice flux into the fjord in the spring months, prior to the onset of ice sheet surface melt. Our results demonstrate that using high resolution satellite imagery to analyze changes in freeboard at floating seasonal ice tongues has considerable potential to reveal in detail the temporal and spatial variations in SMR at tidewater glacier termini.

AUTHOR CONTRIBUTIONS

AM performed all of the analysis and led the writing of the manuscript. NG produced the DEMs and ice velocities. All authors contributed ideas and methodological developments, and provided editorial input on the manuscript.

FUNDING

AM is supported by a Principal's Career Development PhD Scholarship from the University of Edinburgh. We acknowledge NERC grants NE/K015249/1 (to PN) and NE/K014609/1 (to AS), and a NERC PhD studentship (to DS). We also acknowledge DLR projects XTI_GLAC0296 and LAN1534 (to NG). The research leading to these results has also received funding from the Scottish Alliance for Geoscience, Environment and Society's Small Grant Scheme (to AM).

ACKNOWLEDGMENTS

We acknowledge M. Truffer and M. Fahnestock of the University of Alaska, Fairbanks for the use of time lapse camera imagery, which was acquired under the US NSF grant PLR-0909552. Data from the Programme for Monitoring of the Greenland Ice Sheet (PROMICE) were provided by the Geological Survey of Denmark and Greenland (GEUS) at http://www.promice.dk and data from the Danish Meteorological Institute (DMI) are available at http://www.dmi.dk.

SUPPLEMENTARY MATERIAL

The Supplementary Material for this article can be found online at: https://www.frontiersin.org/articles/10.3389/feart.2017.00107/full#supplementary-material

REFERENCES

Abermann, J., van As, D., Wacker, S., and Langley, K. (2017). Mountain glacier vs ice sheet in greenland–learning from a new monitoring site in west greenland. *Geophys. Res. Abstr.* 19, EGU2017–9445.

Ahlstrom, A. P., Gravesen, P., Andersen, S. B., van As, D., Citterio, M., Fausto, R. S., et al. (2008). A new programme for monitoring the mass loss of the Greenland ice sheet. *Geol. Surv. Denmark Greenl. Bull.* 15, 61–64.

Arneborg, L., and Liljebladh, B. (2001). The internal seiches in gullmar fjord. part I: dynamics. *J. Phys. Oceanogr.* 31, 2549–2566. doi: 10.1175/1520-0485(2001)031<2549:TISIGF>2.0.CO;2

Cappelen, J. (ed.). (2016). *Greenland–DMI Historical Climate Data Collection 1784-2016.* DMI Report 17-04, Copenhagen, Available online at: www.dmi.dk/laer-om/generelt/dmi-publikationer/2013.

Carr, J. R., Stokes, C. R., and Vieli, A. (2013). Recent progress in understanding marine-terminating arctic outlet glacier response to climatic and oceanic forcing: twenty years of rapid change. *Prog. Phys. Geog.* 37, 436–467. doi: 10.1177/0309133313483163

Carroll, D., Sutherland, D. A., Hudson, B., Moon, T., Catania, G. A., Shroyer, E. L., et al. (2016). The impact of glacier geometry on meltwater plume structure and submarine melt in Greenland fjords. *Geophys. Res. Lett.* 43, 9739–9748. doi: 10.1002/2016GL070170

Carroll, D., Sutherland, D. A., Shroyer, E. L., Nash, J. D., Catania, G. A., and Stearns, L. A. (2015). Modeling turbulent subglacial meltwater plumes: implications for fjord-scale buoyancy-driven circulation. *J. Phys. Oceanogr.* 45, 2169–2185. doi: 10.1175/JPO-D-15-0033.1

Chauché, N., Hubbard, A., Gascard, J. C., Box, J. E., Bates, R., Koppes, M., et al. (2014). Ice-ocean interaction and calving front morphology at two west Greenland tidewater outlet glaciers. *Cryosphere* 8, 1457–1468. doi: 10.5194/tc-8-1457-2014

Christoffersen, P., O'Leary, M., van Angelen, J. H., and van den Broeke, M. (2012). Partitioning effects from ocean and atmosphere on the calving stability of Kangerdlugssuaq Glacier, East Greenland. *Ann. Glaciol.* 53, 249–256. doi: 10.3189/2012AoG60A087

Cottier, F. R., Nilsen, F., Skogseth, R., Tverberg, V., Skarðhamar, J., and Svendsen, H. (2010). Arctic fjords: a review of the oceanographic environment and dominant physical processes. *Geol. Soc. Lond. Spec. Publ.* 334, 35–50. doi: 10.1144/SP344.4

Cowton, T. R., Slater, D. A., Sole, A., Goldberg, D. N., and Nienow, P. W. (2015). Modelling the impact of glacial runoff on fjord circulation and submarine melt rate using a new subgrid-scale parameterization for glacial plumes. *J. Geophys. Res. Oceans* 120, 796–812. doi: 10.1002/2014JC010324

Dehecq, A., Millan, R., Berthier, E., Gourmelen, N., Trouvé, E., and Vionnet, V. (2016). Elevation changes inferred from TanDEM-X data over the mont-blanc area: impact of the X-band interferometric bias. *IEEE* 9, 3870–3882. doi: 10.1109/JSTARS.2016.2581482

Depoorter, M. A., Bamber, J. L., Griggs, J. A., Lenaerts, J. T., Ligtenberg, S. R., van den Broeke, M. R., et al. (2013). Calving fluxes and basal melt rates of Antarctic ice shelves. *Nature* 502, 89–92. doi: 10.1038/nature12567

Eineder, M., Minet, C., Steigenberger, P., Cong, X., and Fritz, T. (2011). Imaging geodesy–toward centimeter-level ranging accuracy with TerraSAR-X. *IEEE Trans. Geosci. Remote* 49, 661–671. doi: 10.1109/TGRS.2010.2060264

Enderlin, E. M., and Hamilton, G. S. (2014). Estimates of iceberg submarine melting from high-resolution digital elevation models: application to Sermilik Fjord, East Greenland. *J. Glaciol.* 60, 1084–1092. doi: 10.3189/2014JoG14J085

Enderlin, E. M., Hamiton, G. S., Straneo, F., and Sutherland, D. A. (2016). Iceberg meltwater fluxes dominate the freshwater budget in Greenland's iceberg-congested glacial fjords. *Geophys. Res. Lett.* 43, 11287–11294. doi: 10.1002/2016GL070718

Enderlin, E. M., and Howat, I. M. (2013). Submarine melt rate estimates for floating termini of Greenland outlet glaciers (2000-2010). *J. Glaciol.* 59, 67–75. doi: 10.3189/2013JoG12J049

Enderlin, E. M., Howat, I. M., Jeong, S., Noh, M., van Angelen, J. H., and van den Broeke, M. R. (2014). An improved mass budget for the Greenland ice sheet. *Geophys. Res. Lett.* 41, 866–872. doi: 10.1002/2013GL059010

Fried, M. J., Catania, G. A., Bartholomaus, T. C., Duncan, D., Davis, M., Stearns, L. A., et al. (2015). Distributed subglacial discharge drives significant submarine melt at a Greenlandic tidewater glacier. *Geophys. Res. Lett.* 42, 9328–9336. doi: 10.1002/2015GL065806

Funk, M., Echelmeyer, K., and Iken, A. (1994). Mechanisms of fast flow in Jakobshavns Isbræ, West Greenland: part, II. Modeling of englacial temperatures. *J. Glaciol.* 40, 569–585. doi: 10.1017/S0022143000012466

Goelzer, H., Huybrechts, P., Furst, J. J., Nick, F. M., Andersen, M. L., Edwards, T. L., et al. (2013). Sensitivity of Greenland ice sheet projections to model formulations. *J. Glaciol.* 59, 733–749. doi: 10.3189/2013JoG12J182

Gourmelen, N., Goldberg, D., Snow, K., Henley, S., Bingham, R., Kimura, S., et al. (2017). Channelized melting drives thinning under a rapidly melting Antarctic ice shelf. *Geophys. Res. Lett.* 44, 9796–9804. doi: 10.1002/2017GL074929

Hock, R. (2003). Temperature index melt modelling in mountain areas. *J. Hydro.* 282, 104–115. doi: 10.1016/S0022-1694(03)00257-9

Holland, D. M., and Jenkins, A. (1999). Modeling thermodynamic ice-ocean interactions at the base of an ice shelf. *J. Phys. Oceanogr.* 29, 1787–1800. doi: 10.1175/1520-0485(1999)029<1787:MTIOIA>2.0.CO;2

Holland, D. M., Thomas, R. H., de Young, B., Ribergaard, M. H., and Lyberth, B. (2008). Acceleration of Jakobshavn Isbrae triggered by warm subsurface ocean waters. *Nat. Geosci.* 1, 659–664. doi: 10.1038/ngeo316

Howat, I. M., Negrete, A., and Smith, B. E. (2014). The Greenland Ice Mapping Project (GIMP) land classification and surface elevation datasets. *Cryosphere* 8, 1509–1518. doi: 10.5194/tc-8-1509-2014

Iken, A., Echelmeyer, K., Harrison, W., and Funk, M. (1993). Mechanisms of fast flow in Jakobshavns Isbræ, West Greenland: part, I. measurements of temperature and water level in deep boreholes. *J. Glaciol.* 39, 15–25. doi: 10.1017/S0022143000015689

Inall, M., Murray, T., Cottier, F., Scharrer, K., Boyd, T., Heywood, K., et al. (2014). Oceanic heat delivery via Kangerdlugssuaq Fjord to the south-east Greeland ice sheet. *J. Geophys. Res. Oceans* 119, 631–645. doi: 10.1002/2013JC009295

Jackson, R., and Straneo, F. (2016). Heat, salt, and freshwater budgets for a Glacial Fjord in Greenland. *J. Phys. Oceanogr.* 46, 2735–2768. doi: 10.1175/JPO-D-15-0134.1

Jenkins, A. (2011). Convection-Driven melting near the grounding lines of ice shelves and tidewater glaciers. *J. Phys. Oceanogr.* 41, 2279–2294. doi: 10.1175/JPO-D-11-03.1

Jenkins, A., and Doake, C. S. M. (1991). Ice-ocean interaction on Ronne Ice Shelf, Antarctica. *J. Geophys. Res.* 96, 791–813. doi: 10.1029/90JC01952

Johnson, H., Munchow, A., Falkner, K., and Melling, H. (2011). Ocean circulation and properties in Petermann Fjord, Greenland. *J. Geophys. Res.* 116:C01003. doi: 10.1029/2010JC006519

Joughin, I., Abdalati, W., and Fahnestock, M. (2004). Large fluctuations in speed on Greenland's Jakobshavn Isbrae Glacier. *Nature* 432, 608–610. doi: 10.1038/nature03130

Krabill, W. B. (2016). *Ice Bridge ATM L1B Elevation and Return Strength*. Boulder, CO: NASA DAAC at the National Snow and Ice Data Center.

Krieger, G., Moreira, A., Fiedler, H., Hajnsek, I., Werner, M., Younis, M., et al. (2007). TanDEM-X: a satellite formation for high-resolution SAR interferometry. *IEEE Trans. Geosci. Remote* 45, 3317–3341. doi: 10.1109/TGRS.2007.900693

Krug, J., Durand, G., Gagliardini, O., and Weiss, J. (2015). Modelling the impact of submarine frontal melting and ice mélange on glacier dynamics. *Cryosphere* 9, 989–1003. doi: 10.5194/tc-9-989-2015

Lea, J. M., Mair, D. W. F., Nick, F. M., Rea, B. R., Weidick, A., Kjær, K. H., et al. (2014). Terminus-driven retreat of a major southwest Greenland tidewater glacier during the early 19th century: insights for glacier reconstructions and numerical modelling. *J. Glaciol.* 60, 333–344. doi: 10.3189/2014JoG13J163

Luckman, A., Benn, D. I., Cottier, F., Bevan, S., Nilsen, F., and Inall, M. (2015). Calving rates at tidewater glaciers vary strongly with ocean temperature. *Nat. Commun.* 6:8566. doi: 10.1038/ncomms9566

Meire, L., Mortensen, J., Meire, P., Jull-Pedersen, T., Sejr, M. K., Rysgaard, S., et al. (2017). Marine-terminating glaciers sustain high productivity in Greenland fjords. *Glob. Change. Biol.* 23, 5344-5357. doi: 10.1111/gcb.13801

Mernild, S. H., Holland, D. M., Holland, D., Rosing-Asvid, A., Yde, J. C., Liston, G. E., et al. (2015). Freshwater flux and spatiotemporal simulated runoff variability into Ilulissat Icefjord, West Greenland, linked to salinity and temperature observations near tidewater glacier margins obtained using instrumented ringed seals. *J. Phys. Ocean.* 45, 1426–1445. doi: 10.1175/JPO-D-14-0217.1

Mortensen, J., Bendtsen, J., Motyka, R. J., Lennert, K., Truffer, M., Fahnestock, M., et al. (2013). On the seasonal freshwater stratification in the proximity of fast-flowing tidewater outlet glaciers in a sub-Arctic sill fjord. *J. Geophys. Res. Oceans* 118, 1382–1395. doi: 10.1002/jgrc.20134

Mortensen, J., Lennert, K., Bendtsen, J., and Rysgaard, S. (2011). Heat sources for glacial melt in a sub-Arctic fjord (Godthåbsfjord) in contact with the Greenland Ice Sheet. *J. Geophys. Res.* 116:C01013. doi: 10.1029/2010JC006528

Motyka, R., Hunter, L., Echelmeyer, K., and Connor, C. (2003). Submarine melting at the terminus of a temperate tidewater glacier, Le Conte Glacier, Alaska. *Ann. Glaciol.* 36, 57–65. doi: 10.3189/172756403781816374

Motyka, R. J., Cassotto, R., Truffer, M., Kjeldsen, K. K., Van As, D., Korsgaard, N. J., et al. (2017). Asynchronous behavior of outlet glaciers feeding Godthåbsfjord (Nuup Kangerlua) and the triggering of Narsap Sermia's retreat in SW Greenland. *J. Glaciol.* 63, 288–308. doi: 10.1017/jog.2016.138

Motyka, R. J., Dryer, W. P., Amundson, J., Truffer, M., and Fahnestock, M. (2013). Rapid submarine melting driven by subglacial discharge, LeConte Glacier, Alaska. *Geophys. Res. Lett.* 40, 5153–5158. doi: 10.1002/grl.51011

Motyka, R., Truffer, M., Fahnestock, M., Mortensen, J., Rysgaard, S., and Howat, I. (2011). Submarine melting of the 1985 Jakobshavn Isbræ floating tongue and the triggering of the current retreat. *J. Geophys. Res.* 116:F01007. doi: 10.1029/2009JF001632

Nick, F. M., Vieli, A., Howat, L. M., and Joughin, I. (2009). Large-scale changes in Greenland outlet glacier dynamics triggered at the terminus. *Nat. Geosci.* 2, 110–114. doi: 10.1038/ngeo394

Nuth, C., and Kääb, A. (2011). Co-registration and bias corrections of satellite elevation data sets for quantifying glacier thickness change. *Cryosphere* 5, 271–290. doi: 10.5194/tc-5-271-2011

O'Leary, M., and Christoffersen, P. (2013). Calving on tidewater glaciers amplified by submarine frontal melting. *Cryosphere* 7, 119–128. doi: 10.5194/tc-7-119-2013

Paul, F., Bolch, T., Kääb, A., Nagler, T., Nuth, C., Scharrer, K., et al. (2015). The glacier climate change initiative: methods for creating glacier area, elevation change and velocity products. *Remote Sens. Environ.* 162, 408–426. doi: 10.1016/j.rse.2013.07.043

Ribergaard, M. H. (2013). *Oceanographic Investigations off West Greenland 2012*. NAFO Scientific Council Documents, 13/003.

Rignot, E., and Jacobs, S. (2002). Rapid bottom melting widespread near Antarctic Ice Sheet grounding lines. *Science* 296, 2020–2023. doi: 10.1126/science.1070942

Rignot, E., Jacobs, S., Mouginot, J., and Scheuchl, B. (2013). Ice-Shelf melting around Antarctica. *Science* 341, 266–270. doi: 10.1126/science.1235798

Rignot, E., Koppes, M., and Velicogna, I. (2010). Rapid submarine melting of the calving faces of west Greenland glaciers. *Nat. Geosci.* 3, 187–191. doi: 10.1038/ngeo765

Rizzoli, P., Bräutigam, B., Kraus, T., Martone, M., and Krieger, G. (2012). Relative height error analysis of TanDEM-X elevation data. *ISPRS J. Photogramm.* 73, 30–38. doi: 10.1016/j.isprsjprs.2012.06.004

Sciascia, R., Straneo, F., Cenedese, C., and Heimbach, P. (2013). Seasonal variability of submarine melt rate and circulation in an East Greenland fjord. *J. Geophys. Res. Oceans* 118, 2492–2506. doi: 10.1002/jgrc.20142

Slater, D. A., Nienow, P. W., Cowton, T. R., Goldberg, D. N., and Sole, A. J. (2015). Effect of near-terminus subglacial hydrology on tidewater glacier submarine melt rates. *Geophys. Res. Lett.* 4, 2861–2868. doi: 10.1002/2014GL062494

Slater, D. A., Nienow, P. W., Sole, A. J., Cowton, T. R., Mottram, R., Langen, P., et al. (2017). Spatially distributed runoff at the grounding line of a large Greenlandic tidewater glacier inferred from plume modelling. *J. Glaciol.* 63, 309-323. doi: 10.1017/jog.2016.139

Smith, A. M. (1996). Ice shelf basal melting at the grounding line, measured from seismic observations. *J. Geophys. Res.* 101, 22749–22755. doi: 10.1029/96JC02173

Sole, A. J., Mair, D. W. F., Nienow, P. W., Bartholonew, I. D., King, M. A., Burke, M. J., et al. (2011). Seasonal speedup of a Greenland marine-terminating outlet glacier forced by surface melt-induced changes in subglacial hydrology. *J. Geophys. Res.* 116:F03014. doi: 10.1029/2010JF001948

Straneo, F., and Cenedese, C. (2015). The dynamics of Greenland's glacial fjords and their role in climate. *Ann. Rev. Mar. Sci.* 7, 89–112. doi: 10.1146/annurev-marine-010213-135133

Straneo, F., Curry, R. G., Sutherland, D. A., Hamilton, G. S., Cenedese, C., Våge, K., et al. (2011). Impact of fjord dynamics and glacial runoff on the circulation near Helheim Glacier. *Nat. Geosci.* 4, 322–327. doi: 10.1038/ngeo1109

Straneo, F., Hamilton, G. S., Sutherland, D. A., Stearns, L. A., Davidson, F., Hammill, M. O., et al. (2010). Rapid circulation of warm subtropical waters in a major glacial fjord in East Greenland. *Nat. Geosci.* 3, 182–186. doi: 10.1038/ngeo764

Straneo, F., Sergienko, O., Heimbach, P., Bitz, C., Bromwich, D., and Catania, G. (2012). *Understanding the Dynamic Response of Greenland's Marine Terminating Glaciers to Oceanic and Atmospheric Forcing: A White Paper by the U.S.* CLIVER Working Group on Greenland Ice Sheet-Ocean Interactions (GRISO). U.S. CLIVAR Project Office, Washington, DC.

Sundal, A., Shepherd, A., Van Den Broeke, J., Gourmelen, N., and Park, J. (2013). Controls on short-term variations in Greenland glacier dynamics, *J. Glaciol.* 59, 883–892. doi: 10.3189/2013JoG13J019

Sutherland, D. A., and Straneo, F. (2012). Estimating ocean heat transports and submarine melt rates in Sermilik Fjord, Greenland, using lowered acoustic Doppler current profiler (LADCP) velocity profiles. *Ann. Glaciol.* 53, 50–58. doi: 10.3189/2012AoG60A050

Sutherland, D. A., Straneo, F., and Pickart, R. S. (2014). Characteristics and dynamics of two major Greenland glacial fjords. *J. Geophys. Res. Oceans* 119, 3767–3791. doi: 10.1002/2013JC009786

Tedstone, A. J., Nienow, P. W., Gourmelen, N., and Sole, A. J. (2014). Greenland ice sheet annual motion insensitive to spatial variations in subglacial hydraulic structure. *Geophys. Res. Lett.* 41, 8910–8917. doi: 10.1002/2014GL062386

Truffer, M., and Motyka, R. J. (2016). Where glaciers meet water: subaqueous melt and its relevance to glaciers in various settings. *Rev. Geophys.* 54, 220–239. doi: 10.1002/2015RG000494

van den Broeke, M. R., Bamber, J., Ettema, J., Rignot, E., Jan van de Berg, W., van Meijgaard, E., et al. (2009). Partitioning recent Greenland mass loss. *Science* 326, 984–986. doi: 10.1126/science.1178176

Vieli, A., and Nick, F. (2011). Understanding and modeling rapid dynamical changes of tidewater outlet glaciers: issues and implications. *Surv. Geophys.* 32, 437–458. doi: 10.1007/s10712-011-9132-4

Wilson, N., Straneo, F., and Heimbach, P. (2017). Satellite-derived submarine melt rates and mass balance (2011–2015) for Greenland's largest remaining ice tongues. *Cryosphere* 11, 2773–2782. doi: 10.5194/tc-11-2773-2017

Xu, Y., Rignot, E., Fenty, I., Menemenlis, D., and Flexas, M. M. (2013). Subaqueous melting of Store Glacier, west Greenland from three-dimensional, high-resolution numerical modeling and ocean observations. *Geophys. Res. Lett.* 40, 4648–4653. doi: 10.1002/grl.50825

Conflict of Interest Statement: The authors declare that the research was conducted in the absence of any commercial or financial relationships that could be construed as a potential conflict of interest.